

Multiplicity dependent J/ψ production in proton-proton collisions at the LHC

Multiplizitätsabhängige Erzeugung von J/ψ Mesonen in Proton-Proton Kollisionen am LHC

Zur Erlangung des Grades eines Doktors der Naturwissenschaften (Dr. rer. nat.)

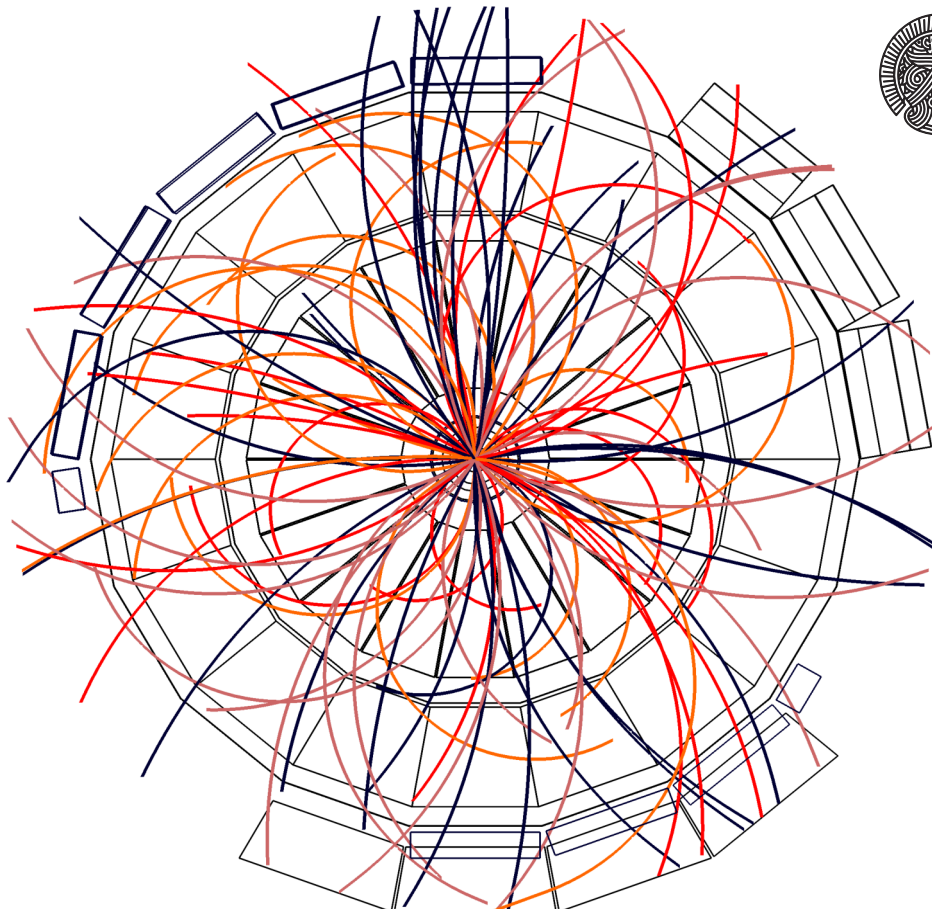
genehmigte Dissertation von Steffen Georg Weber aus Fulda

Tag der Einreichung: 16.10.2018, Tag der Prüfung: 26.11.2018

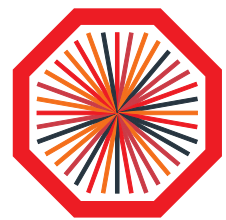
Darmstadt — D 17

1. Gutachten: Prof. Dr. Anton Andronic

2. Gutachten: Prof. Guy Moore, Ph.D.



TECHNISCHE
UNIVERSITÄT
DARMSTADT



Multiplicity dependent J/ψ production in proton-proton collisions at the LHC
Multiplizitätsabhängige Erzeugung von J/ψ Mesonen in Proton-Proton Kollisionen am LHC

Genehmigte Dissertation von Steffen Georg Weber aus Fulda

1. Gutachten: Prof. Dr. Anton Andronic
2. Gutachten: Prof. Guy Moore, Ph.D.

Tag der Einreichung: 16.10.2018

Tag der Prüfung: 26.11.2018

Darmstadt — D 17

Bitte zitieren Sie dieses Dokument als:

URN: urn:nbn:de:tuda-tuprints-84613

URL: <http://tuprints.ulb.tu-darmstadt.de/8461>

Dieses Dokument wird bereitgestellt von tuprints,
E-Publishing-Service der TU Darmstadt
<http://tuprints.ulb.tu-darmstadt.de>
tuprints@ulb.tu-darmstadt.de



Die Veröffentlichung steht unter folgender Creative Commons Lizenz:
Namensnennung – Weitergabe unter gleichen Bedingungen 4.0 International
(CC BY-SA 4.0)
<https://creativecommons.org/licenses/by-sa/4.0/>



There is a crack in everything. That's how the light gets in.
Leonard Cohen, "Anthem"



Abstract

The discovery of the J/ψ particle in 1974 helped to fully establish the quark model of hadrons and sparked an increased interest in particle physics that led to rapid developments in the field in the following years. This period was later coined the November Revolution in particle physics.

Due to the different energy scales at play in J/ψ production, both perturbative and nonperturbative aspects of Quantum ChromoDynamics (QCD) are relevant for an accurate description. Over time, increasingly sophisticated theoretical models have provided a more and more detailed picture of J/ψ production in hadronic interactions, albeit it is still defying a conclusive description of all aspects of its production.

Recently, high particle multiplicities created in proton-proton collisions have been met with increased interest due to observations of apparent collective phenomena traditionally linked with the creation of a medium in heavy-ion collisions. The correlation between J/ψ production and the charged-particle multiplicity is an excellent observable addressing the interplay between hard and soft processes. It can help to shape a complete picture of proton-proton collisions, especially with regard to mechanisms like multiparton interactions and saturation effects in the particle production.

ALICE is an experiment at the LHC, dedicated to the study of the hot and dense medium created in heavy-ion collisions. With its excellent tracking and particle identification capabilities in dense environments it is also well suited for the study of proton-proton collisions with high particle multiplicities. With the Run-2 data taking of the LHC, the highest collision energies ever created in the laboratory have become accessible. A special data taking campaign with the ALICE experiment focused on collecting collisions with high charged-particle multiplicities allows access to unprecedented multiplicity regimes.

In this thesis, a measurement of the self-normalized inclusive J/ψ yield at mid-rapidity in proton-proton collisions at $\sqrt{s} = 13$ TeV as a function of the self-normalized charged-particle multiplicity is presented. The analysis has been performed as a function of the multiplicity at mid-rapidity and at forward rapidity. Transverse momentum integrated J/ψ production and J/ψ production at low and high transverse momenta have been investigated.

A stronger than linear increase of J/ψ production with particle multiplicity is observed, with no significant effect of a rapidity gap between the J/ψ and the region in which the particles are measured. The increase is strongest for J/ψ at high transverse momentum.

The results of the analysis are compared to theoretical model predictions. Though differing in the assumptions on the physical processes, all of them agree at least qualitatively with the experimental results. With a comprehensive study of Monte Carlo simulations often overlooked autocorrelation effects between the J/ψ signal and the particle multiplicity are addressed. Based on this study, a refinement of the presented measurement via the exclusion of the regions most affected by autocorrelation effects from the particle multiplicity measurement is proposed.



Zusammenfassung

Die Entdeckung des J/ψ Teilchens im Jahre 1974 verhalf dem Quark-Modell der Hadronen zum Durchbruch und entfachte ein erhöhtes Interesse an der Teilchenphysik, das zu einer rasanten Entwicklung dieses Fachgebiets in den folgenden Jahren führte. Diese Periode wurde später als November-Revolution in der Teilchenphysik bekannt.

Aufgrund der unterschiedlichen Energieskalen, die bei der Erzeugung von J/ψ auftreten, sind sowohl störungstheoretisch behandelbare Aspekte der Quantenchromodynamik (QCD) für eine akkurate Beschreibung ausschlaggebend, als auch solche die sich einer störungstheoretischen Behandlung entziehen. Im Laufe der Zeit wurde mittels einer zunehmenden Verfeinerung theoretischer Modelle ein immer detaillierter werdendes Bild der Erzeugung von J/ψ in hadronischen Kollisionen erreicht, jedoch entzieht es sich weiterhin einer vollständigen Beschreibung sämtlicher Aspekte seiner Erzeugung.

In jüngster Zeit wird die Erzeugung hoher Teilchenzahlen in Proton-Proton-Kollisionen mit verstärktem Interesse beobachtet. Grund hierfür sind Beobachtungen augenscheinlich kollektiver Phänomene, die üblicherweise mit der Erzeugung eines Mediums in Schwerionenkollisionen in Verbindung gebracht werden. Die Korrelation zwischen der Erzeugung von J/ψ und der Zahl geladener Teilchen ist eine ausgezeichnete Observable des Zusammenspiels hoch- und nierigenergetischer Prozesse. Sie kann dabei helfen, ein vollständiges Bild von Proton-Proton-Kollisionen zu gestalten, insbesondere in Bezug auf Mechanismen wie Multiparton-Interaktionen und Sättigungseffekte in der Teilchenerzeugung.

ALICE ist ein Experiment am LHC, spezialisiert auf die Untersuchung des heißen und dichten Mediums, welches in Schwerionenkollisionen erzeugt wird. Mit seinen exzellenten Fähigkeiten zur Spurfindung und Teilchenidentifikation in dichten Umgebungen ist es auch für die Untersuchung von Proton-Proton-Kollisionen mit hoher Teilchenzahl gut geeignet. Mit der zweiten Datennahmeperiode am LHC werden die höchsten je im Labor erzeugten Schwerpunktenergien zugänglich. Eine spezialisierte Datennahmekampagne des ALICE Experiments mit dem Schwerpunkt auf Kollisionen hoher Teilchenzahlen verschafft Zugriff auf bisher unerreichte Multiplizitätsbereiche.

In dieser Arbeit wird eine Messung der selbstdurchströmten J/ψ -Erzeugung in zentraler Rapidity in Proton-Proton-Kollisionen einer Schwerpunktenergie von $\sqrt{s} = 13$ TeV als Funktion der selbstdurchströmten Multiplizität geladener Teilchen vorgestellt. Die Analyse wurde als Funktion der Multiplizität in zentraler und vorwärts gerichteter Rapidity durchgeführt. Die Transversalimpuls-integrierte J/ψ -Erzeugung und die J/ψ Erzeugung bei niedrigem und hohem Transversalimpuls wurden untersucht.

Die Erzeugung von J/ψ steigt mit zunehmender Teilchenzahl stärker als linear an, eine Rapiditylücke zwischen dem J/ψ und der Region, in der die Teilchen gemessen werden, hat keinen signifikanten Einfluss. Die Zunahme ist am stärksten für J/ψ mit hohem Transversalimpuls.

Die Ergebnisse der Analyse werden mit Vorhersagen theoretischer Modelle verglichen. Obwohl unterschiedliche physikalische Prozesse angenommen werden, stimmen alle zumindest qualitativ mit den experimentellen Ergebnissen überein. Eine ausführliche Untersuchung von Monte Carlo-Simulationen behandelt häufig übersehene Autokorrelations-Effekte zwischen dem J/ψ -Signal und der Teilchenmultiplizität. Basierend auf diesen Untersuchungen wird eine Verfeinerung der vorgestellten Messung mittels des Auschlusses der am stärksten von Autokorrelationen betroffenen Bereiche von der Messung der Teilchenmultiplizität vorgeschlagen.



Contents

1. Introduction	1
1.1. The Standard Model of particle physics	1
1.2. Proton-proton collisions	3
1.3. Charged-particle multiplicities	5
1.4. Heavy-ion collisions	6
1.5. Collectivity in proton-proton collisions?	8
1.6. Charmonium	9
1.6.1. Charmonium in hadronic collisions	11
1.6.2. Prompt charmonium production mechanisms in hadronic collisions	12
1.6.3. Charmonium in heavy-ion collisions	17
1.7. Outline of the thesis	20
2. Charmonium production as a function of event-activity	21
2.1. Experimental results	21
2.1.1. Light-flavor sector	26
2.2. Theoretical models	27
2.2.1. Percolation model	27
2.2.2. Higher Fock states model	28
2.2.3. CGC model	30
2.2.4. EPOS3 event generator	30
2.3. Summary	32
3. The ALICE experiment at the LHC	35
3.1. The Large Hadron Collider	35
3.2. ALICE	36
3.3. The Inner Tracking System	37
3.4. The Time Projection Chamber	38
3.5. The V0	38
3.6. Tracking	39
3.7. Particle identification	40
3.7.1. Particle identification in the TPC	41
4. Analysis	43
4.1. Analysis Strategy	43
4.2. Event Selection	44
4.2.1. Data samples	44
4.2.2. Collision candidate selection	44
4.2.3. High-multiplicity trigger	45
4.3. Monte Carlo simulations	45
4.4. Event normalization	46
4.4.1. Trigger efficiency	46
4.4.2. Vertex finding efficiency	47
4.5. Multiplicity Estimation	48
4.5.1. Mid-rapidity multiplicity	48

4.5.2. Forward rapidity multiplicity	50
4.5.3. Multiplicity intervals used in the analysis	52
4.6. Track Selection	54
4.7. Efficiency correction	56
4.8. Low-mass background suppression	58
4.9. Signal Extraction	59
5. Systematic Uncertainty Estimation	65
5.1. Uncertainty on the charged-particle multiplicity	65
5.2. Uncertainty on the J/ψ yield	68
5.3. Additional checks for possible biases	72
6. Results and discussion	75
6.1. Inclusive J/ψ production at mid-rapidity as a function of charged-particle multiplicity	75
6.2. Comparison to other experimental results	77
6.3. Interpretation	78
6.3.1. Linear increase with offset	78
6.3.2. Stronger-than-linear increase	80
6.3.3. Comparison to predictions from the PYTHIA8 event generator	83
6.3.4. Comparisons to theoretical model predictions	84
6.4. Summary	87
7. PYTHIA8 study	89
7.1. The PYTHIA event generator	89
7.2. Technicalities	91
7.3. Charged-particle multiplicity	91
7.4. Heavy quark and quarkonium production in PYTHIA8	93
7.5. Multiplicity dependence	95
7.6. Multiparton interactions and color reconnection	96
7.7. Investigation of auto-correlation	99
7.8. Summary	105
8. Summary and Outlook	107
8.1. Outlook	108
Appendices	109
A. Signal extraction in $N_{\text{ch,fwd}}$ and p_T bins	109
B. Systematic uncertainties of the results in transverse momentum bins	115
B.1. Uncertainty on the charged-particle multiplicity	115
B.2. Uncertainty on the J/ψ yield	116
C. Additional plots of the experimental results	119
C.1. Fit results	120
Bibliography	135

1 Introduction

1.1 The Standard Model of particle physics

The **Standard Model of particle physics (SM)** contains the basic building blocks of matter, and the interactions between them. Besides gravity — which is not part of the SM, and can be safely neglected at the scales examined in particle physics — these are the following:

- the electromagnetic force, acting between electrically charged particles,
- the weak force, acting between particles carrying weak hypercharge,
- the strong force, acting between particles carrying color-charge.

The forces are mediated by gauge bosons: the photon of the electromagnetic force, the W^\pm and Z^0 bosons of the weak force, and the gluons of the strong force.

Besides the interactions and the gauge bosons, the SM contains fermions on which these forces act and which make up the matter in the universe, at least the part that we understand so far, i.e. excluding dark matter. The elementary fermions come in the form of quarks, which carry both color-charge and electric charge, and of leptons that carry either only electric charge or are neutral (neutrinos). All of them carry mass and the weak hypercharge. Both the quarks and the leptons come in three generations of particles with similar properties but increasing mass. Each type of quark has an associated quantum number, called flavor, which is conserved under strong and electromagnetic interactions. In the case of the leptons, only the total lepton number is conserved under all interactions, whereas the lepton family number is only approximately conserved, as it is broken by neutrino oscillations. To each particle there exists a corresponding antiparticle with identical properties but opposite quantum numbers. The properties of the elementary particles of the SM are summarized in table 1.1.

The forces that act between the particles are described by Quantum Field Theories (QFTs), which will be shortly described in the following.

The first QFT that was developed is **Quantum ElectroDynamics (QED)**, describing the electromagnetic interaction. Technically, QED is an *abelian* gauge theory with $U(1)$ symmetry, i.e. there is only one kind of charge, and the force carrier particles — the photons — do not carry the charge themselves. Furthermore, they are massless, allowing the interaction to act on an infinite range. The electromagnetic coupling α_{em} constant is about $1/137$, this means precise calculations are possible by making an expansion in α_{em} in the framework of perturbation theory.

The **weak interaction** on the other hand is mediated by massive particles, the charged W^\pm and the neutral Z^0 bosons, which gives the interaction a finite range. This is also the reason for the apparent weakness of the weak interaction. The weak interaction is the only one breaking parity (P) symmetry (symmetry under parity transformation, i.e. inversion of all spatial coordinates) and charge-parity (CP) symmetry (symmetry under parity transformation and exchanges of all particles by corresponding antiparticles) and that does not conserve the flavor quantum number. QED and the theory of weak interactions can be combined in the common framework of electroweak theory. The theory also contains the Higgs mechanism as an explanation for the masses of the weak gauge bosons, and of the other elementary particles.

The strong interaction is described by **Quantum ChromoDynamics (QCD)**. It acts between particles carrying color-charge. Its symmetry is $SU(3)$, i.e. there are three distinct color-charges, often labeled

Table 1.1.: The elementary particles of the Standard model [1]. The quoted values for the neutrino masses are from direct measurements based on the analysis of the kinematics of charged particles emitted in weak decays together with the neutrinos. Data on anisotropies in the cosmic microwave background allows, under some model assumptions, to constrain the sum of the neutrino masses to $\sum m_\nu < 0.23 \text{ eV}/c^2$ [2].

	Fermions			Bosons	
	Quarks			Gauge bosons	
Name Mass Electric charge	up u 2.2 MeV/c ²	charm c $\frac{2}{3}e$ 1.275 GeV/c ²	top t 173 GeV/c ²	photon γ 0	W^\pm 80.379 GeV/c ² $\pm 1e$
Name Mass Electric charge	down d 4.7 MeV/c ²	strange s $-\frac{1}{3}e$ 95 MeV/c ²	bottom b 4.18 GeV/c ²	gluon g 0	Z^0 91.1876 GeV/c ² 0
	Leptons			Scalar boson	
Name Mass Electric charge	electron e 511 keV/c ²	muon μ -1e 106 MeV/c ²	tau τ 1.776 GeV/c ²	Higgs H^0 125.09 GeV/c ² 0	
Name Mass Electric charge	e-neutrino ν_e $< 2 \text{ eV}/c^2$	μ-neutrino ν_μ 0 $< 190 \text{ keV}/c^2$	τ-neutrino ν_τ $< 18.2 \text{ MeV}/c^2$		

as red, green, blue. The gauge bosons are called gluons. As the photons of QED they are massless, but unlike the other gauge bosons, they themselves are subject to the force they are carrying, i.e. they carry color-charge and color-anticharge, making QCD a *non-abelian* theory.

An important consequence is the running coupling of QCD: the coupling constant depends strongly on the momentum transfer Q^2 where it is probed and decreases with increasing energy. To first order it follows the form [3] [4]:

$$\alpha_s(Q^2) \approx \frac{4\pi}{\beta_0 \ln(Q^2/\Lambda_{\text{QCD}}^2)} \quad (1.1)$$

with $\beta_0 = \frac{11}{3}n_c - \frac{2}{3}n_f$ the first order in the expansion of the β function of QCD; n_c is the number of colors, n_f the number of active flavors at the given momentum scale. Λ_{QCD} is the QCD scale parameter, a constant of the dimension of an energy that defines the scale down to where perturbative methods can be used in QCD. Its exact value depends on the renormalization scheme used; in the most widely used one its value is $\Lambda_{\text{QCD}} \approx 200 \text{ MeV}$.

The behavior of α_s as a function of Q is illustrated in Fig. 1.1 which shows measured values together with the expectation from QCD. At high-momentum transfer, the coupling constant shrinks, until quarks behave as quasi-free particles, a behavior known as *asymptotic freedom of QCD*.

The strong rise of the coupling constant towards lower energy scales — i.e. larger distances — on the other hand leads to the fact the free color-charged particles are never observed in nature. Due to the gluon self-interaction, the field lines of the strong force between quarks and antiquarks form narrow color-flux tubes, or *strings*, that store potential energy, increasing with the distance between the quark and antiquark. Once enough energy is stored, a new quark-antiquark pair is created, the string breaks. Hence colored particles cannot be separated arbitrarily large from each other, but only exist inside color-neutral composite objects, so-called *hadrons*. This phenomenon is known as *confinement*.

Possible configurations are mesons, i.e. a quark carrying a specific color bound to an antiquark of the corresponding anti-color, or baryons, i.e. three quarks or antiquarks in a color-neutral combination. Color neutral configurations of a larger number of quarks (tetraquarks, pentaquarks) or of gluons (glueballs) are theoretically also possible, and experimental hints of their existence have been found, see e.g. [5, 6].

Due to its complex mathematical structure, QCD cannot be solved analytically. As mentioned, at high-momentum transfers, the coupling constant becomes small, so an expansion in powers of α_s can be done; this procedure is known as **perturbative QCD (pQCD)**.

At low momentum transfer, this is not possible. Here, static properties of the theory can be calculated in the framework of **lattice QCD (lQCD)**: Spacetime is discretized on a 4 dimensional lattice, quarks are put on the lattice sites and gluons on the edges connecting them. QCD can be solved from first principles in this discretized formalism using high-performance computing. The discretized results are then extrapolated to the continuum limit of an infinitely fine-grained lattice. A limitation for lQCD are systems with non-zero baryochemical potential, where it cannot be applied anymore. In situations where neither pQCD nor lQCD are applicable, other methods can be used, such as potential models, or effective field theories.

Since its development the SM has proven very successful in describing known phenomena and predicting new ones. A prominent example is the prediction of the Higgs boson in the 1960s [7–10], and its discovery over half a century later [11, 12]. A shortcoming of the model is that it contains a lot of free parameters: the strengths of the individual interactions, the masses of the elementary particles and mixing angles in the electroweak theory. Due to this and the fact that it cannot explain dark matter or the matter-antimatter asymmetry in the universe, it is usually assumed to be incomplete, theoretical efforts are being undertaken to extend the SM, a prominent example is Supersymmetry (SUSY) [13].

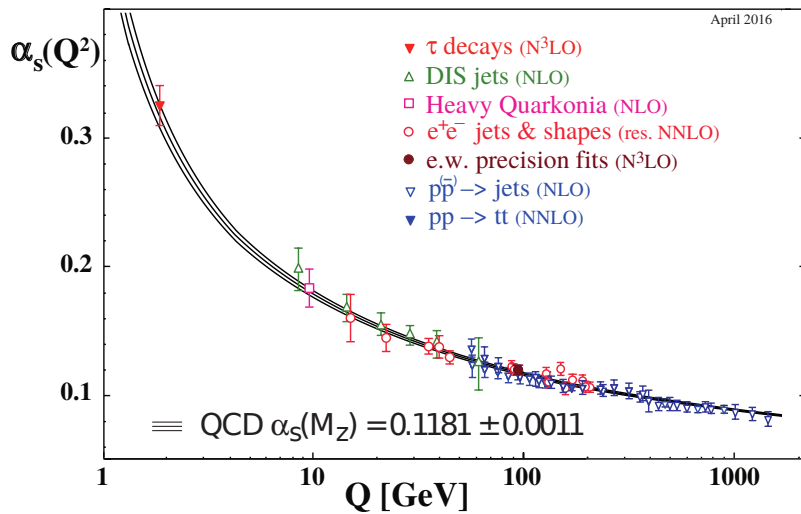


Figure 1.1.: Measurements and theoretical prediction of the strong coupling constant as a function of momentum transfer Q . Figure taken from [14].

1.2 Proton-proton collisions

A tool to study the properties of QCD are inelastic proton-proton (pp) collisions. They can generally be grouped according to the exchanged particle mediating the interaction into *diffractive* and *non-diffractive* collisions. Fig. 1.2 gives a schematic picture of non-diffractive and diffractive proton-proton interactions. In diffractive collisions colorless particles containing the quantum numbers of the vacuum are exchanged, so-called pomerons, or higher order reggeons, as described in Regge theory [17]. In QCD they can be

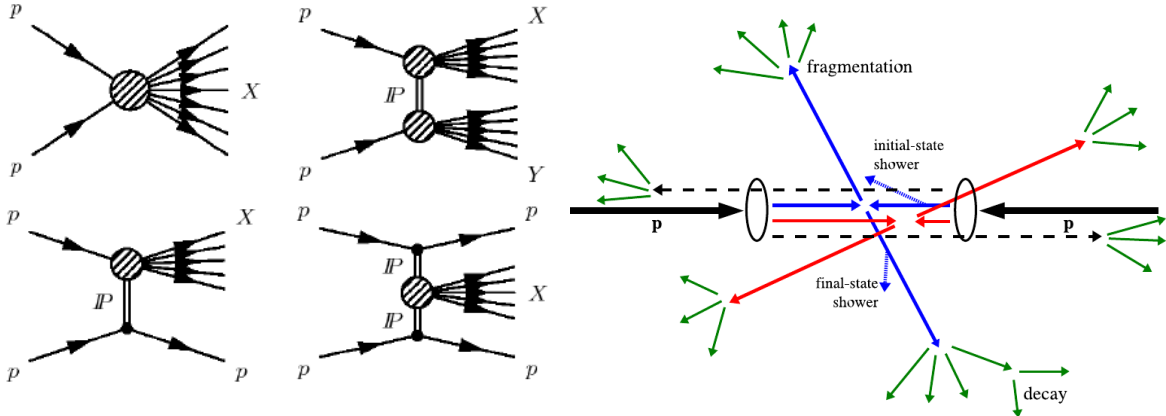


Figure 1.2.: Schematic picture of inelastic proton-proton collisions. Left (clock-wise, starting on the top left): non-diffractive, double-diffractive, central-diffractive, and single-diffractive proton-proton collisions. Figure adapted from [15]. Right: Non-diffractive proton-proton collision, including two hard partonic interactions, initial and final state radiation, beam remnants, and hadronization (fragmentation). Figure taken from [16].

interpreted as colorless groups of gluons. Depending on whether one or both of the protons dissociates, *single* and *double diffractive* collisions can be distinguished. A special case is *central diffraction*, in which two pomerons are exchanged and interact with each other.

About 70 % [18] of the inelastic cross section consists of non-diffractive collisions, in which the interaction happens on the level of *partons*, i.e. quarks and gluons. They are typically composed of a *hard interaction*, and an *underlying event*, Fig. 1.2 (right) gives an illustration. The hard interaction happens at a high-momentum transfer and typically leads to the production of high-momentum partons, which fragment into a *jet* of closely collimated hadrons in the final state. Processes at the hard interaction scale can be described in the framework of pQCD. The underlying event contains processes such as parton rescattering and initial and final state gluon radiation, i.e. before and after the collision, respectively. These effects happen at lower momentum transfers, so pQCD is not applicable. The same is true for the hadronization which can be described via string fragmentation, as explained above.

An important ingredient for the description of proton-proton collisions is the initial parton structure of the protons, expressed as Parton Distribution Functions (PDFs). These are the probability densities for a parton to carry a given momentum fraction x_{Bj} of the proton. Especially at low x_{Bj} the PDFs are strongly dependent on the momentum transfer Q^2 , i.e. the resolution with which they are probed: the closer one looks, the more low momentum partons can be resolved. Especially the gluon distribution increases strongly at low x_{Bj} , until saturation effects set in due to the self-interaction of gluons in QCD. This regime can be described with the **Color Glass Condensate (CGC)** [21] effective field theory. In this approach, the valence quarks are treated as static color sources, while the dynamically produced gluons with momenta below an emergent semi-hard saturation scale Q_s can be appropriately described via classical field theory due to their large number and weak coupling.

Experimentally, PDFs can be determined e.g. by **Deep Inelastic Scattering (DIS)** of leptons off protons [22]. From the measured structure functions, parametrized PDFs can be obtained and evolved in Q^2 according to the DGLAP equations [23–25]. Fig. 1.3 (left) shows an example of proton PDFs at a momentum transfer of $Q^2 = 10 \text{ GeV}^2$, which is relevant for low $p_{\text{T}} \text{J}/\psi$ production [19].

Fig. 1.3 (right) illustrates which values of Q^2 and x_{Bj} are probed with proton-proton collisions at $\sqrt{s} = 13 \text{ TeV}$ with probes of different masses at different rapidities. For mid-rapidity J/ψ production at low p_{T} ($Q \approx m_{\text{J}/\psi} = 3.1 \text{ GeV}/c^2$), this corresponds to $10^{-4} \lesssim x_{\text{Bj}} \lesssim 10^{-3}$, i.e. a region of high gluon density.

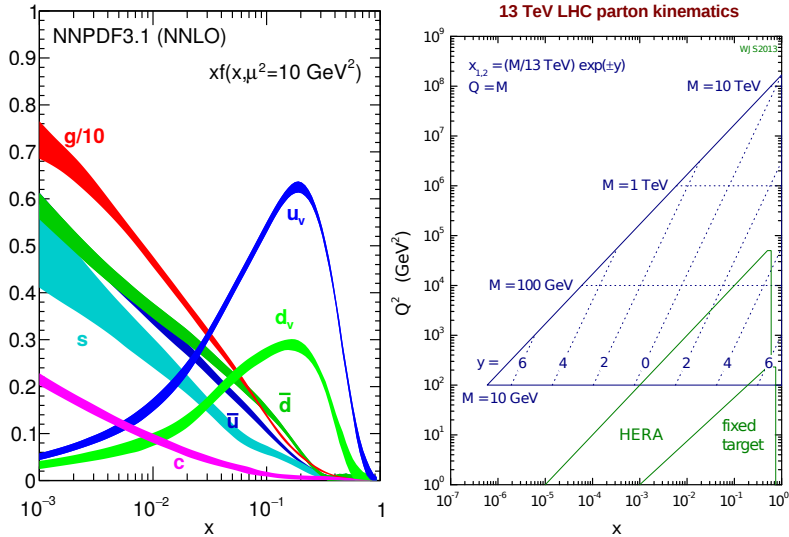


Figure 1.3.: Left: Parton distribution functions for a momentum transfer $Q^2 = 10 \text{ GeV}^2$ as occurring in J/ψ production at low p_T . Figure taken from [19]. Right: Regions of Q^2 and x_{Bj} probed with different masses and rapidities in proton-proton collisions at LHC energy. Also shown is the region accessible with DIS at HERA. Figure taken from [20].

To describe proton-proton interactions, typically QCD-inspired models containing both hard and soft interactions are used, implemented in Monte Carlo (MC) collisions generators, such as PYTHIA [26] or EPOS [27]. They often have a large set of free parameters that are constrained by experimental data.

These models commonly implement a scenario where several elementary collisions happen in one proton-proton collision, such as Multiparton Interactions (MPI) in PYTHIA or multiple pomeron exchanges in EPOS. The assumption of having several collisions is supported by experimentally observed charged-particle multiplicity distributions [28] and e.g. by the observation of more than one particle produced in a hard interaction, cf. e.g. the measurement of double-charm production from LHCb [29].

More details on models describing proton-proton interactions will be given in section 2.2.4 for EPOS and chapter 7 for PYTHIA.

1.3 Charged-particle multiplicities

Experimentally, the number of charged particles produced per collision is one of the easiest accessible quantities. From a theoretical point of view, it is a complicated quantity, since the total number of produced particles is largely governed by the low energy physics of the strong interaction, which cannot be addressed perturbatively, necessitating the use of effective models.

At collision energies below the LHC one, the charged-particle multiplicities can be described with models incorporating simple general assumptions, such as Feynman scaling [30]. From basic principles it was conjectured that asymptotically the total average particle multiplicity $\langle N \rangle$ in a collision should scale proportionally to the logarithm of the collision energy $\langle N \rangle \propto \ln(\sqrt{s})$. Given the fact that the maximum available rapidity in a collision increases in the same way, the particle rapidity density should asymptotically be independent of collision energy $\frac{dN}{dy} = \text{const.}$

Experimentally it is found that Feynman scaling is violated. Fig. 1.4 (left) shows for different experiments the average charged particle pseudorapidity ¹ density in $|\eta| < 0.5$ as a function of the collision energy for inelastic collisions, and for $\text{INEL} > 0$ collisions, i.e. inelastic collisions in which at least one charged particle was produced at mid-rapidity. In both cases, the collision energy dependence can be

¹ Pseudorapidity is defined as $\eta = \text{artanh}(p_L/p)$ with p_L the longitudinal momentum, i.e. the projection of the momentum on the beam axis, and p the absolute value of the momentum of a particle.

empirically parametrized with a powerlaw function of the collision energy. An alternative parametrization is a second order polynomial of the logarithm of the collision energy, see e.g. [31].

The probability distribution to have collisions of a give charged-particle multiplicity $P(N)$ is called the multiplicity distribution. Based on Feynman scaling is the concept of KNO scaling [32], according to which the multiplicity distribution normalized to its mean value $P(N)/\langle N \rangle$ should be independent of collision energy. While KNO scaling works well at lower energies, from around $\sqrt{s} = 200$ GeV onwards a broadening of multiplicity distributions is observed. This effect is usually interpreted as arising from the occurrence of multiparton interaction.

The actual shape of multiplicity distributions has been successfully described at lower collisions energies with Negative Binomial Distributions (NBD)

$$P_{p,k}^{\text{NBD}}(N) = \binom{N+k-1}{N} (1-p)^N p^k. \quad (1.2)$$

At higher energies, combinations of two or more NBDs have been used. The physical origin of this shape has not yet been ultimately understood, a combination of two NBDs can be interpreted as representing the distributions for soft and semi-hard collisions.

At LHC energies charged-particle multiplicity distributions and their energy dependences are usually understood in the context of QCD inspired models, that assume the presence of multiple elementary interaction. Reasonable agreement with experimental data can be reached, as illustrated in Fig. 1.4 (right), which shows the charged-particle multiplicity measured by ATLAS in pp collisions at $\sqrt{s} = 13$ TeV, together with model predictions from different MC event generators.

An extensive review of the physics behind and models describing particle multiplicities and distributions can be found in [33].

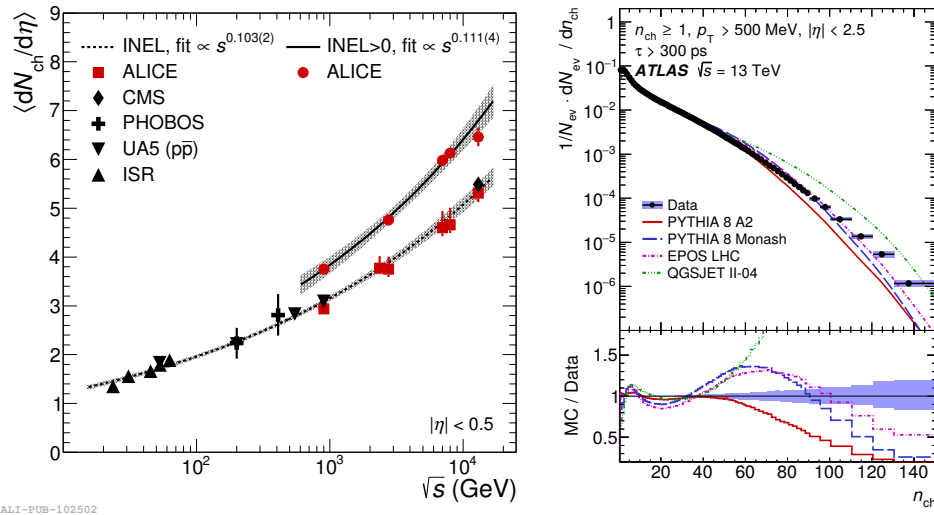


Figure 1.4.: Charged-particle pseudorapidity density at mid-rapidity in proton-proton collisions. Left: Mean multiplicity as a function of the collision energy for inelastic collisions (INEL) and inelastic collisions with at least one charged particle produced at mid-rapidity (INEL>0), together with powerlaw fits. Figure taken from [34]. Right: Charged particle multiplicity distribution at $\sqrt{s} = 13$ TeV measured by ATLAS and model comparisons. Figure taken from [35].

1.4 Heavy-ion collisions

From the asymptotic freedom of QCD it was early on inferred that at high energy densities — as existed for about 10 microseconds after the electroweak phase transition after the Big Bang — the

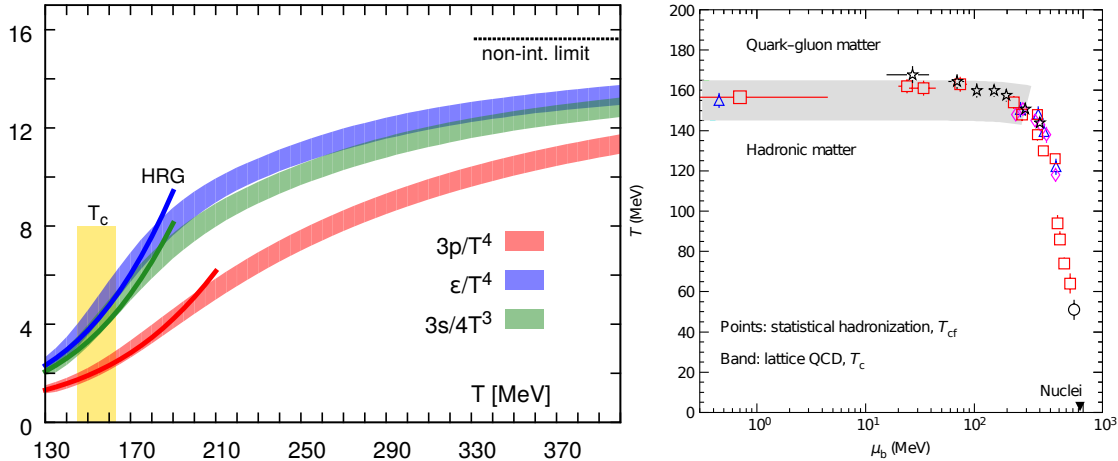


Figure 1.5.: Phase transition of QCD matter. Left: Calculations from lattice QCD. Evolution of energy density, pressure and entropy as a function of temperature T , scaled by appropriate powers of T . At low T the results are compared to predictions from the hadron resonance gas (HRG) model. The horizontal line on the right shows the Stefan-Boltzmann limit – the expectation for non-interacting particles – for three flavors. Figure taken from [36]. Right: Compilation of fit results of the temperature and net baryon density obtained from the thermal model for various experiments at different collision energies. Figure taken from [37].

relevant degrees of freedom should be quarks and gluons instead of hadrons [38]. In parallel it was conjectured by Hagedorn from the analysis of hadron yields in high-energy collisions [39] that a limiting temperature of hadronic matter exists. Cabibbo and Parisi interpreted this temperature as the phase transition to a new deconfined state of matter [40], called **Quark-Gluon Plasma (QGP)**.

From lattice QCD calculations it is known that at low baryon density and high temperature the phase transition is of the crossover type, i.e. thermodynamic quantities are changing smoothly. Fig. 1.5 (left) shows lQCD calculations for thermodynamic quantities as a function of temperature. Around a critical temperature $T_c \approx 155$ MeV the quantities change: below they are in agreement with the predictions from a gas of interacting confined particles (hadron resonance gas), above they slowly approach the limit of a gas of non-interacting free partons.

Experimentally, in ultra-relativistic heavy-ion collisions, energy densities can be created sufficient for the formation of a QGP. Evidence for a limiting energy density of the hadronic phase comes from the analysis of particle yields: In a heavy-ion collision, after the QGP is created, the system expands and cools until the energy density is low enough that the transition back to the hadronic phase takes place. The abundancies of light-flavor hadrons can then be successfully described with a grand canonical ensemble based on the mass of the hadrons, as implemented in the **Thermal Model** [41]. Parameters of the model are the temperature T and the baryo-chemical potential μ_b at the time when the particle yields were frozen, plus the volume of the system as an overall scaling factor. Fig. 1.5 (left) shows the values of T and μ_b obtained from the thermal model for experiments at different collision energies. At low μ_b , T is about 155 MeV, coinciding with the phase transition temperature from lQCD. Starting from $\mu_b \approx 200$ MeV, T decreases with increasing μ_b .

There are further experimental observations that support the picture of a thermalized medium produced in ultra-relativistic heavy-ion collisions, like

- signatures of a collective motion of the medium (e.g. *elliptic flow* [42]),
- the suppression of high p_T particles and jets due to energy loss of the partons in the hot and dense medium (*jet quenching* [43])
- an enhanced production of strange and multistrange particles [44].

Charmonium has a special role among the probes for the QGP. Initially [45], a suppression of charmonium production due to the screening of the binding potential by the free color-charges was proposed as key observable of a deconfined environment; later [46] [47], novel mechanisms were proposed for higher collision energies, leading to regeneration of charmonium, counteracting the suppression or even surpassing it. These topics will be discussed in detail in section 1.6.3.

1.5 Collectivity in proton-proton collisions?

Recently, very high multiplicity proton-proton collisions came into the focus of attention, as phenomena were observed that traditionally are explained with collective effects arising from a thermalized medium.

An example is the emergence of long-range correlations ("near side ridge") in high-multiplicity proton-proton collisions [48]. The effect is shown in Fig. 1.6 (left): For a given particle with intermediate p_T the distribution in $\Delta\eta$ and $\Delta\varphi$ of the other particles produced in the same collision is shown. In minimum bias collisions (top), a peak at $\Delta\eta = 0$ and $\Delta\varphi = 0$ from the jet fragmentation, and a ridge $\Delta\varphi = \pi$, elongated in η due to the fragmentation of back-to-back jets can be seen. In collisions with high particle multiplicities (bottom) another ridge-like structure at $\Delta\varphi = 0$ emerges, expanding in η at least until $|\eta| = 4$. In heavy-ion collisions, such long-range correlations are usually interpreted as the result of the hydrodynamic expansion of the thermalized medium.

Another observation is the enhancement of strange and multistrange particle production as a function of the charged-particle density, seemingly smoothly transitioning to proton-nucleus and nucleus-nucleus collisions [49], see Fig. 1.6 (right). In heavy-ion collision, an enhanced strangeness production is linked with the deconfined nature of the medium, in which strange quarks can be abundantly produced in partonic interactions, whereas in proton-proton collisions strangeness production is suppressed due to phase space reduction from the exact conservation of the strangeness quantum number [50].

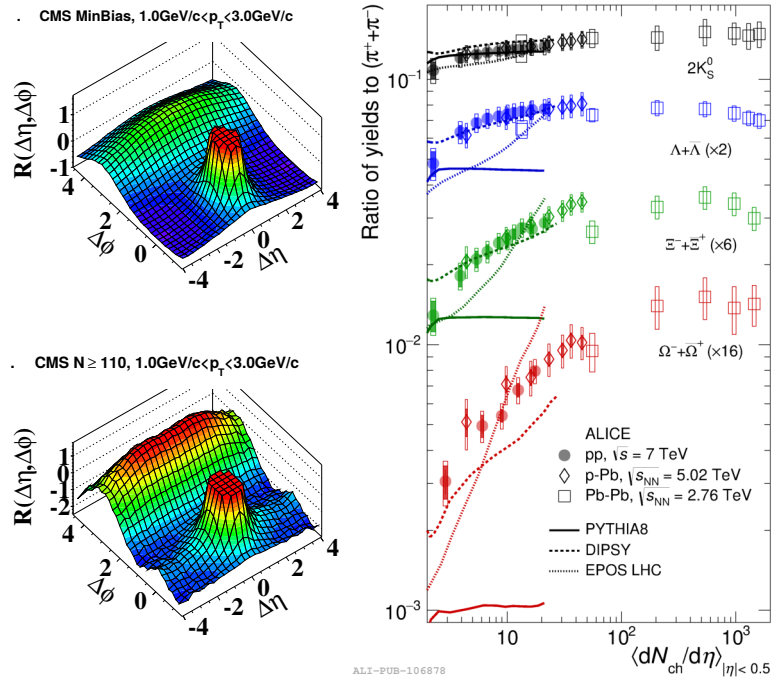


Figure 1.6.: Experimental hints for collectivity in high-multiplicity proton-proton collisions. Left: Emergence of long-range near-side angular correlations at high multiplicities [48]. Right: Enhancement of strange and multi-strange hadron production as a function of multiplicity [49].

The observation of these phenomena in high-multiplicity proton-proton collisions resembling collective effects from heavy-ion collisions has been met with great interest from theorists. There are two main directions how to interpret the observations: One idea is that indeed at high enough multiplicities in proton-proton collisions, a medium is formed, for which a hydrodynamic description is adequate. The same concepts as for nuclear collision then can be applied, one has "one fluid to rule them all" [51].

The other approach is to explain the observations without the formation of a deconfined medium. In order to do this, one has to give up the interpretation of one proton-proton collision as the independent superposition of several partonic interactions.

For example, the flow-like patterns in the azimuthal particle correlations can be ascribed to QCD interference between the produced partons [52], saturation effects in the initial state parton density functions in the framework of CGC [53], or the rearrangement of the initial color strings of the produced partons, known as "color reconnection" [54]. The observed strangeness enhancement with multiplicity can be explained under the assumption of interacting strings fusing into ropes ("rope hadronization" [55]). Further extensions of the rope model ("rope shoving", see [56]) are also able to explain the azimuthal particle correlations.

It can thus be said that the emergence of effects reminiscent of collective phenomena in small systems at high-multiplicity is theoretically not well understood yet, but of great importance for the correct interpretation of effects in heavy-ion collisions, which are traditionally seen as clear indications for the creation of a medium.

1.6 Charmonium

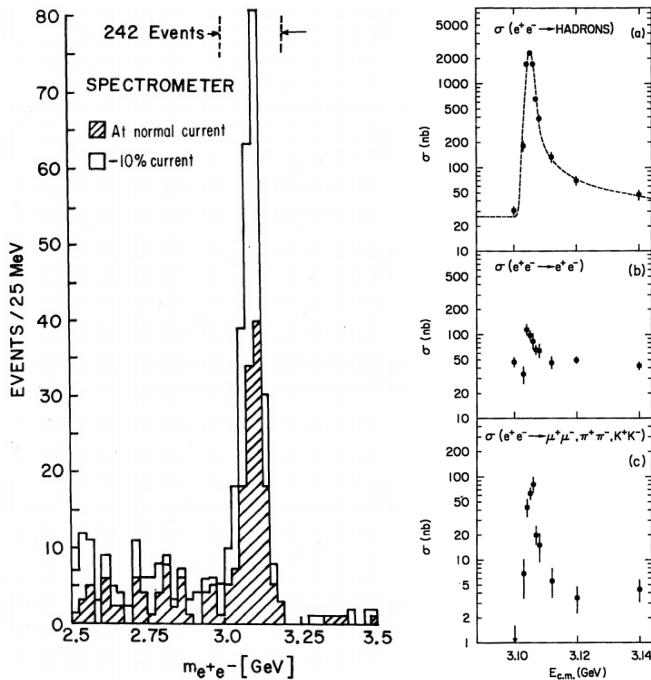


Figure 1.7.: Discovery of the J/ψ . Left: Invariant mass distribution of dielectrons pairs, measured in p-Be collisions. Figure taken from [57]. Right: Cross section of electron-positron annihilation as a function of center-of-mass energy in hadronic channel (top), dielectron channel (middle), and dimuon, dipion, dikaon channel (bottom). Figure taken from [58].

The existence of a fourth quark flavor was early on speculated on theoretical grounds (e.g. based on an assumed symmetry between the number of leptons and quarks by Bjorken and Glashow in [59]). In 1970 Glashow, Iliopoulos and Maiani proposed the GIM mechanism [60], named after the authors,

to explain an experimental observation, namely that the branching ratio of the dimuon decay channel of neutral kaons is very small compared to the hadronic decay channel. The mechanism required the existence of a fourth quark.

Experimentally, the fourth quark flavor *charm* was observed independently by two groups, who discovered the bound state of a charm quark and a charm antiquark, a *charmonium* state, the J/ψ . The observation was announced simultaneously by the two groups on November 11th 1974. At Brookhaven National Laboratory (BNL), a proton beam from the Alternating-Gradient Synchrotron was shot on a beryllium target and a sharp mass peak was observed in the electron-positron channel [58]. Fig. 1.7 (left) shows the invariant mass distribution of e^+e^- pairs in the relevant mass region. At the Stanford Linear Accelerator Center (SLAC), a sharp resonance was observed in an electron-positron annihilation experiment in the SPEAR collider [58] in hadronic and dilepton channels. Fig. 1.7 (right) shows the cross section of the different channels as a function of the center-of-mass energy. The newly discovered particles were baptized J by the BNL group and ψ by the SLAC groups, hence the peculiar double name that it kept ever since.

The narrow width — or long lifetime — of the observed particle could only be explained by the fact that a new conserved quantum was at play. Its mass $m_{J/\psi}$ and width $\Gamma_{J/\psi}$, as they are known today, are [1]

$$m_{J/\psi} = (3096.900 \pm 0.006) \text{ GeV}/c^2 \quad (1.3)$$

$$\Gamma_{J/\psi} = (92.9 \pm 2.8) \text{ keV}/c^2. \quad (1.4)$$

From the creation in electron-positron annihilation, it was immediately known that the newly discovered state must have the quantum numbers of the photon, i.e. it had to be a vector meson ($J^{PC} = 1^{--}$), with J the total spin, P the parity quantum number ($P = (-1)^{L+1}$) and C the charge conjugation quantum number $C = (-1)^{L+S}$.

The mass is below the open charm threshold — twice the mass of the lightest open charm hadron $2 \cdot m_{D^0} \approx 3730 \text{ GeV}/c^2$ [1] — so the strong decay into two D mesons is not possible. Neither is the decay into one gluon, due to color-charge conservation. Since the J/ψ has negative C parity it can also not decay via a state of two gluons, which has a positive one. The first allowed strong decay proceeds via three virtual gluons which necessarily have high virtualities, this means the coupling at the strong interaction vertices is weak. This decay is thus suppressed, the mechanism is known as OZI suppression, after Okubo, Zweig and Iizuka, who proposed it in the 1960s [62–64]. Thus, the electromagnetic decays into dileptons via a virtual photon become relevant. The branching ratios are [1]

$$B.R.(J/\psi \rightarrow e^+e^-) = (5.971 \pm 0.032)\% \quad (1.5)$$

$$B.R.(J/\psi \rightarrow \mu^+\mu^-) = (5.961 \pm 0.033)\% \quad (1.6)$$

The discovery thus proved the existence of a fourth quark flavor and gave strong support to the quark model in general. It sparked rapid changes in the field of particle physics, these became known as the *November revolution of particle physics*. In 1976, Burton Richter and Samuel Ting — the heads of the experimental groups who made the discovery — were awarded the Nobel Prize in Physics.

Only a few days after the discovery of the $J/\psi(1S)$ the radial excitation $\psi(2S)$ was discovered [65]. From the radiative decays between them, observed in e^+e^- storage rings, the existence of intermediate states with even C parity [66, 67] — the P -wave spin-triplet $\chi_{cJ}(1P)$ — and of the spin singlet state $\eta_c(1S)$ with a mass below the J/ψ [68] could be inferred. The precise determination of their masses was later done in $p\bar{p}$ annihilation experiments [69].

The remaining charmonia states below the open charm threshold were identified unambiguously much later: the radial excitation of the spin singlet state $\eta_c(2S)$ was observed in 2002 [70], and the P -wave spin singlet $h_c(1P)$ in 2005 [71–73]. Many more resonances have been found above the open charm

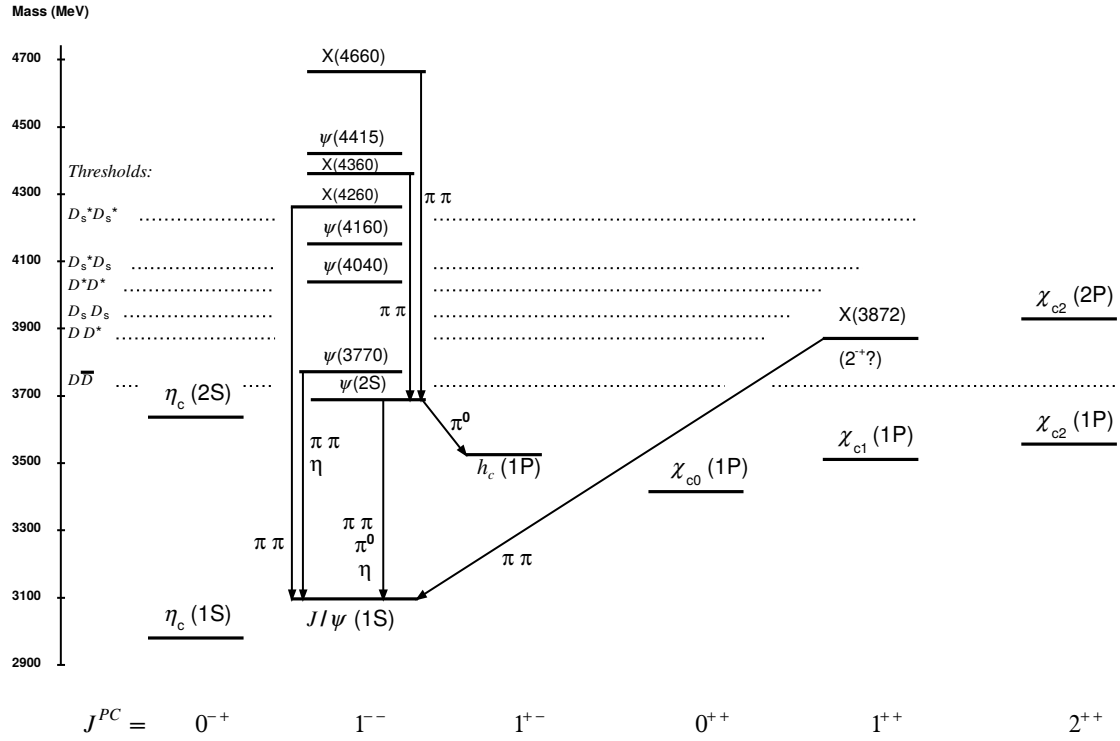


Figure 1.8.: Experimentally observed charmonium states, and important hadronic transitions between them (photonic transitions omitted for clarity). Also shown are the mass thresholds for the decay to open charm mesons. Figure taken from [61].

threshold, some of which are of uncertain quark content and are candidates for exotic states, such as hybrid mesons containing valence gluons, tetraquarks or mesonic molecules. See [74] for a recent review.

Fig. 1.8 shows the different charmonium states with their masses and J^{PC} quantum numbers, hadronic transitions between them, and the different open charm thresholds. A very similar spectrum arises at higher mass for the *bottomonium* particles, the analogue system for bottom quarks (the ψ states of charmonium correspond to Υ states of bottomonium, the names of the other states are similar). Bottomonium and charmonium are also referred to as *quarkonium*.

1.6.1 Charmonium in hadronic collisions

In a measurement of inclusive J/ψ production, one usually has to deal with several contributions, as is illustrated in Fig. 1.9 (right):

- **Non-prompt J/ψ .** A part of the observed J/ψ yield comes from the weak decay of hadrons containing beauty quarks, e.g. $B^+ \rightarrow J/\psi K^+$. Due to the longer lifetime of the B mesons ($c\tau \approx 500\mu\text{m}$) this contribution can be experimentally distinguished via the displaced production vertex of the J/ψ , hence the name *non-prompt J/ψ* . *Prompt J/ψ* on the other hand refers to J/ψ not originating from a weak decay.

The fraction f_B of non-prompt J/ψ in the total yield at mid-rapidity has been measured by various experiments at the LHC and by CDF at the Tevatron at different collision energies in proton-proton and proton-nucleus collisions, see [75] and references therein. At low transverse momentum the non-prompt fraction is about 10 % and rises with p_T . The shape is quite similar for the different

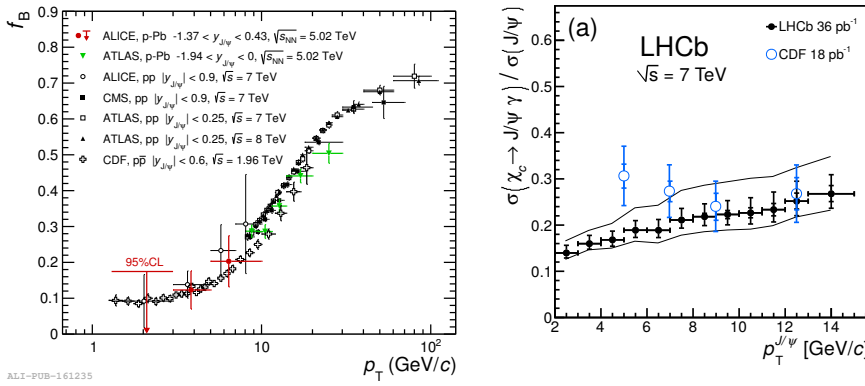


Figure 1.9.: Sources of inclusive J/ψ in hadronic collisions. Left: Fraction of non-prompt J/ψ in pp and p-Pb collisions at various energies as a function of p_T . Figure taken from [75]. Middle: Fraction of prompt J/ψ from χ_c decay as a function of p_T . Figure taken from [76]. Right: Illustration of the fractions of the different contributions to the inclusive J/ψ yield.

collisions systems, which might be accidental. Fig. 1.9 (left) shows f_B as a function of p_T obtained from different experiments.

- **Higher charmonia feed-down.** A further contribution is the feed-down of J/ψ from higher mass charmonia decays, e.g. via $\chi_c \rightarrow J/\psi\gamma$ or $\psi(2S) \rightarrow J/\psi\pi\pi$. The fraction of χ_c feed-down to the total prompt J/ψ yield can be measured [76, 77]. It amounts to about 10 to 30 %, increasing with p_T , as shown in Fig. 1.9 (middle). The $\psi(2S)$ contribution can be estimated from the measured cross section of prompt $\psi(2S)$ and J/ψ production, and the known branching ratio for $\psi(2S)$ to decay to $J/\psi + X$. It makes up around 8 % of the prompt J/ψ yield [78].
- **Direct production.** The relevant production mechanisms will be described in the next section.

1.6.2 Prompt charmonium production mechanisms in hadronic collisions

In hadronic quarkonium production [79] several different energy scales are at play (the numerical values are an estimate for charmonium based on [80]):

- the heavy quark mass $M \approx 1.5$ GeV
- the typical momentum of the heavy quark $Mv \approx 0.9$ GeV
- the typical energy of the heavy quark inside the quarkonium $Mv^2 \approx 0.5$ GeV.

Due to the high quark mass in comparison to their energy, quarkonia can be treated non-relativistically. The momentum transfers required for the production of these high mass quarks are furthermore higher than the QCD scale parameter Λ_{QCD} , so pQCD can be used to calculate heavy-quark production cross section. The total charm cross section in proton-proton collisions can to a reasonable accuracy be described with next-to-leading order (NLO) predictions [81]. For the total beauty cross section calculations at NLL, i.e. LO plus logarithmic terms in the NLO contributions have proven successful, as implemented in the FONLL (Fixed Order plus Next-to-Leading Log) framework [82, 83].

The subsequent binding into quarkonia on the other hand happens at the scales of the momentum and energy of the heavy quarks, making it a nonperturbative process. The different processes make quarkonium production a complex process, though due to the different relevant energy scales, the different steps can be described in a decoupled way, known as *factorization*. Several models are on the market that provide predictions for quarkonium production in hadronic collisions.

Color Evaporation Model [84]

The **Color Evaporation Model (CEM)** is a simple model suited for predictions of quarkonia production cross sections. Based on the principle of quark-hadron duality [85], it assumes that a heavy-quark pair with a mass smaller than the open-heavy-quark threshold has a statistical probability to evolve into a quarkonium state, regardless of the quantum state in which the pair was produced. The total quarkonium cross section is then

$$\sigma_{\text{onium}} = \frac{1}{9} \int_{2m_c}^{2m_D} dm \frac{d\sigma_{Q\bar{Q}}}{dm} \quad (1.7)$$

with $\sigma_{Q\bar{Q}}$ the perturbative heavy-quark pair production cross section.

The transition into colorless quarkonium states happens via soft gluon emissions, the color is so-to-say evaporated, hence the name. The probability to transition into a specific quarkonium state is assumed to be global, i.e. the same for collisions at different collision energy, collision system and kinematic variables. The advantage of this model lies in its simplicity and strong predictive power with the relative abundancies of the different quarkonia states as the only free parameters.

Rough estimates of the p_T distribution and energy dependence of quarkonium production are possible, see e.g. [86]. In Fig. 1.10 a recent result obtained with CEM is shown, i.e. the total J/ψ cross section at forward rapidity as a function of collision energy [87, and references therein]. The experimental data is at the upper end of the (large) theoretical uncertainty band of the model.

A recent development is the **Improved Color Evaporation Model (ICEM)** [88] which includes into the model the effect that the cross sections of quarkonia of different masses have different p_T -dependencies.

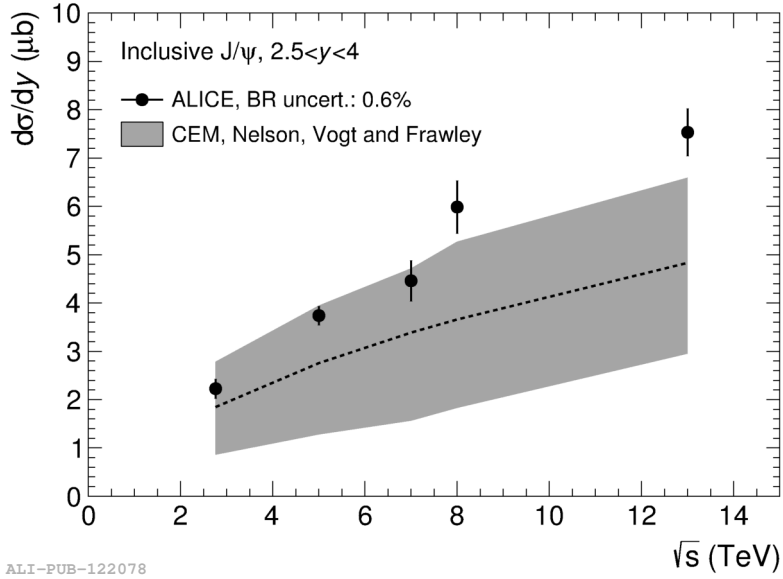


Figure 1.10.: Total J/ψ cross section at forward rapidity as a function of collision energy, compared to a prediction from the Color Evaporation Model. Figure taken from [87].

Color Singlet Model [89]

In the **Color Singlet Model (CSM)**, pQCD is used to calculate the cross section of partonic interactions producing heavy-quark pairs. Only those processes are taken into account that produce a heavy-quark pair with the same quantum numbers as the quarkonium state under consideration, most notably this means only color-singlet states are considered. At collider energies gluonic processes are most relevant, the lowest order one is shown in the left panel of Fig. 1.11.

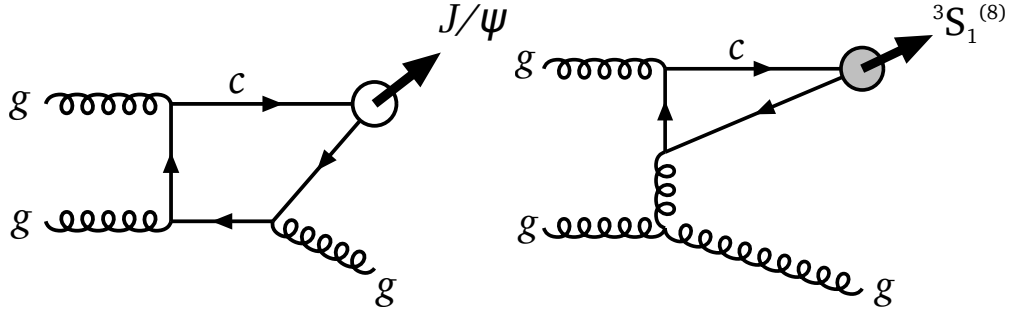


Figure 1.11.: Typical J/ψ production processes. Left: Lowest order color-singlet channel. Right: Color-octet production from gluon splitting channels. Figures adapted from [90].

While the cross sections for the heavy-quark production are calculated perturbatively, the evolution to a bound quarkonium state can be obtained from potential model calculations: In order to proceed to a bound quarkonium state, the heavy quarks have to be close to each other. The probability for a heavy-quark pair to transition to quarkonium is thus proportional to the radial wave function at the origin $R_S(0)$ for S -wave states, and to the first derivative of the wave function $R'_P(0)$ for a P -wave state. The wave functions in term can be extracted from the leptonic decay widths Γ_{ee} .

A known problem of the CSM is the occurrence of infrared divergences in the cross section calculations for P -wave states, which have to be mitigated by low p_T cutoffs. It is naturally solved by taking also color-octet production into account within the NRQCD framework, which will be described in the next section.

While initially at lower collision energy a very good description of experimental data could be achieved with this model [91], it underestimates cross sections at higher energies, especially at high p_T . E.g. the cross section for ψ' production at the CDF experiment was underestimated by a factor 50 [92]. The discrepancy could be fixed with inclusion of color-octet processes.

However, it is worth to note that with the inclusion of higher-order color-singlet processes, a better description of data can be achieved. Fig. 1.12 illustrates this; here the measured p_T differential J/ψ cross section at forward rapidity in proton-proton collisions at $\sqrt{s} = 7$ TeV is compared to CSM calculations at complete leading order (LO), complete next-to-leading order (NLO), and taking into account also leading p_T next-to-next-to-leading order contributions (NNLO*) [93, and references therein]. As can be seen, the agreement with data gets increasingly better with the inclusion of higher orders processes.

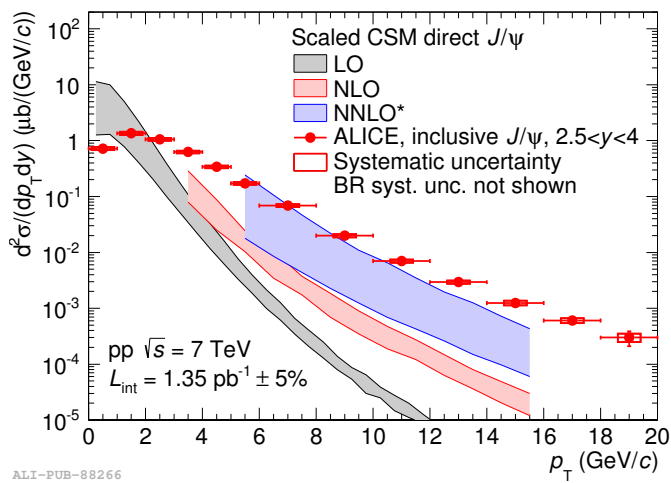


Figure 1.12.: J/ψ production cross section as a function of transverse momentum at forward rapidity in proton-proton collisions at $\sqrt{s} = 7$ TeV, compared to predictions from the Color Singlet Model at leading order (LO), next-to-leading order (NLO), and NLO with leading p_T next-to-next-to-leading order contributions (NNLO*). Figure taken from [93].

Non-Relativistic QCD [94]

The most rigorous approach to model quarkonium is the use of the Non-Relativistic QCD (NRQCD) effective field theory. It makes use of the factorization of the different energy scales relevant for quarkonium production $M \gg M\nu \gg M\nu^2$. The probability to produce a quarkonium state H can be split into the product of the short-distance perturbative cross section to produce a heavy-quark pair in a specific quantum state and the nonperturbative probability to evolve into the quarkonium state under consideration. The total cross section is then the sum over all possible quantum states in which the heavy-quark pair can have been produced:

$$d\sigma(H) = \sum_{\kappa} d\sigma_{\kappa} \langle \mathcal{O}_{\kappa}^H \rangle. \quad (1.8)$$

The sum runs over the quantum number of the produced heavy-quark pair state $\kappa = {}^{2S+1}L_J^{[c]}$, with c denoting the color state, i.e. either color-octet or color-singlet; $d\sigma_{\kappa}$ are the short-range production amplitudes to for a heavy-quark pair in the given state, convoluted with the parton distribution functions; \mathcal{O}_{κ}^H are the nonperturbative *long-distance matrix elements* (LDMEs), that describe the transition from the heavy-quark pair to a quarkonium state.

While the heavy-quark production cross sections are obtained from a perturbative expansion in α_s , the LDMEs are expanded in powers of the heavy quark velocity ν . The LDMEs are assumed to be universal and can be obtained from experimental data, e.g. from decay rates of beauty mesons to charmonia or from the scaling of transverse momentum shapes obtained with the model to experimental data [95]. From the assumed universality of the LDMEs the model obtains its predictive power, since predictions for cross sections at different energies or collision systems are possible.

Most notably, in contrast to the CSM model, in this approach also pQCD processes producing heavy-quark pairs in a color-octet state are considered. By taking into account only the processes in lowest order of ν , the CSM is recovered. An example process that is not included in the CSM since it can only produce color-octet states is illustrated in the right panel of Fig. 1.11.

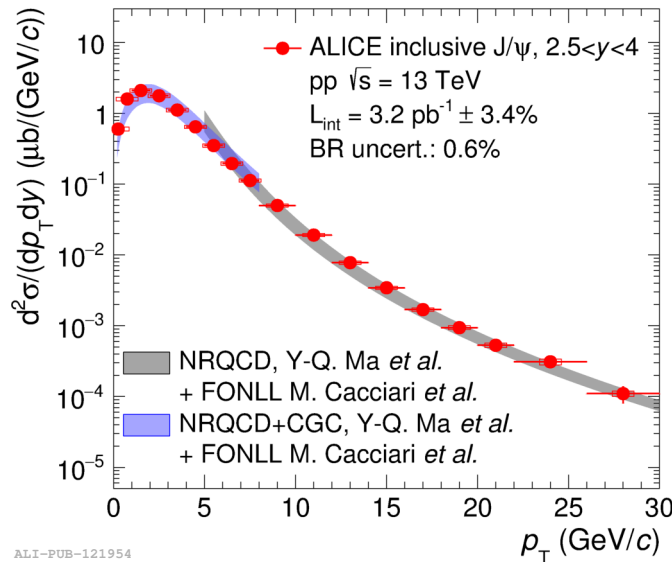


Figure 1.13.: J/ψ production cross section as a function of transverse momentum at forward rapidity in proton-proton collisions at $\sqrt{s} = 13$ TeV, compared to predictions from NRQCD. In NRQCD+CGC, effects from the CGC model are included at low p_T . The non-prompt contribution is taken from FONLL. Figure taken [87].

Especially at high p_T very good agreement with data can be achieved in NRQCD. At low p_T it was shown [96] that the inclusion of initial state effects from the CGC framework into the short-range heavy-quark production amplitudes provides an equally good description of the data. Fig. 1.13 shows the inclusive J/ψ cross section at forward rapidity as a function of transverse momentum in proton-proton collisions at $\sqrt{s} = 13$ TeV, together with two model predictions [87, and references therein]. One model is based on NRQCD and makes predictions at high p_T , a second one is based on NRQCD combined with CGC and makes predictions for J/ψ at low p_T . The non-prompt contribution is calculated from FONLL and added to the prompt J/ψ cross section. With this combination of models an excellent description of the cross section over the full transverse momentum range of the measurement can be achieved.

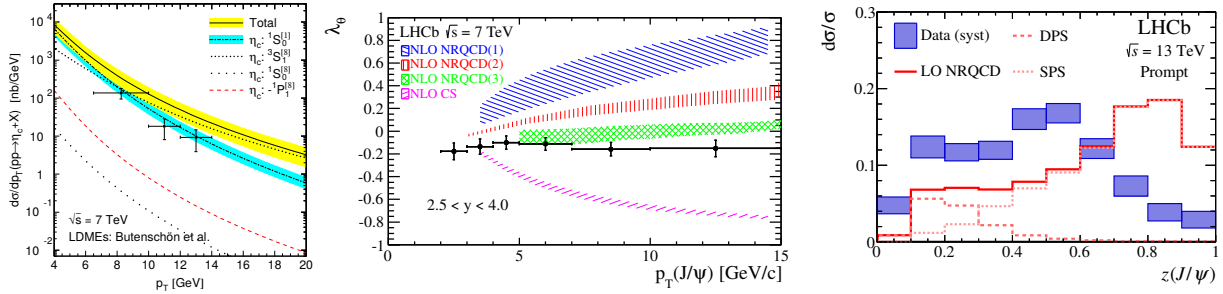


Figure 1.14.: Disagreement between predictions from NRQCD and experimental results of charmonium production in pp collisions from the LHCb experiment. Left: η_c cross section as a function of p_T at $\sqrt{s} = 7$ TeV, compared to NLO NRQCD. Also shown is the color-singlet contribution to the cross section. **Middle:** J/ψ polarization at $\sqrt{s} = 7$ TeV, compared to NLO NRQCD. Also shown is the prediction from the CSM model. **Right:** J/ψ production inside jets at $\sqrt{s} = 13$ TeV, compared to LO NRQCD. Figures taken from [97], [98], [99].

In a contrast, Fig. 1.14 shows some experimental results that cannot be reproduced with NRQCD. The left panel shows a measurement of the p_T -dependent η_c cross section in pp collisions at $\sqrt{s} = 7$ TeV [97], compared to a prediction from NRQCD. The full calculation is shown, and the contributions of the individual intermediate $c\bar{c}$ states. The full NRQCD calculation overpredicts the data significantly, while the color-singlet contribution alone matches the data. The calculations are based on the assumption of Heavy Quark Spin Symmetry (HQSS) to convert the J/ψ -LDMEs for the case of η_c [100]. The disagreement with data can hint to the fact that this assumption does not hold.

An important observable, which so far has often challenged theoretical predictions is the J/ψ polarization, i.e. the projection of the total angular momentum on the z -axis, J_z . Experimentally, small longitudinal J/ψ polarization has been observed in different experiments and in different kinematic regions, cf. [98, and references therein]. The various theoretical models provide ambiguous predictions: CSM predicts significant transverse polarization at leading order, but large longitudinal polarization at higher orders. NRQCD expects large transverse polarization at high transverse momentum, since gluon fragmentation is the dominant production process at high p_T and the J/ψ is assumed to carry over the gluon polarization. In the CEM, polarization is necessarily absent, since any initial polarization is destroyed by soft gluon exchanges [101]. The middle panel of Fig. 1.14 shows a measurement of J/ψ polarization as a function of p_T in pp collisions at $\sqrt{s} = 7$ TeV compared to CSM and several NRQCD predictions by different groups, using different experimental data to constrain the LDMEs. Clearly, the CSM is in disagreement with data, while the various NRQCD predictions strongly differ among each other, with one of them being close to the data. It is worth to note that theoretical predictions of J/ψ polarization are complicated by the contribution of radiatively decaying P -wave χ_c states to the J/ψ yield. Under extreme assumptions for the polarization of the J/ψ from χ_c feed-down, the CSM can be brought into agreement with data [102].

Another interesting disagreement between NRQCD predictions and experimental data is a measurement of J/ψ production inside jets [99], which is shown in the right panel of Fig. 1.14. The momentum

fraction of the jet carried by prompt J/ψ is higher than expected from LO NRQCD predictions implemented in the PYTHIA8 event generator.

In conclusion, charmonium production in pp collisions is currently not fully understood theoretically, and none of the used models is able to simultaneously describe all experimentally observed features, such as production cross sections and polarization. See also [79] for an extensive review.

Central Exclusive Production (CEP) of J/ψ

In contrast to the production in partonic interactions, J/ψ can also be produced in a process where the protons interact with each other as a whole, in Central Exclusive Production (CEP), or photoproduction, see [103] for a review. As the J/ψ has the same quantum numbers as a photon, it can be produced from one via the exchange of a particle carrying the quantum numbers of the vacuum. The process, sketched in Fig. 1.15 is sensitive to the gluon density in the proton (or nucleon if investigated in collisions of nuclei), and can be used as a probe for gluon saturation at low x_{Bj} . Experimentally, its distinct signature can be exploited for detection, e.g. in the dilepton channels, a dilepton pair in an otherwise empty detector is observed. See [104] and [105] for recent results from proton-proton collisions in LHCb and proton-lead collisions in ALICE, respectively.

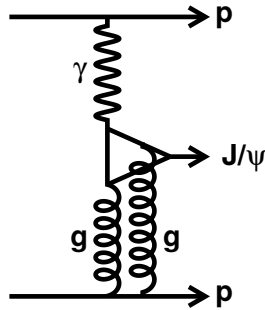


Figure 1.15.: Sketch of central-exclusive J/ψ production in diffractive collision. Figure taken from [106].

1.6.3 Charmonium in heavy-ion collisions

The importance of quarkonia for the study of the medium created in heavy-ion collisions lies in the fact that on the one hand the mass of heavy quarks is too large for a relevant thermal production inside the medium. They are thus created in initial hard partonic interactions and maintain their identity throughout the evolution of the medium. The binding into quarkonia on the other hand happens at much lower energy scales, and is hence susceptible to effects of the medium. An early idea, proposed in 1986 by Matsui and Satz [45] was J/ψ suppression due to color screening.

Due to the high mass of the charm quarks the potential between them can be described with the non-relativistic quark-antiquark potential ("Cornell potential"):

$$V(r) = -\frac{4}{3} \frac{\alpha_s}{r} + \sigma r \quad (1.9)$$

where α_s is the strong coupling constant and σ the string tension due to confinement. $-\frac{4}{3} \frac{\alpha_s}{r}$ is denoted the Coulomb-like term of the potential and σr the confinement term. Fig. 1.16 (left) shows lattice QCD calculations for the non-relativistic quark-antiquark potential as a function of the separation of the quark and antiquark. The results agree very well with the Cornell potential, also shown in the figure.

In the presence of a deconfined medium the potential is damped by a temperature dependent term in a manner similar to Debye screening in electromagnetic potentials; the effect is thus called color screening. The potential at finite temperature T can be parametrized as [108]

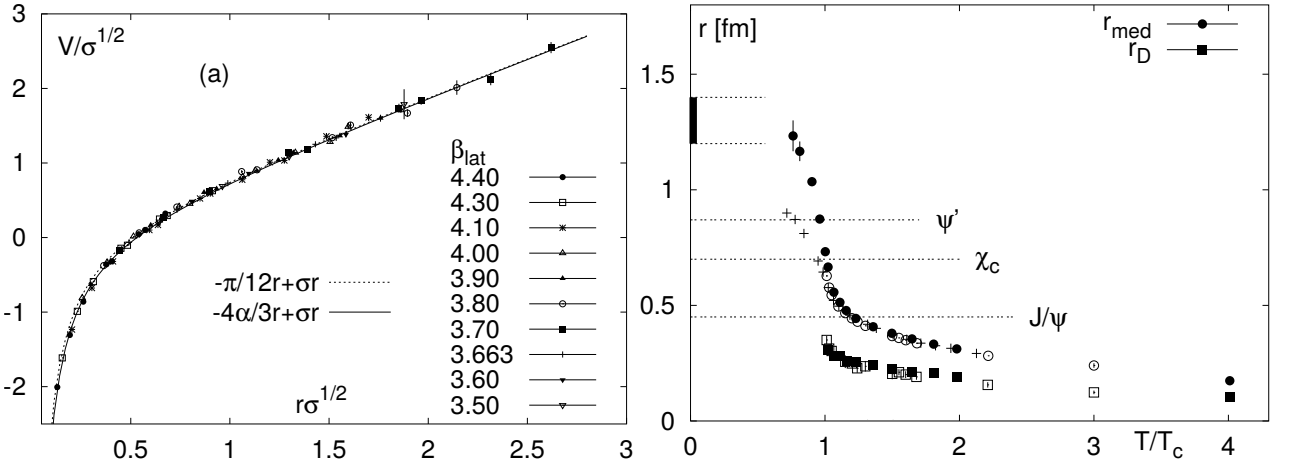


Figure 1.16.: Lattice QCD calculations for the heavy-quark potential. Left: Potential at $T = 0$, compared to Cornell potential (solid line). Right: Evolution of the screening radius (r_{med}) with temperature, in comparison to the radii of the different charmonia states. Figures taken from [107].

$$V(r, T) = V(r, r_D(T)) = -\frac{4}{3} \frac{\alpha_s}{r} e^{-r/r_D(T)} + \sigma r_D(T) (1 - e^{-r/r_D(T)}) \quad (1.10)$$

with $r_D(T)$ the screening length which increases with temperature.

As soon as the screening length becomes comparable to the radius of a quarkonium state, the state is effectively prevented from forming. This process is colloquially referred to as "quarkonium melting" in the medium. The effect is demonstrated in Fig. 1.16 (right) which shows calculations for the screening length from lattice QCD as a function of the temperature in comparison to the radii of J/ψ and the higher charmonia states. Since the higher charmonia states have larger radii, they are expected to dissociate already at lower temperatures than the J/ψ .

Experimentally this effect should manifest itself in a step-wise decrease of total J/ψ production with increasing temperature (i.e. either with increasing collision energy or centrality), as the contributions from higher charmonia feed-down cease, until eventually also the directly produced J/ψ disappears. At lower energies, the modification of J/ψ production due to the hot medium can be quantified e.g. with the ratio to dielectrons from the Drell-Yan process ($q\bar{q} \rightarrow l\bar{l}$). As an electroweak process it is unaffected by the presence of a color-charged medium. At LHC energies most of the charm quarks are produced in gluon fusion processes, so the comparison to lepton pairs from quark-antiquark annihilation is not adequate. The preferred choice for the investigation of medium effects is the nuclear modification factor R_{AA} :

$$R_{\text{AA}}(p_{\text{T}}) = \frac{dN_{\text{AA}}(p_{\text{T}})/dp_{\text{T}}}{\langle N_{\text{coll}} \rangle dN_{\text{pp}}(p_{\text{T}})/dp_{\text{T}}} \quad (1.11)$$

with $N_{\text{AA}}(p_{\text{T}})$ the p_{T} dependent J/ψ yield in nuclear collisions, $N_{\text{pp}}(p_{\text{T}})$ the same in proton-proton collisions, and $\langle N_{\text{coll}} \rangle$ the estimated average number of nucleon-nucleon collision in one nuclear collision. Indeed, in experiments up to SPS energy (i.e. a few 100 GeV), an increasing suppression of J/ψ production could be observed, above the one expected from nuclear matter effects, compare e.g. the results from the NA50 collaboration [109].

For the TeV collision energies at the LHC, new production mechanisms were proposed independently by two different groups around the year 2000. The general idea is, that at those high collision energies, charm yields are high enough that one can expect the production of several charm quark-antiquark pairs in one collision (the temperature is still too low for relevant thermal production of charm quarks though).

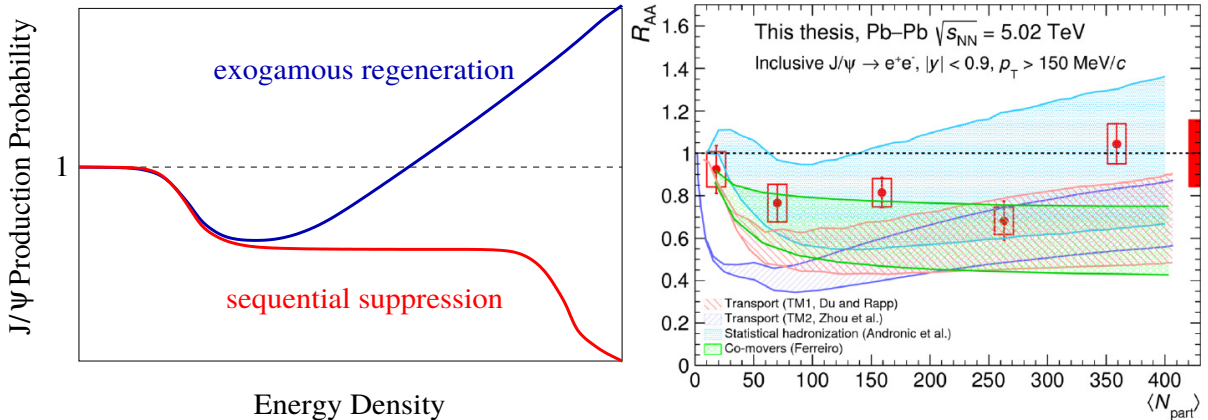


Figure 1.17.: J/ψ suppression / (re)generation in a deconfined medium. Left: General expectation from color screening (sequential suppression) versus (re)generation. Figure taken from [110]. Right: Recent experimental results: J/ψ - R_{AA} as a function of centrality in Pb-Pb collisions at $\sqrt{s_{NN}} = 5.02$ TeV. Figure taken from [111].

It becomes thus possible that a charm quark and an antiquark produced independently in two different pairs (re)combine into a charmonium state. Fig. 1.17 (left) illustrates the consequence: at low collision energy, the sequential suppression mechanism is dominant, while at higher energies, the suppression is reduced due to the recombination mechanism, and possibly overcompensated at high enough energies, so that even an enhancement of J/ψ production can be expected and interpreted as clear sign of the deconfined medium. The idea was implemented in the **Statistical Hadronization Model (SHM)** [46, 112] on the one hand, and in **Transport Model (TM)** calculations [47] on the other hand.

The SHM assumes that no charmonia are formed before the formation of the QGP, or if they are, they will not survive the initial hot phase of the QGP. The typical time scales for these processes support this picture, since both happen approximately at similar timescales between 0.1 fm to 1.0 fm. The charm quarks then move freely in the medium, until they bind either to open or hidden charm hadrons at the same hadronization time as the light flavor hadrons, i.e. at temperature and baryo-chemical potential as determined from thermal model fits to light-flavor hadron abundancies.

In transport models, rate equations are used to model continuous generation, dissociation and re-generation of charmonia states inside the QGP. Due to this microscopic approach, more quantities of J/ψ production can be predicted, such as the p_T distribution. Within the SHM, for such predictions additional external input is needed. However, the transport models also require additional assumptions on not well-constrained quantities, such as medium properties and inelastic charmonium-gluon cross sections. Various implementations of transport model calculations by different groups exist.

Fig. 1.17 (right) shows the nuclear modification factor of inclusive J/ψ in Pb-Pb collisions at $\sqrt{s_{NN}} = 5.02$ TeV measured by ALICE. The data [111] are compared to predictions from SHM and two different implementations of the TM [113, 114], as well as a model assuming a co-moving partonic medium that leads to J/ψ absorption [115]. The models describe the data reasonably well, though they suffer from large uncertainties.

A crucial ingredient of the models is the total charm cross section in nucleus-nucleus collisions, which is not measured with sufficient precision. The perturbative cross section is convoluted with the **nuclear parton distribution functions (nPDF)** in the nucleus, which are not the same as inside a proton, due to phenomena such as gluon saturation at low x_{Bj} , gluon shadowing and gluon anti-shadowing (see [116] for the most commonly used set of nPDFs).

Besides the modified PDFs, other **Cold Nuclear Matter (CNM)** effects — i.e. effects not related to the hot medium created in the collision — might play a role. Examples of these effects are multiple scatterings of the incoming partons before the hard scattering, (coherent) gluon radiation and absorption in the nuclear medium, see [117] and references therein.

These effects can be addressed in the study of J/ψ production in proton-nucleus collisions, in which no creation of a hot medium is expected, however CNM effects are at play the same as in nucleus-nucleus collisions. See [118] for a study of J/ψ production in proton-lead collisions from ALICE.

1.7 Outline of the thesis

Summarizing, it can be stated that especially nonperturbative aspects of particle production in proton-proton collisions still offer room for improvement of our current knowledge. Especially collisions with high particle multiplicities are of high interest, since they provide access to effects related to multiple partonic interactions in one collisions and one might witness the onset of collective effects in them. The J/ψ particle is of special interest in these investigations, since the different energy scales relevant for its production allow access to both perturbative and nonperturbative aspects of the strong interaction.

One highly interesting observable is the charged-particle multiplicity dependence of J/ψ production, which will be introduced in chapter 2. Experimental observations and theoretical model expectations will be presented. The observable will be further studied with an analysis on experimental data taken in proton-proton collisions at $\sqrt{s} = 13$ TeV from the ALICE experiments. The ALICE detector will be described in chapter 3, and the analysis will be presented in chapter 4 and chapter 5, the latter describing the estimation of the systematic uncertainties of the analysis. The results will be discussed in chapter 6. A Monte Carlo study based on the PYTHIA8 event generator will be presented in chapter 7. A summary and an outlook to future experimental opportunities will be given in chapter 8.

2 Charmonium production as a function of event-activity

In this chapter, experimental and theoretical results on charmonium production as a function of event-activity and related observables will be introduced. First some experimental results will be presented, followed by a brief description of theoretical models that can be used for predictions in this regard.

2.1 Experimental results

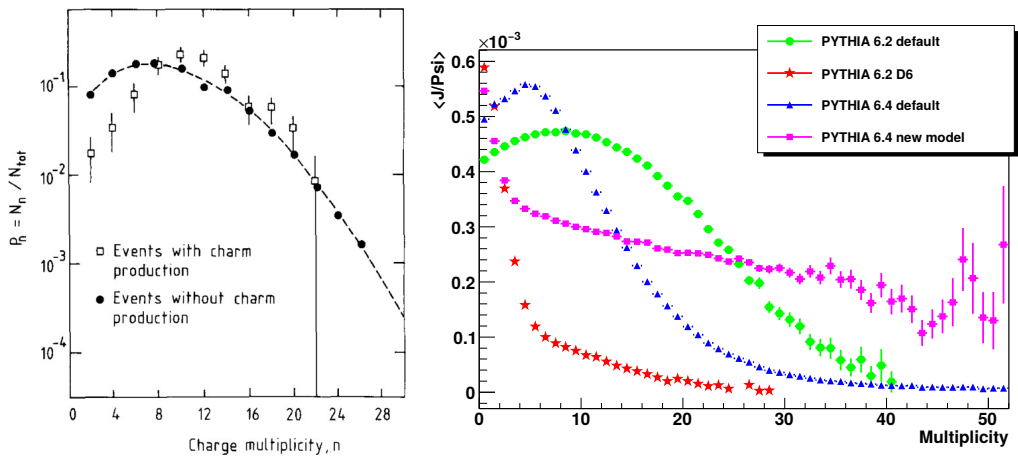


Figure 2.1.: Left: Multiplicity distribution for events with and without charm production from the NA27 experiment. Figure taken from [119]. Right: Expectation for direct J/ψ production as a function of mid-rapidity multiplicity in pp collisions at $\sqrt{s} = 10$ TeV from PYTHIA6, using different settings for multiparton interactions. Figure taken from [120].

The NA27 experiment at CERN compared [119] events with and without open charm production in pp collisions at $\sqrt{s} = 27$ GeV. It was found that the average charged-particle multiplicity of events containing open charm is about 20 % higher than that of events without, and the dispersion of the multiplicity distribution is about 15 % narrower, as shown in Fig. 2.1 (left). Also, a more isotropic shape of events with charm production was observed, as compared to events without charm in experiments at lower energies.

The idea to measure J/ψ production as a function of charged-particle multiplicity was proposed by Porteboeuf and Granier de Cassagnac in [120]. Predictions of the dependence of the J/ψ yield on the charged-particle multiplicity from PYTHIA6.2 and PYTHIA6.4 with different settings for multiparton interactions were presented, as shown in Fig. 2.1 (right). (The predictions were done for a collision energy of 10 TeV. Only directly produced J/ψ particles were considered, but no decay daughters from beauty mesons or higher charmonia states. The charged-particle multiplicity is determined only from particles with $p_T > 0.9$ GeV/c and $|\eta| < 2.4$, corresponding to the acceptance of the CMS experiment.) Quite different behaviors for the different model settings could be observed, indicating large uncertainty especially on the multiparton-interaction treatment, but in any case a decrease of J/ψ production with multiplicity was expected.

ALICE measured [121] the yield of inclusive J/ψ produced at forward ($2.5 < y < 4.0$) and at mid-rapidity ($|y| < 0.9$) as a function of the charged-particle multiplicity at mid-rapidity ($|\eta| < 1.0$) in pp

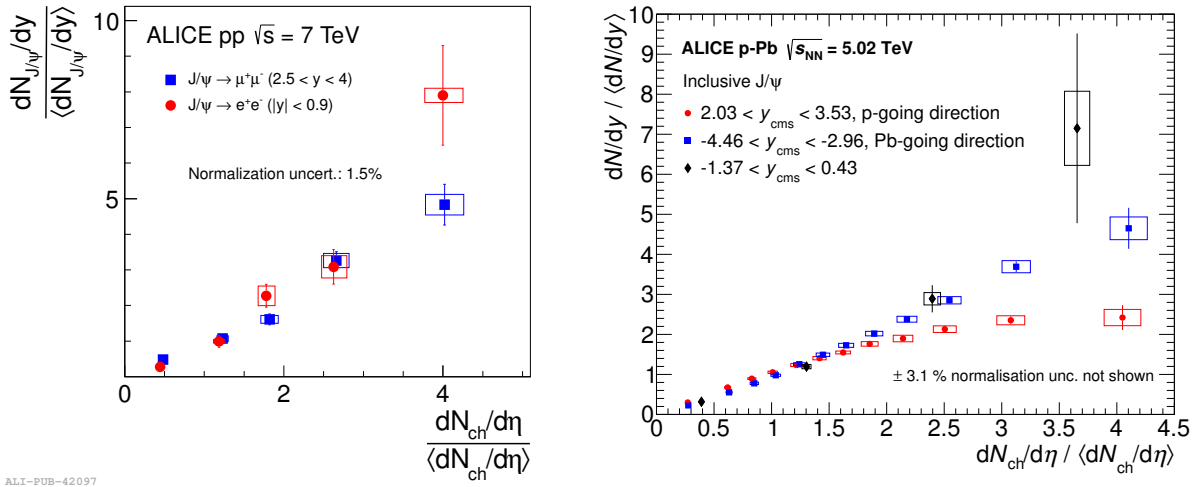


Figure 2.2.: ALICE results on J/ψ production at mid-, forward and backward rapidity as a function of charged-particle multiplicity at mid-rapidity in pp collisions at $\sqrt{s} = 7$ TeV (left), and p-Pb collisions at $\sqrt{s_{NN}} = 5.02$ TeV (right). Figures taken from [121], [122].

collisions at $\sqrt{s} = 7$ TeV. Both values were normalized to their mean values in minimum bias collisions. The result is shown in Fig. 2.2 (left). An increase of J/ψ production with multiplicity was observed in both cases. J/ψ production at forward rapidity seems to rise linearly with the mid-rapidity charged-particle multiplicity, while for J/ψ at mid-rapidity there is a hint of a stronger-than-linear increase. Simulations with the PYTHIA6 model still predicted a decrease of J/ψ production with multiplicity and thus could not describe the data. The analysis was later refined [123] to include only prompt J/ψ . The results were in agreement with the inclusive analysis. The STAR collaboration confirmed with preliminary results [124] the increase of J/ψ production with multiplicity in pp collisions at a lower collision energy of $\sqrt{s} = 500$ GeV. The measurement was done p_T -integrated and for J/ψ with $p_T > 4$ GeV/c. In the high-momentum case the increase is clearly stronger than linear. The data could be well described with the percolation model (see section 2.2.1), and simulations from PYTHIA8 (compare chapter 7 for a study based on the analysis presented in this thesis).

ALICE observed [122] an increase of J/ψ production with charged-particle multiplicity also in p-Pb collisions at $\sqrt{s_{NN}} = 5.02$ TeV. Here, a more differentiated picture emerged, as shown in Fig. 2.2 (right): In the Pb-going direction (backward rapidity) and at mid-rapidity the increase is linear, possibly stronger than linear at mid-rapidity. In the p-going direction (forward rapidity), the increase flattens with higher multiplicities. For the relative mean p_T (mean p_T at given multiplicity divided by mean p_T in minimum bias collisions) of J/ψ , an increase with multiplicity was observed up to around 1.5 times the mean multiplicity, then it flattens out, both at forward and backward rapidity in a very similar manner, and in contrast to the relative mean p_T of charged hadrons at mid-rapidity, which continues rising.

The simultaneous increase of J/ψ with multiplicity in combination with a flattening of the mean p_T can be interpreted on the basis of J/ψ production from an incoherent superposition of parton-parton interactions. The flattening at forward rapidity could be due to shadowing or saturation effects, since the x_{Bj} values of the collisions are in the relevant regions ($2 \cdot 10^5 < x_{Bj} < 8 \cdot 10^5$ for forward rapidity, $1 \cdot 10^2 < x_{Bj} < 5 \cdot 10^2$ for backward rapidity).

In the bottomonium sector, the CMS experiment investigated [125] the event activity dependence of $\Upsilon(nS)$ production (for $n = 1, 2, 3$) at mid-rapidity ($|y_{cm}| < 1.93$) in pp collisions at $\sqrt{s} = 2.76$ TeV and p-Pb collisions at $\sqrt{s_{NN}} = 5.02$ TeV. Two different event activity estimators were used: the charged-particle multiplicity measured at mid-rapidity ($|\eta| < 2.4$), and the sum of transverse energy deposited at forward rapidity ($4.0 < |\eta| < 5.2$). For p-Pb collisions, a linear increase with event activity was observed for both estimators. For pp collisions, if the event activity is estimated in the same region where the $\Upsilon(nS)$ signals

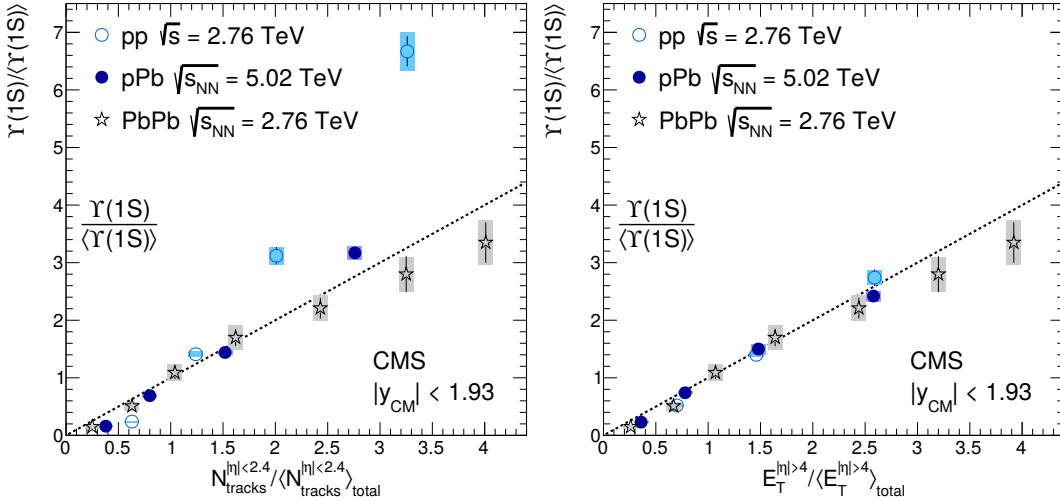


Figure 2.3.: CMS results on mid-rapidity Υ production as a function of event activity in pp, p-Pb and Pb-Pb collisions at $\sqrt{s} = 2.76$ TeV, $\sqrt{s_{NN}} = 5.02$ TeV, and $\sqrt{s_{NN}} = 2.76$ TeV, respectively. Event activity estimated at mid-rapidity (left), or forward rapidity (right). Figure taken from [125].

are measured, a stronger-than-linear increase is seen. If an η gap between the estimator and the signal is introduced, the increase is the same as for the p-Pb case, i.e. linear. The results were also compared with Pb-Pb collisions at $\sqrt{s_{NN}} = 2.76$ TeV, which show a linear, or slightly weaker than linear increase with multiplicity for both estimators. The results are shown in Fig. 2.3 for the case of the $\Upsilon(1S)$.

It was also observed, that the ratio of the excited states $\Upsilon(2S)$ and $\Upsilon(3S)$ to the ground state $\Upsilon(1S)$ decreases with multiplicity, both in pp and p-Pb collisions. The effect is stronger in the case where the multiplicity is estimated in the same rapidity region as the signal. The measurements were also compared to the values from Pb-Pb collisions. A continuous decrease of the ratio seems to be present for all three collision systems, though in Pb-Pb collisions the effect is not significant due to larger statistical uncertainties.

It is interesting to compare the results on quarkonia with the open heavy-flavor sector. Here, ALICE has measured open-charm and open-beauty production as a function of multiplicity in pp collisions at $\sqrt{s} = 7$ TeV [123] and open-charm production in p-Pb collisions at $\sqrt{s_{NN}} = 5.02$ TeV [126]. For the open-charm measurement, fully reconstructed D-mesons were measured. Open beauty was accessed via the measurement of non-prompt J/ψ . In the D-meson measurement, the dependence on two different multiplicities was investigated: the mid-rapidity multiplicity, and forward rapidity multiplicity, in pp collisions estimated from the sum of the signals of the V0A and V0C detectors, in p-Pb collisions from the multiplicity in the V0A detector, i.e. in the Pb-going direction. See chapter 3 for a description of ALICE and its subdetectors.

The results of the D-meson measurements are shown in Fig. 2.4. As a function of multiplicity in the same rapidity region as the signal, the D-meson yield increases faster than linearly both in pp and p-Pb collision, in the latter case the increase is probably slightly weaker. Plotting against the multiplicity at forward rapidity, the increase in pp collisions stays stronger than linear, in p-Pb it becomes linear. In pp collisions, a p_T differential study was performed. No significant p_T dependence of the increase with multiplicity was found, although there is a hint for a stronger increase at higher p_T . The non-prompt J/ψ measurement was done as a function of the mid-rapidity multiplicity. As can be seen in Fig. 2.5 (right), an increase with multiplicity was observed, consistent with linearity, but with the hint of a stronger-than-linear increase.

The results on D-meson production in pp collisions have been compared to several models, as presented in Fig. 2.5 (left), these are the percolation model (see section 2.2.1), the PYTHIA8 event generator (see chapter 7), and the EPOS3 event generator, either with or without hydrodynamical expansion

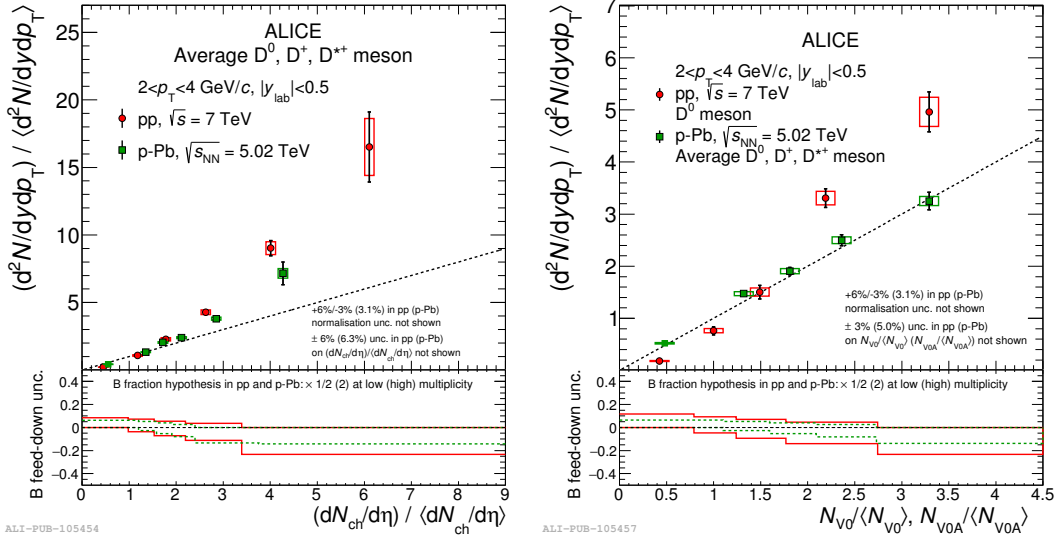


Figure 2.4.: ALICE results on D-meson production at mid-rapidity in pp collisions at $\sqrt{s} = 7$ TeV and p-Pb collisions at $\sqrt{s_{NN}} = 5.02$ TeV as a function of charged-particle multiplicity at mid-rapidity (left), and forward rapidity (right). Figures taken from [126].

of the system (compare section 2.2.4). All the models qualitatively describe the data. In case of the EPOS3 model, the inclusion of hydrodynamics is crucial for a quantitative description of the data. When including it, a good description of the data is reached. The PYTHIA8 generator seems to underpredict the increase.

In a detailed study with the PYTHIA8 generator the influence of the different heavy-flavor production mechanisms was investigated. It was found, that multiparton interactions are crucial in order to understand the increase with multiplicity. More details on the different mechanisms in PYTHIA8, and a comparable study for the J/ψ case will be presented in chapter 7.

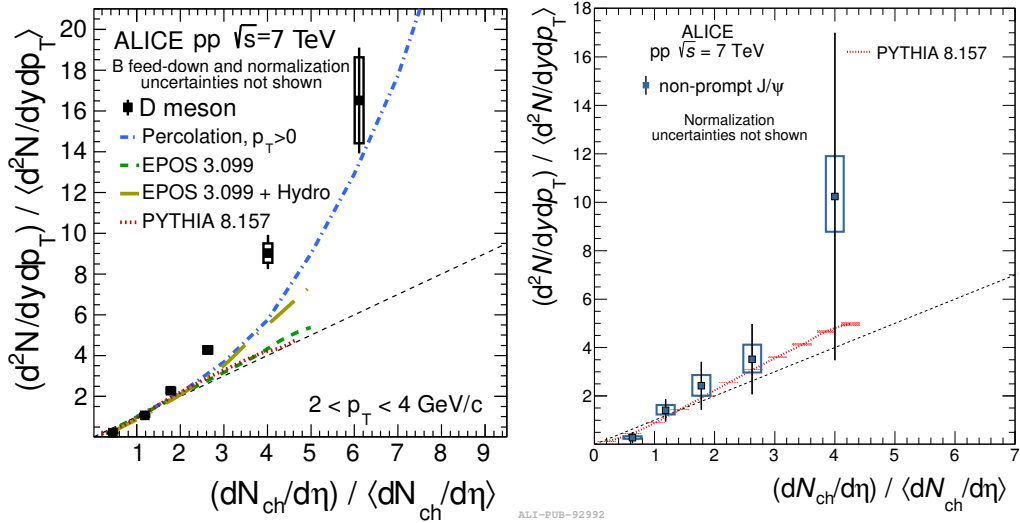


Figure 2.5.: ALICE results on open heavy-flavor production at mid-rapidity as a function of charged-particle multiplicity at mid-rapidity in pp collisions at $\sqrt{s} = 7$ TeV. Left: D-mesons, compared to model predictions from percolation model, EPOS3, and PYTHIA8.1. Right: Non-prompt J/ψ , compared to prediction from PYTHIA 8.1. Figures taken from [123].

Table 2.1 (top) summarizes the findings for open heavy-flavor and quarkonium production as a function of multiplicity in pp collisions. It can be stated that if both multiplicity and the signal are measured at mid-rapidity, a stronger-than-linear increase is observed. If the multiplicity is measured at forward rapidity, the increase remains stronger than linear in the case of open heavy-flavor, for quarkonium it becomes linear. For the latter, only a measurement on bottomonium exists so far. (The charmonium case will also be covered in this thesis. It has to be noted however, that in this thesis an analysis of inclusive J/ψ is presented, containing a significant fraction of non-prompt J/ψ , an open heavy-flavor component.) At forward rapidity the measurement of J/ψ shows only a linear increase with multiplicity at mid-rapidity.

The situation in p-Pb collisions is summarized in table 2.1 (bottom). Here, a difference is that mid-rapidity bottomonium production increases only linearly with mid-rapidity multiplicity, while for open charm the increase remains stronger than linear, and for charmonium there is a hint for a stronger-than-linear increase. Again, it has to be kept in mind that the J/ψ measurement contains an open heavy-flavor component. When the multiplicity is measured at forward rapidity, the increase is both in case of open charm and bottomonium linear. Similar to pp collisions, charmonium production at forward rapidity increases linearly with mid-rapidity multiplicity when measured in the Pb going direction; in the p going direction, a weaker than linear increase is observed.

Table 2.1.: Summary of results on heavy-flavor production in pp and p-Pb collisions as a function of multiplicity. Results for **charmonium**, **bottomonium**, D-mesons and **B mesons**. "Stronger", "weaker" and "linear" denotes a stronger-than-linear, weaker-than-linear, or linear increase of the yield as a function of multiplicity, respectively.

Proton-proton collision

Signal Multiplicity	Mid-rapidity	Forward rapidity
Mid-rapidity	stronger [121, 123, 124]	linear [121]
	stronger [125]	–
	stronger [123]	–
	stronger(?) [123]	–
Forward rapidity	(this thesis)	–
	linear [125]	–
	stronger [123]	–
	–	–

Proton-lead collision

Signal Multiplicity	Mid-rapidity	p-going	Pb-going
Mid-rapidity	stronger(?) [122]	weaker [122]	linear [122]
	linear [125]	–	–
	stronger [126]	–	–
Forward rapidity (p and Pb-going combined) (Pb-going)	–	–	–
	linear [125]	–	–
	linear [126]	–	–

2.1.1 Light-flavor sector

Going away from heavy flavors, high- p_T charged hadrons represent another hard probe. In a preliminary measurement [127], ALICE investigated the increase of mid-rapidity charged-hadron production above different minimum p_T values as a function of the mid-rapidity multiplicity in pp collisions at $\sqrt{s} = 13$ TeV. The results are shown in Fig. 2.6. A stronger-than-linear increase is observed, the increase gets steeper with higher minimum p_T . The result is qualitatively very similar to the observations in the heavy-flavor sector. The PYTHIA8 model qualitatively describes the experimental observation.

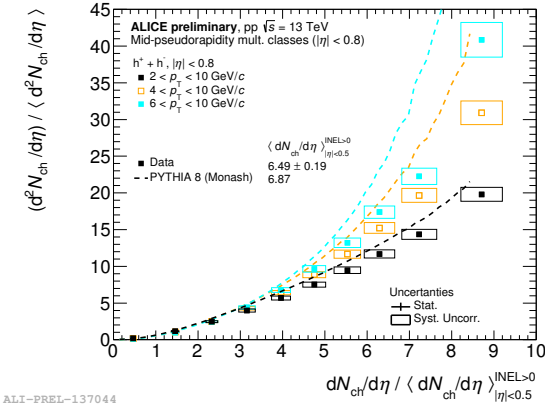


Figure 2.6.: Preliminary ALICE results on high- p_T charged-hadron production at mid-rapidity as a function of mid-rapidity charged-particle multiplicity, compared to prediction from the PYTHIA8 model. Figure taken from [127].

2.2 Theoretical models

2.2.1 Percolation model

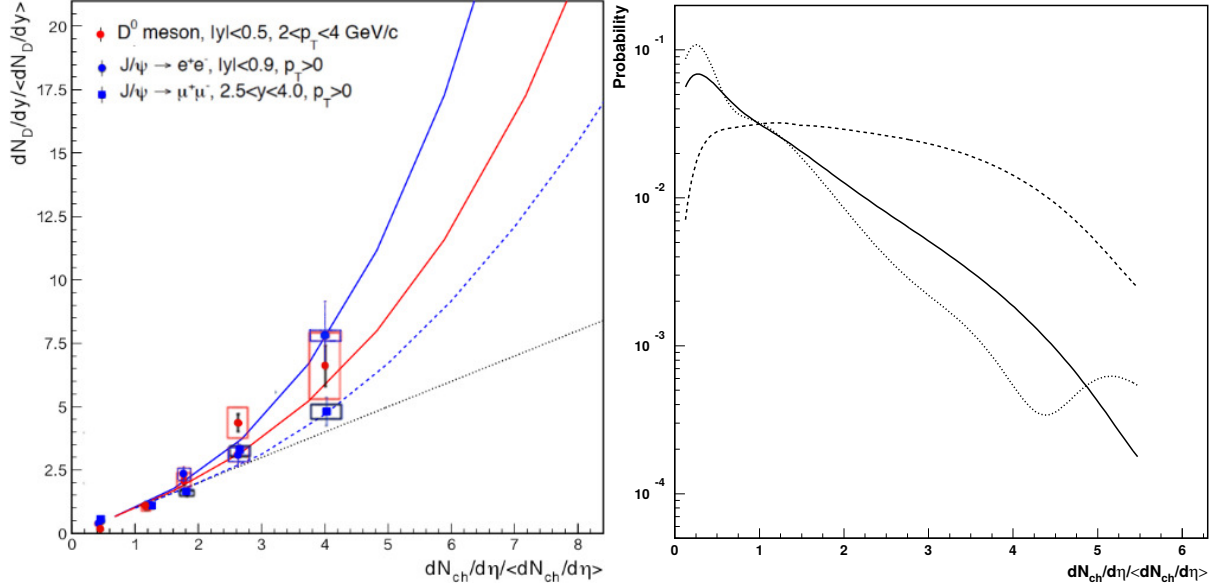


Figure 2.7.: Predictions from the percolation model [128], [129]. Left: mid and forward rapidity J/ψ and mid-rapidity D-meson production as a function of mid-rapidity multiplicity in pp collisions at $\sqrt{s} = 7$ TeV, compared to ALICE experimental data [121, 123]. Right: Probability distributions for the charged-particle multiplicities for minimum bias events (solid line), events with J/ψ produced at mid-rapidity from PYTHIA6 (dotted line), and from the percolation model (dashed line).

In their model [128, 129], E. G. Ferreiro and C. Pajares attribute the observed stronger-than-linear increase of J/ψ production with charged-particle multiplicity to a saturation of soft particle production in high-multiplicity proton-proton collisions.

The basic assumption is that the color strings as elementary sources of particle production have a non-zero transverse size. At high density they start to overlap, thus reducing their effective number.

Hard probes — such as the J/ψ —, are produced in parton-parton interactions; their number $N_{J/\psi}$ is proportional to the number of produced strings N_s . For the relative values normalized to their mean values $n_{J/\psi} \equiv N_{J/\psi} / \langle N_{J/\psi} \rangle$ and $n_s \equiv N_s / \langle N_s \rangle$ thus holds

$$n_{J/\psi} = n_s \quad (2.1)$$

The overall charged-particle multiplicity density on the other hand, is governed by soft particles which are subject to the overlapping of the strings. The number of charged particles per unit of rapidity $dN/d\eta$ can be expressed as

$$dN_{ch}/d\eta = F(\rho)N_s\mu_1 \quad (2.2)$$

with μ_1 the multiplicity produced from a single string, and a damping factor $F(\rho)$, caused by the string interactions and depending on the string density ρ :

$$F(\rho) = \sqrt{\frac{1 - e^{-\rho}}{\rho}}. \quad (2.3)$$

Combining equations 2.1 and 2.2, one finds for the dependence of the self-normalized J/ψ yield on the relative charged-particle multiplicity $n_{\text{ch}} = \frac{dN/d\eta}{\langle dN/d\eta \rangle}$ following approximate behavior:

$$n_{J/\psi} = (1 - \langle \rho \rangle) n_{\text{ch}} + \langle \rho \rangle n_{\text{ch}}^2 \quad (2.4)$$

At low string density — so at low multiplicity — the J/ψ yield grows linearly with multiplicity, changing into a quadratic increase at higher multiplicity.

As shown in Fig. 2.7 (left), the model describes accurately the increase of J/ψ and D-meson yields with the charged particle multiplicity at $\sqrt{s} = 7$ TeV as measured by ALICE [121, 123]. At forward rapidity a lower string density is assumed, so the increase of J/ψ is weaker. The uncertainty of the string density also gives the main uncertainty of the model of about 20 %.

From the model also the difference of the multiplicity distributions for events with and without production of J/ψ particles can be predicted. This is shown in Fig. 2.7 (right), which shows the multiplicity distributions for minimum bias events from experimental data, compared to events with J/ψ production from the PYTHIA6 event generator, and from the percolation model. In contrast to PYTHIA6, which expects a lower multiplicity for events containing J/ψ , in this model a depletion of low multiplicity events and an enhancement of high multiplicity ones is expected.

2.2.2 Higher Fock states model

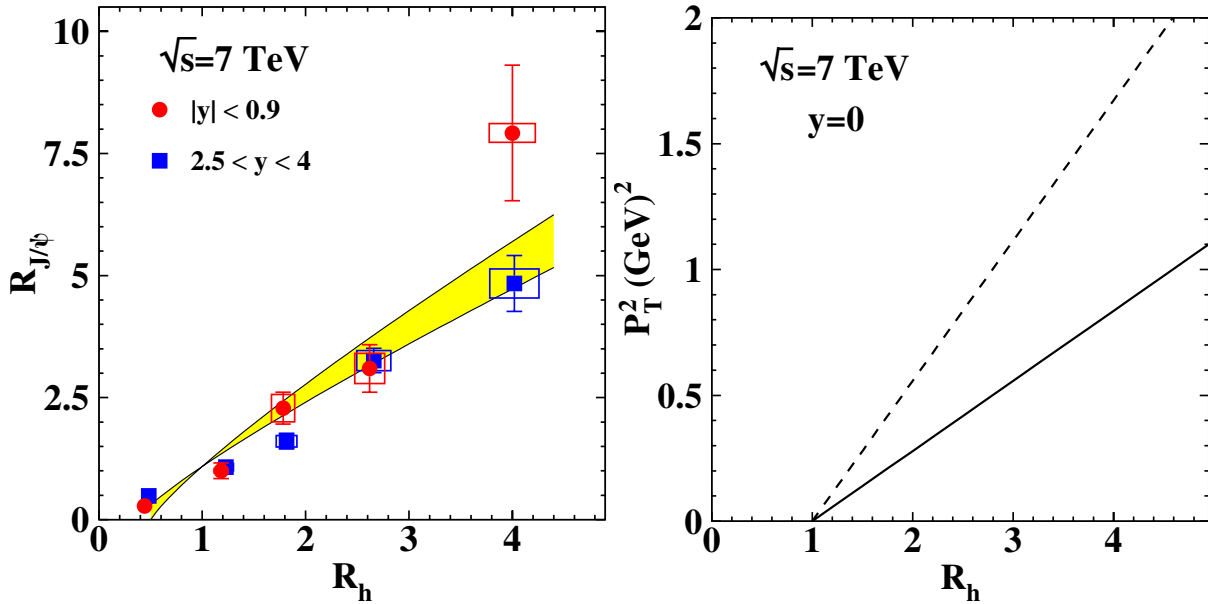


Figure 2.8.: Predictions from the higher-Fock-states model [130]. Left: J/ψ production at mid- and forward rapidity as function of mid-rapidity multiplicity in pp collisions at $\sqrt{s} = 7$ TeV, compared to ALICE results [123]. Right: J/ψ transverse-momentum broadening as a function of multiplicity. Dashed (solid) line: excluding (including) gluon shadowing corrections.

The model [130] by B. Z. Kopeliovich, H. J. Pirner, I. K. Potashnikova, K. Reijgers and I. Schmidt draws an analogy between high-multiplicity pp collisions and proton-nucleus (pA) collisions: in high energy nuclei there is an overlap of gluons in the longitudinal direction at small x_{Bj} , so that the nucleus acts as a single source of gluons. In a single nucleon this corresponds to the contributions of higher Fock states. From this analogy it is conjectured that observations from pA collisions can be used to make predictions for pp collisions.

First, the ratio of the average hadron densities in pA collisions and pp collisions $R_h^{pA} \equiv \frac{\langle dN_h^{pA}/dy \rangle}{\langle dN_h^{pp}/dy \rangle}$ is parametrized to depend on the number of collisions N_{coll} in the following way:

$$R_h^{pA} = 1 + \beta(N_{\text{coll}} - 1) \quad (2.5)$$

The β parameter describes the departure of the hadron multiplicity from pure N_{coll} scaling due to cold nuclear matter effects. Based on experimental observations from fixed-target experiments at Fermilab and collider experiments at RHIC, it is estimated to be in the range $0.5 < \beta < 0.65$. The upper and lower limit of this estimate are taken as uncertainty of the model.

Identifying the nuclear inelastic cross section with the geometric one, the number of colliding nucleons can be related to the nuclear mass number A :

$$N_{\text{coll}} \approx \frac{\sigma_{\text{inel}}^{pp}}{\pi r_0^2} A^{1/3} \quad (2.6)$$

with r_0 the nucleon radius and $\sigma_{\text{inel}}^{pp}$ the inelastic proton-proton cross section.

The ratio of the mean J/ψ yield in pA and pp collisions $R_{J/\psi}^{pA} \equiv \frac{\langle dN_{J/\psi}^{pA}/dy \rangle}{\langle dN_{J/\psi}^{pp}/dy \rangle}$ on the other hand depends on N_{coll} and A in the following way:

$$R_{J/\psi}^{pA} = N_{\text{coll}} A^{\alpha-1} \quad (2.7)$$

with α a collision energy and rapidity dependent parameter. At mid-rapidity a value $\alpha = 0.95$ is assumed. Again, this parametrization is motivated by experimental data.

Inserting equations 2.5 and 2.6 into equation 2.7, one arrives at the correlation between the J/ψ yield and charged-particle multiplicity in pA collisions:

$$R_{J/\psi}^{pA} = \left(1 + \frac{R_h^{pA} - 1}{\beta} \right)^{3\alpha-2} \left(\frac{\sigma_{\text{inel}}^{pp}}{\pi r_0^2} \right)^{3(1-\alpha)} \quad (2.8)$$

A crucial assumption of the model is now to infer that equation 2.8 also holds for the corresponding ratios of high-multiplicity and minimum bias pp collisions $R_h^{pp} \equiv \frac{\langle dN_h^{pp}/dy \rangle}{\langle dN_h^{pp}/dy \rangle}$ and $R_{J/\psi}^{pp} \equiv \frac{\langle dN_{J/\psi}^{pp}/dy \rangle}{\langle dN_{J/\psi}^{pp}/dy \rangle}$.

A comparison with the ALICE measurement of the increase of the J/ψ yield at forward and mid-rapidity as a function of the charged-particle multiplicity in pp collisions at $\sqrt{s} = 7 \text{ TeV}$ is shown in Fig. 2.8 (left). The model agrees well with the data.

Extending further the analogy between high-multiplicity pp collisions and pA collisions, the model predicts a linear p_T broadening with increasing charged-particle multiplicity, i.e. an increase of the mean transverse momentum squared $\Delta p_T^2 \equiv \langle p_T^2 \rangle_{R_h^{pA} > 1} - \langle p_T^2 \rangle_{R_h^{pA} = 1}$:

$$\Delta p_T^2 \propto (R_h^{pp} - 1). \quad (2.9)$$

The prediction for J/ψ at mid-rapidity in pp collisions at $\sqrt{s} = 7 \text{ TeV}$ is shown in Fig. 2.8 (right).

2.2.3 CGC model

In their model [131], Ma, Tribedy, Venugopalan and Watanabe combine the CGC effective field theory with the NRQCD EFT and the improved Color Evaporation Model (ICEM) (cf. chapter 1). With it they describe the observed increase of J/ψ production as a function of charged-particle multiplicity measured by ALICE in pp collisions at $\sqrt{s} = 7$ TeV [121] and the preliminary results [132] of the analysis at $\sqrt{s} = 13$ TeV, described in this thesis. Also the multiplicity dependence of D-meson and forward-rapidity J/ψ production and the measurements in p-Pb collision are described with the model.

According to the model, high multiplicity pp collisions select events with high parton densities in the incoming protons, leading to strongly correlated gluons. Within the CGC model, the parton density increase with multiplicity can be treated via an increase of the saturation scale Q_s .

As shown in Fig. 2.9 (left), this approach, employing the ICEM model, provides a very good description of mid-rapidity J/ψ production as a function of multiplicity both at $\sqrt{s} = 7$ TeV and $\sqrt{s} = 13$ TeV.

Utilizing the NRQCD approach, one finds that the color octet and color singlet channels have different dependences on the dynamics of the saturated gluons. They show thus a different dependences on the charged-particle multiplicity, as shown in Fig. 2.9 (right). At high multiplicity the color octet 3S_1 channel dominates, indicating the dominance of gluon fragmentation in this region. From these findings an interesting possibility for the use of multiplicity-dependent J/ψ measurements arises, namely the possibility to extract the long distance matrix elements of the NRQCD model from these kind of measurements, especially at low and intermediate p_T .

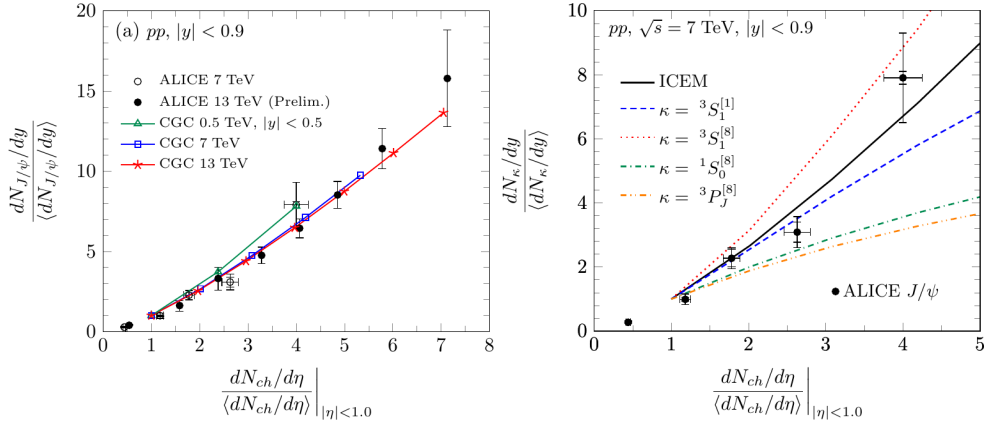


Figure 2.9.: Predictions for mid-rapidity J/ψ production as function of mid-rapidity multiplicity from the CGC model compared to ALICE data [121, 132]. Left: Combining CGC with the ICEM model. Right: Contribution of the different channels according to the CGC+NRQCD model, compared to GCG+ICEM. Figure taken from [131].

2.2.4 EPOS3 event generator

EPOS [27] (Energy conserving quantum mechanical multiple scattering approach, based on Partons (parton ladders), Off-shell remnant, and Splitting of parton ladders) is a universal model for proton-proton, proton-nucleus and nucleus-nucleus collisions.

In this model, the elementary scattering is expressed in the so called Parton-Based Gribov-Regge theory (PBGRT) formalism. The elementary scattering objects are parton ladders, or pomerons, which are exchanged between the partons participating in the collision. Motivated by CGC, a saturation of pomeron exchanges is implemented. The parton ladders consist of a hard pQCD scattering vertex, accompanied by initial (space-like) and final (time-like) state parton emission. Fig. 2.10 shows a sketch of a proton-proton collision in EPOS; it also shows where in the collision heavy quark production can happen.

In the latest version of the model (EPOS3 [133]), after the initial interactions a split into a core and a corona part is performed, based on the momentum and density of the string fragments. The soft particles in the core are treated with a viscous hydrodynamic expansion, whereas the hard particles in the corona escape. At a constant temperature, the core particles hadronize [134], a hadronic afterburner phase follows, using the UrQMD model [135, 136].

This model can well describe the stronger than linear increase of D-meson production as a function of event activity in pp and p-Pb collisions. In the following, the origin of the effect in the EPOS3 model will be sketched. The explanations are based on [137] and to a large extend should also apply to the case of charmonium.

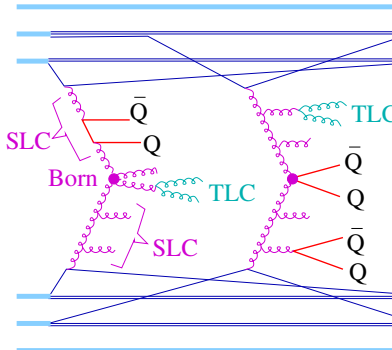


Figure 2.10.: Schematic picture of a proton-proton collision in EPOS and heavy-quark production mechanisms in hard scattering (Born), space-like parton cascades (SLC), and time-like parton cascades (TLC). Figure taken from [137].

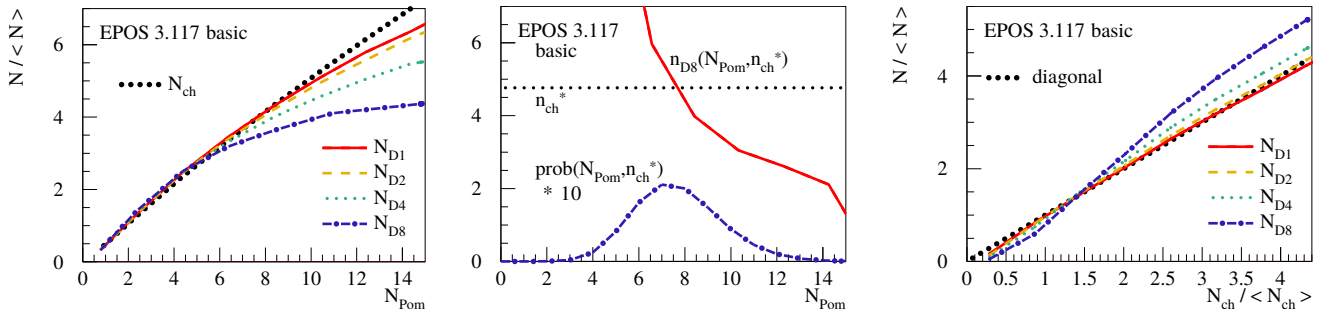


Figure 2.11.: EPOS3 model without hydrodynamic expansion. Right: D-meson production at different p_T as a function of the number of exchanged pomerons. Middle: For a given charged-particle multiplicity n_{ch}^* : probability to have N_{Pom} pomerons exchanged (blue dotted line), and relative high- p_T D-meson production at given N_{Pom} and n_{ch}^* (red line). Right: D-meson production as a function of charged-particle multiplicity. Figures taken from [137].

First, the situation without the hydrodynamic expansion of the system is considered. Heavy quarks are produced during the initial stage of the collision, as are the other particles. The charged-particle multiplicity N_{ch} increases linearly with the number of exchanged pomerons N_{Pom} , as shown in Fig. 2.11 (left). The increase of D-meson production is slightly weaker, especially at high p_T due to the mentioned saturation effects from the CGC.

Though N_{ch} depends linearly on N_{Pom} , it is a broad distribution, so that a collision with a high N_{ch} can either have a high number of exchanged pomerons with average hardness each, or a small number of hard pomerons, each producing a high number of particles. This is illustrated in Fig. 2.11 (middle): for a given relative charged-particle multiplicity n_{ch}^* the probability to have N_{Pom} pomerons exchanged is shown.

The production of a hard probe is more likely for events with hard pomerons exchanged, this implies that for a given charged-particle multiplicity, events with fewer but harder pomerons are favored. This fact is illustrated Fig. 2.11 (middle) with the line showing the relative high p_T D-meson production probability at the given multiplicity as a function of the number of exchanged pomerons: the probability for D-meson production falls steeply with the number of exchanged pomerons.

This effect then leads to a stronger than linear increase of D-meson production with charged-particle multiplicity, the increase getting stronger with p_T , as shown in Fig. 2.11 (right).

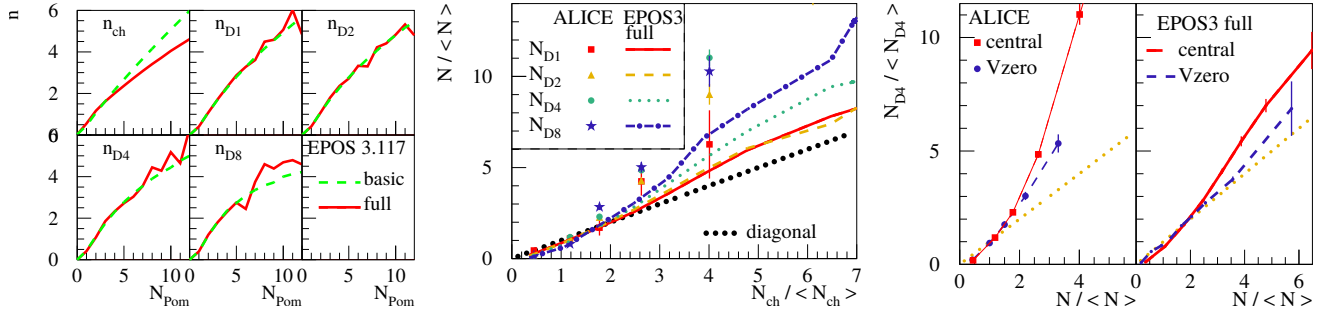


Figure 2.12.: Effect of hydrodynamic expansion in EPOS3. Left: Relative charged-particle and D-meson production as a function of the number of exchanged pomerons in EPOS3 with and without hydrodynamic expansion. Middle and right: Full model prediction of D-meson production as a function of multiplicity in pp collisions at $\sqrt{s} = 7$ TeV, compared to experimental data from ALICE [123]. Middle: different p_T intervals, left: comparison between mid-rapidity and forward rapidity multiplicity dependence. Figures taken from [137].

The subsequent hydrodynamic evolution of the system then amplifies this effect. As shown in Fig. 2.12 (left), the charged-particle multiplicity is reduced by the hydrodynamic expansion, but not the D-meson production. This can be interpreted in such a way, that a part of the available energy goes into the transverse flow rather than particle production, reducing the multiplicity. D-mesons, being hard probes do not take part in the hydrodynamic expansion, so are unaffected.

The full model prediction is shown in Fig. 2.12 (middle), together with the experimental data from the ALICE experiment [123]. A good description of the data is achieved.

When investigating the increase of mid-rapidity D-meson production with the multiplicity at forward rapidities, the overall effect is weakened. The reason is the reduced correlation between multiplicity in this region with D-meson production. The model prediction for this case is shown in Fig. 2.12 (right), again compared to experimental data from the ALICE experiment [123] and shows a good agreement with it.

2.3 Summary

Summarizing the current knowledge on the production of hard probes as a function of event activity in proton-proton collisions, one can state the following:

Hard-probe production in pp collisions increases with multiplicity. When both the signal and the multiplicity are measured at the same rapidity, the increase is stronger than linear. By introducing a gap in rapidity between the signal and the multiplicity the effect is weakened, and in the case of hidden heavy flavor seems to be only linear. This hints to the fact that a relevant amount of the observed increased might be due to auto-correlation effects between the hard probe and the overall measured multiplicity. The results for light, open and hidden heavy flavor are similar, so it is adequate to assume the origin of the effect in the hardness of the probe, and to be independent of the microscopic composition.

The observations seem to be independent of collision energy, but it will be interesting to investigate the highest currently available LHC energy. Some questions were not yet addressed exhaustively, like

whether there is a p_T dependence of the increase with multiplicity in the case of quarkonia, and the effect of a rapidity gap between the signal and the multiplicity estimator for charmonia in pp collisions. Furthermore it would be interesting to investigate the different quarkonia production mechanisms in PYTHIA8 and their behavior with multiplicity, as was done for the open heavy flavor case. And finally, no quarkonium measurement so far was able to go to higher relative multiplicities than about 4. The theoretical models start to disagree above this value, so it will be very interesting to extend the measurements. All this open points will be addressed in this thesis.

From the theory point of view, the picture can be summarized in the following way: In order to have at least a linear increase of hard probe production with multiplicity, some mechanism for multiple interactions within one pp collision is crucial, be it the intrinsic multi-scattering approach of EPOS, or multiple partonic interactions. The non-linearity of the increase can be attributed to a reduction of the charged-particle multiplicity, e.g. via overlapping strings in the percolation model, or the hydrodynamical expansion in EPOS3.

In proton-nucleus collisions, both the results and the theoretical interpretation seem to be less straight forward, a main reason is that the multiplicity has to be seen as a convolution of the number of individual hadronic collisions and the multiplicity of one of these collisions.



3 The ALICE experiment at the LHC

3.1 The Large Hadron Collider

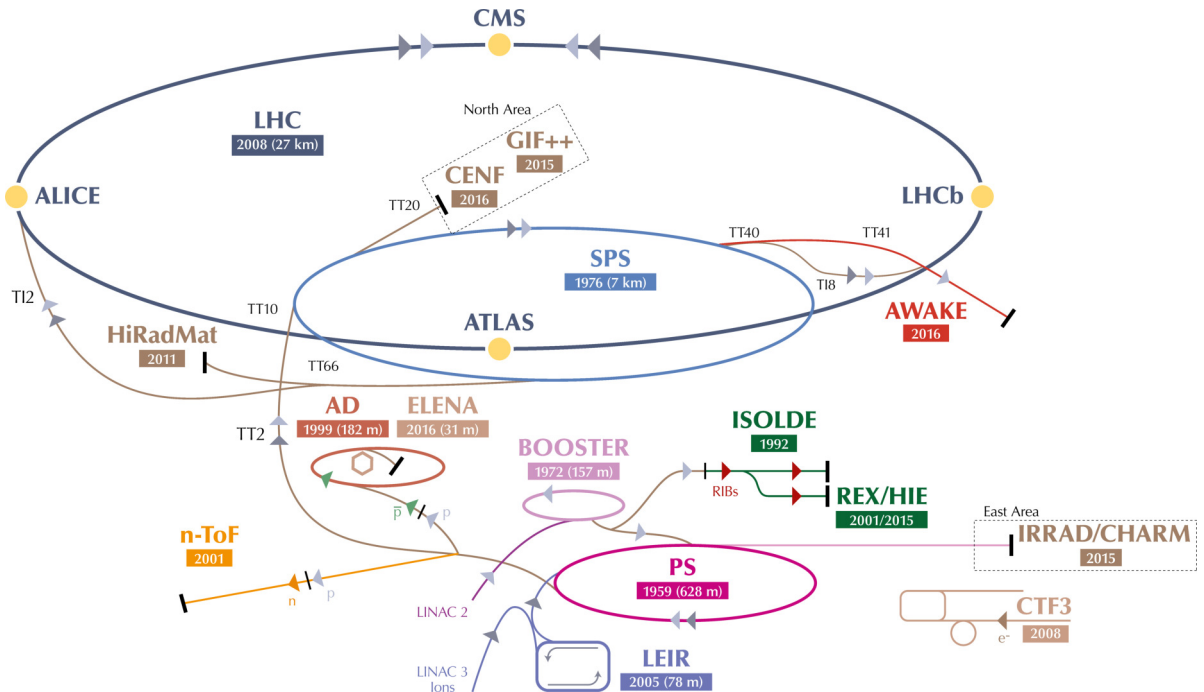


Figure 3.1.: Schematic view of the CERN accelerator complex and its four largest experiments. Figure taken from [138].

The Large Hadron Collider (LHC), located at the European Organization for Nuclear Research (CERN) in Geneva, is the largest collider ever built, reaching the highest collision energies. The ring collider with a circumference of 26.7 km was built into the tunnel originally constructed for the Large Electron Positron Collider (LEP), 45 to 170 m below the surface. The accelerator complex with its pre-accelerators is shown in Fig. 3.1. Details can be found in [139].

Operation began in November 2009. The Run-1 of data taking concluded in February 2013. In this period, the LHC delivered proton-proton (pp) collisions at center-of-mass energies of up to $\sqrt{s} = 8$ TeV, proton-lead (p-Pb) collisions at $\sqrt{s_{NN}} = 5.02$ TeV and lead-lead (Pb-Pb) collisions at $\sqrt{s_{NN}} = 2.76$ TeV. This data taking period lead to the discovery by ATLAS and CMS [11] [12] of the Higgs boson, the last missing elementary particle predicted by the Standard model of particle physics.

After a two year maintenance and upgrade phase, called the Long Shutdown 1 (LS1), Run-2 started in April 2015. Up to now, experiments were provided with pp collisions at $\sqrt{s} = 13$ TeV, p-Pb collisions of up to $\sqrt{s_{NN}} = 8.16$ TeV, Pb-Pb collisions at $\sqrt{s_{NN}} = 5.02$ TeV, and – introducing a whole new collision system to the LHC – xenon-xenon (Xe-Xe) collisions at $\sqrt{s_{NN}} = 5.44$ TeV. In pp collisions, instantaneous luminosities of over $2 \cdot 10^{34} \text{ cm}^{-2} \text{ s}^{-1}$ were reached, more than twice the design value of $1 \cdot 10^{34} \text{ cm}^{-2} \text{ s}^{-1}$.

Seven experiments are operating at the LHC, four of which are large ones with broad scientific scope. They are complemented by smaller, more specialized experiments that are located in the same caverns as the large experiments. The experiments are:

- **ATLAS (A Toroidal LHC ApparatuS)** [140] is with a length of 46 m and a diameter of 25 m the largest of the LHC experiments, and the largest detector ever built for particle physics. Several cylindrical tracking and transition radiation layers are hosted around the interaction point, complemented by calorimeters and muon spectrometers. ATLAS is a general purpose particle physics detector. Besides the mentioned discovery of the Higgs boson and measurements of its properties, it searches for physics beyond the standard model, such as supersymmetry.
- **CMS (Compact Muon Solenoid)** [141] is the second general-purpose particle-physics detector at the LHC. Smaller but heavier than ATLAS and with a different detector layout, it has similar physics goals. Its inner tracking and calorimeter layers are surrounded by a strong solenoidal magnet. Outside of the magnet and interleaved with an iron structure called the "return yoke" that guides and contains the magnetic field are the eponymous muon detectors.
- **ALICE (A Large Ion Collider Experiment)** [142] is a general purpose detector dedicated to the study of heavy-ion collisions at the LHC. More details on this detector will be given in the next section.
- **LHCb (Large Hadron Collider beauty)** [143] is mainly focused on heavy-flavor physics and in particular CP violations. In contrast to the other large experiments, it is entirely built at forward rapidity, using high-precision tracking layers and various particle-identification techniques. By injecting gas in the interaction region, LHCb can be operated in a fixed-target mode and investigate cosmic ray physics. One of the highlights of its Run-1 data-taking campaign was the discovery of a pentaquark candidate [5]. In the LHC Run-2 LHCb started a heavy-ion program with the successful participation in the Pb-Pb data taking period in 2015.
- **TOTEM (Total Cross Section, Elastic Scattering and Diffraction Dissociation at the LHC)** [144] consist of several subdetectors located around the CMS detector at distances up to 217 m from the interactions vertex. Besides the measurement of the total proton-proton interaction cross section, it focuses on elastic proton collisions and diffractive processes.
- **MoEDAL (Monopole and Exotics Detector at the LHC)** [145] is located around the intersection region of the LHCb detector. With an array of plastic nuclear track detectors it searches for exotic such as magnetic monopoles, dyons and electrically-charged stable massive particles.
- **LHCf (Large Hadron Collider forward)** [146] consist of two subdetectors at a distance of 140 m on either side of the ATLAS detector. It is dedicated to measure neutral pions produced in the collisions at very forward regions as an input to calibrate models of high energy cosmic rays.

3.2 ALICE

ALICE is unique among the LHC experiments in its particle tracking ability down to low transverse momenta and particle identification in wide kinematic regions employing a wide range of different techniques. Fig. 3.2 shows a schematic layout of the ALICE detector. A short summary of its individual components will be given here; the ones relevant for the presented analysis will be further described in more detail below.

The main part of ALICE is the central barrel, the part of the detector built cylindrically around the interaction point. Surrounding the beam pipe is the **ITS** [148], mainly responsible for the determination of the primary interaction vertex and secondary vertices. It is encased by the **TPC** [149, 150], the main tracking and PID device of the detector, and the largest of its kind in the world. On its outer edge additional tracking and PID detectors are located. These are the **TRD** [151], **TOF** [152], **EMCal** [153], **DCal** [154], **PHOS** [155] and **HMPID** [156]. The **PMD** [157] serves as a photon multiplicity detector. Several forward detectors [158] inside the central barrel serve specialized purposes: the **T0**

THE ALICE DETECTOR

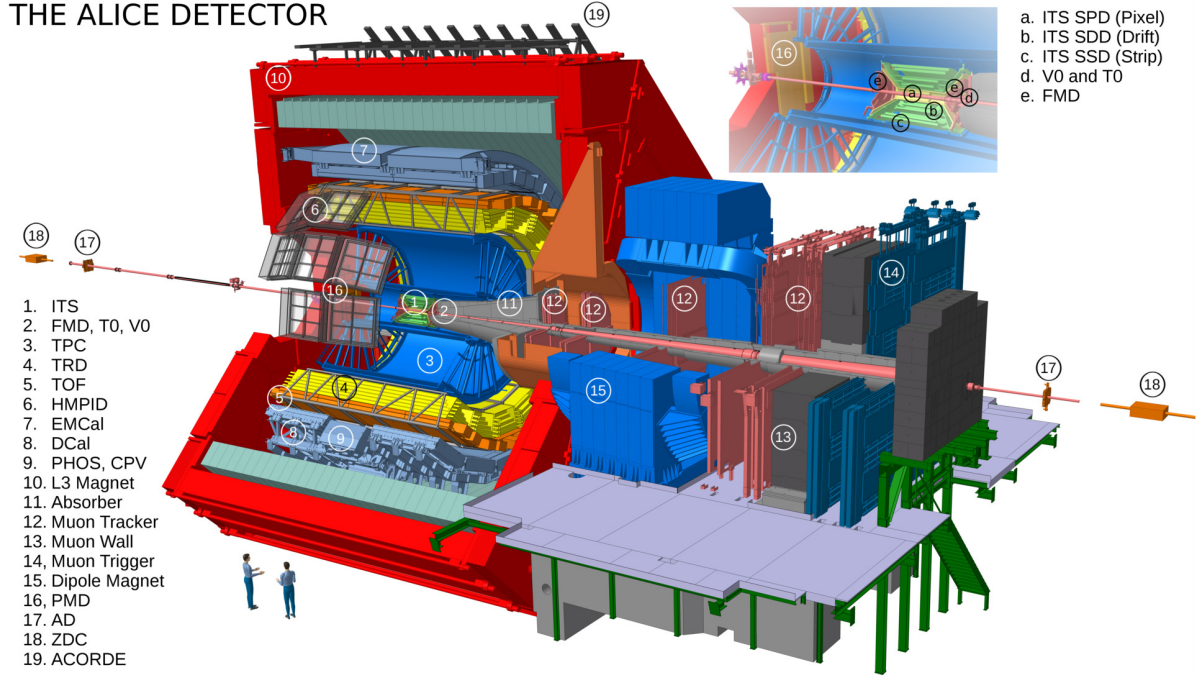


Figure 3.2.: Schematic view of the ALICE detector. Figure taken from [147].

[159] provides a trigger and exact measure for the time of collisions, **V0** [160] is used for triggering, centrality determination in heavy-ion collisions, as well as for charged-particle multiplicity determination at forward rapidity. In the latter purpose it is complemented by the **FMD** [161]. The central barrel is encased by the L3 magnet, a huge solenoid that provides a homogeneous magnetic field of 0.5 T parallel to the beam axis, forcing the outgoing charged particles on helical paths. On top of the magnet lies the **ACORDE** [162] subdetector, for the detection of high-momentum cosmic rays.

In forward direction the **muon arm** [163] is located: behind a hadron absorber with a thickness of about 10 interaction lengths sits a sequence of highly granular tracking planes. A dipole magnet provides a field of 0.67 T. Behind an iron wall shielding of about 7.2 interaction lengths follows the muon trigger. Further away from the main detectors, the **AD** [164] and the **ZDC** [165] detectors are located; both consist of two parts, located on either side of the interaction point. Located at very forward rapidities, the AD detectors are specialized in triggering on diffractive collisions. The ZDC detectors are located at even smaller angles to the beam. They measure the energy of spectator nucleons and thus serve as a centrality estimator in heavy-ion collisions.

3.3 The Inner Tracking System

The **Inner Tracking System (ITS)** consists of six cylindrical silicon layers, employing three different technologies. All layers cover the full azimuth, but different ranges in pseudorapidity.

The two innermost layers make up the **Silicon Pixel Detector (SPD)**. Positioned at radii of 3.9 cm and 7.6 cm, they cover a pseudorapidity range of $|\eta| < 2$ and $|\eta| < 1.4$, respectively. They are composed of about 10 million hybrid silicon pixel cells with a size of $50 \mu\text{m}$ in $r\varphi$ direction and $425 \mu\text{m}$ in z direction. It is the high granularity of the SPD and its proximity to the interaction point that dominates the precision in the determination of the primary interaction vertex and secondary vertices from particle decays.

The low material budget of about 1 % of a radiation length per layer allows the tracking of low momentum particles down to about $80 \text{ MeV}/c$. It also results in a low bremsstrahlung probability for electrons, and a low pair-conversion probability for photons. Both facts are advantageous for the presented analysis.

of J/ψ particles reconstructed in the dielectron decay channel. The information from the SPD detector was used to estimate the charged-particle multiplicity at mid-rapidity, as will be explained in section 4.5.

The third and fourth layer of the ITS are positioned at radii of 15 cm and 23.9 cm and cover $|\eta| < 0.9$ both. They form the **Silicon Drift Detector (SDD)**, which provides highly granular tracking information both in the drift and z direction.

The last two ITS layers compose the **Silicon Strip Detector (SSD)**. They are located at radii of 38 cm and 43 cm and cover $|\eta| < 0.98$ both. They provide, together with the SDD a specific energy loss signal dE/dx that can be used for particle identification.

3.4 The Time Projection Chamber

The **Time Projection Chamber (TPC)** is the main tracking and particle identification device of the ALICE detector, providing three dimensional reconstruction of charged-particle tracks. Shaped like a hollow cylinder with an inner radius of 84.8 cm, an outer radius of 2.466 m, and a length in beam direction of 4.994 m, it covers the full azimuth and $|\eta| < 0.9$ for tracks crossing the full radial length of the detector. At higher pseudorapidities, tracks do still cross parts of the detector, e.g. up to $|\eta| < 1.5$, tracks with 1/3 radial length can be reconstructed. The central high voltage cathode divides the active volume into two halves. Set to a voltage of -100 kV, it provides a homogeneous electric drift field of 400 V/cm along the beam direction.

The active volume is filled with a gas mixture of Ar – CO₂. Traversing charged particles ionize the gas. The freed electrons drift along the electric field towards the two end-caps on either side of the TPC. Collisions with the gas molecules compensate the acceleration from the electric field, so the electrons acquire a constant drift velocity of 2.65 cm/ μ s, the maximum drift time is 94 μ s. The ions drift in the opposite direction; their velocity is about a factor 1000 smaller.

The end-caps of the TPC are segmented in 18 sectors in azimuthal direction. Each sector is equipped with two Multi-Wire Proportional Chambers with cathode pad readout, ordered in radial direction, the inner and outer readout chambers (IROC, OROC). The chambers are segmented into pads with sizes between 4×7.5 mm² and 6×15 mm², depending on their radial position. Arranged in 159 rows in radial direction, there are in total 278784 pads on either side of the TPC. Due to the constant drift velocity of the electrons, their arrival time can be translated into the z coordinate of their creation, with 1000 samples in this direction. This leads to 557 million voxels in space to reconstruct the three dimensional flight path of the particles.

The radius of curvature in the constant magnetic field gives the momentum of the traversing particles. From the deposited charge in the readout pads their specific energy loss per path length dE/dx , which depends on their velocity β , is measured. Combining these two informations, the mass of the particle can be determined and the particle thus be identified. More details on particle identification in the TPC will be given in section 3.7.1.

3.5 The V0

The **V0** system is composed of two scintillator arrays on either side of the interaction point: the **V0A**, located 329 cm from the nominal vertex, covering a pseudorapidity range $2.8 < \eta < 5.1$, and the **V0C**, located on the front face of the hadron absorber between 86 cm and 88 cm from the nominal vertex, covering a pseudorapidity range $-3.7 < \eta < -1.7$. Each one of them is segmented in four rings in radial direction, and eight sectors in azimuthal direction. Each of these 2×32 channels consist of a plastic scintillator connected via wave-length shifting fibers to a photomultiplier tube. The V0 can be used to provide a trigger signal for data taking. In the presented analysis, the minimum bias trigger consists of a coincidence signal from both V0 arrays. The V0 can also provide a high-multiplicity trigger, by requiring a deposited energy above a given threshold in the system. This trigger was also used in the presented analysis to selected collisions with high multiplicity.

Furthermore, the V0 can be used to reject background from interactions between the beam and the residual gas in the beam pipe and from interactions between the beam halo and various accelerator components. Finally, the charged-particle multiplicity at forward rapidity can be estimated based on the energy deposited in the scintillators. This was done in the presented analysis. Details will be given in section 4.5.

3.6 Tracking

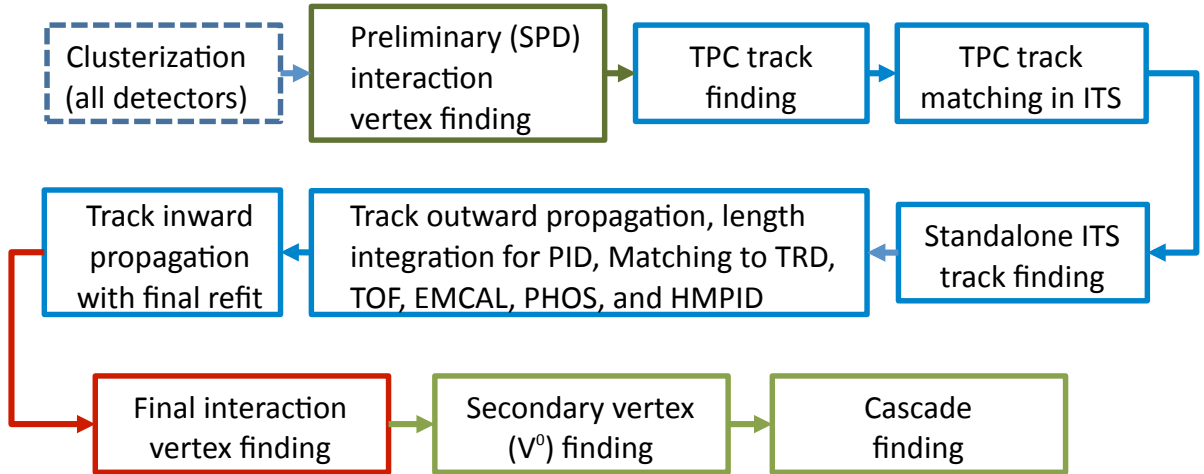


Figure 3.3.: ALICE central barrel event reconstruction flow. Figure taken from [166].

The ALICE central barrel tracking and vertex finding procedure consist of several steps which are shown schematically in Fig. 3.3 and are explained in [166]. A short summary will be given here, more details on tracking can be found in [167] and in [168] especially on TPC tracking. The vertex finding procedure is described in [169].

The first step is the merging of the detector signals into clusters, based on their position in space and time. This step is done for each detector individually. From the clusters in the SPD, a preliminary interaction vertex is constructed. For this, tracklets are constructed as lines defined by pairs of clusters in the first and second SPD layer, and a point of convergence for a maximum number of tracklets is searched. The procedure is repeated several times to also find additional interaction vertices of pileup events.

The next step is the track finding and fitting, which is itself a three-stages procedure, following an inward-outward-inward scheme. It starts with combining clusters in the outermost regions of the TPC to track seeds. The seeding is done once with the information of the interaction vertex taken into account and once without. The track seeds are propagated inward towards the inner TPC wall, using a Kalman filter approach by adding clusters compatible with the estimated track parameters. Special care is taken to avoid that too many seeds use the same clusters. A preliminary PID hypothesis is done based on the specific energy loss dE/dx in the TPC. The assumed mass is used to correct for the energy loss of the traversing particle in the gas.

The reconstructed TPC tracks are then propagated to the outermost ITS layer, becoming the seeds for the track finding in the ITS. Again, seeding is done once with and once without the information on the primary vertex. The seeds are propagated inwards, taking into account shared clusters and dead zones of the detector. Due to the reduced tracking efficiency in the TPC at low transverse momenta, a standalone ITS tracking is performed afterwards with clusters that were not used for the ITS-TPC tracks.

Afterwards, the tracks are propagated outwards, starting from the point of closest approach to the preliminary interaction vertex. Matching to the detectors at larger radii than the TPC, i.e. TRD, TOF, EMCAL, PHOS and HMPID is attempted.

The third and last stage of tracking is the propagation back inwards starting from the outer wall of the TPC. The tracks are refitted both in the TPC and the ITS, using the previously found clusters. The final values of the track parameters and corresponding covariance matrices are determined.

Afterwards, with the combined ITS-TPC tracks, a final interaction vertex is determined, with a higher precision than the preliminary one from SPD tracklets alone.

During the tracking procedure, kink, V0 and cascade topologies are searched for and the tracks belonging to them are flagged accordingly. The kink topology consist of an incoming track, called the kink mother, and an outgoing track, the kink daughter, which continues outward under some finite angle to the kink mother. They are typically produced by charged particles weakly decaying into a charged and a neutral particle, e.g. $K^+ \rightarrow \mu^+ + \nu_\mu$. The V0 topology consist of two outgoing tracks that have the closest approach to each other at some secondary vertex distinct from the interaction vertex. They are produced either by neutral particles decaying to two charged particles, e.g. $K_s^0 \rightarrow \pi^+ \pi^-$, or by photon conversions to electron positron pairs in the detector material. Cascades are more complicated topologies originating from a cascading decay chain of charged and neutral particles, e.g. $\Xi^- \rightarrow \Lambda^0 \pi^-$, followed by $\Lambda^0 \rightarrow p \pi^-$.

3.7 Particle identification

Particle identification (PID) is done in ALICE with different subdetectors employing various techniques, which will be briefly summarized here. More details can be found in [166].

- The **ITS** provides an ionization energy loss signal from its four outer layers. By normalizing to the path length, a dE/dx value can be obtained from each layer, from which a truncated mean is calculated, discarding the highest charge clusters. It is especially useful in the low momentum region, where the ITS is used for standalone tracking.
- The **TPC** measures the dE/dx from the charge deposited on the up to 159 pad rows. This is the only detector used for PID in the presented analysis, more details will be given in section 3.7.1.
- The **TRD (Transition Radiation Detector)** provides particle identification based on the specific energy loss and **transition radiation (TR)** of traversing particles. TR is emitted by relativistic particles when they traverse the interface of two materials with different dielectric constants. The onset of TR happens around $\beta\gamma = \frac{p}{m} \gtrsim 1000$. This means electrons with momenta above $p \gtrsim 0.5 \text{ GeV}/c$ emit TR, while hadrons do not up to much higher momenta. TR can thus be used to distinguish electrons from hadrons. The TRD covers the full central barrel acceptance. It has a six layer structure, each layer consisting of a radiator (polypropylene fiber mats sandwiched between two Rohacell foam sheets) followed by a drift chamber filled with Xe-Co₂. The TR photons are absorbed in the gas of the drift chamber, depositing energy. Particle identification can be obtained either from the deposited energy alone, or also taking into account the time dependence of the energy loss, which gives additional discrimination power. The TRD can also be used as a physics trigger on high-momentum electrons, jets and nuclei [170].
- The **TOF (Time-Of-Flight)** detector identifies particles by measuring the time interval they need to travel a defined distance. The start time is provided by the T0 detector [159], which consist of two arrays of Cherenkov counters on either side of the interaction point. The TOF itself is composed of Multigap Resistive Plate Chambers and covers the full central barrel acceptance. It can measure the arrival time of particles with a resolution of about 80 ps. Together with the momentum information from the tracking detectors, TOF provides particle identification in the intermediate momentum range: kaons and pions can be identified up to $p = 2.5 \text{ GeV}/c$, protons up to $p = 4 \text{ GeV}/c$.
- **EMCal (ElectroMagnetic Calorimeter)**, **DCal (Di-Jet Calorimeter)** and **PHOS (Photon Spectrometer)** are electromagnetic calorimeters. They can also be used for the identification of

electrons due to the fact that those deposit their entire energy in an electromagnetic calorimeter whereas hadrons typically only lose a small fraction. With the momentum measured by the tracking detectors, the fraction of deposited energy in the calorimeters can be determined, and electrons thus be discriminated from hadrons. All three detectors cover a limited acceptance in pseudorapidity and azimuth. The DCAL serves as an extension of the EMCal, enabling the study of hadron-jet and di-jet correlations. The detectors can also be used to provide triggers on high-momentum electrons or photons. In parallel to the analysis presented in this thesis, an independent analysis of high-momentum J/ψ production as a function of charged-particle multiplicity was performed using the triggering and PID capabilities of the EMCal.

- The **HMPID (High Momentum Particle Identification Detector)** is a ring-imaging Cherenkov detector. It provides hadron separation up to high momenta; kaons can be distinguished from pions up to $p_T = 3 \text{ GeV}/c$, protons up to $p_T = 5 \text{ GeV}/c$. Its acceptance is limited, covering only 5 % of the acceptance of the central barrel.

3.7.1 Particle identification in the TPC

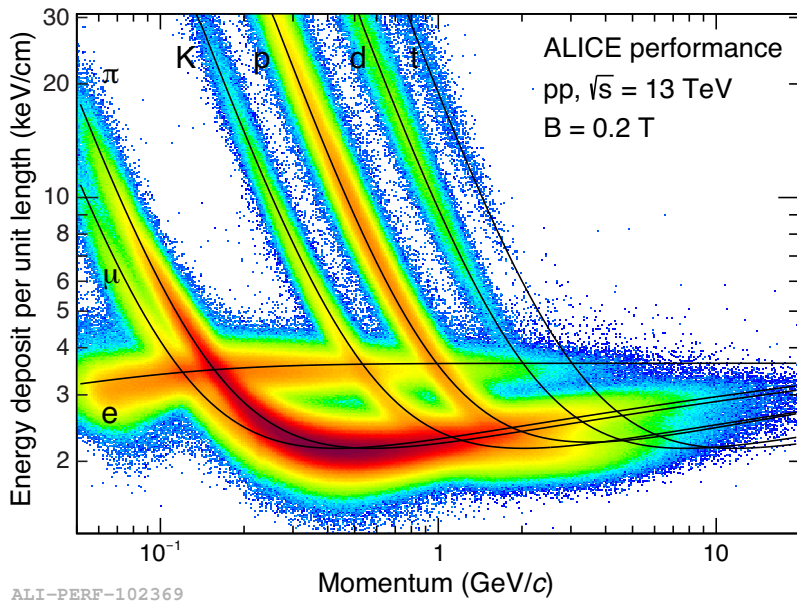


Figure 3.4.: Specific energy loss (dE/dx) in the TPC versus particle momentum in pp collisions at $\sqrt{s} = 13 \text{ TeV}$. The lines show the parametrizations of the expected mean energy loss for different particle species. Figure taken from [171].

The particle identification in the TPC is based on the simultaneous measurement of the specific energy loss dE/dx and the rigidity (momentum divided by charge) of each track. For a given material the energy loss depends to first order on the charge, velocity β and Lorentz factor γ . It can be described with the Bethe-Bloch curve [172, 173]. In the TPC the energy loss is measured in up to 159 samples from the individual readout pad rows. From these individual values, a truncated mean is calculated.

The velocity dependence can be parametrized with the following formula, originally proposed by the ALEPH collaboration [174]:

$$f(\beta\gamma) = \frac{P_1}{\beta^{P_4}} \left(P_2 - \beta^{P_4} - \ln\left(P_3 + \frac{1}{(\beta\gamma)^{P_5}}\right) \right) \quad (3.1)$$

where β is the relativistic particle velocity, γ the Lorentz factor and P_{1-5} fit parameters. Fig. 3.4 shows experimentally obtained dE/dx values as a function of the particle momentum, together with the expected

energy loss for the various particle species from the parametrized Bethe-Bloch curve. A clear separation between the particle species in wide momentum regions is visible, as well as regions of overlap between them. At high momentum the curves merge and an identification is no longer possible for individual tracks. However particle abundancies can still be determined on a statistical basis with Gaussian fits to the energy loss in slices of momentum.

The resolution of the dE/dx is around 5.2%, and the distribution at a given $\beta\gamma$ for a given particle species is Gaussian down to at least three orders of magnitude. The width of the distributions can be quantified with the standard deviation σ . In analyses typically the variable $n\sigma_{\text{TPC},i}$ is used, which is the deviation of the measured energy loss to the expected energy loss of a certain particle species $i \in \{\text{electron, pions, protons, etc.}\}$ divided by the width σ_i of the distribution for this particle species:

$$n\sigma_{\text{TPC},i} = \frac{dE/dx_{\text{measured}} - dE/dx_{\text{expected},i}}{\sigma_i}. \quad (3.2)$$

The expected energy loss and the width are for each track corrected for additional detector effects, depending e.g. on the pseudorapidity and the number of TPC clusters used for PID.

4 Analysis

In this chapter the analysis of J/ψ production as a function of the charged-particle multiplicity in pp collisions at $\sqrt{s} = 13$ TeV will be described. First, the analysis strategy will be explained, then the individual steps of the analysis will be presented in more detail.

4.1 Analysis Strategy

The general idea of the analysis is to extract the self-normalized inclusive J/ψ yield at mid-rapidity ($|y| < 0.8$) as a function of self-normalized charged-particle multiplicity at mid-rapidity ($|\eta| < 1$) and forward rapidity ($-3.7 < \eta < -1.7 \cup 2.8 < \eta < 5.1$). The analysis is done for p_T -integrated J/ψ , J/ψ with $p_T < 4$ GeV/c, and J/ψ with $p_T > 4$ GeV/c. The steps that have to be followed in the analysis are the following:

1. Selection of collision candidates, correction for selection efficiency.
2. Estimation of the charged particle multiplicities.
3. Identification of J/ψ decay daughters, reconstruction of the J/ψ , efficiency correction.
4. Calculation of the J/ψ yield as a function of multiplicity, normalization.

Collision candidates are selected based on trigger conditions. For the presented analysis two different configurations were used: on the one hand a minimum bias (MB) trigger, on the other hand a trigger to select events with high particle multiplicities (HM). The condition for the minimum bias trigger is a coincidence signal in both V0 subdetectors; the condition for the high multiplicity trigger is a deposited energy above a certain threshold in the V0 detector, corresponding to roughly 5 times the average deposited energy in a minimum bias event.

For the estimation of the multiplicity at mid-rapidity the number of *SPD-tracklets* (track segments composed of detector hits in both layers of the SPD) in $|\eta| < 1$ is used. For the multiplicity at forward rapidity the signals from the deposited energy in the V0C and V0C subdetectors are used.

In order to convert these detector signals into a measure for the charged-particle multiplicities, Monte Carlo simulations are used.

The J/ψ is reconstructed in the dielectron decay channel. Electron candidates are selected based on track quality criteria from the ITS and TPC detectors and the particle identification information from the TPC detector. The efficiency of these selection criteria is estimated from a Monte Carlo simulation.

The J/ψ candidates are then identified via their invariant mass. The background beneath the J/ψ peak is estimated from a description of the background in the side-bands of the signal and subtracted. The J/ψ signal is extracted and the per-event J/ψ yield $N_{J/\psi}$ calculated. The yield is normalized to the mean per-event yield in inelastic collisions $\langle N_{J/\psi} \rangle$ to obtain the *self-normalized* J/ψ yield

$$n_{J/\psi} = \frac{N_{J/\psi}}{\langle N_{J/\psi} \rangle}. \quad (4.1)$$

This self-normalized yields are extracted in event classes based on the multiplicity at mid- and forward rapidity, and plotted as a function of the self-normalized charged-particle multiplicity $n_{ch,mid}$ and

$n_{\text{ch,fwd.}}$, i.e. the mean multiplicities $N_{\text{ch,mid}}$ and $N_{\text{ch,fwd.}}$ in the respective event class divided by the mean multiplicities in inelastic events $\langle N_{\text{ch,mid}} \rangle$ and $\langle N_{\text{ch,fwd.}} \rangle$:

$$n_{\text{ch,mid}} = \frac{N_{\text{ch,mid}}}{\langle N_{\text{ch,mid}} \rangle}, \quad n_{\text{ch,fwd.}} = \frac{N_{\text{ch,fwd.}}}{\langle N_{\text{ch,fwd.}} \rangle}. \quad (4.2)$$

The usage of self-normalized quantities facilitates the comparison of results at different collision energies and in different collision systems. A linear increase of J/ψ production with multiplicity is present if the self-normalized J/ψ yield is equal to the self-normalized charged-particle multiplicity.

Derived quantities are the double ratios of the J/ψ yield and the charged particle multiplicities:

$$r_{\text{J}/\psi, \text{mid}} = \frac{n_{\text{J}/\psi}}{n_{\text{ch,mid}}}, \quad r_{\text{J}/\psi, \text{fwd.}} = \frac{n_{\text{J}/\psi}}{n_{\text{ch,fwd.}}}. \quad (4.3)$$

Though expressing the same physics as the self-normalized yields, these quantities have the advantage that, when represented in a plot, the quantitative behavior in the whole analyzed multiplicity range can be equally well appreciated, e.g. deviations from linearity especially in the low multiplicity region.

With the usage of multiplicity estimators at different pseudorapidities it can be investigated, if the J/ψ yield depends differently on the charged-particle multiplicity in its vicinity and far away from it. A strong dependence on the latter hints to an underlying global effect influencing the collision as a whole, while for the former also local effects are relevant, such as the production inside jets.

Additionally, an auto-correlation between the multiplicity estimator and the J/ψ signal can occur. If both the J/ψ and the multiplicity are measured in the same pseudorapidity, the decay daughters of the J/ψ can enter into the multiplicity estimation. If the multiplicity is measured with some gap in pseudorapidity to the J/ψ , this might not be the case.

4.2 Event Selection

4.2.1 Data samples

For the presented analysis, data from pp collisions taken in 2016 at $\sqrt{s} = 13 \text{ TeV}$ are used. With the selection criteria (see next section) applied, 686 million events are analyzed, of which 528 million are selected based on the MB trigger condition, and 158 million based on the HM trigger condition.

4.2.2 Collision candidate selection

Collision candidates ("events") are selected when either the MB or the HM trigger condition is fulfilled in coincidence with the crossing of the beams at the ALICE interaction point. Beam induced and electromagnetic background is removed with the timing information from the V0 detectors.

Collisions are required to have a reconstructed primary interaction vertex. In order to have the full detector acceptance available, only collisions are considered that have a displacement of the primary interaction vertex νtx_z within $\pm 10 \text{ cm}$ of the nominal point in beam direction.

Pileup events, i.e. several collisions reconstructed in one event are rejected from the analysis. For this, information on the correlation between signals from the V0 and the SPD detectors are used. Additionally, events are rejected as pileup if a second primary interaction vertex can be reconstructed from the SPD tracklets with a minimum number of tracklets contributing to the secondary vertex (3 tracklets for low-multiplicity events, 5 for high-multiplicity) [166].

4.2.3 High-multiplicity trigger

The performance of the V0 detector used for the HM trigger is varying with time due to ageing effects in the photomultiplier tubes of the detector. The trigger threshold was adjusted during data taking to compensate this effect. On average, the trigger threshold corresponds to a value of about five times the mean deposited energy in minimum bias collisions, though it is not identical for the complete analyzed data set.

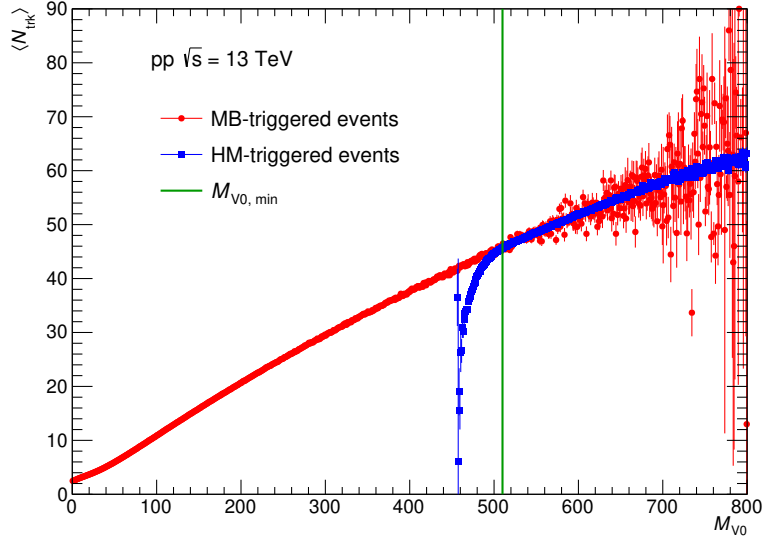


Figure 4.1.: High-multiplicity trigger onset curve. Mean number of SPD tracklets in $|\eta| < 1$ as a function of the V0 signal for MB and HM-triggered events. HM-triggered events with $M_{\text{V0}} < M_{\text{V0, min}}$ are rejected in the analysis.

The deposited energy in the V0 detectors can be converted into an estimator for the particle multiplicity in this region, the V0 signal M_{V0} [160]. Fig. 4.1 shows the mean number of SPD tracklets $\langle N_{\text{trk}} \rangle$ in $|\eta| < 1$ per collision as a function of the M_{V0} both for MB and HM-triggered events. For this figure a subset of the data sample with a constant setting of the HM trigger-threshold was chosen. $\langle N_{\text{trk}} \rangle$ increases with the M_{V0} . For HM-triggered events just above the trigger threshold — i.e. at values between approximately $M_{\text{V0}} = 480$ and 510 — the average number of SPD tracklets is much lower than in MB-triggered events. The value increases rapidly with M_{V0} . From $M_{\text{V0}} = 510$ on the two trigger classes are in agreement with each other. The region below $M_{\text{V0}} = 510$ is the *trigger onset curve*. Events with an unusual event topology (higher than usual multiplicity at forward rapidity compared to mid-rapidity) are preferred. This might be caused e.g. by a displaced primary vertex. Events in this region are rejected from the analysis, i.e. for HM-triggered events, a minimum V0 signal $M_{\text{V0, min}}$ is required, as indicated by the green vertical line in Fig. 4.1. The value of $M_{\text{V0, min}}$ is adapted to the different settings of the HM trigger threshold.

4.3 Monte Carlo simulations

Monte Carlo simulations were used in order to estimate the trigger efficiency of the analyzed experimental data and the relationship between the multiplicity estimator and the true charged particle multiplicities.

Proton-proton collisions were simulated with the EPOS-LHC event generator [175]. Compared to the full EPOS3 model (cf. section 2.2.4), instead of a full hydrodynamic evolution of the core, a fast covariant approach is used. The model has proven to provide good descriptions of various experimental data of the LHC experiments, especially for the charged-particle multiplicity in wide multiplicity and

pseudorapidity ranges [34, 35, 176]. The detector was simulated with the GEANT3 package [177], a framework simulating the passage of particles through detectors and their interactions with it.

In order to determine the J/ψ reconstruction efficiency, an enhanced Monte Carlo sample was used. Inelastic proton-proton collisions were simulated with the PYTHIA8 event generator [178]. In each event, an additional J/ψ particle was injected and forced to decay in the dielectron decay channel. The emission of internal bremsstrahlung in the decay was handled by the PHOTOS Monte Carlo QED package [179]. The detector was simulated with the GEANT3 package [177] also in this case.

4.4 Event normalization

The results presented in this thesis are normalized to inelastic collisions. The efficiency for an event to pass the selection criteria, i.e. fulfill the trigger condition and have a reconstructed primary vertex with $|\nu tx_z| < 10$ cm are multiplicity dependent. The events used in the analysis have to be corrected for the ones not selected in order to not bias the results. The trigger efficiency $\epsilon_{\text{trigger}}$ is estimated based on the Monte Carlo simulation. The vertex reconstruction efficiency of triggered events ϵ_{vertex} is determined from a data-based approach. The events are corrected by applying a multiplicity dependent weighting factor $w = \frac{1}{\epsilon_{\text{trigger}} \epsilon_{\text{vertex}}}$ to the selected events to compensate for those that were not selected. For the efficiency of non-pileup events to pass the pileup rejection no multiplicity dependence is expected.

4.4.1 Trigger efficiency

Since the trigger requirement is defined as a coincidence between a signal in the V0A and the V0C detectors, the trigger efficiency is essentially 100 % for events which have both a V0A and V0C multiplicity above a certain threshold. If the signal in one of the two detectors is very small, the trigger efficiency is smaller. This fact is illustrated in Fig. 4.2 (left). It shows the trigger efficiency — obtained from the Monte Carlo simulations — as a function of the signal in the V0A and the V0C detectors. If both signals are above approximately one, the trigger efficiency is close to 100 %, if either one is smaller, the efficiency drops rapidly. In Fig. 4.2 (right) this 2 dimensional trigger efficiency dependence is projected on one dimension by plotting it against the minimum of the V0A and the V0C multiplicity $V0_{\min} = \min(M_{\text{V0A}}, M_{\text{V0C}})$. The trigger efficiency first increases steeply up to 90 % up to a multiplicity of about one, then the increase flattens until around a multiplicity of about two almost 100 % is reached.

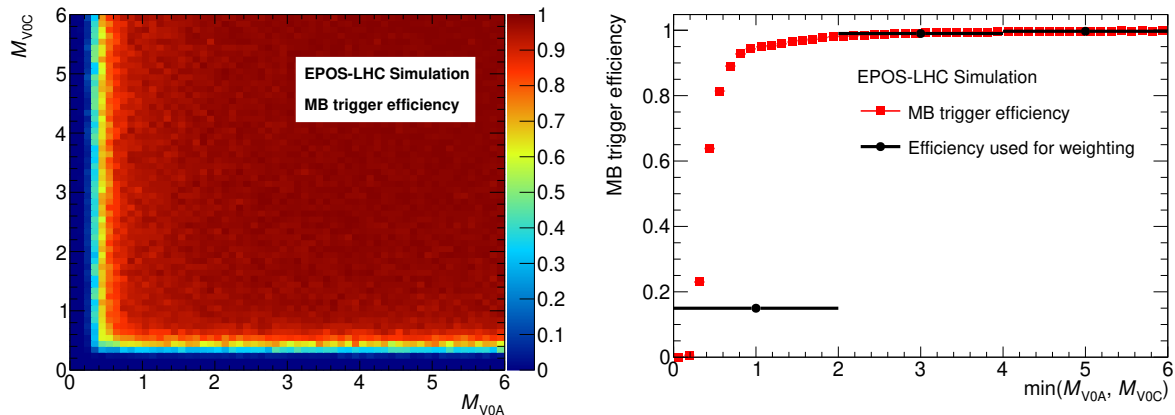


Figure 4.2.: MB trigger efficiency as a function of the signal in the V0A and V0C detectors from EPOS-LHC Monte Carlo simulation. Left: 2 dimensional dependence of the trigger efficiency on the two multiplicities; right: trigger efficiency as a function of the minimum of the V0A and V0C signal.

In order to correct for the trigger efficiency, events are given a weight $1/\epsilon_{\text{trigger}}(V0_{\min})$ depending on their value of $V0_{\min}$. For this weighting procedure the efficiency is calculated in wider bins of $V0_{\min}$, as indicated in the figure. This is done to take into account that the exact shape of the trigger onset might not be described correctly in the simulation.

4.4.2 Vertex finding efficiency

The probability that a triggered collision has a reconstructed primary interaction vertex can be estimated in a data-driven way. In the region $|vtx_z| < 10$ cm the full detector acceptance is available, and the vertex reconstruction efficiency is independent of vtx_z . The distribution of vtx_z is therefore unbiased and follows a Gauss function, as is illustrated in Fig. 4.3 (left). It shows the distribution of vtx_z for selected collision candidates in the analysis, together with a fit of a Gaussian function to the distribution. By integrating the Gauss function from $vtx_z = -\infty$ to $vtx_z = \infty$ and dividing the integral by the number of triggered events without the vertex reconstruction requirement, the vertex reconstruction efficiency ϵ_{vertex} is obtained.

To obtain the multiplicity dependence of this efficiency, the events are classified based on their number of tracks that passed the ITS refit step in the tracking $N_{\text{ITS refit}}$ (cf. section 3.6). The described vertex efficiency determination is then performed in these event classes. The usual mid-rapidity multiplicity estimator — the number of SPD tracklets N_{trk} — could not be used in this case, since the SPD efficiency is vtx_z dependent. For events with a very low N_{trk} the vtx_z distribution is biased and not Gaussian anymore, so the described procedure cannot be applied. Fig. 4.3 (right) shows the vertex reconstruction efficiency as a function of $N_{\text{ITS refit}}$. For events with $N_{\text{ITS refit}} \gtrsim 5$, the vertex finding efficiency is close to 100 %, for lower multiplicities it decreases with decreasing $N_{\text{ITS refit}}$, down to 45 % for events with less than 3 tracks.

Based on their number of $N_{\text{ITS refit}}$, the events in the analysis are weighted with a factor $1/\epsilon_{\text{vertex}}(N_{\text{ITS refit}})$. Since the vertex finding efficiency is obtained for triggered events, the efficiency for an event to be selected in the analysis can be calculated from the sum of the trigger and the vertex finding efficiency, and the full weighting factor becomes $w = 1/(\epsilon_{\text{trigger}}(V0_{\min}) \cdot \epsilon_{\text{vertex}}(N_{\text{ITS refit}}))$.

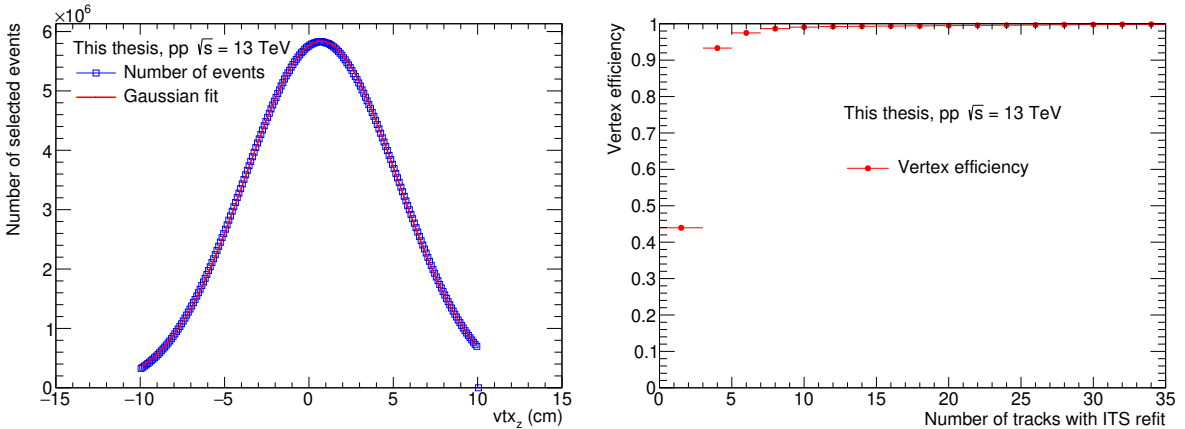


Figure 4.3.: Left: Distribution of the z coordinate of the primary interaction vertex of events selected for the analysis. Right: Vertex finding efficiency as a function of number of tracks with ITS refit flag.

4.5 Multiplicity Estimation

The necessary corrections to convert the detector quantities to the multiplicity estimators will be described.

4.5.1 Mid-rapidity multiplicity

Normalization

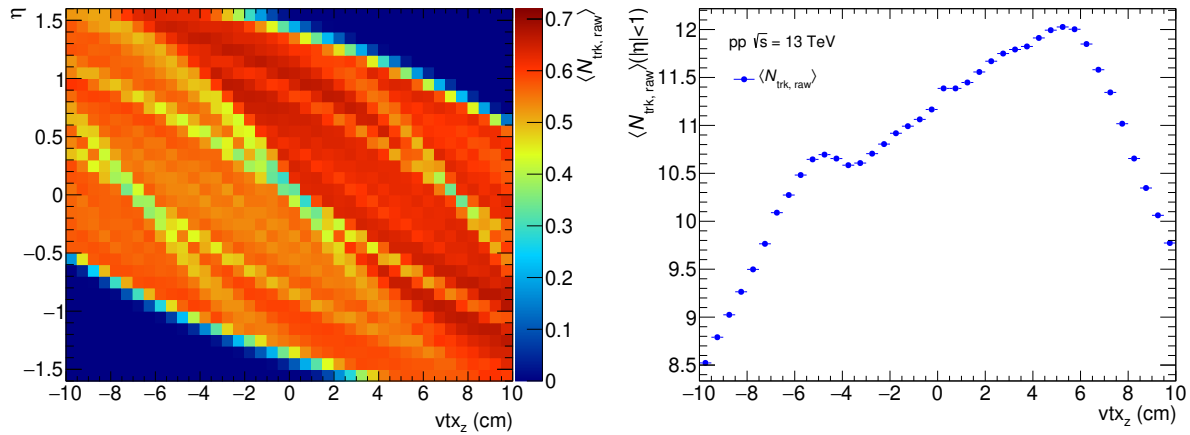


Figure 4.4.: Average number of SPD tracklets in minimum bias collisions as a function of the z-coordinate of the primary vertex in η intervals (left), and integrated in $|\eta| < 1$ (right).

The average number of SPD tracklets $N_{\text{trk, raw}}$ in a collision is dependent of the z-coordinate of the primary collision vertex vtx_z . This is due to the geometric acceptance of the SPD detector and detector inefficiencies. Fig. 4.4 (left) shows $N_{\text{trk, raw}}$ at different pseudorapidities as a function of vtx_z . For collisions at the nominal vertex position ($vtx_z = 0 \text{ cm}$), tracklets can be reconstructed up to $|\eta| < 1.4$, this region shifts towards negative pseudorapidity for $vtx_z > 0 \text{ cm}$ and towards positive for $vtx_z < 0 \text{ cm}$. For events with a vertex displacement $|vtx_z| > 5 \text{ cm}$, tracklets can not be reconstructed in the full pseudorapidity interval used in the analysis $|\eta| < 1.0$. In the figure, bands in the $\eta - vtx_z$ distribution can be seen with lower average $N_{\text{trk, raw}}$. These correspond to SPD regions with reduced efficiency due to inactive pixels. In Fig. 4.4 (right) $N_{\text{trk, raw}}$ is integrated over η for $|\eta| < 1$, and plotted as a function of vtx_z . The obtained distribution is the result of the described effects. Since the true charged-particle multiplicity is independent of the position of the primary vertex, this effect has to be corrected in the estimator: For a given event, $N_{\text{trk, raw}}$ is scaled by the ratio of a reference number $N_{\text{trk, ref}}$ and the average number of SPD tracklets in events with the same vtx_z as the event $\langle N_{\text{trk}}(vtx_z) \rangle$ to obtain the corrected number of SPD tracklets:

$$N_{\text{trk}} = N_{\text{trk, raw}} \frac{N_{\text{trk, ref}}}{\langle N_{\text{trk, raw}}(vtx_z) \rangle} \quad (4.4)$$

As reference number $N_{\text{trk, ref}}$, the number of SPD tracklets in the vtx_z interval with the highest efficiency is chosen.

In addition to this vtx_z effect the detector efficiency might be time dependent due to a dependence on the experimental conditions during data taking. Depending on the data taking period, the average number of SPD tracklets in MB-triggered events changes within 1 % of the average value. No correction is applied for this change.

Correlation between charged-particle multiplicity at mid-rapidity and number of SPD tracklets

The correlation between the primary charged-particle multiplicity at mid-rapidity $N_{\text{ch, mid}}$ and N_{trk} can be estimated from Monte Carlo simulations, including a simulation of the detector response. Fig. 4.5 (left) shows the 2 dimensional probability distribution for a generated inelastic pp collision to have a certain $N_{\text{ch, mid}}$ and N_{trk} . N_{trk} increases with $N_{\text{ch, mid}}$, but for a given $N_{\text{ch, mid}}$, different N_{trk} values are possible. In Fig. 4.5 (right) the average $\langle N_{\text{trk}} \rangle$ is shown as function of $N_{\text{ch, mid}}$, together with a linear fit $\langle N_{\text{trk}} \rangle = a + m \cdot N_{\text{ch, mid}}$. The fit describes the simulated values well with a slope parameter $m = 0.79$, and a small offset $a = 0.009$. This means the detector exhibits a linear response to the charged-particle multiplicity, an event with n times the mean $N_{\text{ch, mid}}$ will on average be reconstructed with n times the mean N_{trk} .

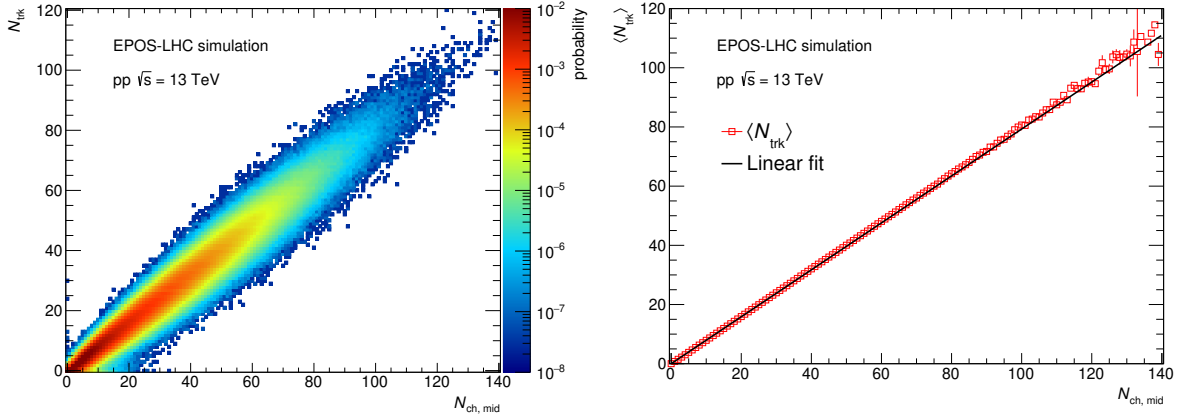


Figure 4.5: Correlation between charged-particle multiplicity at mid-rapidity and number of SPD tracklets from Monte Carlo simulation. Left: 2 dimensional probability distribution, right: mean number of SPD tracklets as a function of charged-particle multiplicity at mid-rapidity.

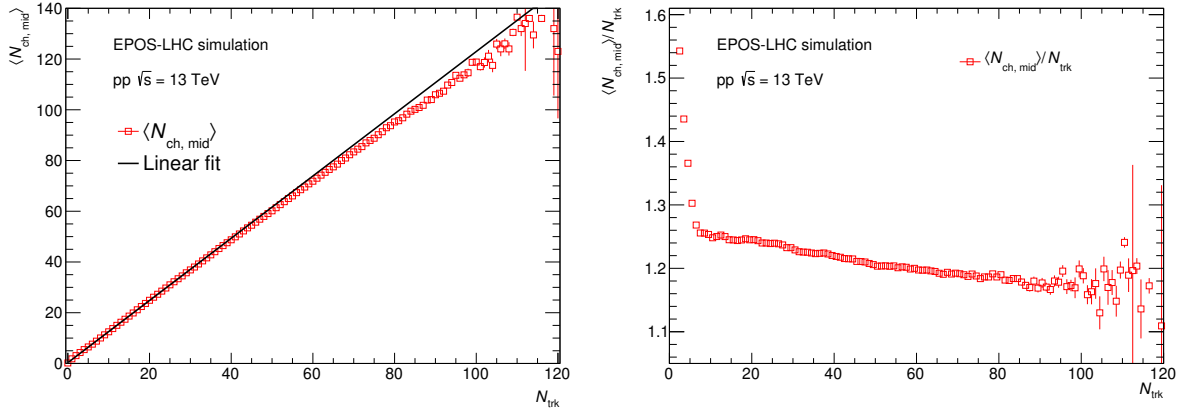


Figure 4.6.: Correlation between charged-particle multiplicity at mid-rapidity $N_{\text{ch, mid}}$ and number of SPD tracklets in $|\eta| < 1$ from Monte Carlo simulation. Left: Mean $N_{\text{ch, mid}}$ in events selected according to N_{trk} as a function of N_{trk} . Right: Mean ratio of $N_{\text{ch, mid}}$ and number N_{trk} (α factor) as a function of N_{trk} .

However, by selecting events based on N_{trk} , a selection bias effect is introduced. For a given $N_{\text{ch, mid}}$, the N_{trk} distribution has a certain width. A high N_{trk} can result from either a high $N_{\text{ch, mid}}$, or from an upward fluctuation of N_{trk} in an event with an average N_{ch} . As the N_{ch} distribution is steeply falling, this smearing leads to a reduced selection power for high multiplicities when using N_{trk} .

Fig. 4.6 (left) illustrates this effect: it shows the average $N_{\text{ch, mid}}$ as a function of N_{trk} for events selected based on the N_{trk} , together with the attempt of a linear fit. From about $N_{\text{trk}} = 50$ upwards, the fit overshoots the points. This means, by selecting events based on N_{trk} not the same selective power can be achieved than by using $N_{\text{ch, mid}}$. Events with n times the mean N_{trk} do not have n times the mean $N_{\text{ch, mid}}$. In data, the true $N_{\text{ch, mid}}$ is not available, only the smeared N_{trk} , so a correction of the reduced resolution has to be applied in order to recover the true charged-particle multiplicity.

This effect is further illustrated in Fig. 4.6 (right) which shows the ratio $\alpha = \frac{N_{\text{ch, mid}}}{N_{\text{trk}}}$ as a function of N_{trk} . Two regimes are visible: For events with $N_{\text{trk}} < 5$, the ratio drops rapidly. The reason can be understood by consulting Fig. 4.5 (left). The $N_{\text{ch, mid}}$ distribution for a given N_{trk} is cut off at zero in this region — there are no events with less than zero charged particles. For this cut distribution, the mean value is shifted to higher values than for the uncut distribution at higher N_{trk} values. Above $N_{\text{trk}} = 5$, α decreases approximately linearly with N_{trk} .

The exact correlation between N_{trk} and $N_{\text{ch, mid}}$ depends on the shape of the multiplicity distribution and the detector response for a given $N_{\text{ch, mid}}$. To make a realistic estimate of $N_{\text{ch, mid}}$ based on the measured N_{trk} , these information can be used in an unfolding algorithm [16]. For the presented analysis, such a precision is not necessary, and a rough estimation of the charged-particle multiplicity is sufficient.

The charged-particle multiplicity is estimated with the average $N_{\text{ch, mid}}$ for a given N_{trk} of an event as obtained from the Monte Carlo simulation. At $N_{\text{trk}} > 60$, the correlation is parametrized with a 2nd order polynomial, in order to not suffer from statistical uncertainties of the Monte Carlo sample.

4.5.2 Forward rapidity multiplicity

Normalization

As for the number of SPD tracklets, the average signals in the V0A and the V0C detectors are dependent on the z-coordinate of the primary collision vertex, due to the change of acceptance in the detectors. The effect is illustrated in Fig. 4.7: The average V0A signal decreases with increasing vtx_z , the V0C signal increases. The combined signal (V0M), is within 2 % independent of vtx_z . Due to the smallness of the effect, no correction is applied in the presented analysis.

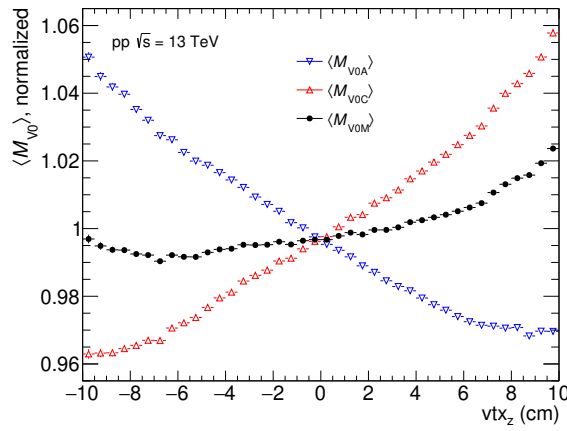


Figure 4.7.: Average signal in the V0A and V0C detectors and combined value in minimum bias collisions as a function of the z-coordinate of the primary vertex, scaled to the mean values.

The average V0 signal $M_{V0, \text{raw}}$ changes with time. The channels in the detector suffer from radiation damage, which results in a decrease of their performance with time. The effect amounts to a reduction of the average $M_{V0, \text{raw}}$ with time of up to 40 %. To correct for this effect, the average $\langle M_{V0, \text{raw}}(t) \rangle$ was calculated in time intervals. As time intervals, *runs* were chosen. A run is a time period (time scale

between minutes and hours) of continuous data taking with constant detector conditions. The per-event $M_{V0, \text{raw}}$ was then rescaled by the ratio of a reference value $M_{V0, \text{ref}}$ and $\langle M_{V0, \text{raw}}(t) \rangle$.

$$M_{V0} = M_{V0, \text{raw}} \frac{M_{V0, \text{ref}}}{\langle M_{V0, \text{raw}}(t) \rangle} \quad (4.5)$$

As reference value $M_{V0, \text{ref}}$, the average M_{V0} in the Monte Carlo sample is used.

Correlation between the charged-particle multiplicity at forward rapidity and V0 signal

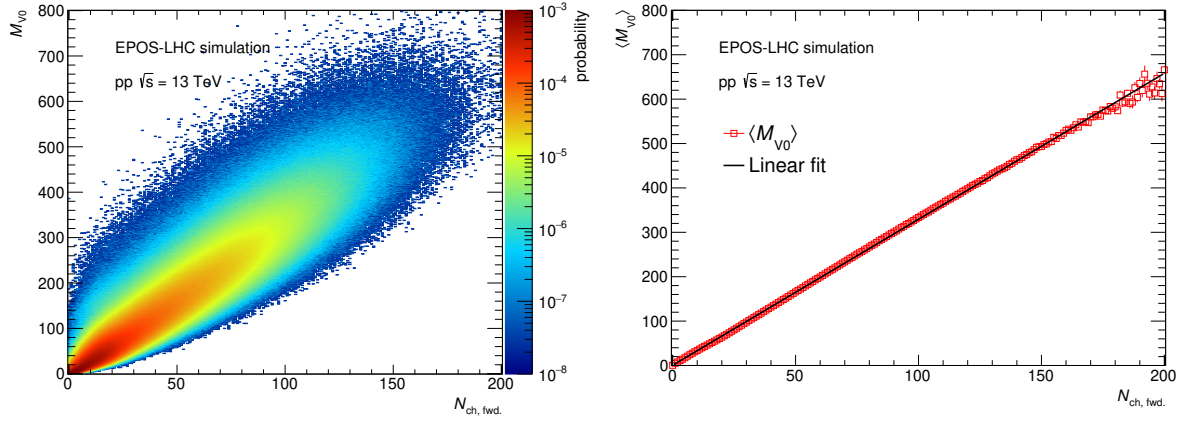


Figure 4.8.: Correlation between charged-particle multiplicity at forward rapidity and V0 signal from Monte Carlo simulation. Left: 2 dimensional probability distribution, right: mean V0 signal as a function of charged-particle multiplicity at forward rapidity.

Fig. 4.8 (left) shows the 2 dimensional probability distribution for a generated inelastic pp collision to have a certain charged-particle multiplicity at the V0 rapidity $N_{\text{ch,fwd.}}$ and a certain M_{V0} . Compared to the correlation between the $N_{\text{ch,mid}}$ with N_{trk} , the distribution is much wider, so for a given $N_{\text{ch,fwd.}}$, many M_{V0} are possible. Since the V0 detectors are far away from the primary interaction, their signal is stronger contaminated by secondary particles, such as daughter particles from weak decays or particles produced by interactions with the detector material. As for the SPD tracklets, the detector response to the multiplicity is linear, as shown in Fig. 4.8 (right).

From the wider distribution of M_{V0} for a given $N_{\text{ch,fwd.}}$ follows a stronger selection bias. This is illustrated in Fig. 4.9, which shows in the left the mean $N_{\text{ch,fwd.}}$ as a function of M_{V0} for events selected based on M_{V0} . From a $M_{V0} = 250$ onward, the linear fit to the increase is clearly failing. Analogously, the α factor, shown in Fig. 4.9 (right) varies stronger with multiplicity as in the mid-rapidity case. The $N_{\text{ch,fwd.}}$ estimator is obtained similarly to the mid-rapidity case from this correlation obtained from the Monte Carlo simulation.

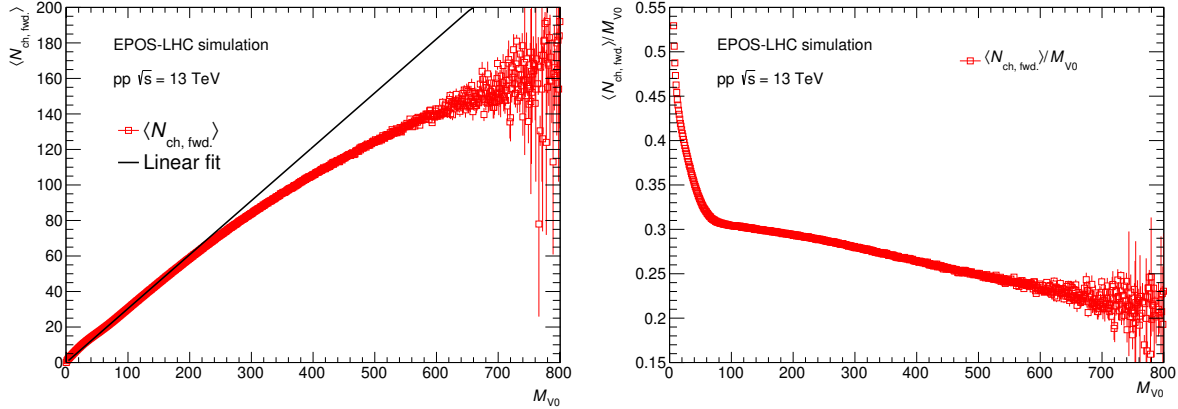


Figure 4.9.: Correlation between charged-particle multiplicity at forward rapidity $N_{ch,fwd.}$ and V0 signal M_{V0} from Monte Carlo simulation. Left: Mean $N_{ch,fwd.}$ in events selected according to M_{V0} as a function of M_{V0} . Right: Mean ratio of $N_{ch,fwd.}$ and M_{V0} (α factor) as a function of M_{V0} .

4.5.3 Multiplicity intervals used in the analysis

The described procedure to obtain the charged-particle multiplicities was applied to the events used in the analysis. Fig. 4.10 shows the distribution of the multiplicity values at mid-rapidity (top) and forward rapidity (bottom) for events obtained with the MB and the HM trigger. In HM-triggered events the average mid-rapidity multiplicity is about 5.1 times the one in MB-triggered events; the average forward rapidity multiplicity is about 4.8 times the one in MB-triggered events.

The vertical lines indicate the interval limits used for the extraction of the J/ψ signal. Dashed lines represent the intervals used in the p_T -integrated analysis. In the analysis in p_T intervals, some intervals had to be merged due to the lower signal counts, in order to be able to extract a significant signal. The interval limits are indicated by solid lines.

In the first HM-triggered $N_{ch,fwd.}$ interval the effect of the different settings for the trigger threshold can be seen by the bumps in the distribution. In the second $N_{ch,fwd.}$ interval, in which the trigger is fully efficient, the shape of the MB and the HM distribution is identical, the enhancement factor of the HM events is about 410. For $N_{ch,mid}$ even in the highest multiplicity interval the distributions from the two trigger classes are different. There is a wide overlap between the two distributions. This makes it possible to compare the obtained J/ψ yields at the same multiplicity in the different trigger classes. No significant difference in the extracted observable between the trigger classes was observed. The comparison will be shown in section 5.3. For $N_{ch,fwd.}$ the HM trigger sets in only in a region in which the number of MB events is too low to extract a J/ψ signal reliably, so no comparison between the trigger classes can be performed

The multiplicity values serve as a rough estimator for the analysis, no full description of the actual charged-particle multiplicity distribution is attempted. One obvious shortcoming is that with the presented correction method, fractional multiplicity values can occur, whereas in reality they are necessarily integer. As the N_{ch} intervals used in the analysis have width of 10, 20 or 30 this should not be relevant though.

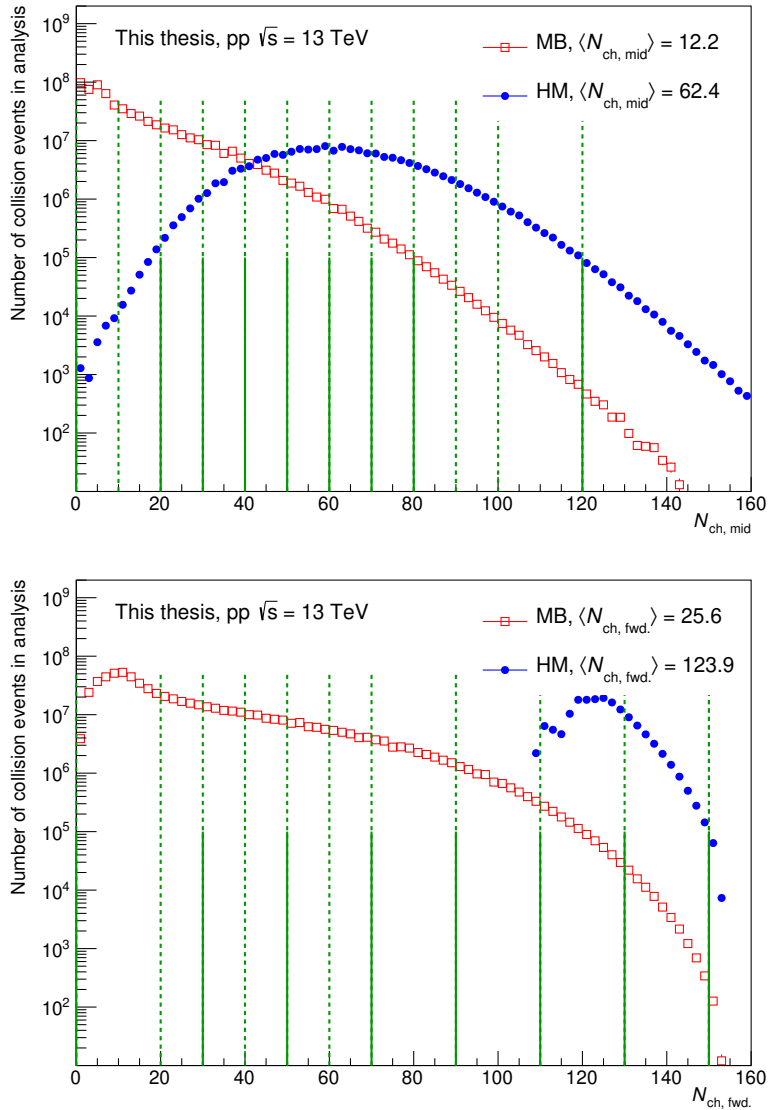


Figure 4.10.: Distribution of the estimated mid- (top) and forward rapidity (bottom) charged-particle multiplicity in the MB and HM-triggered events used in the analysis. Dashed lines indicate the limits of the multiplicity intervals used in the p_T -integrated analyses, solid lines the one in the analysis in p_T intervals.

4.6 Track Selection

In order to reconstruct J/ψ particles from their dielectron decay channel, its decay daughters have to be reconstructed. With the usage of track selection criteria, an efficient reconstruction of tracks from J/ψ daughter electrons is attempted, at the same time minimizing the contamination with electrons from other sources, as well as with hadrons and muons. The selection criteria used in this analysis will be presented in the following, they are summarized in table 4.1.

- **Kinematic region** Only tracks with an absolute value of pseudorapidity $|\eta| < 0.8$ are used in the analysis in order to have the full radial length in the TPC available and to avoid edge effects. Tracks are required to have a transverse momentum of at least $1 \text{ GeV}/c$. This requirement reduces background composed of tracks from electrons from other sources than J/ψ decay. Due to the high mass of the J/ψ its decay products have typically a high momentum, roughly 85 % of the daughters have $p_T > 1 \text{ GeV}/c$, estimated from Monte Carlo simulations. Furthermore, particles are identified using the energy loss in the TPC. As explained in section 3.7.1, the expected curves of the energy loss for the different particles cross at specific values of momentum. Around $p = 1 \text{ GeV}/c$ the curve for protons crosses the ones for electrons. In order to use electrons in this momentum region, the protons have to be rejected, e.g. with information from the TOF detector, which provides a clear discrimination between protons and electrons at this momentum. However, the TOF detector was not present in the complete data period, and its usage requires additional efficiency corrections, and might introduce a new source of systematic uncertainty. For these reasons it was decided to rejects tracks with $p_T < 1 \text{ GeV}/c$ from the analysis.
- **Track quality criteria** For a correct determination of the kinematic and PID quantities of the tracks, a high tracking quality is required. For this reason, only tracks are used that underwent the final refitting procedure both in the TPC and ITS (TPC, ITS *refit*) as explained in section 3.6. Tracks are required to have at least 70 clusters out of the 159 possible in the TPC. A χ^2 per cluster from the track reconstruction procedure smaller than 4 is required. In the ITS, tracks are required to have at least 3 clusters out of possible 6.

Table 4.1.: Track selection criteria used in the analysis.

Quantity	Selection criterion
Pseudorapidity	$ \eta < 0.8$
Transverse momentum	$p_T > 1 \text{ GeV}/c$
Impact parameter (transverse direction)	$ dca_{xy} < 1 \text{ cm}$
Impact parameter (longitudinal direction)	$ dca_z < 3 \text{ cm}$
Kink topologies	daughters rejected
TPC refit	required
ITS refit	required
Number of TPC clusters	$N_{\text{cls. TPC}} > 70$
Tracking quality	$\chi^2/N_{\text{cls. TPC}} < 4$
Number of ITS clusters	$N_{\text{cls. ITS}} \geq 3$
Hit in SPD	required in at least one layer
Electron inclusion	$-2 < n\sigma_{\text{TPC},e} < 3$
Proton exclusion	$n\sigma_{\text{TPC},p} > 3.5$
Pion exclusion	$n\sigma_{\text{TPC},\pi} > 3$

- **Particle identification** PID is performed based on the specific energy loss in the TPC, with the $n\sigma_{\text{TPC},i}$ values as described in section 3.7.1. Candidate tracks are required to have an energy loss compatible with the one expected for electrons within 2σ towards lower values and 3σ towards higher values: $-2 < n\sigma_{\text{TPC},e} < 3$. The asymmetric selection criterion originates from the fact that pions suffer at the same transverse momentum a lower energy loss than electrons. By accepting tracks with too low negative $n\sigma_{\text{TPC},e}$ values, a considerable contamination by pions remains in the sample. On the other hand, particles suffering a higher energy loss than electrons at the same p_T for $p_T > 1 \text{ GeV}/c$ are deuterons and heavier nuclei, of which orders of magnitude fewer are produced, so contamination by them is negligible. To further reduce hadronic background, tracks with an energy loss within 3σ of the pion expectation, or 3.5σ of the proton expectation are also excluded. From Fig. 3.4 is can be seen, that by these criteria, kaons are already implicitly excluded from the analysis, as their specific energy loss is below the one of protons. Fig. 4.11 shows for the tracks selected in the analysis the $n\sigma_{\text{TPC},e}$ as a function of the track momentum p . The curvature at low p originates from the proton exclusion, the pion exclusion has the effect of the "cut-off corner" at lower $n\sigma_{\text{TPC},e}$ at high p .
- **Secondary rejection** Several further criteria are applied in order to reduce contamination from secondary particles. A hit in one of the first two layers of the ITS is required. The distance of closest approach of each track to the primary vertex is required to be less than 1 cm in radial direction and 3 cm in z -direction. Daughter tracks from kink topologies are rejected. To further reject electrons from low-mass sources, such as photon conversions in the detector material and partially reconstructed π^0 Dalitz decays, a prefilter technique is applied. Details on it will be given in section 4.8.

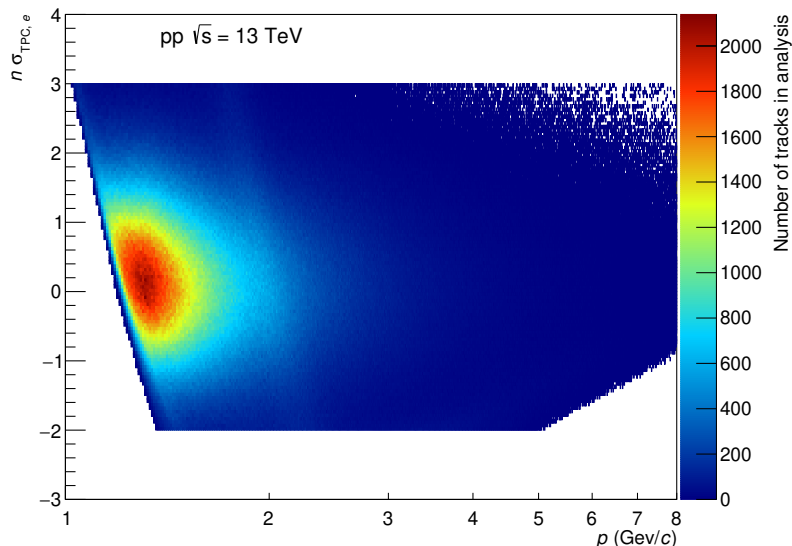


Figure 4.11.: Distribution of the momentum and $n\sigma_{\text{TPC},e}$ values of the tracks selected in the analysis.

4.7 Efficiency correction

The track selection criteria presented in the last section, as well as other steps of the analysis have a certain efficiency. Since the presented observable is self-normalized, no full efficiency correction is necessary. However, the dependence of the reconstruction efficiency on the charged-particle multiplicity has to be corrected. Furthermore, the dependence on the p_T of the J/ψ can lead to a multiplicity dependence, if the p_T shape of J/ψ changes with multiplicity, so it also has to be corrected.

For the efficiency correction a weighting procedure is applied. The reconstruction efficiency $\epsilon(p_T, N_{\text{trk}})$ is determined from the enhanced Monte Carlo simulation including a full detector simulation as a function of p_T and N_{trk} . When filling the invariant mass distribution the entries are weighted with a factor $w \propto \epsilon(p_T, N_{\text{trk}})^{-1}$ proportional to the inverse efficiency. Since only a relative efficiency correction is necessary, not the full inverse efficiency is used in the weighting, but $\epsilon(p_T, N_{\text{trk}})^{-1}/\langle \epsilon(p_T, N_{\text{trk}})^{-1} \rangle$, i.e. the inverse efficiency divided by the inverse average efficiency. This fact has no influence on the result, as this additional factor cancels out in the self-normalized yields. It merely serves the purpose that in the invariant mass distributions, the number of entries is close to the real number of reconstructed entries, which can give a better impression of the statistics.

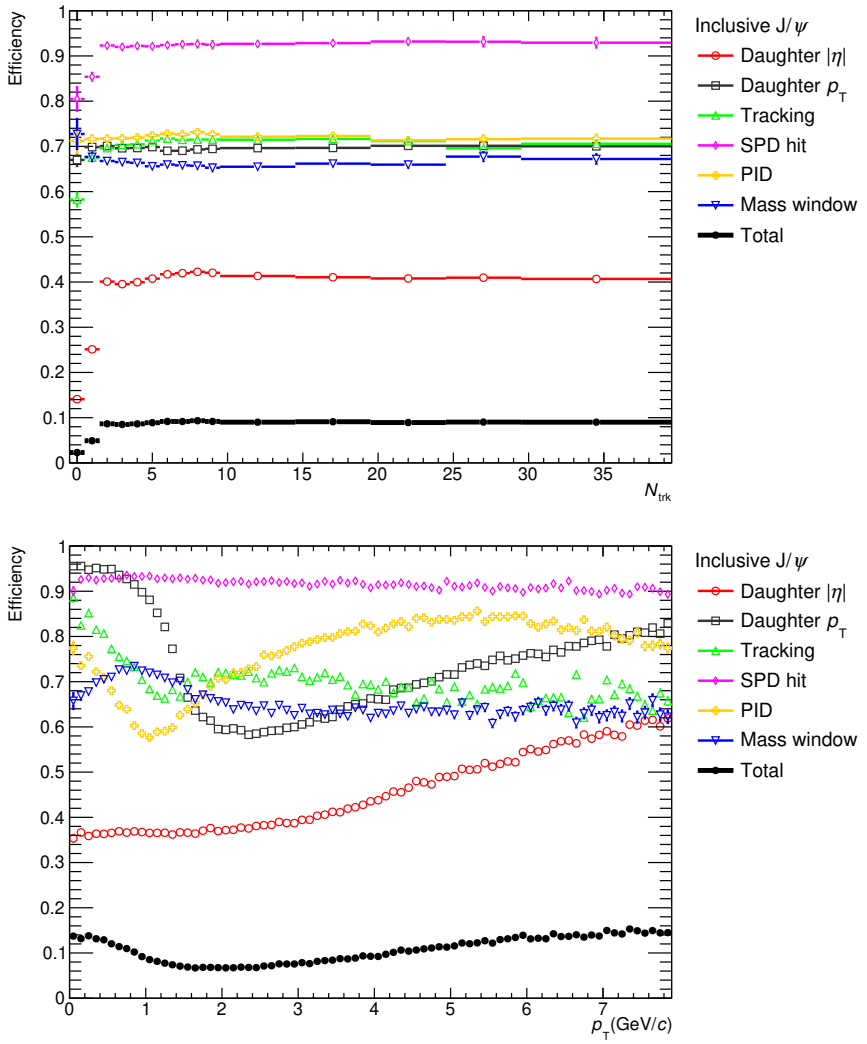


Figure 4.12.: J/ψ reconstruction efficiency as a function of the number of SPD tracklets (top) and as a function of the transverse momentum of the J/ψ (bottom). Besides the total efficiency the individual efficiencies of the analysis steps are shown.

In order to reconstruct a J/ψ the requirements listed below have to be fulfilled. The efficiency of these are plotted in Fig. 4.12 as a function of N_{trk} (top) and p_T (bottom). Both the total reconstruction efficiency is shown and the efficiency of the single analysis steps. These are always to be understood as the probability for a J/ψ that passed the previous requirements passes the next one, so e.g. the *tracking* efficiency is calculated for J/ψ that passed the *acceptance* and *kinematics* requirement.

- **Acceptance.** Both daughter particles have to fall into the acceptance of the detector, i.e. $|\eta| < 0.8$. As the opening angle of the daughter particles is dependent on the energy of the mother particle, the efficiency of this requirement has some p_T dependence, as can be seen in Fig. 4.12 (bottom). In Fig. 4.12 (top), it can also be seen that, though multiplicity independent from multiplicities of 2 onwards, in events with zero or one reconstructed tracklets, the efficiency for this requirement is much lower. This is an autocorrelation effect: By selecting events, in which a J/ψ is produced in $|\eta| < 0.8$, but which have only one or two SPD tracklets in $|\eta| < 1$, it is likely that the decay daughters did not produce an SPD tracklet because they were produced outside of the detector acceptance.
- **Kinematics.** Both daughter particles have to have a transverse momentum of at least $1 \text{ GeV}/c$. This requirement shows a specific p_T dependence related to the kinematics of the decay, but is independent of multiplicity.
- **Tracking.** Both tracks have to have left a reconstructed track in the detector, that passes the quality cuts (TPC, ITS refit, $\chi^2/N_{\text{cls,TPC}}$, N_{cls} and dca requirements). The efficiency is slightly decreasing with p_T , and independent of multiplicity, except for $N_{\text{trk}} < 2$. This is again an autocorrelation effect: These are events in which a J/ψ is produced and its decay daughters are within $|\eta| < 0.8$, but the number of SPD tracklets in $|\eta| < 1$ is below two. It is likely that the J/ψ decay daughters were produced in a region with inactive pixels in the SPD, which reduces their tracking efficiency.
- **SPD hit.** Both tracks are required to have a hit in one of the two layers of the SPD. The efficiency is weakly dependent on the p_T of the J/ψ , and independent of multiplicity, except for $N_{\text{trk}} < 2$, another iteration of the known autocorrelation effect.
- **PID.** Both tracks have to fulfill the particle identification requirements from the TPC. As the pion and proton exclusion cuts effect the electron sample in a different way depending on the p_T of the track, the efficiency is also dependent on the p_T of the J/ψ . No multiplicity dependence is observed.
- **Mass window.** The J/ψ are reconstructed by counting the yield in the invariant mass distribution in a specific invariant mass window. Due to energy loss of the daughter particles in the detector material or internal bremsstrahlung, it can happen that a too low invariant mass is reconstructed. In this case, the J/ψ signal is lost. The probability to fall into the mass window shows a slight p_T dependence and no significant multiplicity dependence.

To summarize, most of the requirements of the analysis have a specific p_T dependent efficiency associated to them. The efficiencies are independent of multiplicities up to the highest multiplicity that can be reached with the available Monte Carlo sample used in the analysis with sufficient statistical precision, which is around 40 tracklets. From this fact and from the knowledge of earlier analysis in environments with much higher multiplicities, such as Pb-Pb collisions [111], it is assumed, that no deterioration of the reconstruction efficiencies at high multiplicities occurs. At very low multiplicities, however, autocorrelation effects lead to a reduced reconstruction efficiency, which is taken into account and corrected for in the weighting procedure.

The efficiencies were obtained for inclusive J/ψ , no significant difference between prompt and non-prompt J/ψ was observed.

4.8 Low-mass background suppression

Most of the produced electrons and positrons in a pp collision originate from low mass sources, as becomes evident when looking at the distribution of invariant masses m_{inv} of electron-positron pairs, as shown in Fig. 4.13 (left). Mind the logarithmic scale of the y-axis. These sources include Dalitz decays of light pseudoscalar mesons, like $\pi^0 \rightarrow \gamma e^+ e^-$ (B.R. $(1.174 \pm 0.035)\%$ [1]), and electron-positron pair creation from a photon conversion in the detector material. The conversion probability is p_T dependent and saturates at around 8.5 % for $p_T \gtrsim 2 \text{ GeV}/c$ [166]. The photons in turn originate predominantly from decays of light mesons [180], like $\pi^0 \rightarrow \gamma\gamma$ (B.R. $(98.823 \pm 0.034)\%$ [1]), π^0 Dalitz decays (see above), or $\eta \rightarrow \gamma\gamma$ (B.R. $(39.41 \pm 0.20)\%$ [1]).

Electron-positron pairs of higher m_{inv} are then to a large extend random combinations of electrons and positrons from these low mass sources. By excluding tracks from low m_{inv} pairs from the analysis, the background under the J/ψ peak can be reduced. This can be done with a *prefilter* technique. Tracks selected for the analysis are paired with associated tracks with less restrictive selection criteria. If a low-mass pair (i.e. $m_{\text{inv}} < 50 \text{ MeV}/c^2$) is found, the corresponding track is removed from the further analysis. The selection criteria that were released for the associated tracks are:

- Minimal transverse momentum: $p_T > 0.2 \text{ GeV}/c$ instead of $1 \text{ GeV}/c$.
- Wider pseudorapidity window in order to also find pairs at the edges of the acceptance : $|\eta| < 0.9$.
- Relaxed PID requirement: $-3 < n\sigma_{\text{TPC},e} < 3$, no proton exclusion cut.
- No hit in any SPD layer required, no requirement on the number of ITS clusters.

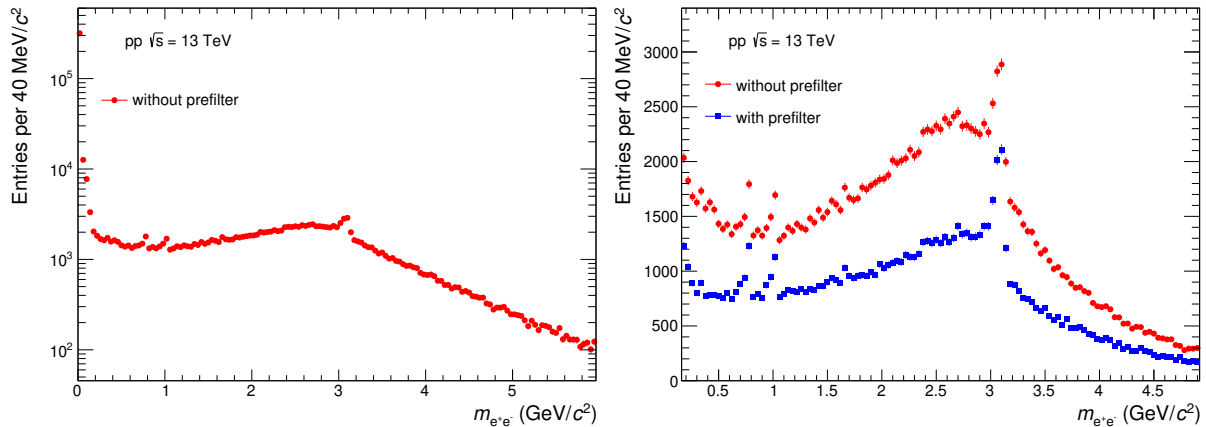


Figure 4.13.: Invariant mass distribution of electron-positron pairs without low-mass rejection (left), and comparison of the distributions with and without low-mass rejection (right).

Fig. 4.13 (right) shows the effect of the prefilter. The background in the invariant mass region around the J/ψ peak is reduced considerably. A possible bias can be introduced, as a track from a J/ψ daughter might randomly form a low m_{inv} pair with another track, and thus be removed from the analysis, leading to a signal loss. This effect was investigated, and it was found that no significant signal loss occurs. The investigation is presented in section 5.3.

4.9 Signal Extraction

From the selected pairs of electrons and positrons the invariant mass m_{inv} is calculated. Fig. 4.14 shows the m_{inv} distribution of J/ψ -candidate dielectron pairs from the presented analysis. Around $m_{\text{inv}} = 3.1 \text{ GeV}/c^2$ the peak originating from the J/ψ can be identified. At lower invariant masses two additional peaks are present. They originate from the dielectron decays of vector mesons, the one at $m_{\text{inv}} = 783 \text{ MeV}/c^2$ from the ω mesons, the one at $m_{\text{inv}} = 1019 \text{ MeV}/c^2$ from the ϕ mesons at [1].

The J/ψ peak sits on top of a background distribution. To a large part it consist of *combinatorial* background by random combinations of uncorrelated electrons. This part of the background can be modeled with the *event-mixing* technique: a given electron (positron) track is paired with the positron (electron) tracks of the other collisions of the analyzed data sample and the invariant mass m_{EM} is calculated. Any correlation between positrons and electrons of the same collision is not present in tracks from different collisions. The distribution of m_{EM} is shown in green in Fig. 4.14. In order to compare the shape to the m_{inv} distribution, it has been scaled to the latter in the invariant mass region above the J/ψ peak $3.2 < m_{\text{inv}} < 5 \text{ GeV}/c^2$. The shape of the m_{EM} distribution qualitatively resembles the m_{inv} distribution. However, the agreement is not perfect, as can be seen by the disagreement at lower invariant masses.

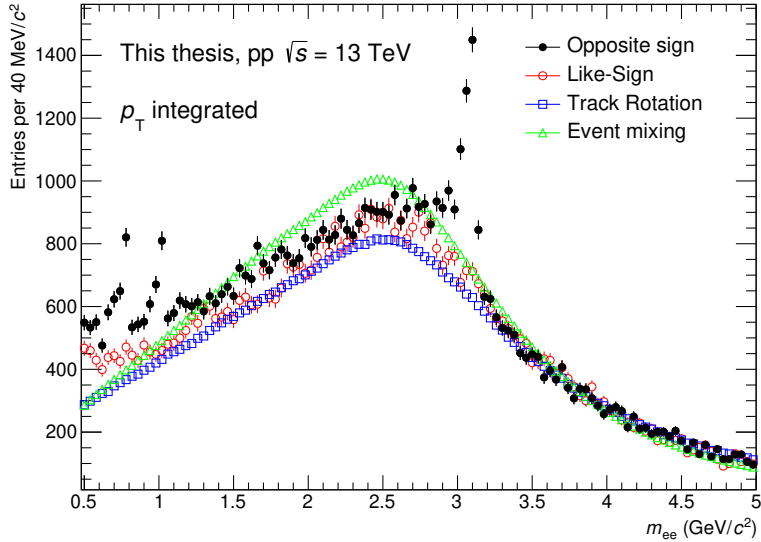


Figure 4.14.: Efficiency weighted invariant mass distribution of electron-positron pairs, together with background estimated by the event-mixing, like-sign and track-rotation methods.

This simple event-mixing method does not take into account the shape of the events in pp collisions. The invariant mass of electron-positron pairs can be approximated by the formula for massless particles:

$$m_{\text{inv}}^2 \approx 2p_{\text{T}1}p_{\text{T}2}(\cosh(\Delta\eta) - \cos(\Delta\varphi)) \quad (4.6)$$

with $p_{\text{T}1,2}$ the transverse momenta of the daughter particles, $\Delta\eta = \eta_2 - \eta_1$ the difference in pseudorapidity, and $\Delta\varphi = \varphi_2 - \varphi_1$ the opening angle in the azimuth.

With the event-mixing technique, the tracks are randomly oriented towards each other. The tracks of a single event on the other hand can be oriented either more or less isotropically. Especially high-momentum particles are typically produced inside jets, so they are close in η and φ . Also, in the analysis events of very different particle multiplicities are used, which can have very different event topologies. In addition, the η distributions can be different for events with different vtx_z due to acceptance effects in the detector.

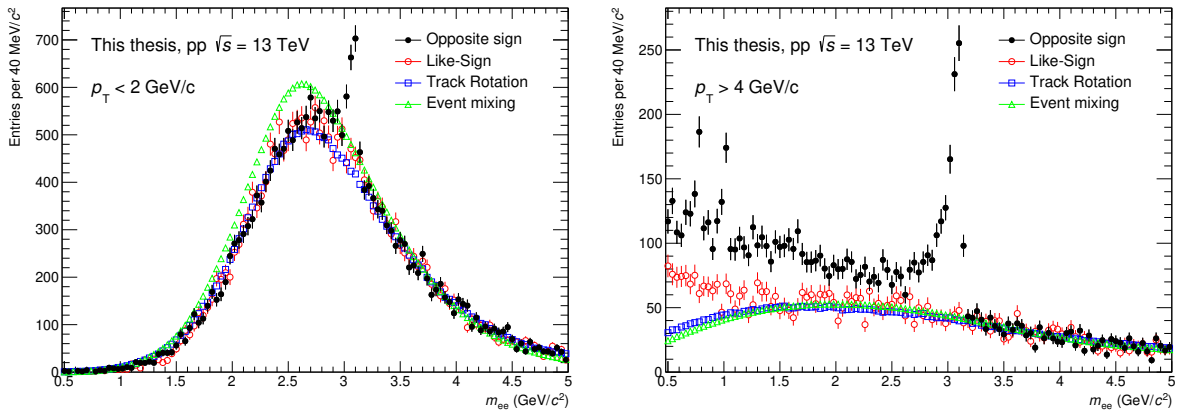


Figure 4.15.: Efficiency weighted invariant mass distribution of electron-positron pairs, compared to background estimated from the different discussed methods. Left: $p_T < 2 \text{ GeV}/c$, right: $p_T > 4 \text{ GeV}/c$.

To take these different event topologies into account, the mixed-event technique can be refined by mixing only events with similar global properties, e.g. with similar vtx_z , or similar particle multiplicities. Another way is the usage of the *track-rotation* technique. One of the tracks of a dielectron pair from the same event is rotated by a random angle in azimuth. The correlation in φ gets destroyed, whereas the event shape in η is maintained. The procedure can be repeated to obtain more pairs and reduce the statistical uncertainty. The track-rotated invariant mass distribution m_{TR} is shown in Fig. 4.14 in blue. Compared to the event-mixing technique, the track-rotation method better describes the shape of the m_{inv} distribution. In the mass region above the J/ψ peak m_{TR} was scaled to the m_{inv} distribution, here the distributions agree well with each other. In the mass region below the peak the m_{TR} distribution is consistently beneath the m_{inv} distribution.

Even closer to the m_{inv} distribution should be the *like-sign* distribution m_{LS} : electrons are paired with electrons and positrons with positrons from the same event. The event-shape effect on the invariant mass distribution is the same as for opposite-sign pairs. Fig. 4.14 shows the m_{LS} distribution in red. The distribution is closer to the m_{inv} distribution than the other estimators. The remaining difference is due to *correlated* background. In the invariant mass region around the J/ψ peak, this is mainly due to heavy quark pairs $c\bar{c} \rightarrow e^+e^-$ and $b\bar{b} \rightarrow e^+e^-$, via semileptonic decays of pairs of open charm and open beauty hadrons [181].

Fig. 4.15 shows the m_{inv} distribution together with the various methods to describe the background for low- p_T ($p_T < 2 \text{ GeV}/c$) and high- p_T ($p_T > 4 \text{ GeV}/c$) dielectron pairs. The overall shape is very different in the two transverse momentum regions. For low p_T pairs (left), the distributions from the like-sign and track-rotation method are in good agreement with m_{inv} in the whole invariant mass region, the one from event-mixing is not. At high p_T (right), all the background estimators underestimated the m_{inv} distribution at lower invariant masses. This hints to the fact, that the contribution to the background from correlated heavy quarks is more relevant at high p_T , as is expected.

To take into account the remaining correlated background, the ratio between the m_{inv} and the m_{TR} was calculated and fitted with an exponentially decreasing function $f(m_{\text{inv}}) = a \cdot \exp(-bm_{\text{inv}})$ with a and b parameters of the fit. The functional shape was chosen in order to reflect the shape of the correlated background, cf. [181]. The fit was performed in an invariant mass region $1.5 < m_{\text{inv}} < 4.5 \text{ GeV}/c^2$, excluding the region around the J/ψ peak $2.2 < m_{\text{inv}} < 3.2 \text{ GeV}/c^2$. The m_{TR} distribution was then scaled with the obtained function and used to describe the background in the m_{inv} distribution.

Fig. 4.16 shows on top the candidate invariant mass distribution together with the background estimate, and for comparison the distribution from the track-rotation method as estimate of the combinator-

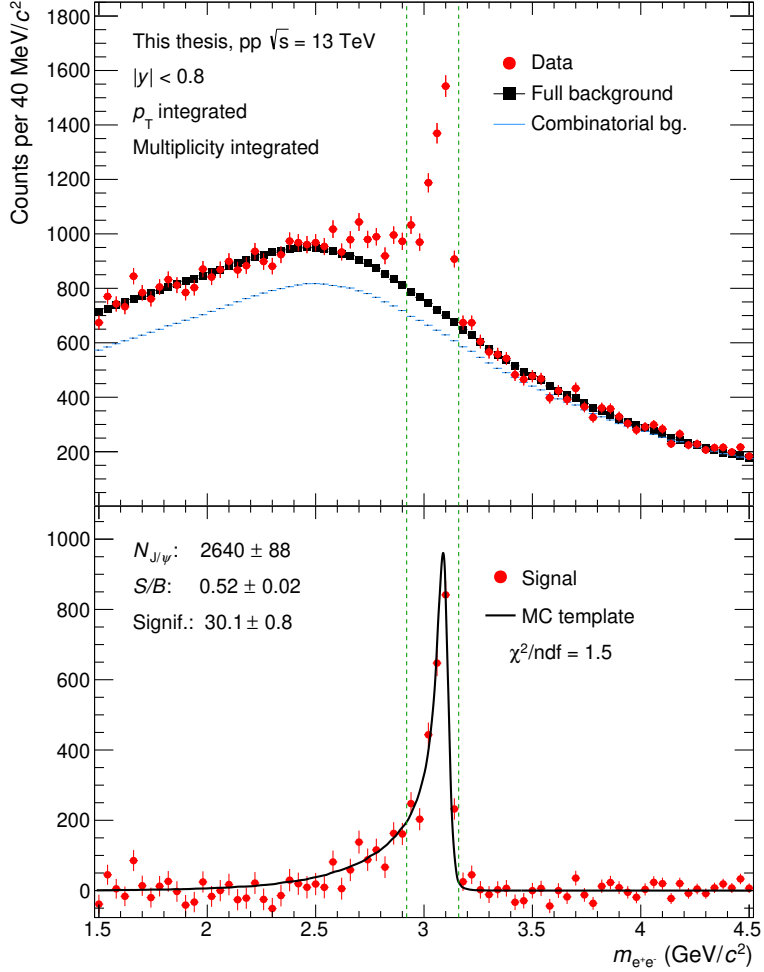


Figure 4.16.: Top: Efficiency weighted invariant mass distribution of electron-positron pairs, together with background estimation. Also shown is the combinatorial background contribution from the track-rotation method. Bottom: J/ψ signal after background subtraction. Plotted for comparison is the line shape as expected from the Monte Carlo simulation.

trial part of the background. The background is well described by the estimate. To extract the signal, the background estimate is subtracted from the m_{inv} distribution, as shown in Fig. 4.16 (bottom).

The peak of the J/ψ is asymmetric. The tail towards lower masses is caused by internal and external bremsstrahlung. The former refers to QED corrections in the J/ψ decay, such as $J/\psi \rightarrow e^+e^+\gamma$ ($B.R. = 8.8 \pm 1.4 \times 10^{-3}$ for $E_\gamma > 100 \text{ MeV}$ [1]), and higher orders processes. The latter refers to bremsstrahlung of the decay electrons from interactions with the detector material.

In these cases, the invariant mass from the electron and the positron is lower than the mass of the J/ψ , since the energy carried by the photons is not taken into account. The expected shape of the signal is shown in Fig. 4.16 (bottom) with the black solid line. It shows the reconstructed mass for simulated J/ψ from the Monte Carlo sample. The agreement to the signal obtained in the data is good, the χ^2 per number of degrees of freedom ndf between the expected and the observed line shape is 1.5.

The signal is obtained by counting the entries in the invariant mass region $2.92 \text{ GeV}/c^2 < m_{e^+e^-} < 3.16 \text{ GeV}/c^2$. This mass window is illustrated in the figure by the dashed green vertical lines. A total multiplicity and p_T -integrated signal count of $S = 2640 \pm 88$ is obtained. The uncertainty on the signal consists of the statistical uncertainty from the entries in the m_{inv} distributions, and the uncertainty from the scaling of the background estimate as obtained from the fit procedure. The signal-over-

background ratio $S/B = 0.52 \pm 0.02$ can be calculated from the obtained signal S and the integrated estimated background B in the mass window were the signal is counted. The significance of the signal $Signif. = 30.1 \pm 0.8$ was calculated as $Signif. = \frac{S}{\sqrt{S+B}}$. This simplified formula neglects the uncertainty of the background (which is small), and the fact, that S and B do not represent pure counts, but efficiency-weighted entries. However, since the applied weighting factor is normalized to its mean value the actually applied weightings are close to unity. The given significance value is thus a reasonable approximation for the true statistical significance of the signal.

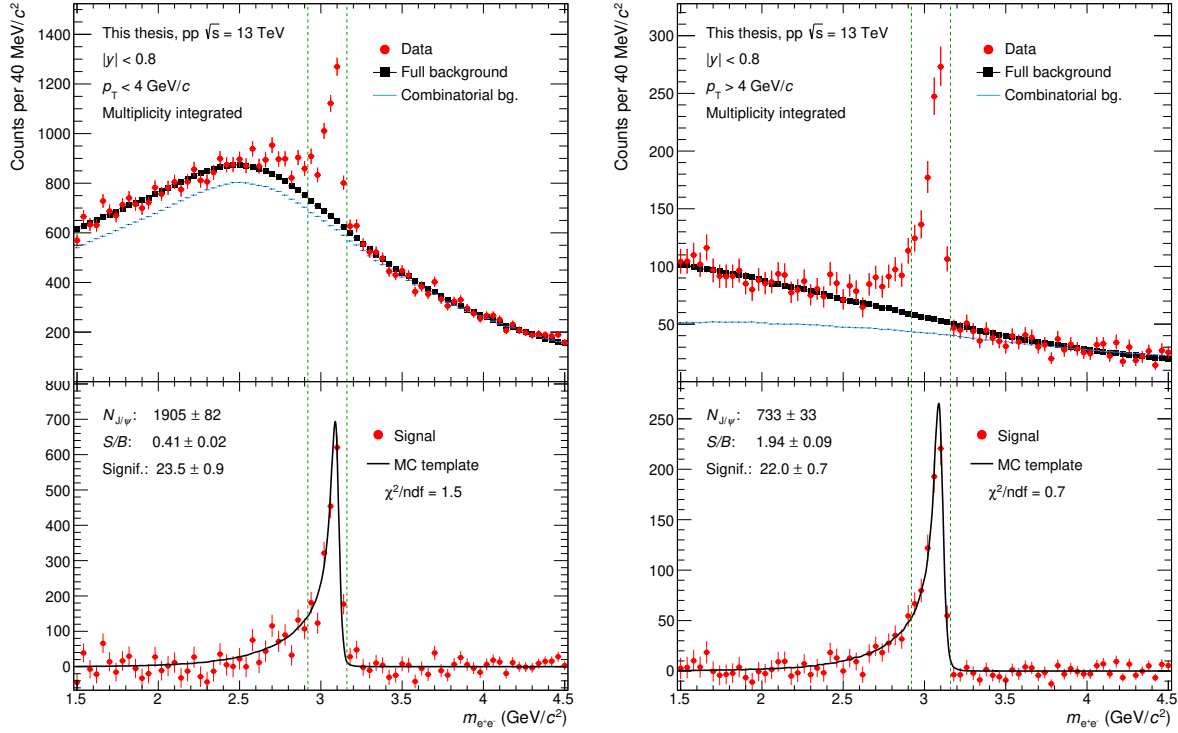


Figure 4.17.: Efficiency weighted invariant mass distribution (top) of electron-positron pairs, together with background estimation; J/ψ signal after background subtraction (bottom). Pairs with $p_T < 4 \text{ GeV}/c$ (left), and $p_T > 4 \text{ GeV}/c$ (right).

For the analysis in p_T intervals, the signal extraction was performed for dielectron pairs with $p_T < 4 \text{ GeV}/c$ and with $p_T > 4 \text{ GeV}/c$. The invariant mass distribution and signal extraction in these p_T intervals is shown in Fig. 4.17; low p_T on the left, high p_T on the right. The background is well described, the difference to the pure combinatorial part is stronger for high- p_T pairs. The signal over background ratio is more than 4 times as high at high p_T compared to low p_T ; the extracted signal agrees with the line shape from Monte Carlo with a $\chi^2/ndf = 1.5$ for low p_T and $\chi^2/ndf = 0.7$ for high p_T .

The described signal extraction is performed in events selected in intervals of charged-particle multiplicity at mid- or forward rapidity, as defined in section 4.5. Fig. 4.18 shows as examples the signal extraction in the lowest (left) and highest (right) mid-rapidity multiplicity interval. The background is much lower in the low multiplicity interval ($S/B = 4.56 \pm 0.62$) compared to the multiplicity-integrated signal extraction, and slightly higher in the high multiplicity interval ($S/B = 0.42 \pm 0.07$). The line shape is in good agreement with the expectation from Monte Carlo in both cases with $\chi^2/ndf = 1.2$ and 1.0, respectively.

The performance of the signal extraction in the multiplicity intervals is illustrated in Fig. 4.19 and Fig. 4.20. It shows for the p_T -integrated analysis as a function of the mid-rapidity multiplicity the raw J/ψ signal count (Fig. 4.19, left), the signal-over-background ratio (Fig. 4.19, right), the significance of the signal (Fig. 4.20, left), and the χ^2/ndf between the extracted signal and the scaled line shape from

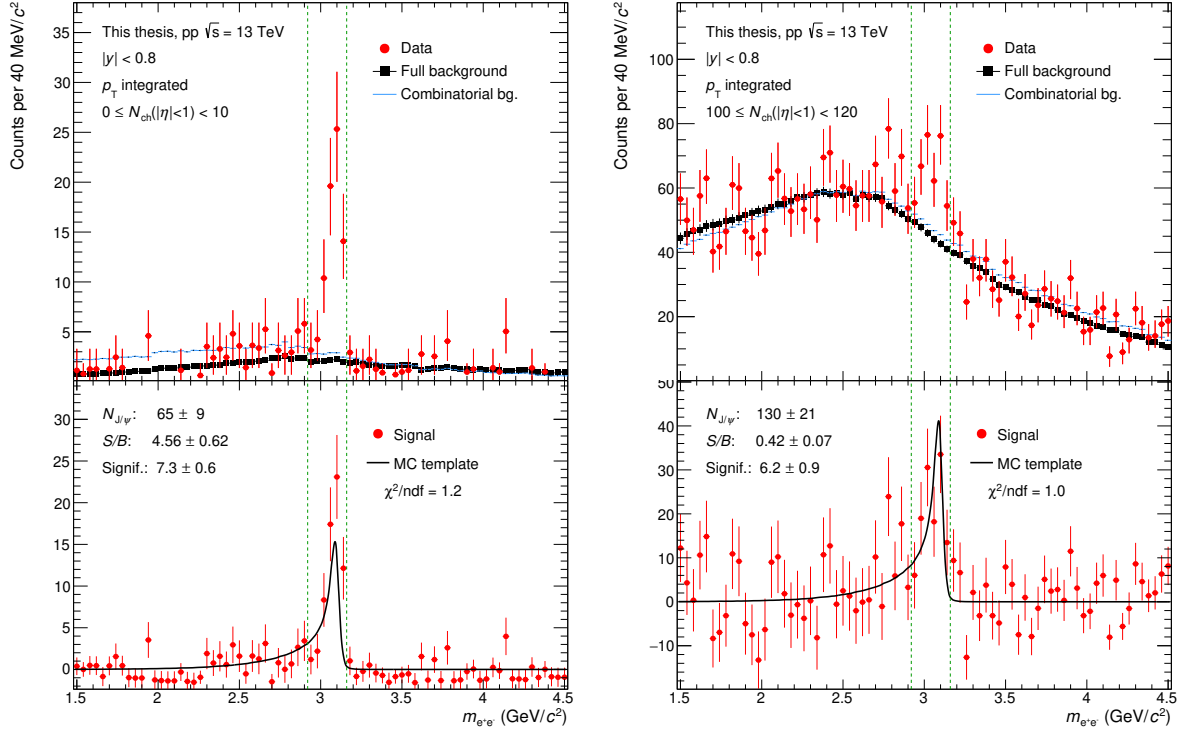


Figure 4.18.: Efficiency weighted invariant mass distribution (top) of electron-positron pairs, together with background estimation; J/ψ signal after background subtraction (bottom). Lowest (left) and highest (right) mid-rapidity multiplicity interval used in the analysis.

Monte Carlo simulations (Fig. 4.20, right). The horizontal error bars represent the width of the multiplicity intervals. The data points themselves are positioned at the mean charged-particle multiplicity in the intervals.

With increasing charged-particle multiplicity the background increases, resulting in a decreasing signal-over-background ratio. The significance is above six in all multiplicity intervals, so a significant signal extraction has been possible in all intervals. The line shape is agreeing reasonably well with the expectation from Monte Carlo with a χ^2/ndf between 0.9 and 1.8. The corresponding plots for the signal extraction as a function of $N_{ch,fwd.}$, as well as the ones in p_T intervals can be found in appendix A.

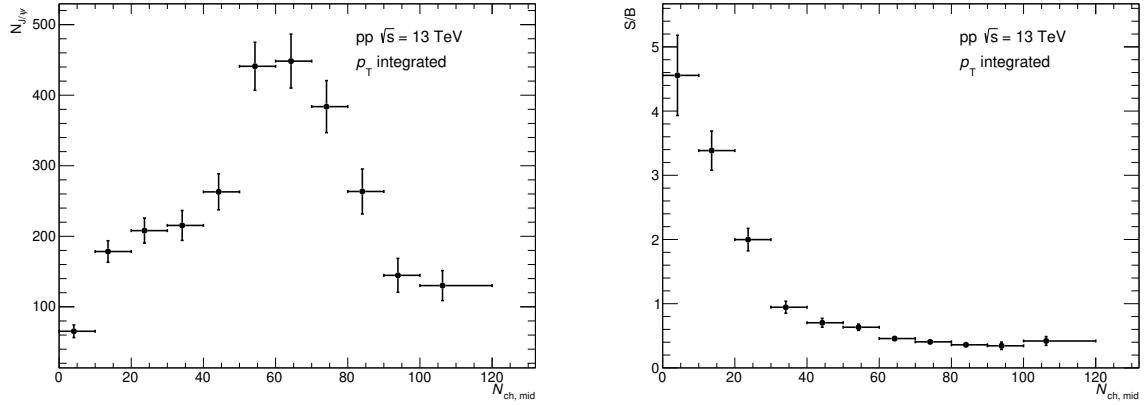


Figure 4.19.: Performance of the p_T -integrated signal extraction as a function of $N_{ch,mid}$. Left: Raw (efficiency corrected) signal count; Right: Signal-over-background ratio.

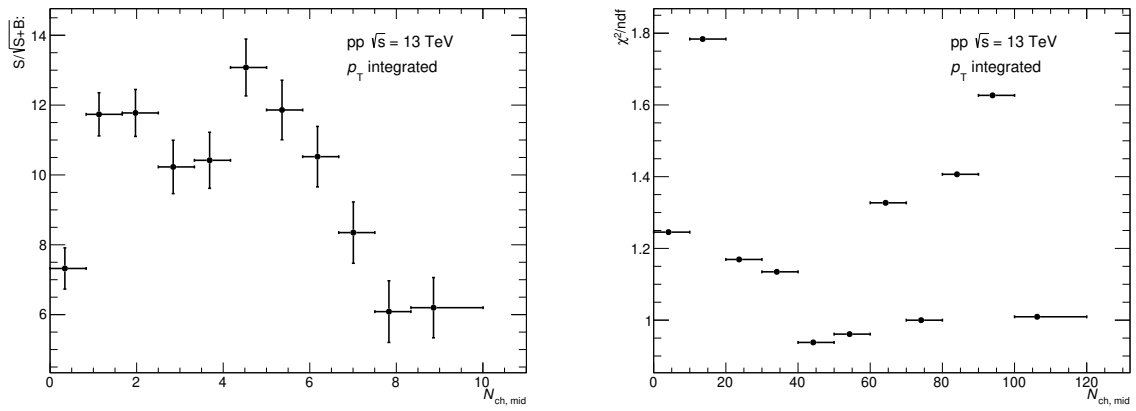


Figure 4.20.: Performance of the p_T -integrated signal extraction as a function of $N_{ch,mid}$. Left: Significance of the extracted signal; Right: χ^2/ndf between the extracted signal and the scaled line shape from Monte Carlo simulations.

5 Systematic Uncertainty Estimation

The presented analysis might suffer from systematic biases arising from the underlying assumptions that were used within it. Possible causes are disagreements between the true values and the values estimated from Monte Carlo simulations on

- the p_T and multiplicity dependence of the J/ψ reconstruction efficiency
- the multiplicity dependence of the minimum bias trigger efficiency
- the relation between the charged-particle multiplicity and the estimators from the detectors.

Furthermore, the extraction of the J/ψ yield from the invariant mass distribution might be biased, e.g. through an inaccurate description of the background in the signal region. This bias can be multiplicity dependent and thus distort the results. Possible additional biases arise from a disagreement between the event properties of MB and HM-triggered events and from a possible signal loss caused by the low-mass pair rejection.

An estimation of the systematic uncertainties of the analysis from these effects is presented in this chapter.

5.1 Uncertainty on the charged-particle multiplicity

The uncertainty on the self-normalized charged-particle multiplicity n_{ch} arises from the assumptions made in the analysis on the multiplicity dependence of the trigger efficiency and on the correlation between the true charged-particle multiplicities and the detector quantities. These values were determined from Monte Carlo simulations using the EPOS-LHC events generator and modeling the ALICE detector with the GEANT3 framework.

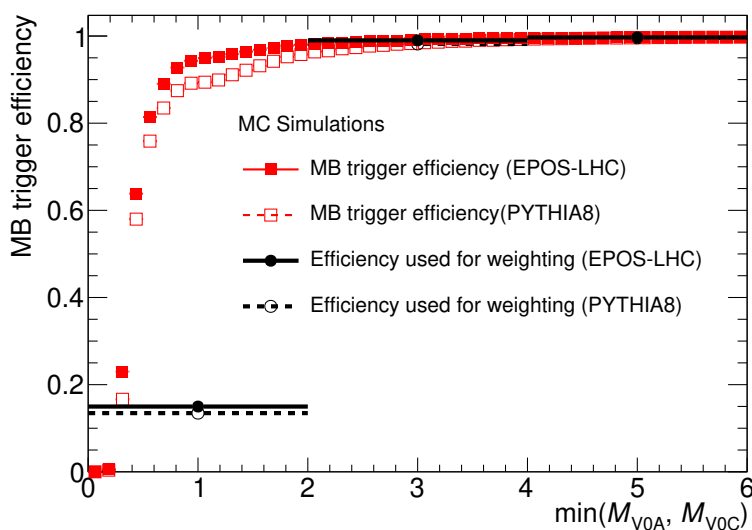


Figure 5.1.: Trigger efficiency as a function of the minimum of the V0A and V0C signal from Monte Carlo simulations using the EPOS-LHC event generator (default) and the PYTHIA8 event generator (variation to determine uncertainty).

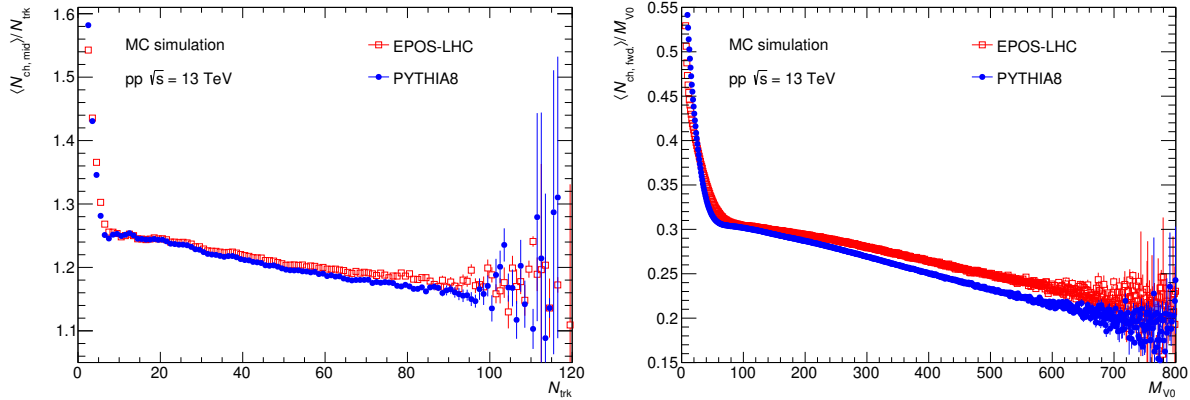


Figure 5.2.: Ratio α between charged-particle multiplicity and multiplicity estimator, as function of the value of the estimator, from Monte Carlo simulations based on the EPOS-LHC and PYTHIA8 event generators. Left: Multiplicity at mid-rapidity, number of SPD tracklets; Right: Multiplicity in the V0 acceptance, V0 signal.

To estimate the uncertainty on these values, the PYTHIA8 event generator was used as an alternative. The differences between the two estimators were then propagated to the relative charged particle multiplicity values and used as systematic uncertainties.

The choice of the EPOS-LHC event generator as default, and PYTHIA8 as variation was done because of the better description by EPOS-LHC of multiplicity distributions in various rapidity ranges in pp collisions at the LHC in previous analyses [34, 35, 176]. However it is not guaranteed that the multiplicities both at mid and forward rapidity are correctly described up to the high multiplicity values used in the presented analysis. For this reason, the disagreement between the models was chosen for the systematic uncertainty estimation.

Fig. 5.1 shows the minimum bias trigger efficiency as a function of the minimum of the signals in the VOA and the VOC detectors, estimated with the EPOS-LHC and the PYTHIA8 event generator. The onset curve is slightly slower for the PYTHIA8 event generator. Since the detector description is similar in both Monte Carlo samples, the reason for the difference is probably a difference in the correlation of the particles multiplicities in the VOA and the VOC acceptance. The trigger efficiency in the lowest multiplicity interval used for the weighting of the events is about 10 % lower in the PYTHIA8 Monte Carlo sample, in the higher intervals it is anyway close to 100 %, regardless of the generator used.

In Fig. 5.2 (left), the α factor, i.e. the ratio between the charged-particle multiplicity and the multiplicity estimator is shown for mid-rapidity, calculated with the two different Monte Carlo simulators. The models disagree slightly at very low and high multiplicities. The reason is the different multiplicity distribution in the generators, which leads to different strengths of the selection bias. At forward rapidity, the width of the distribution of the estimator values for a given charged-particle multiplicity is wider than at mid-rapidity. A difference in the underlying multiplicity distribution from the different generators results in a stronger change in the α factors, as shown Fig. 5.2 (right).

The described uncertainties were propagated to n_{ch} in the multiplicity intervals. It was calculated, what would be the mean n_{ch} of this interval when using the PYTHIA8 simulation instead of the default EPOS-LHC for the determination of the trigger efficiency or of the α factor. The absolute value of the difference was used as systematic uncertainty (symmetrically both towards higher and lower values) in the multiplicity interval i . So, the trigger efficiency uncertainty is $\Delta_{\text{trigger}} = |n_{\text{ch, default}} - n_{\text{ch, trig. eff. from PYTHIA}}|$, the uncertainty from the α factor $\Delta_{\alpha} = |n_{\text{ch, default}} - n_{\text{ch, } \alpha \text{ from PYTHIA}}|$. The two uncertainties were regarded as independent, and the total uncertainty calculated as the square root of the sum of the uncertainties squared:

$$\Delta_{\text{mult}} = \sqrt{\Delta_{\text{trigger}}^2 + \Delta_{\alpha}^2}. \quad (5.1)$$

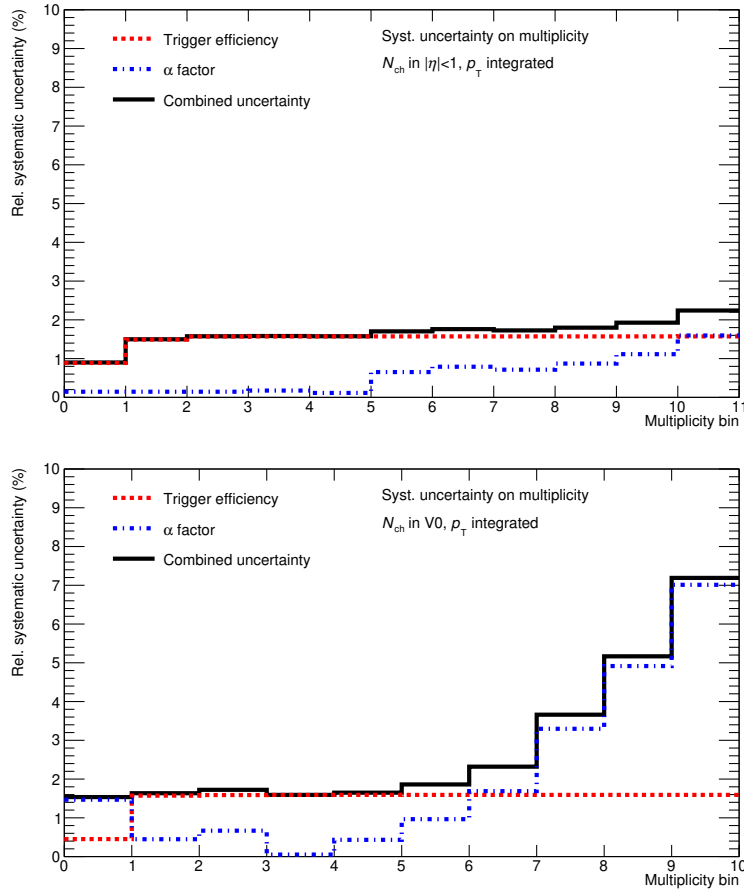


Figure 5.3.: Relative systematic uncertainty on the self-normalized multiplicity at mid-rapidity (top), and at forward rapidity (bottom), as function of the multiplicity interval. Uncertainty due to trigger efficiency, α factor, and total uncertainty as combination of the two.

In Fig. 5.3 the relative systematic uncertainties on n_{ch} — the systematic uncertainty divided by the default n_{ch} in the interval — are plotted as a function of n_{ch} . The multiplicity intervals of the p_{T} -integrated analyses were used. The top panel shows the mid-rapidity multiplicity, the bottom panel the forward rapidity one. The uncertainty from the trigger efficiency, from the α factor, and the combined value are shown.

The trigger efficiency enters the n_{ch} twice: it affects the average multiplicity of all inelastic collisions (denominator), and the average multiplicity in the multiplicity interval (numerator). The trigger efficiency is different from 100 % only for low multiplicity events however. This means, for all multiplicity intervals except the lowest ones, only the denominator is affected by the uncertainty of the trigger. The uncertainty is thus constant at around 1.6 % for all multiplicity intervals except the lowest. In the lowest intervals, the effect in the numerator and the denominator partially cancel, so the uncertainty is lower.

The uncertainty from the α factor grows with increasing multiplicity. For the $n_{\text{ch},\text{mid}}$, it is below the uncertainty from the trigger efficiency — with exception of the highest interval, where they are of equal size. For $n_{\text{ch},\text{fwd.}}$, it dominates the uncertainty from the seventh interval onwards and reaches a value of 7 % in the highest interval.

The total uncertainty on $n_{\text{ch},\text{mid}}$ is below 2 % in all multiplicity intervals, except the highest, where it is slightly above. For $n_{\text{ch},\text{fwd.}}$ the total uncertainty is relatively constant in the first five intervals, where the trigger efficiency uncertainty dominates. At the higher intervals it increases with multiplicity, in the highest interval it is slightly above 7 %.

5.2 Uncertainty on the J/ψ yield

Table 5.1.: Settings for track selection. Default values used in the analysis and variations to estimate systematic uncertainties.

Quantity	Default value, variations
Pseudorapidity	$ \eta < 0.7, 0.75, \mathbf{0.8}, 0.85, 0.9$
Transverse momentum	$p_T > 0.8, 0.9, \mathbf{1.0}, 1.1, 1.2 \text{ GeV}/c$
Impact parameter (transverse direction)	$ dca_{xy} < 0.2, 0.5, \mathbf{1.0}, 3.0 \text{ cm}$
Impact parameter (longitudinal direction)	$ dca_z < 1.0, 2.0, \mathbf{3.0}, 5.0 \text{ cm}$
Kink topologies	rejected , accepted
Number of TPC clusters	$N_{\text{cls.TPC}} > 50, \mathbf{70}, 80, 90$
Tracking quality	$\chi^2/N_{\text{cls.TPC}} < 2.5, 3.0, \mathbf{4.0}, 10.0$
Number of ITS clusters	$N_{\text{cls.ITS}} \geq 2, \mathbf{3}, 4$
Hit requirement in SPD	any layer , first layer
Electron inclusion lower limit	$n\sigma_{\text{TPC,e}} > -2.5, -2.25, \mathbf{-2.0}, -1.75, -1.5$
Electron inclusion upper limit	$n\sigma_{\text{TPC,e}} < 2.5, 2.75, \mathbf{3.0}, 3.25, 3.5$
Proton exclusion	$n\sigma_{\text{TPC,p}} > 3.0, 3.25, \mathbf{3.5}, 3.75, 4.0$
Pion exclusion	$n\sigma_{\text{TPC,}\pi} > 2.5, 2.75, \mathbf{3.0}, 3.25, 3.5$

The calculation of the self-normalized J/ψ yield $n_{J/\psi}$ at a specific multiplicity relies on the fact that the multiplicity and p_T dependence of the reconstruction efficiency is correctly described in Monte Carlo.

In order to test the agreement of the reconstruction efficiency between the experimental data and the Monte Carlo simulation, variations of the selection criteria for the J/ψ daughter tracks are used. They are varied around their default values and the analysis is performed with these modified settings. Table 5.1 lists the track selection criteria used in the analysis, and the variations investigated. Where possible and sensible, two more and two less restrictive settings are used, e.g. for the PID settings and the minimum p_T . Some selection criteria used in the analysis are already very inclusive, e.g. the minimum number of required TPC clusters, or the maximum $\chi^2/N_{\text{cls.TPC}}$ of the tracking. In these cases only one less restrictive setting is tested, and two more restrictive ones. The TPC and ITS refit requirements can not be dropped, as they are vital for a sufficiently high track quality to extract a signal. From the ITS refit requirement implicitly a minimum requirement two ITS clusters follows. A requirement of four ITS clusters is used as more restrictive setting. A requirement of five or six clusters rejects too many tracks, increasing the statistical uncertainty too much as to extract the J/ψ signal reliably.

The requirement to have a hit in one of the SPD layers is vital for the analysis. Without it there is too much contamination with secondaries to perform a reliable signal extraction in all intervals. As a more restrictive variation, a hit in the first SPD layer is required. This requirement is the most restrictive one investigated, reducing the J/ψ yield by about one third. In the default analysis, tracks from kink topologies are rejected, as a variation they are kept in.

The rapidity in which the J/ψ is extracted, and the pseudorapidity range of the daughter particles is also varied from $|y| < 0.8$ to two narrower and two wider values in steps of 0.05.

Fig. 5.4 demonstrates the effect of the described variations for one multiplicity interval. The lowest $n_{\text{ch,mid}}$ interval has been chosen, since it has the highest relative uncertainty from the track selection criteria.

In the top panel of Fig. 5.4 the self-normalized J/ψ yield $n_{J/\psi}$ is shown for the default analysis in the first bin, and for the analysis with the varied track selection settings in the other bins. The vertical error bars indicate the statistical uncertainties. The horizontal solid line shows the value of $n_{J/\psi}$ with the default settings; the dashed lines show the lower and upper statistical uncertainty on it. For most of the variations, $n_{J/\psi}$ fluctuates slightly around the default value. Some variations, such as the $n\sigma_p > 3.0$

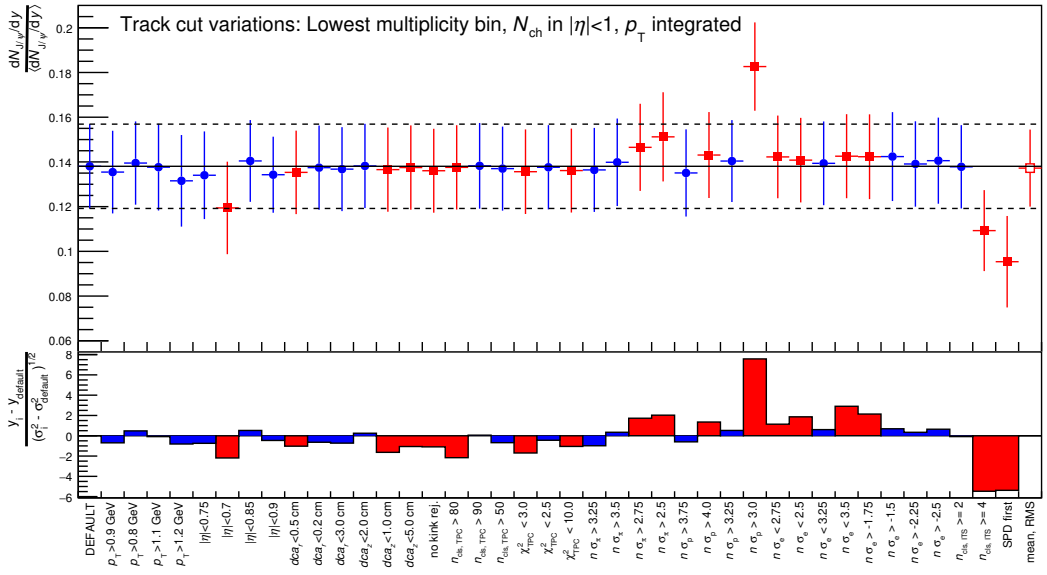


Figure 5.4.: Top: Self-normalized J/ψ yield in the lowest $n_{\text{ch, mid}}$ interval for default settings (first bin), and varied selection settings for the J/ψ daughter particle tracks. The solid line represents the default yield, the dashed line the default statistical uncertainty. The last bin shows the mean and RMS of $n_{J/\psi}$ for significant variations. Bottom: Difference to the default yield, normalized to the square root of the difference of the squared uncertainties. Variations with (without) a significant difference are marked in red (blue).

requirement, or the more restrictive ITS requirements, seem to show a significant deviation from the default $n_{J/\psi}$. In order to estimate quantitatively if a difference is significant the Barlow criterion [182] is used. According to it, a variation is significant if the difference to the default value is larger than the square root of the difference of the squared statistical uncertainties:

$$y_{\text{variation}} - y_{\text{default}} > \sqrt{\sigma_{\text{variation}}^2 - \sigma_{\text{default}}^2}. \quad (5.2)$$

In the bottom of Fig. 5.4, this difference to the default yield, divided by $\sqrt{\sigma_{\text{variation}}^2 - \sigma_{\text{default}}^2}$ is shown. An absolute value larger than one of this normalized difference indicates a significant variation. Here and in the top of the figure, the significant variations are plotted in red, the non-significant ones in blue. From the distribution of $n_{J/\psi}$ for the settings with significant variations, the mean and the RMS is calculated. The value of $n_{J/\psi}$ in last bin in Fig. 5.4 (top) shows the mean of this distribution, the error bar indicates the RMS. The RMS is assigned as systematic uncertainty from the track selection Δ_{tracks} .

Table 5.2.: Settings for the signal extraction. Default values used in the analysis and variations to estimate systematic uncertainties.

Quantity	Default value, variations
Fit of residual background	exponential, 2 nd order polynomial, 3 rd order polynomial
Fit range lower limit	1.2, 1.5 , 2.0 GeV/c^2
Fit range upper limit	4.0, 4.5 , 5.0 GeV/c^2
Signal extraction	interval counting, MC line shape, Crystal Ball function
Signal extraction window lower limit	2.88, 2.92 , 2.96 GeV/c^2
Signal extraction window upper limit	3.12, 3.16 , 3.20 GeV/c^2

An additional source of systematic uncertainty is the signal extraction from the invariant mass distribution. It relies on a correct description of the background in the m_{inv} region where the signal is extracted. The overall method of signal extraction is not changed for the systematic uncertainty estimation. However, the exact settings were varied as listed in table 5.2. The assumed shape of the residual background is changed from an exponential function to a 2nd and a 3rd order polynomial. The lower and upper limits of the m_{inv} range used in the fit are independently varied to lower and higher values, likewise the limits of the m_{inv} window in which the signal is counted. Additionally two different methods to extract the signal are examined: In the first alternative method the shape of the reconstructed signal from the Monte Carlo simulation is used as a template and scaled to the signal from data by minimizing the χ^2/ndf . The signal is then extracted by integrating the Monte Carlo peak shape in the same m_{inv} window as is used in the counting method. In the second alternative method, the signal is fitted with a Crystal Ball function and the signal extracted as the integral of the function in the default m_{inv} window. The Crystal Ball function is a continuous combination of a Gauss function describing the detector resolution with a powerlaw tail at lower m_{inv} :

$$f(m_{\text{inv}})_{\bar{m}_{\text{inv}}, \alpha, n, \sigma, N} = N \begin{cases} \exp(-\frac{m^2}{2}), & \text{for } m > -\alpha \\ a(b-m)^{-n}, & \text{otherwise} \end{cases} \quad (5.3)$$

with $m = \frac{m_{\text{inv}} - \bar{m}_{\text{inv}}}{\sigma}$, $a = \left(\frac{n}{|\alpha|}\right)^n \cdot \exp(-\frac{\alpha^2}{2})$, and $b = \frac{n}{|\alpha|} - |\alpha|$.

\bar{m}_{inv} , α , n , σ , and N are the parameters of the fit, with \bar{m}_{inv} denoting the position of the peak.

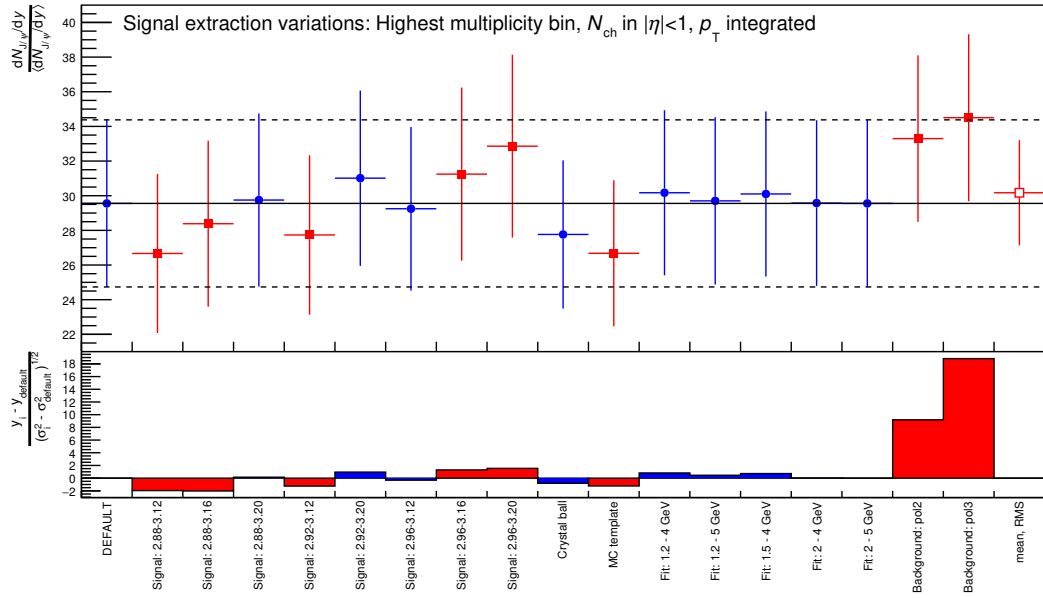


Figure 5.5.: Top: Self-normalized J/ψ yield in the highest $n_{\text{ch},\text{mid}}$ interval for default settings (first bin), and varied signal extraction settings. The solid line represents the default yield, the dashed line the default statistical uncertainty. The last bin shows the mean and RMS of $n_{J/\psi}$ for significant variations. **Bottom:** Difference to the default yield, normalized to the square root of the difference of the squared uncertainties. Variations with (without) a significant difference are marked in red (blue).

Fig. 5.5 shows $n_{J/\psi}$ in the highest $n_{\text{ch},\text{mid}}$ interval for the default signal extraction method and the ones with varied parameters. This multiplicity interval was chosen, because it has among the highest relative systematic uncertainties from the signal extraction. Especially the usage of different fit functions for the residual background results in a significantly differently $n_{J/\psi}$. As for the track selection variations, the

RMS of the distribution of $n_{J/\psi}$ for significant variations is used as estimate for the systematic uncertainty from the signal extraction Δ_{signal} .

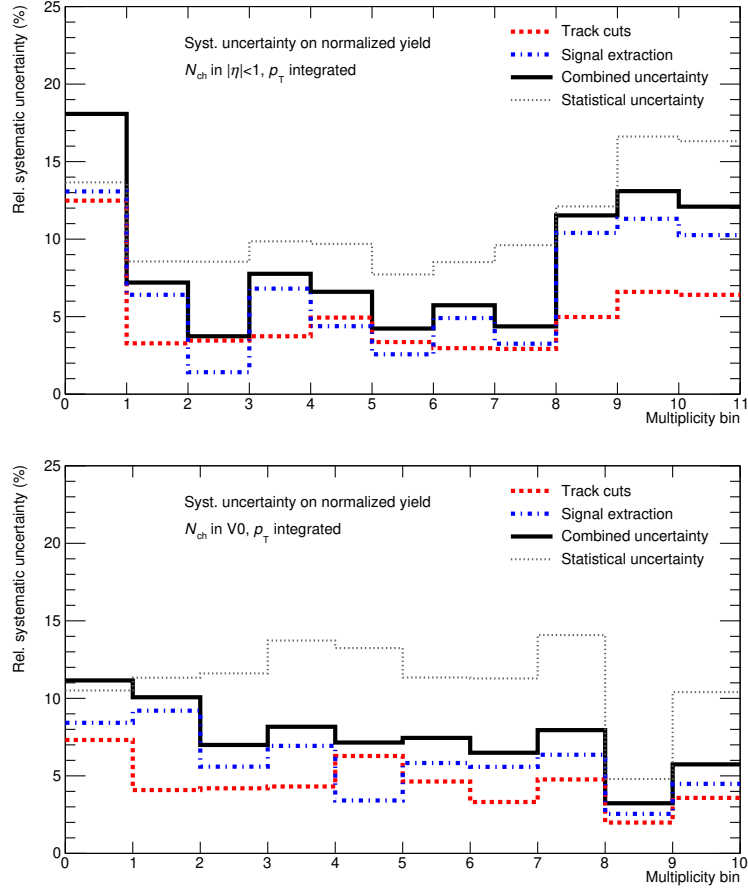


Figure 5.6.: Relative systematic uncertainty on the self-normalized J/ψ yield as a function of the multiplicity interval at mid-rapidity (top) and at forward rapidity (bottom). Uncertainty due to the track selection, the signal extraction, and the total systematic uncertainty as combination of the two. Statistical uncertainty shown for comparison.

The two uncertainties were regarded as independent, and the total uncertainty calculated as the square root of the sum of the two uncertainties squared:

$$\Delta_{\text{yield}} = \sqrt{\Delta_{\text{tracks}}^2 + \Delta_{\text{signal}}^2}. \quad (5.4)$$

Fig. 5.6 shows the relative systematic uncertainties on the J/ψ yield from the track selection and the signal extraction, as well as the combined value as function of multiplicity. In the top panel it is shown for the $n_{\text{ch,mid}}$ intervals, in the bottom panel for the $n_{\text{ch,fwd}}$ ones. Both sources of uncertainty are of comparable size. Δ_{tracks} is fluctuating around 5 %. In the lowest $n_{\text{ch,mid}}$ interval it is higher, mainly due to the uncertainty from the ITS requirements as was demonstrated before. Δ_{signal} is close to the one from the track selection in all intervals, except for the three highest $n_{\text{ch,mid}}$, where it is higher, around 11 %.

For comparison, also the statistical uncertainty is displayed in Fig. 5.6. For all multiplicity intervals, both at mid- and forward rapidity, the systematic uncertainty is slightly smaller than the statistical one. An exception are the respective lowest intervals, where it is higher. The combined relative systematic uncertainty is slightly decreasing as a function of $n_{\text{ch,fwd}}$, in the highest intervals it is around 5 %. In these intervals the uncertainties on the multiplicity (around 7 %) is dominating over the one from the J/ψ yield, whereas for all others the latter one is larger. A better understanding of the charged-particle

multiplicity in the V0 at very high relative values is thus necessary for future analyses. The discussion of the systematic uncertainties of the p_T -differential results can be found in appendix B.

5.3 Additional checks for possible biases

The usage of two different trigger classes might introduce a bias in the results, as the collision candidates from the different trigger classes can have different properties. As was mentioned in section 4.2, for the HM trigger, events lying in the trigger onset curve are excluded from the analysis, as there the correlation between $N_{\text{ch},\text{mid}}$ and $N_{\text{ch},\text{fwd}}$ is very different from the one in MB-triggered events. From Fig. 4.10 (bottom) it is furthermore evident that the $N_{\text{ch},\text{mid}}$ distribution in HM-triggered events has a very different shape than the one in MB-triggered events.

In order to investigate a possible influence on the presented results, the multiplicity dependent J/ψ yield can be calculated separately for MB and HM-triggered events. As shown in Fig. 4.10 (top), for $n_{\text{ch},\text{mid}}$ the multiplicity distributions for the two trigger classes have a wide overlap. The comparison is presented in Fig. 5.7. In the multiplicity range $20 < N_{\text{ch}} < 90$, it is possible to extract the J/ψ yield in both trigger classes, though with very limited statistics for MB-triggered events above $N_{\text{ch}} = 60$. Within the statistical uncertainties, the results from the two trigger classes are in agreement with each other. This indicates that a higher charged-particle multiplicity at forward rapidity has little influence on the J/ψ yield at mid-rapidity for a given charged-particle multiplicity at mid-rapidity.

A similar comparison of the yield in the different trigger classes as a function of $n_{\text{ch},\text{fwd}}$ is not possible, since in the multiplicity region where the HM trigger sets in, the number of MB-triggered events is too low for a reliable extraction of the J/ψ yield.

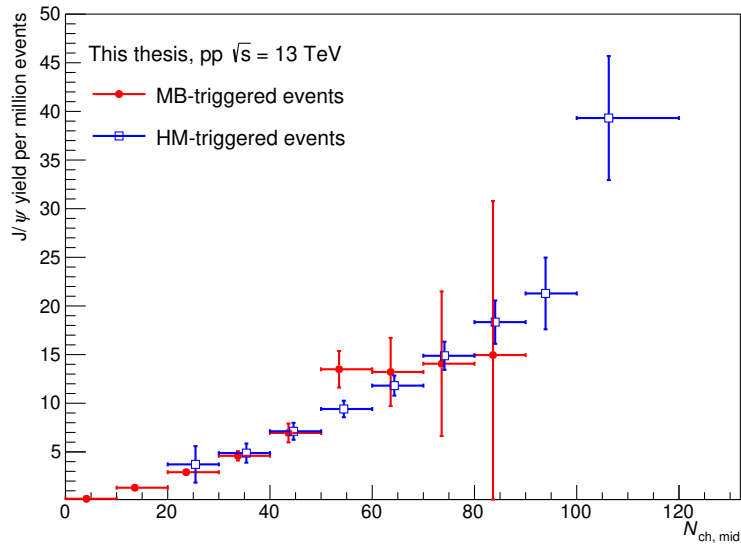


Figure 5.7.: J/ψ yield per event as a function of charged-particle multiplicity at mid-rapidity in pp collisions at $\sqrt{s} = 13$ TeV, separately for MB and HM-triggered events.

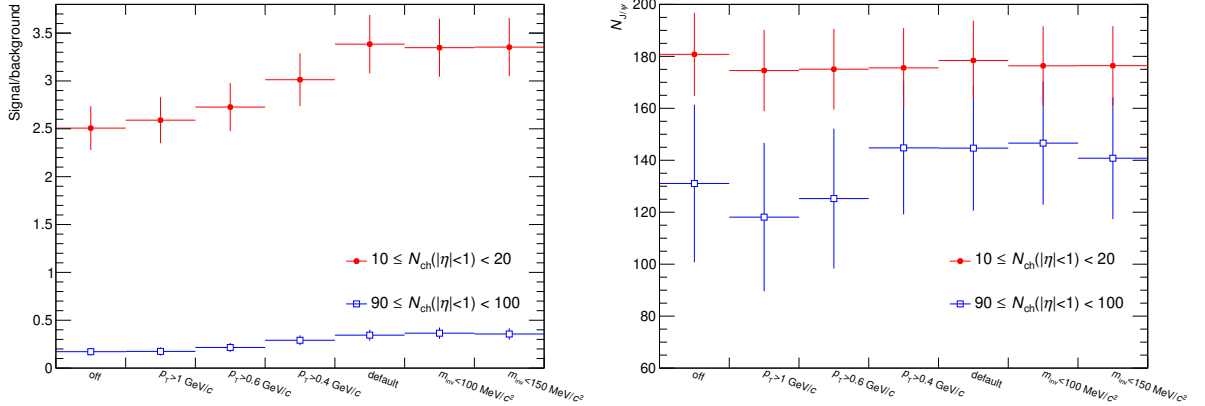


Figure 5.8.: Effect of different settings for the low-mass rejection. Left: signal over background ratio, right: extracted J/ψ signal. From left to right the settings get more rejective.

Another possible systematic bias comes from the low-mass rejection via the prefilter. Tracks that form pairs of low invariant mass — or small opening angle — are excluded from the analysis. By this, also tracks of J/ψ daughter particles can be excluded, if by chance another track is produced under a small opening towards them. This can lead to a signal loss, which can be expected to be more pronounced in high-multiplicity collisions. With more tracks there is a higher statistical chance to have a random combination of J/ψ daughter tracks with another track fulfilling the prefilter condition.

One could attempt to estimate the strength of this effect from Monte Carlo simulations. This requires a large sample of a Monte Carlo simulated data with a realistic description of J/ψ production, and its correlation with the underlying event. The Monte Carlo sample with injected J/ψ signals that is used for the efficiency estimation does not fulfill the latter requirement. The minimum bias Monte Carlo sample used to estimate the trigger efficiency and the α factors on the other hand does not contain enough J/ψ particles to make a statistically relevant investigation. This direction was thus not pursued. In order to see a possible bias, the analysis is run without the low-mass rejection, and with different settings for it. Settings are tested with a weaker rejection, i.e. a higher p_T of the associated track is required: $p_T > 0.4, 0.6, 1.0 \text{ GeV}/c$; the default is $p_T < 0.2 \text{ GeV}/c$. Also, settings resulting in a stronger rejection are investigated, i.e. also pairs of higher invariant mass are rejected: $m_{\text{inv}} < 100, 150 \text{ MeV}/c^2$; the default is $m_{\text{inv}} < 50 \text{ MeV}/c^2$.

Fig. 5.8 illustrates the effect of the prefilter. In the top panel the signal over background ratio is shown as a function of the prefilter settings. The bottom panel shows the extracted J/ψ signal. The values for the second lowest and the second highest $n_{\text{ch,mid}}$ interval are shown. In the lowest and the highest multiplicity interval, the signal extraction could not be performed reliably without the low-mass rejection due to too high statistical uncertainties.

The leftmost bin in the plots corresponds to the analysis without low-mass rejection, with increasing bin number more pairs are rejected. Lowering the required minimum p_T of prefilter tracks results in a higher signal over background ratio; increasing the rejected invariant mass has no additional effect. For all settings, the extracted signal is compatible within errors, no general downward trend is recognizable.

From the presented investigation it was concluded that the low-mass rejection does not lead to a significant signal loss, and thus does not bias the self-normalized J/ψ yield. No systematic uncertainty has been assigned.



6 Results and discussion

In this chapter the results of the analysis will be presented, i.e. the self-normalized inclusive J/ψ yield at mid-rapidity as a function of charged-particle multiplicity at mid- and forward rapidity in transverse-momentum intervals and p_T -integrated. The results will be compared to related analyses, to analytical functions, and expectations from theoretical models.

6.1 Inclusive J/ψ production at mid-rapidity as a function of charged-particle multiplicity

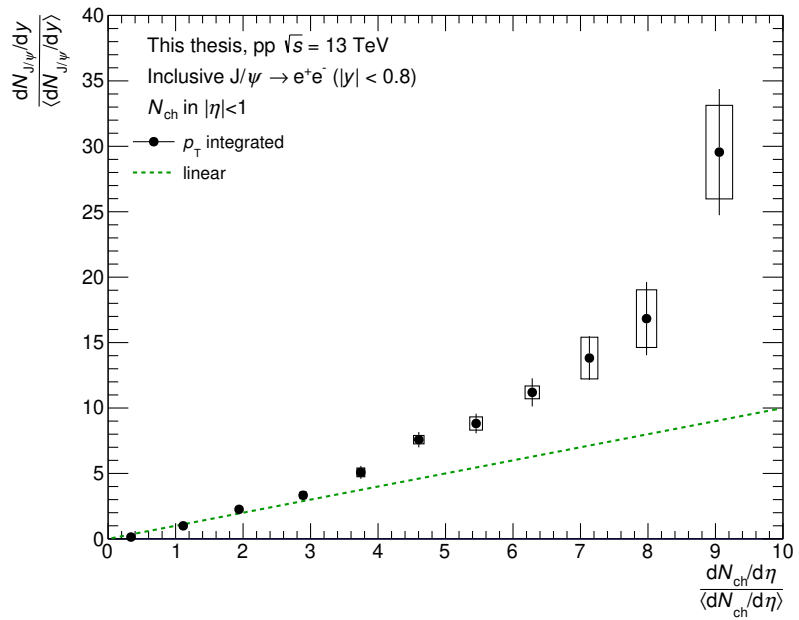


Figure 6.1.: Self-normalized inclusive J/ψ yield at mid-rapidity as a function of self-normalized charged-particle multiplicity at mid-rapidity in pp collisions at $\sqrt{s} = 13\text{ TeV}$. Error bars indicate the statistical uncertainty of the J/ψ yield, boxes the systematic uncertainty on the yield and the charged-particle multiplicity.

Fig. 6.1 shows the self-normalized inclusive J/ψ yield $n_{J/\psi}$ at $|y| < 0.8$ as a function of the self-normalized mid-rapidity charged-particle multiplicity $n_{ch,mid}$ in pp collisions at $\sqrt{s} = 13\text{ TeV}$. The error bars indicate the statistical uncertainty of the extracted yield, the boxes the systematic uncertainty on the yield and the charged-particle multiplicity. For comparison, the expectation for a linear increase $n_{J/\psi} = n_{ch}$ is shown with the dashed line. With the highest data point, a relative charged particle multiplicity of $n_{ch} = 9$ is reached. Up to a relative multiplicity of 3, the J/ψ yield is compatible with a linear increase with multiplicity, above it the increase is significantly stronger than linear.

To better visualize the departure from a linear increase in the full multiplicity range covered in the analysis, the self-normalized yield can be divided by the self-normalized charged-particle multiplicity, to give the double ratio $r_{J/\psi, mid}$ as a function of the charged particle multiplicity. In this representation, a linear increase corresponds to a horizontal line at $r_{J/\psi, mid} = 1$. In Fig. 6.2 (left), the data is shown in this representation. The boxes representing the systematic uncertainties are not rectangular, since the measurement and the systematic error estimation were performed on $n_{J/\psi}$ and not on $r_{J/\psi}$. A shift

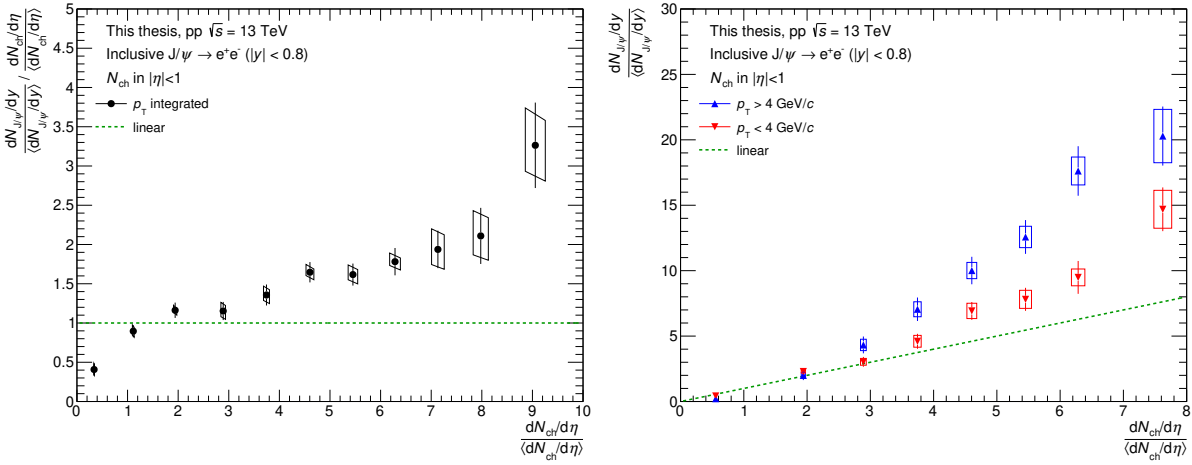


Figure 6.2.: Ratio between inclusive J/ψ yield and multiplicity as a function of self-normalized charged-particle multiplicity at mid-rapidity in pp collisions at $\sqrt{s} = 13$ TeV. Left: p_T -integrated results, right: results in p_T intervals.

towards a higher n_{ch} leads to a lower $r_{J/\psi}$, and vice versa. The upper and lower limits of the uncertainties are shifted analogously, resulting in the asymmetric uncertainties.

At low multiplicities, $r_{J/\psi, \text{mid}}$ lies significantly below the line of linear increase, at $n_{ch, \text{mid}} \approx 2$ it crosses it, and for $n_{ch, \text{mid}} > 3$ lies significantly above it, and diverges further from it with increasing multiplicity. From visual inspection, the data points follow a smooth line with a constant or only slowly changing slope. The data point in the highest multiplicity interval seems to be exceptionally high, indicating a possible change of slope at $n_{ch, \text{mid}}$ between 8 and 9. The effect is of low significance however and might be a statistical fluctuation.

Fig. 6.2 (right) shows $n_{J/\psi}$ as a function of $n_{ch, \text{mid}}$ for J/ψ with transverse momenta below and above $4 \text{ GeV}/c$. For $n_{ch, \text{mid}} < 3$, the results at the different transverse momenta are compatible with each other, and with a linear increase with multiplicity. Above $n_{ch, \text{mid}} = 3$, the increase is clearly stronger than linear for both transverse-momentum intervals, and the increase for high- p_T J/ψ is stronger than for low- p_T J/ψ . Since the three highest multiplicity intervals were merged in the analysis in p_T intervals, not the same $n_{ch, \text{mid}}$ value as for the highest interval in the p_T -integrated analysis can be reached.

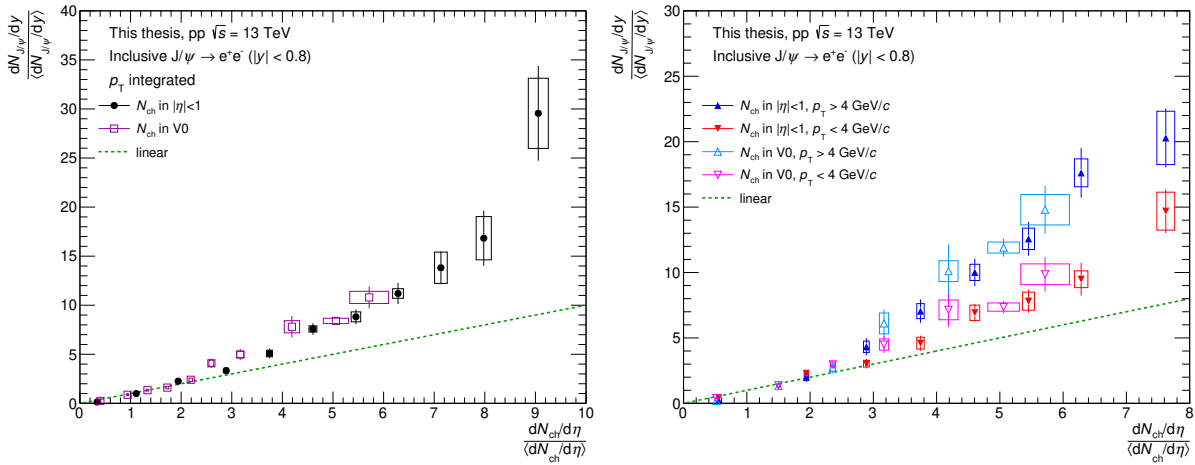


Figure 6.3.: Self-normalized inclusive J/ψ yield at mid-rapidity as a function of self-normalized charged-particle multiplicity at mid- and forward rapidity in pp collisions at $\sqrt{s} = 13$ TeV. Left: p_T -integrated results, right: results in p_T intervals.

In Fig. 6.3 the different multiplicity rapidities are compared, i.e. the self-normalized J/ψ yield is shown as a function of $n_{\text{ch, mid}}$ and of $n_{\text{ch, fwd}}$. On the left the p_{T} -integrated results are compared, on the right the ones p_{T} intervals. At high $n_{\text{ch, fwd}}$, the systematic uncertainty on the multiplicity is dominating over the uncertainty of the J/ψ yield. Within the uncertainties, the increase as a function of forward rapidity multiplicity is identical to the one as a function of mid-rapidity multiplicity.

6.2 Comparison to other experimental results

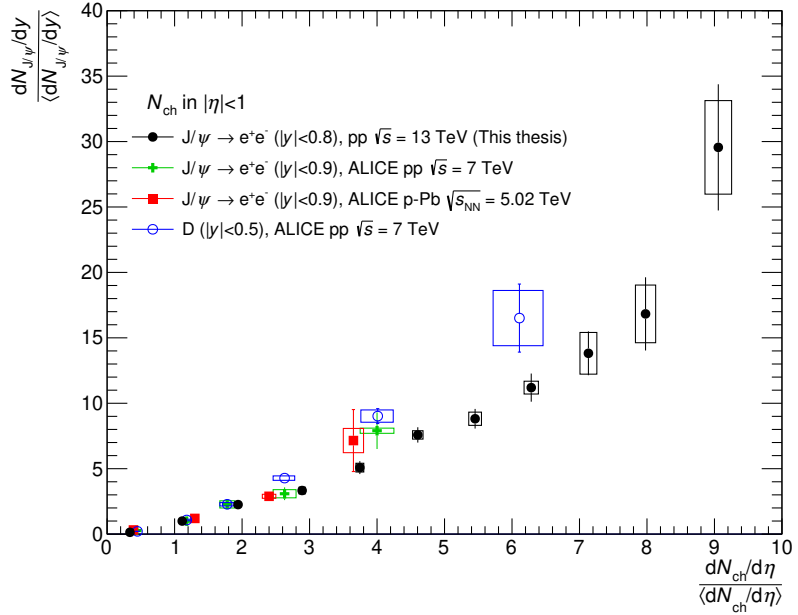


Figure 6.4.: Self-normalized inclusive J/ψ yield at mid-rapidity as a function of self-normalized charged-particle multiplicity at mid-rapidity in pp collisions at $\sqrt{s} = 13$ TeV, compared to self-normalized multiplicity-dependent ALICE results at lower collision energies: inclusive J/ψ production in $|y| < 0.9$ in pp collisions at $\sqrt{s} = 7$ TeV [121]; inclusive J/ψ production in $|y| < 0.9$ in p-Pb collisions at $\sqrt{s_{\text{NN}}} = 5.02$ TeV [122]; D-meson production in $|y| < 0.5$ in pp collisions at $\sqrt{s} = 7$ TeV [123].

In Fig. 6.4, the results of the presented analysis are compared to ALICE results at lower collision energies on heavy-flavor production as a function of mid-rapidity multiplicity. These are results on J/ψ production in pp collisions at $\sqrt{s} = 7$ TeV [121] and in p-Pb collisions at $\sqrt{s_{\text{NN}}} = 5.02$ TeV [122], as well as results on D-meson production in pp collisions at $\sqrt{s} = 7$ TeV [123]. The J/ψ results are for $|y| < 0.9$, the D-meson results for $|y| < 0.5$.

Within the uncertainties, the self-normalized multiplicity dependence of J/ψ production is independent of collision energy, and identical in pp and p-Pb collisions. For D-meson production, there is a hint of a stronger increase with multiplicity compared to J/ψ for $n_{\text{ch, mid}} \geq 2$. A possible interpretation can be that the charged-particle multiplicity in collisions that produce a D-meson is further enhanced by the D-meson itself. The heavy quark is always produced as a pair together with an antiquark. So, each D-meson will be produced with another open-charm hadron, which in turn will decay and enhance the charged-particle multiplicity. The second open charm hadron does not necessarily have to be produced at the same rapidity as the D-meson, so also the introduction of a rapidity gap between the signal and the multiplicity estimator will not fully remove this effect. An evaluation of these auto-correlation effects for the case of J/ψ production will be shown in chapter 7 with the PYTHIA event generator, with an emphasis on the case of non-prompt J/ψ , which is a proxy for open heavy-flavor production.

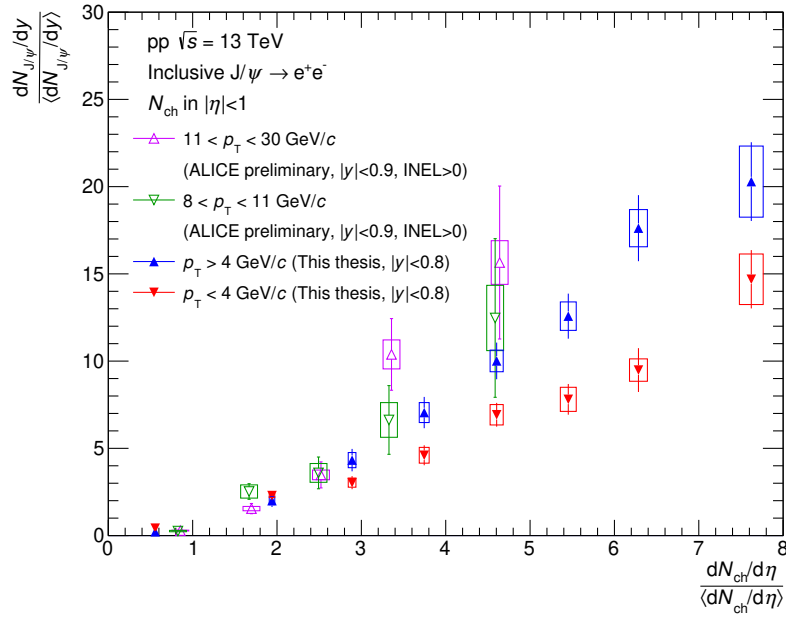


Figure 6.5.: Self-normalized inclusive J/ψ yield at mid-rapidity in transverse momentum intervals as a function of self-normalized charged-particle multiplicity at mid-rapidity in pp collisions at $\sqrt{s} = 13$ TeV. Results from this analysis are compared to results from preliminary ALICE results from an analysis at high p_T at the same collision energy [183].

In Fig. 6.5, the results of the presented analysis are compared to preliminary ALICE results [183] for inclusive J/ψ production at higher transverse momenta at the same collision energy. This analysis has been performed with the EMCal subdetector in the p_T intervals $8 < p_T < 11$ GeV/c and $11 < p_T < 30$ GeV/c. The J/ψ is measured in $|y| < 0.9$ in $INEL > 0$ events, i.e. only collisions are considered that produce at least one charged particle within $|\eta| < 1$. No uncertainties on the charged-particle multiplicity were calculated in this analysis, the horizontal width of the boxes indicating the systematic uncertainty is without meaning and just serves the purpose to make the uncertainty on the yield visible. There is a hint of a stronger increase with multiplicity at these higher p_T -values compared to the ones investigated in the presented analysis, supporting the observed trend of a stronger increase at higher p_T .

6.3 Interpretation

6.3.1 Linear increase with offset

A linear dependence of the self-normalized J/ψ yield on the charged-particle multiplicity in the strict sense, i.e. $n_{J/\psi} = n_{ch}$ can be excluded. However, it could still be that from a certain minimal multiplicity $n_{ch,min}$ onward the J/ψ yield grows linearly with multiplicity, with a slope m different from one.

The physical interpretation is that a pp collision is composed of an independent superposition of individual elementary processes in which both the J/ψ and the charged-particle multiplicity are produced, e.g. within the MPI picture. Both the probability to produce a J/ψ and the charged-particle multiplicity increase linearly with the number of these elementary processes.

The offset $n_{ch,min}$ is then caused by the fact that the J/ψ also influences the charged-particle multiplicity via its decay daughters, or via additional particles produced together with it. These additional particles shift the charged-particle multiplicity distribution to higher values in those collisions in which a J/ψ was produced, resulting in the offset $n_{ch,min}$. J/ψ production in events with lower multiplicity than $n_{ch,min}$ is caused by events in which the multiplicity fluctuates to lower-than-average values.

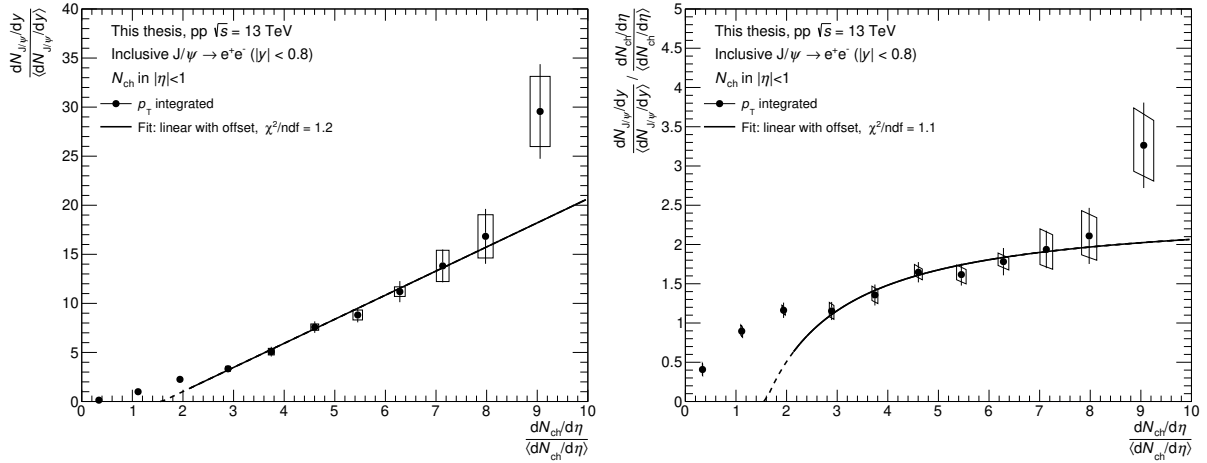


Figure 6.6.: Inclusive J/ψ production at mid-rapidity as a function of self-normalized charged-particle multiplicity at mid-rapidity in pp collisions at $\sqrt{s} = 13$ TeV, compared to linear increase with an offset. Left: self-normalized J/ψ yield, right: ratio of J/ψ yield and multiplicity.

In order to test this picture, a fit was performed to the increase of $n_{J/\psi}$ with n_{ch} in the region $n_{ch} > 2$ with the following formula:

$$n_{J/\psi}(n_{ch}) = m \cdot (n_{ch} - n_{ch,min}). \quad (6.1)$$

The resulting fitted function is shown as a line in Fig. 6.6 (left) together with the experimental data. The functional form is extended beyond the range of the fit towards lower multiplicities, indicated by the dashed line. As can be seen, in the range of the fit the experimental data is well described by the fit with a χ^2/ndf of 1.2. An exception is the point in the highest multiplicity interval, which is far above the fit, however the statistical significance of the deviation is low, about 1.5σ , when considering both the statistical and the systematic uncertainty.

The same fit can also be performed on the double ratio $r_{J/\psi}$. Because of the normalization to n_{ch} , the functional form becomes

$$r_{J/\psi}(n_{ch}) = m \cdot (1 - n_{ch,min}/n_{ch}). \quad (6.2)$$

The result of the fit is shown in Fig. 6.6 (right). The data points below $n_{ch,min}$ are not described by the fit, above they are in good agreement. The fits were performed also to the other results of the presented analysis, as well as the high- p_T data from the EMCAL-based analysis. The corresponding plots can be found in appendix C.

The resulting values of the fit parameters are shown in Fig. 6.7. No difference in the fit parameter values was observed between the fit to $n_{J/\psi}$ or $r_{J/\psi}$ as a function of n_{ch} . The error bars indicate the uncertainty of the fit parameters obtained from the fit, the boxes indicate the uncertainty from the systematic uncertainty of the charged-particle multiplicity. They were obtained in the following way: The experimental data points were shifted once towards lower multiplicities and once towards higher multiplicities by the amount of the systematic uncertainty. The fit was then performed on this shifted values, and the difference of the values of the fit parameters assigned as systematic uncertainty. In the bottom panel of Fig. 6.7 the χ^2/ndf values are shown. For the results in p_T intervals these are quite low, this is related to the fact that a low number of data points (6 for the results in p_T intervals from this analysis, and 3 for the ones from the EMCAL-based analysis) were fitted with two free parameters.

The offset parameter $n_{ch,min}$ has a value of around 1.5 and is independent of p_T for the analysis as a function of $n_{ch,mid}$. The values are similar between the results of this analysis and the EMCAL-based analysis. For the analysis as a function of $n_{ch,fwd}$, $n_{ch,min}$ increases slightly with p_T , starting at values around 0.8 for low p_T and reaching the same value as in the mid-rapidity case for high p_T .

The slope parameter m increases with transverse momentum. Its values from the fit to the analyses as a function of $n_{\text{ch, mid}}$ and $n_{\text{ch, fwd}}$ are in agreement with each other, with a hint of a stronger increase with p_T in the $n_{\text{ch, fwd}}$ case. The values from the EMCAL-based analysis have large uncertainties, but follow the same trend as the ones obtained in the presented analysis.

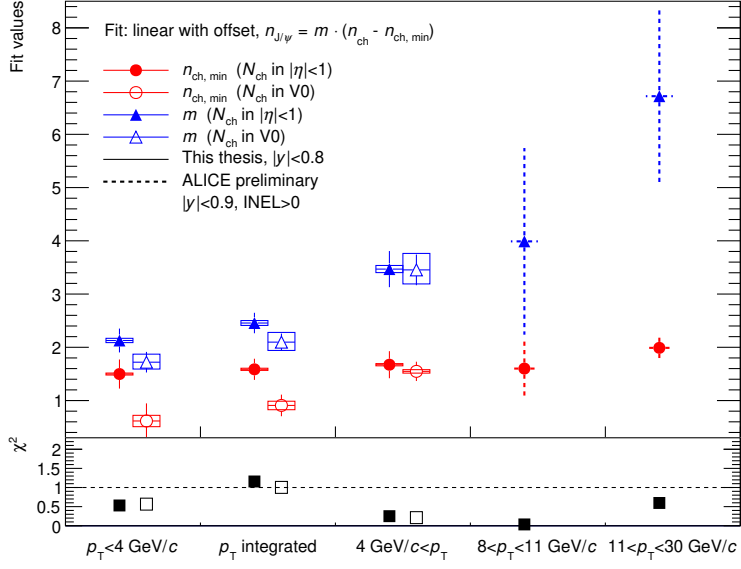


Figure 6.7.: Results of the fit of a linear function with an offset to the self-normalized J/ψ yield as function of the self-normalized charged-particle multiplicity.

6.3.2 Stronger-than-linear increase

Instead of interpreting the results as a linear increase of J/ψ production with the charged-particle multiplicity above a minimal multiplicity, one can assume a universal behavior that can be described with one function in the complete analyzed multiplicity region. One possible functional form is a polynomial with a linear term and a quadratic one. It can be parametrized as $n_{J/\psi}(n_{\text{ch}}) \propto \rho n_{\text{ch}}^2 + (1 - \rho)n_{\text{ch}}$ with $0 < \rho < 1$ quantifying the strength of the quadratic amount of the increase with multiplicity.

Another possibility is a powerlaw function of the form $n_{J/\psi}(n_{\text{ch}}) \propto x^\alpha$, with α a real number larger one. These functional forms can be used to describe the shape of the multiplicity dependence of J/ψ production, it remains an overall normalization factor. From the fact that both the J/ψ yield and the charged-particle multiplicity are normalized to their mean values, it can be argued that the normalization factor should not be too far away from unity, and be correlated with the average increase of the function.

To take this fact approximately into account, the functions were scaled with the value of their derivation at the mean multiplicity, so $dn_{J/\psi}/dn_{\text{ch}}(n_{\text{ch}} = 1) = 1 + \rho$ in the case of the polynomial function, and $dn_{J/\psi}/dn_{\text{ch}}(n_{\text{ch}} = 1) = \alpha$ in the case of the powerlaw function. An additional scaling parameter ν was introduced in the fitting function to correct for deviations from this estimate. The overall parametrizations for $n_{J/\psi}$ and $r_{J/\psi}$ then read for the polynomial function

$$n_{J/\psi}(n_{\text{ch}}) = \nu \frac{\rho n_{\text{ch}}^2 + (1 - \rho)n_{\text{ch}}}{1 + \rho}, \quad r_{J/\psi}(n_{\text{ch}}) = \nu \frac{\rho n_{\text{ch}} + (1 - \rho)}{1 + \rho}. \quad (6.3)$$

For the powerlaw function they read

$$n_{J/\psi}(n_{\text{ch}}) = \nu \frac{n_{\text{ch}}^\alpha}{\alpha}, \quad r_{J/\psi}(n_{\text{ch}}) = \nu \frac{n_{\text{ch}}^{\alpha-1}}{\alpha}. \quad (6.4)$$

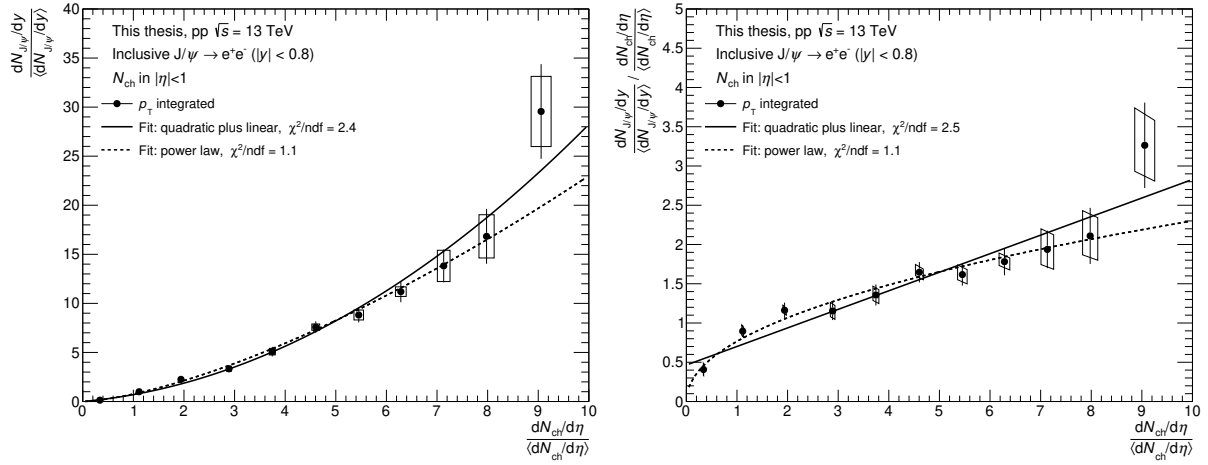


Figure 6.8.: Inclusive J/ψ production as a function of self-normalized charged-particle multiplicity at mid-rapidity in pp collisions at $\sqrt{s} = 13$ TeV, compared to a polynomial fit (solid line), and a powerlaw fit (dashed line). Left: self-normalized J/ψ yield, right: ratio of J/ψ yield and multiplicity.

In Fig. 6.8 (left) the p_T -integrated $n_{J/\psi}$ as a function of $n_{ch, \text{mid}}$ is fitted by the two functions. Both functions describe the experimental data well. At high multiplicities, the powerlaw function is closer to the data, with the exception of the data point in the highest multiplicity interval, to which the polynomial function is closer. The χ^2/ndf of the powerlaw function is with 0.9 better than the one of the polynomial function, which has a value of 2.2.

In Fig. 6.8 (right) the fits are compared to the p_T -integrated $r_{J/\psi, \text{mid}}$ as a function of $n_{ch, \text{mid}}$. In this representation it becomes apparent that the powerlaw function provides a better description of the experimental data. The polynomial function seems to systematically underpredict the data at low multiplicities, and overpredict the data at high multiplicities. The powerlaw function is in very good agreement with the experimental data in the whole multiplicity region. An exception is again the data point in the highest multiplicity interval, with which the polynomial function is in better agreement.

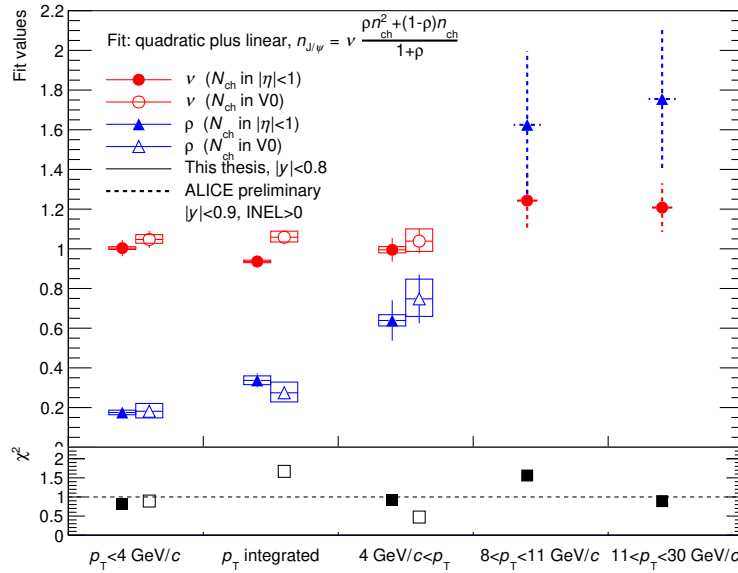


Figure 6.9.: Results of the fit of a polynomial function to the self-normalized J/ψ yield as a function of the self-normalized charged-particle multiplicity.

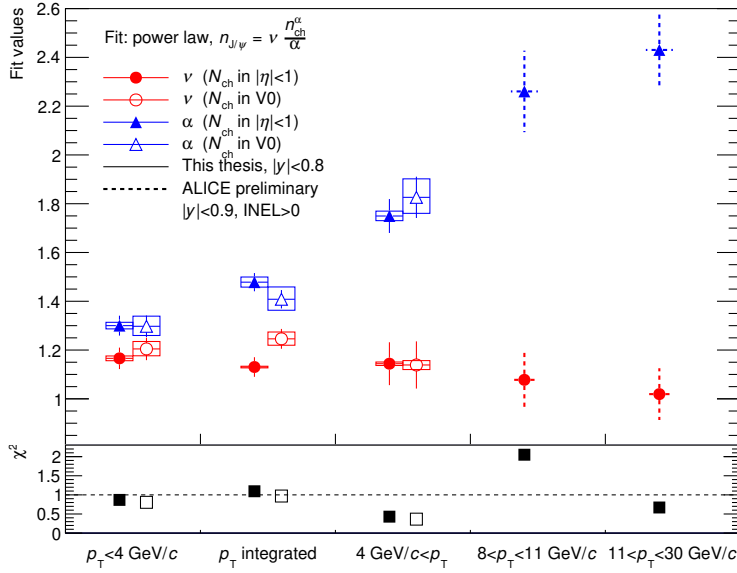


Figure 6.10.: Results of the fit of a powerlaw function to the self-normalized J/ψ yield as a function of the self-normalized charged-particle multiplicity.

The fits were performed also for the results in p_T intervals, as well as the results as function of $n_{ch,fwd.}$, and the results from the EMCAL-based analysis. In all cases, a good description of the experimental data is obtained. The corresponding plots can be found in appendix C.

The obtained values of the fit parameters are shown in Fig. 6.9 for the polynomial function and in Fig. 6.10 for the powerlaw function. For the systematic uncertainty, the data points at $n_{ch} < 2$ were shifted once towards lower multiplicities and once towards higher multiplicities by the amount of the systematic uncertainty, and the data points at $n_{ch} > 2$ correspondingly in the other direction. The χ^2/ndf values of the fits are shown in the bottom of the figures, they are scattered around 1.

The values of the normalization parameters v are close to unity and within uncertainties independent of p_T for the results of the presented analysis. There is a hint that they are overall slightly larger for the results obtained as function of $n_{ch,fwd.}$ than the ones as function of $n_{ch,mid.}$ For the results from the EMCAL-based analysis there is a hint of slightly higher values in case of the polynomial function and slightly lower values in case of the powerlaw function. It has to be kept in mind that these results are normalized to a different event class.

The values of the ρ and α parameters grow with increasing p_T and are compatible between the results as a function of $n_{ch,mid.}$ and $n_{ch,fwd.}$.

For the high- p_T data of the presented analysis, the value of the ρ parameter is close to one, and of the α parameter slightly below two. Both these values indicate that there is an almost quadratic increase of J/ψ production with charged-particle multiplicity.

For the EMCAL-based analysis, the value of the α parameter further increases to 2.4 for the highest p_T interval, indicating an even stronger than quadratic increase with multiplicity. Correspondingly, the ρ parameter in the polynomial function rises above one — yet with large uncertainties. This indicates that the assumed behavior of a linear part of the increase with multiplicity and a quadratic part is not adequate at this high transverse momentum, as the prefactor of the linear part becomes negative in this case.

6.3.3 Comparison to predictions from the PYTHIA8 event generator

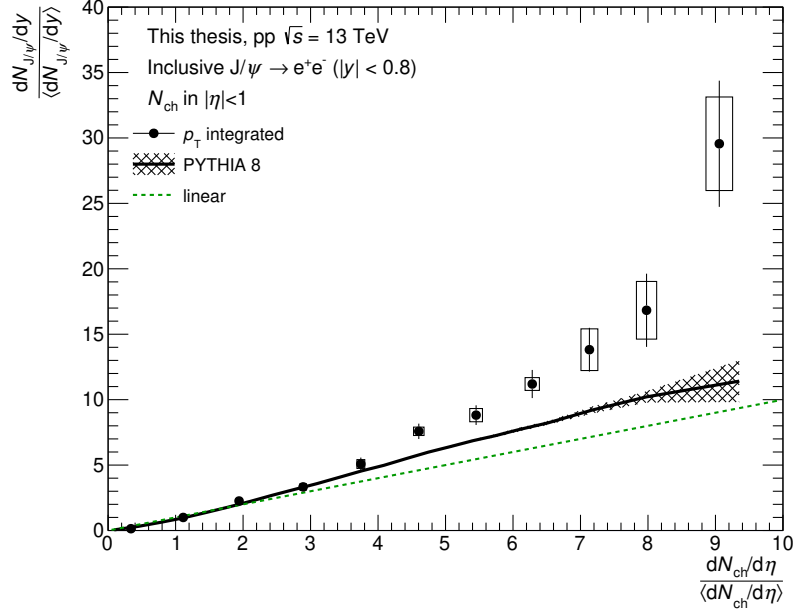


Figure 6.11.: Self-normalized inclusive J/ψ yield at mid-rapidity as a function of self-normalized charged-particle multiplicity at mid-rapidity in pp collisions at $\sqrt{s} = 13$ TeV, compared to prediction from the PYTHIA8 event generator.

For this thesis simulations were performed with the PYTHIA8 event generator to obtain predictions of the self-normalized J/ψ yield as a function of the charged-particle multiplicity. As in the experimental analysis, both prompt and non-prompt J/ψ was included in the simulation and the influence of those contributions was studied separately. Additionally physical mechanisms such as multiparton interaction and color reconnection were studied, as well as auto-correlation effects. The detailed results of these simulations will be presented in chapter 7, here only the comparison of the prediction with the experimental data will be shown.

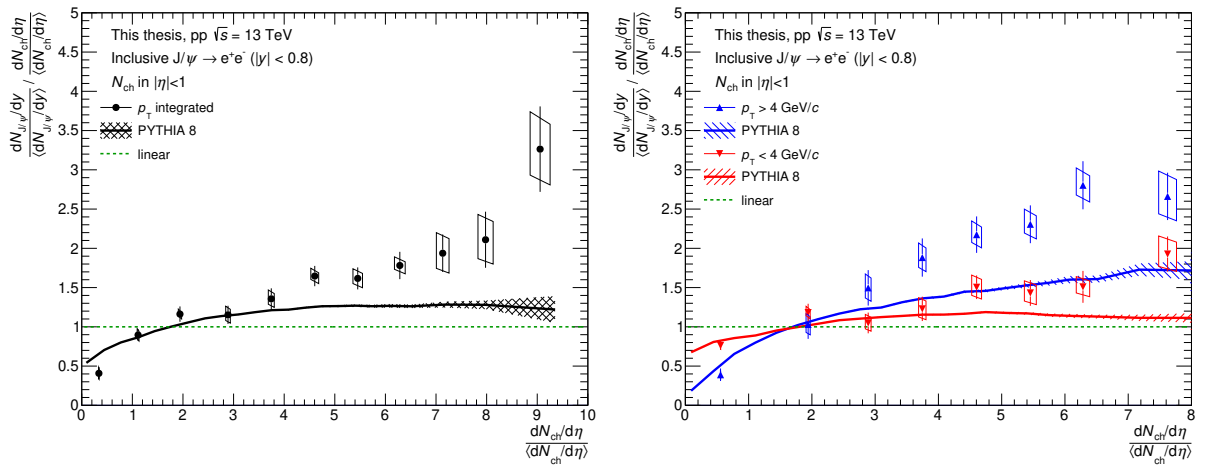


Figure 6.12.: Inclusive J/ψ production at mid-rapidity as a function of self-normalized charged-particle multiplicity at mid-rapidity in pp collisions at $\sqrt{s} = 13$ TeV, compared to prediction from the PYTHIA8 event generator. Left: self-normalized J/ψ yield, right: ratio of J/ψ yield and multiplicity.

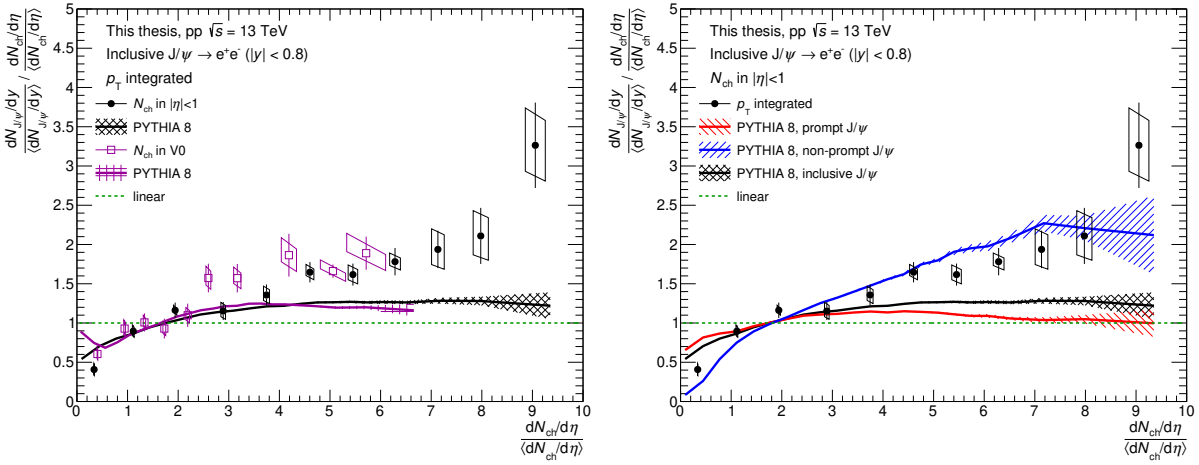


Figure 6.13.: Ratio between inclusive J/ψ yield and multiplicity as a function of the self-normalized charged-particle multiplicity compared to predictions from PYTHIA8 event generator. Left: comparison between multiplicity at mid and forward rapidity. Right: PYTHIA8 predictions for prompt and non-prompt J/ψ separately.

In Fig. 6.11, $n_{J/\psi}$ as a function of $n_{ch, \text{mid}}$ is compared to the prediction from the PYTHIA8 event generator. The error band of the PYTHIA8 prediction does not represent an uncertainty of the model, but denotes the statistical uncertainty of the generated Monte Carlo sample. From relative multiplicities of 4 onwards, the PYTHIA8 prediction largely underpredicts the experimental data. Qualitatively the predictions are in agreement with the experimental data, i.e. a stronger than linear increase of J/ψ production with multiplicity is reproduced.

In Fig. 6.12 (left) the prediction on $r_{J/\psi, \text{mid}}$ is compared to the experimental data. This is to show that the PYTHIA8 prediction is essentially a linear increase at high multiplicities, manifest by a constant value of the double ratio. As was demonstrated before, the experimental data at high multiplicity can be described with this functional form, though with a higher slope than predicted by PYTHIA8. The PYTHIA8 predictions for the different transverse momentum intervals are shown in Fig. 6.12 (right). As in data, the increase is stronger for J/ψ at higher p_T , but for $n_{ch} \geq 4$ (for the low- p_T interval) and $n_{ch} \geq 3$ (for the high- p_T interval), the PYTHIA8 model clearly underpredicts the data.

The predictions for the different multiplicity estimators are shown in Fig. 6.13 (left). As in data, the two cases are very similar to each other within the statistical uncertainties.

Fig. 6.13 (right) $r_{J/\psi, \text{mid}}$ as a function of $n_{ch, \text{mid}}$ is compared to predictions from the PYTHIA8 model for prompt and non-prompt J/ψ separately. The non-prompt J/ψ yield shows a stronger increase with multiplicity than the prompt J/ψ one. The former is actually in agreement with the experimental data on inclusive J/ψ . The increase of the latter is only weakly stronger than linear. The slope of the increase of prompt J/ψ actually gets lower at higher multiplicities, resulting in a slightly decreasing double ratio from $n_{ch} = 5$ onwards. A separate experimental measurement of the multiplicity dependence of prompt and non-prompt J/ψ is clearly called for in order to test these expectations from the model.

6.3.4 Comparisons to theoretical model predictions

Theoretical model predictions for the self-normalized J/ψ yield as a function of the self-normalized charged-particle multiplicity have been provided by several authors. In Fig. 6.14, the experimental data is compared to prediction from the percolation model [128, 185], the model involving higher Fock-states [130, 184], the model including the CGC effective field theory [131], and to a prediction from the EPOS3 event generator [133, 186]. For details on the models cf. section 2.2. Overall, all models provide a decent description of the data. The percolation model is in good agreement with the data in the highest

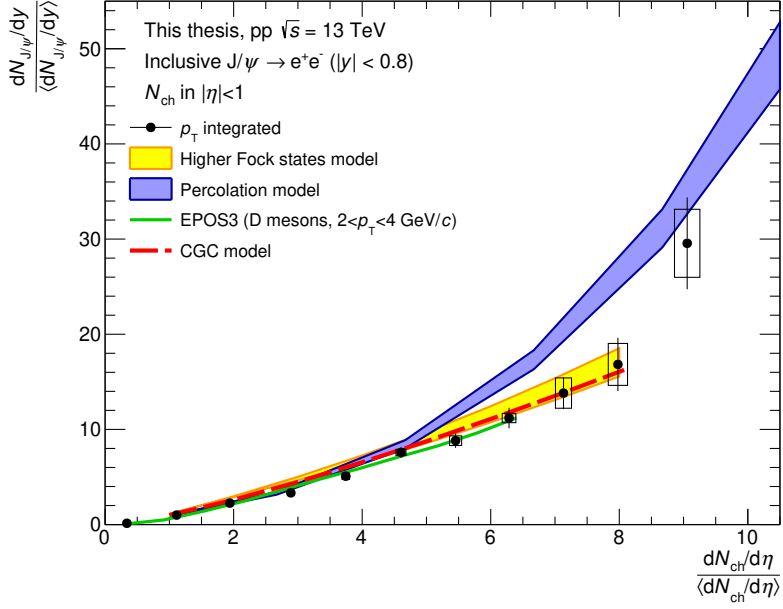


Figure 6.14.: Self-normalized inclusive J/ψ yield at mid-rapidity as a function of self-normalized charged-particle multiplicity at mid-rapidity in pp collisions at $\sqrt{s} = 13$ TeV, compared to theoretical model predictions by the higher-Fock-states model [130, 184], the percolation model [128, 185], the EPOS3 event generator [133, 186], and the CGC-based model [131].

multiplicity interval, but overpredicts the data at lower multiplicities. The other model predictions are in good agreement with the data, though they do not reach the multiplicity of the highest data point.

The prediction based on the EPOS3 event generator was performed not for J/ψ particles, but for D-mesons in the transverse momentum interval $2 < p_T < 4$ GeV/c. These prediction should to a reasonable degree be valid for J/ψ particles at a similar transverse momentum [186]. The p_T interval of the prediction was thus chosen in such a way that the mean p_T is in rough agreement with the mean p_T of J/ψ in pp collisions. In Fig. 6.15 the model prediction is divided by $n_{ch, \text{mid}}$ to give a prediction for $r_{J/\psi, \text{mid}}$. In the whole multiplicity range where the model makes a prediction, it shows a very good agreement with the experimental data.

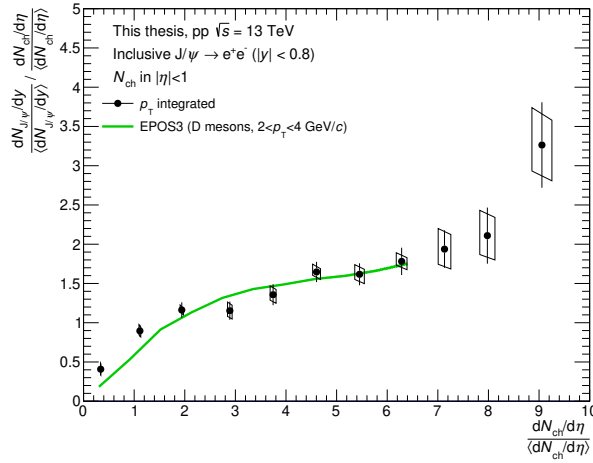


Figure 6.15.: Ratio of J/ψ yield and multiplicity as a function of self-normalized charged-particle multiplicity at mid-rapidity in pp collisions at $\sqrt{s} = 13$ TeV, compared to predictions from the EPOS3 event generator for D-mesons with $2 < p_T < 4$ GeV/c.

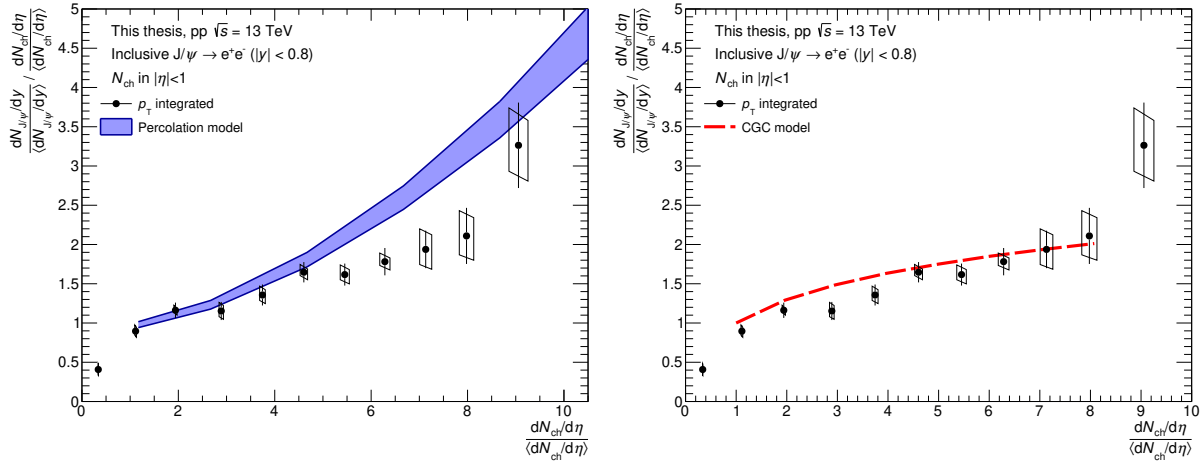


Figure 6.16.: Ratio of J/ψ yield and multiplicity as a function of self-normalized charged-particle multiplicity at mid-rapidity in pp collisions at $\sqrt{s} = 13$ TeV, compared to predictions from the percolation model (left) and the CGC-based model (right).

In Fig. 6.16 (left), the percolation model was similarly scaled by $n_{\text{ch},\text{mid}}$ to obtain a prediction for the $r_{J/\psi, \text{mid}}$. The upper edge of the error band corresponds to the default version of the model, as discussed in [128], the lower edge includes an additional QGP inspired suppression mechanism [185]. In the intermediate multiplicity region $1 < n_{\text{ch},\text{mid}} < 5$, the model agrees well with the experimental data, likewise for the data in the highest multiplicity interval. In the multiplicity intervals in between it overpredicts the data. Overall, the inclusion of the QGP like effects improves the agreement with the experimental data.

In Fig. 6.16 (right), the CGC-based model prediction is divided by $n_{\text{ch},\text{mid}}$ and compared to the experimental data on $r_{J/\psi, \text{mid}}$. In the range of the model it describes the data well.

The predictions from the higher-Fock-states model [130] were updated [184] to include saturation effects on the gluon distributions. The new model predictions are compared to the experimental data in Fig. 6.17 for the p_T -integrated results on the left and in p_T intervals on the right.

The error band in the p_T -integrated prediction represents the uncertainty on the α value of the model (cf. section 2.2.2). The upper edge of the error band corresponds to the default value $\alpha = 0.98$, while the lower edge corresponds to $\alpha = 0.95$. For the prediction in p_T intervals, the default value was chosen.

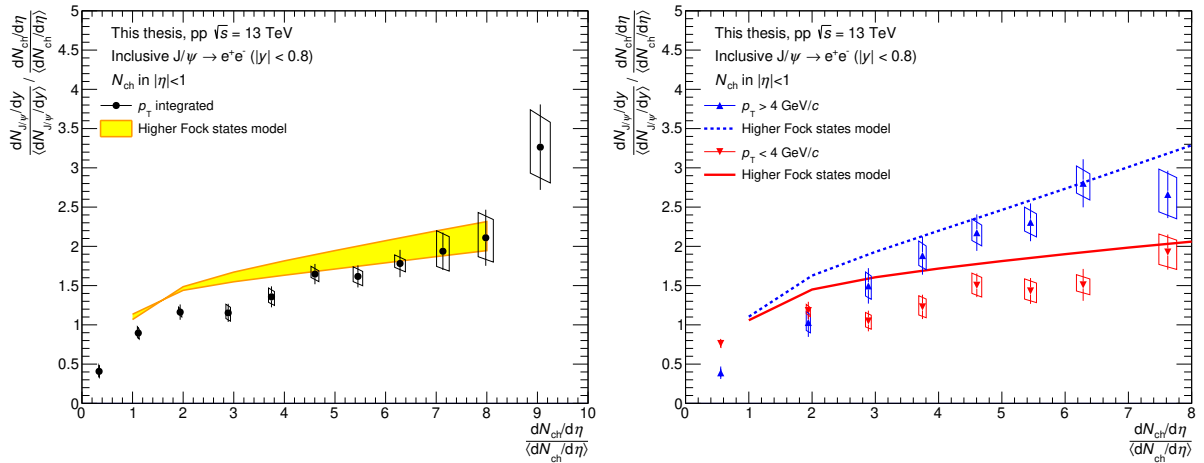


Figure 6.17.: Ratio of J/ψ yield and multiplicity as a function of charged-particle multiplicity at mid-rapidity in pp collisions at $\sqrt{s} = 13$ TeV, compared to predictions from the higher-Fock-states model. Left: p_T -integrated results, right: results in p_T intervals.

The high- p_T prediction is for a p_T interval $4 < p_T < 8 \text{ GeV}/c$, whereas the data are for $4 \text{ GeV}/c < p_T$. The difference should be negligible however, due to the much lower total yield of J/ψ production at this high p_T -values. Starting from multiplicities of around $4 n_{\text{ch}}$, the model is in good agreement with the experimental data, whereas it slightly overpredicts the data at lower multiplicities. Overall, the lower edge of the error band, corresponding to the lower α value is in better agreement with the experimental data.

6.4 Summary

Summarizing, it can be stated that the presented analysis shows a clearly stronger than linear increase of inclusive J/ψ production at mid-rapidity with the charged-particle multiplicity. The result is independent on the rapidity region where the charged-particle multiplicity was measured. The increase is stronger for J/ψ at higher transverse momentum. The results from the EMCal-based analysis support this observation. The data can be interpreted both as a linear increase of J/ψ production with charged-particle multiplicity with an offset, or as a stronger than linear increase with charged-particle multiplicity. In the latter case, the increase can be parametrized with a polynomial or a powerlaw function. The different theoretical model predictions provide a reasonable or good description of the experimental data. The PYTHIA8 event generator, though reproducing qualitatively the mentioned features, fails to quantitatively describe the data. A clearly different multiplicity dependence of prompt and non-prompt J/ψ is predicted, which remains to be experimentally tested. A hint of a stronger increase of open-heavy-flavor hadrons can be obtained from the experimental results on D-meson production as a function of charged-particle multiplicity in pp collisions at $\sqrt{s} = 7 \text{ TeV}$ [123].



7 PYTHIA8 study

In this chapter a study of multiplicity dependent J/ψ production within the PYTHIA8 [178] model will be presented. The main components of the model will be described briefly in the following with emphasis on aspects relevant for the presented study. The results for the multiplicity dependence of J/ψ production and the different phenomena which cause it will be discussed afterwards.

7.1 The PYTHIA event generator

PYTHIA is a QCD inspired event generator for collisions of protons, leptons and nuclei. It has a complex physics model with a multitude of different processes implemented at different stages of the collision. Fig. 7.1 gives an impression of its complexity by sketching the physics mechanisms at play in one proton-proton collision. The main components of a proton-proton collision – with a focus on their relevance for the presented analysis – will be described briefly in the following.

An in-depth description of the physics implemented in the PYTHIA model is given in [187] for version 6 of the model. Recent changes in the new version 8 are summarized in [178].

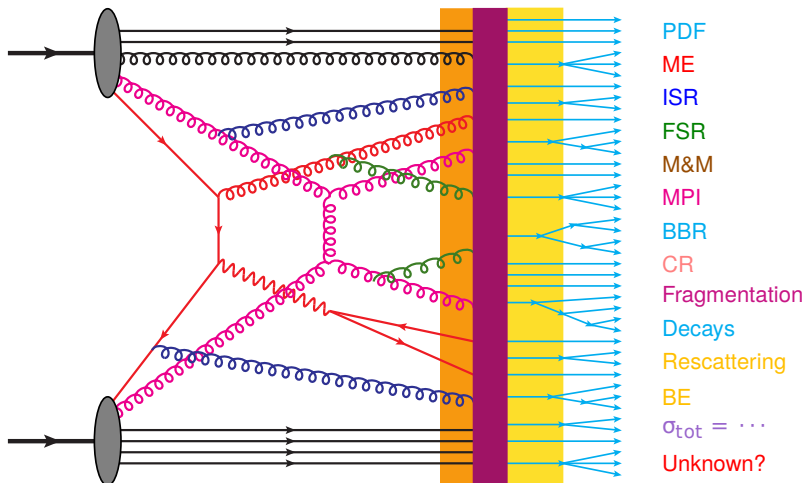


Figure 7.1.: Schematic picture of a proton-proton collision in PYTHIA. Figure taken from [188].

- **Partonic scattering:** Each non-diffractive proton-proton collision contains (at least) one interaction between two partons, one from each of the two beams. The partons can either be the valence quarks of the incoming protons, gluons, or sea quarks. Strong and electroweak processes are implemented in terms of matrix elements for the transition of an initial to a final state. Typically, high p_T partons are produced in such scatterings, which then further evolve into jets. Also heavy quark-antiquark pairs can be created, as well as quarkonium states [189], according to the NRQCD formalism (compare section 1.6.2). More details will be given in section 7.4.
- **Parton showers** [191]: The partonic interactions are accompanied by space-like Initial State Radiation (ISR) and time-like Final-State Radiation (FSR). Gluons emitted in ISR, FSR, or gluons produced in partonic scattering processes can split into heavy flavor quark-antiquark pairs, giving another source of heavy flavor production in PYTHIA. For these processes, also the QED analog exists, i.e. a photon splitting into a heavy quark-antiquark pair, albeit with a much smaller cross section.

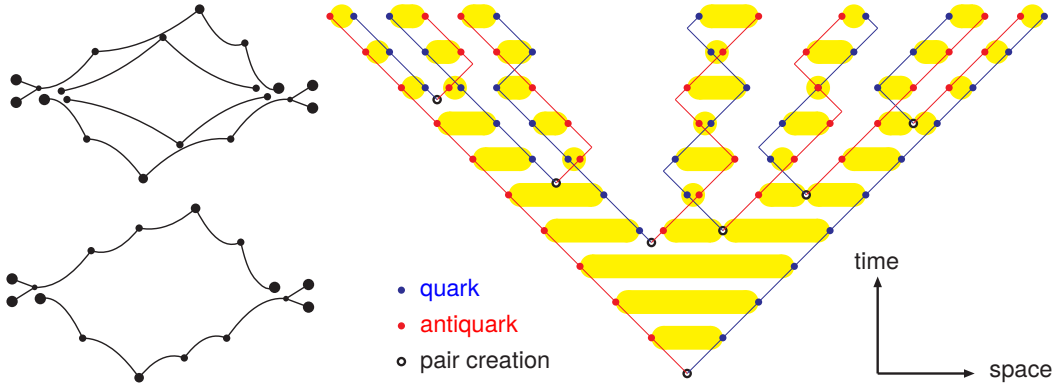


Figure 7.2.: Important components of the PYTHIA model. Left: Color Reconnection (CR): Reduction of the total string length by recombining strings from different MPI. The dots represent outgoing partons after the collisions, the lines the strings connecting them. Top: string topology before CR, bottom: after CR. Figure taken from [190]. Right: Lund string fragmentation: the hadronization mechanism of PYTHIA based on iterative breaking of color strings spanned between partons. Figure taken from [188].

- **MultiParton Interactions (MPI)** [192]: Within one proton-proton collision, not only one partonic interaction (PI) can occur, but multiple. A typical event at LHC energies contains roughly between four and ten interactions [193]. In PYTHIA, the individual interactions are ordered by transverse momentum in descending order until a lower cutoff p_T is reached. They are treated identically, so heavy quark and quarkonium production can happen in any of them.
- **Beam remnants** [193]: After one or more partons of the incoming beams undergo interactions, the remaining ones in the beam remain in a colored state. The beam remnant partons are the remaining valence quarks that did not interact yet, and so-called companion quarks, i.e. for each sea quark (antiquark) that entered an interaction a corresponding quark (antiquark) of the same flavor remains in the beam to preserve the flavor content; these can also be heavy quarks. The beam remnants may form composite color-singlet objects, or serve as endpoints to strings in the string fragmentation process, as discussed below.
- **Color Reconnection (CR)** [194]: The created partons are connected via strings, i.e. Lorentz-invariant descriptions of the linear confinement potential. Each string has a color charge (quark) at one end and the corresponding anti-color charge (antiquark) at the other end. Diquarks are treated similarly to antiquarks. Gluons have both color and anti-color charge, so they correspond to kinks in the strings. Without CR, partons keep the color connections as they were established during their productions, this means that partons from different PI are not directly connected to each other. With CR, strings can be rearranged between partons so as to reduce the total string length. The process is illustrated in Fig. 7.2 (left). The reduction of the total string length leads to a reduction of the total multiplicity, since the bulk of particles are produced from the string breaking mechanism as will be explained in the next bullet. Different models of CR are implemented in PYTHIA, as it is a theoretically not well established effect on the border between perturbative and nonperturbative QCD. In the default implementation of color reconnection, lower p_T PI are merged with higher p_T ones.
- **Hadronization** is implemented according to the Lund String fragmentation model [195]. As quarks and antiquarks move apart, the potential energy stored in the string connecting them increases linearly due to the confining force. Once the energy stored is large enough, the string breaks, producing a quark-antiquark pair. The system then contains two quark-antiquark pairs connected by a shorter string each. If one of the strings contains enough energy, the process re-

peats itself, until small enough pieces of string remain, which are then identified with on-shell hadrons. Since diquarks are treated the same as antiquarks this mechanism also produces baryons. A schematic depiction of the process is given in Fig. 7.2 (right).

Heavy-quark production in string breaking is strongly suppressed ($u : d : s : c \approx 1 : 1 : 0.3 : 10^{-11}$) due to their large mass and thus large energy required to be stored in the string. That's why this mechanism can safely be neglected and is not implemented in the PYTHIA model. However, quarkonia can also be created at this stage, namely when a heavy quark and corresponding anti-quark, which were produced earlier in the collision – by any of the aforementioned mechanisms – are connected by a exceptionally short string. It can then happen that the potential energy stored in the string is too low to produce quark-antiquark pairs, so the usual iterative string fragmentation scheme is not applicable. Instead the heavy quark and antiquark then collapse directly into a hadron, producing a quarkonium state. This process is called cluster collapse [196].

- **Decays:** Unstable particles decay further, according to the known branching ratios [1]. In particular, non-prompt J/ψ and ψ' from feed-down from higher charmonia states are created here.
- **Diffraction** [197]: Besides non-diffractive collisions, also single, double and central diffraction is included in PYTHIA. Diffractive collisions are treated as collision between a proton and a pomeron (implemented as a color singlet group of gluons). The subsequent evolution is then – provided that the diffractive mass is sufficient – similar to a non-diffractive collisions, including MPI, ISR and FSR.

The various components in PYTHIA are governed by a multitude of parameters, which can be determined by comparison to data. Typically, parameters are not modified individually, but sets of parameters are used, so-called tunes, which typically attempt to simultaneously describe many observables for a given collision energy, or even for different energies. The default tune of PYTHIA8 is the Monash 2013 tune [198]. Minimum bias, Drell-Yan and underlying-event data from the LHC were used to constrain initial-state radiation and MPI parameters. SPS and Tevatron data were used to constrain energy scaling.

7.2 Technicalities

PYTHIA version 8.230 [26] was used with the default Monash 2013 tune.

For the results presented in this chapter however, only non-diffractive events were considered requirement. The overall physics picture does not change by exclusion of diffractive events, but some arguments become more clear with this more natural event selection. For the comparison to experimental data, as presented in chapter 6, inelastic events were simulated, i.e. including also diffractive processes.

Multiplicity is defined as the number of primary charged particles, according to the ALICE definition [199]. The dependence of J/ψ production on the multiplicity at mid-rapidity ($|\eta| < 1$) was investigated, as well as at forward rapidity, i.e. at the pseudo-rapidity of the V0 detectors ($2.8 < \eta < 5.1$ and $-3.7 < \eta < -1.7$).

In the default settings, MPI and CR are part of the model. To demonstrate their influence on the on the described observations, they were for comparison turned off, without retuning of the other parameters of the model. It has to be kept in mind that in these cases the simulation does not provide a realistic description of proton-proton collisions anymore, for example the charged-particle multiplicity as measured in experimental data is not reproduced by PYTHIA8 with these settings.

7.3 Charged-particle multiplicity

The probability distributions for the charged-particle density at mid-rapidity of diffractive and non-diffractive events are shown in Fig. 7.3 for the full simulation, for CR switched off, and for MPI switched

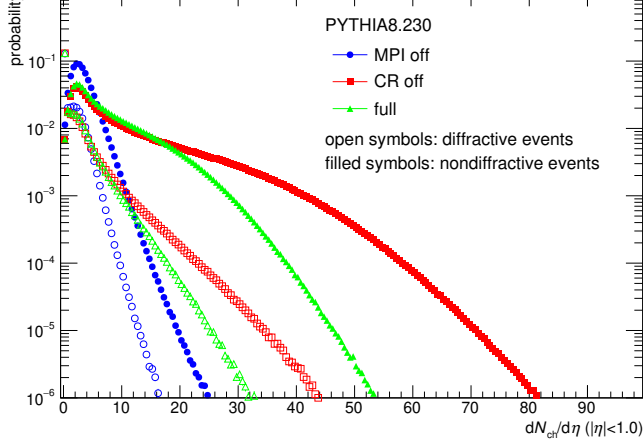


Figure 7.3.: Charged-particle multiplicities for inelastic pp collisions at $\sqrt{s} = 13$ TeV in PYTHIA8 with default settings, CR off, and MPI off. Left: probability distributions, right: mean values and RMS of the distributions.

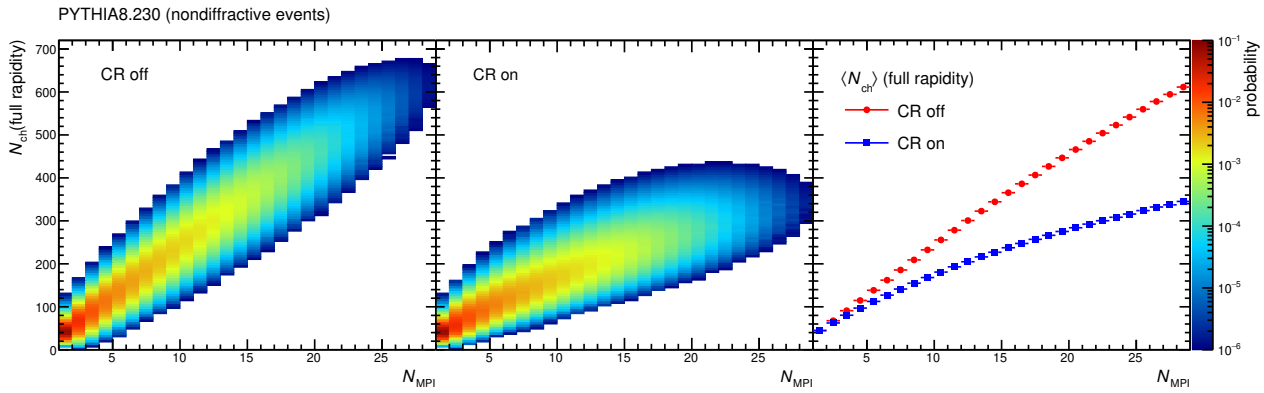


Figure 7.4.: Correlation between the number of PI and charged-particle multiplicity in PYTHIA8, without (left) and with CR (middle). Right: mean multiplicity as a function of the number of PI for both cases.

off. The table gives the mean values and the RMS for all inelastic events. As can be seen, the inclusion of MPI increases the multiplicity by more than a factor 2 and the distribution becomes much wider. The color reconnection mechanism reduced the multiplicity again by about 30 % and also makes the distribution narrower. From earlier experiments it is known that the full simulation including MPI and CR reproduces the measured charged-particle multiplicity distribution reasonably well [34, 35]. The table in 7.3 also gives the mean value and width of the total charged-particle multiplicity in the full phase space. It shows that the mentioned enhancement and reduction of multiplicity with MPI and CR affects the total multiplicity in a similar way as at mid-rapidity.

As explained, without the CR mechanism the individual PIs are independent of each other, thus the total charged-particle multiplicity N_{ch} increases roughly linearly with the number of PI per collision N_{MPI} as shown in Fig. 7.4 (left), which shows the two-dimensional probability distribution of events with a certain N_{ch} and N_{MPI} . In the right panel of the figure the mean value of N_{ch} is shown as a function of N_{MPI} . In fact, the increase is a bit weaker than linear without CR, since the total momentum transfer that is possible in one proton-proton collision is limited, such that for a higher number of PI the individual PIs are on average softer and produce less particles.

As can be seen from Fig. 7.4 (middle) and (right), with CR the charged-particle multiplicity distribution for a given N_{MPI} gets wider and the mean grows slower with N_{MPI} .

7.4 Heavy quark and quarkonium production in PYTHIA8

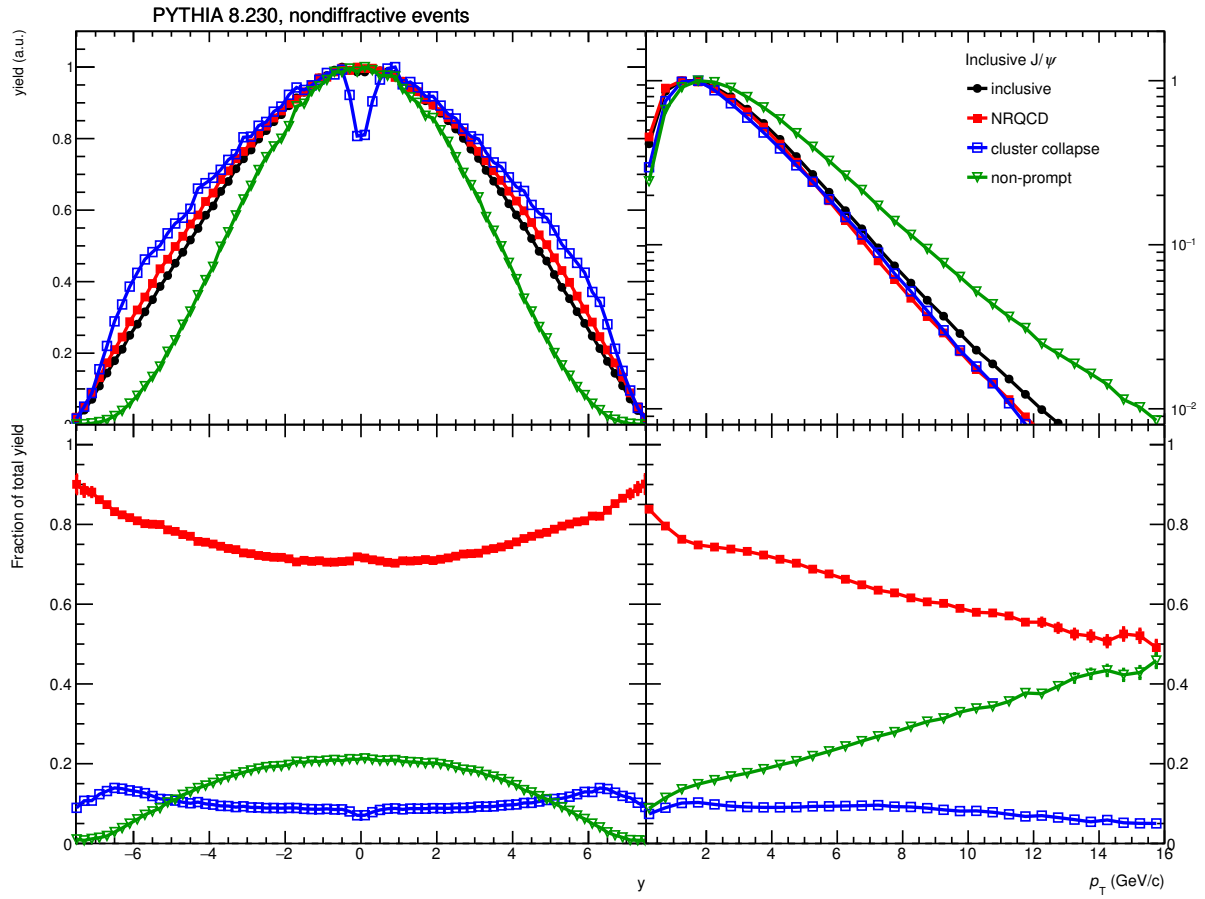


Figure 7.5.: Top: Rapidity and transverse momentum distribution of inclusive J/ψ production in PYTHIA8, split in different production mechanisms. Bottom: Relative contribution to the total yield as a function of rapidity and transverse momentum.

Heavy quarks can be produced in PYTHIA in hard scattering processes according to pQCD matrix elements, can be formed from a gluon that splits into a heavy quark pair, or they can come as a companion quark to a heavy sea quark that entered a hard scattering process. Relevant pQCD mechanisms are gluon-fusion $gg \rightarrow Q\bar{Q}$ (Q either charm or bottom) or light quark-antiquark annihilation $q\bar{q} \rightarrow Q\bar{Q}$. In combination with the parton shower mechanism more complex topologies like flavor excitation are possible.

Quarkonia production can happen either via an NRQCD process in the hard scattering, via the binding of a heavy quark and an heavy antiquark at hadronization ("cluster collapse"), or in case of charmonium via the weak decay of a beauty hadron. In about 95 % of all cases this is a B meson (e.g. $B^+ \rightarrow J/\psi K^+$), in the others it is a beauty baryon, such as Λ_b .

For the NRQCD part, leading order processes are implemented in PYTHIA8. The pre-resonant states can be in color-singlet or color-octet states with different quantum numbers. The mass of the color-octet state is set to the mass of the corresponding physical color-singlet state to which it will decay plus a fixed singlet-octet mass splitting parameter, which by default is $200 \text{ MeV}/c^2$. The color-octet state then decays to the color-singlet state by radiating off a gluon. Production of quarkonia is implemented in the $2S+1L_J$ -states 3S_1 (ψ , Υ), 3P_J (χ_c , χ_b) and 3D_J ($\psi(3370)$). The processes are of the form: $g g \rightarrow [Q\bar{Q}]g$ (gluon-fusion), $g q \rightarrow [Q\bar{Q}]q$ (gluon splitting) or $q\bar{q} \rightarrow [Q\bar{Q}]g$ (quark-antiquark annihilation) ($[Q\bar{Q}]$ denotes the pre-resonant quarkonium state). At LHC energies at mid-rapidity the gluon-fusion processes

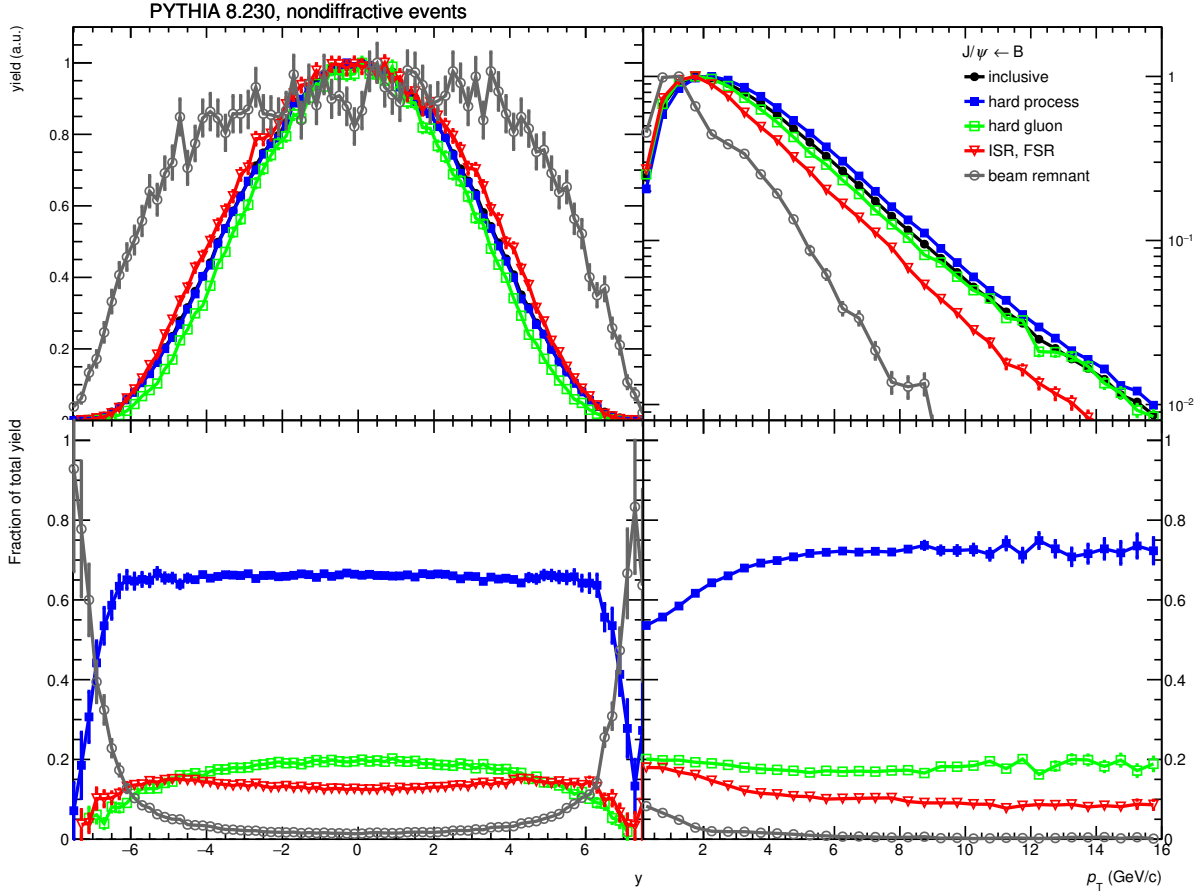


Figure 7.6.: Top: Rapidity and transverse momentum distribution of J/ψ production from a B decay in PYTHIA8, split in different production mechanisms of the initial b quark. Bottom: Relative contribution to the total yield as a function of rapidity and transverse momentum.

are dominating because of the high gluon density. The higher-mass charmonium states can decay later to J/ψ (e.g. $\psi(2S) \rightarrow J/\psi \pi\pi$) at the hadronic decay stage of the simulation.

For quarkonium production from cluster collapse it has to be noted that only the lowest-mass quarkonium states, i.e. η_c , J/ψ , (or η_b and $\Upsilon(1S)$ in the case of bottomonium) can be produced. The heavy quark and antiquark can have been produced in the same process or in different ones; with the CR mechanism it is also possible that a heavy quark from one PI binds with a heavy antiquark from another PI.

Fig. 7.5 shows for the different sources of J/ψ production the rapidity and transverse-momentum distributions, and the relative contribution to the total J/ψ yield as a function of rapidity and p_T . The distributions are normalized in such a way that the maximum is at one, so that differences in the shapes are best visible. Non-prompt J/ψ production has a harder p_T spectrum than prompt J/ψ . The relative contribution rises from around 10 % at zero p_T to over 40 % at $p_T = 16$ GeV/c. This is in agreement with experiment, see e.g. [200].

Prompt J/ψ from NRQCD or from cluster collapse have a similar p_T distributions. The cluster collapse component has a dip at mid-rapidity, the reason for which is still to be understood. In total it amounts to about 10 % of the J/ψ yield.

Non-prompt J/ψ are mostly J/ψ from the decay of a B meson. For this case the origin of the initial b quark was investigated. This is shown in Fig. 7.6, which depicts the rapidity and transverse-momentum distributions of J/ψ from B for the different sources of b quark production.

About 65 % of all b quarks were produced in a hard scattering process, about 20 % in the splitting of a gluon, which was in turn produced in a hard scattering, and the remaining 15 % in the splitting of a gluon from initial or final-state radiation. In the latter case, the p_T distribution is a bit softer than in the cases where a hard scattering is involved. The contribution of b quarks from the beam remnant is negligible at mid-rapidity and only relevant close to the beam rapidities.

7.5 Multiplicity dependence

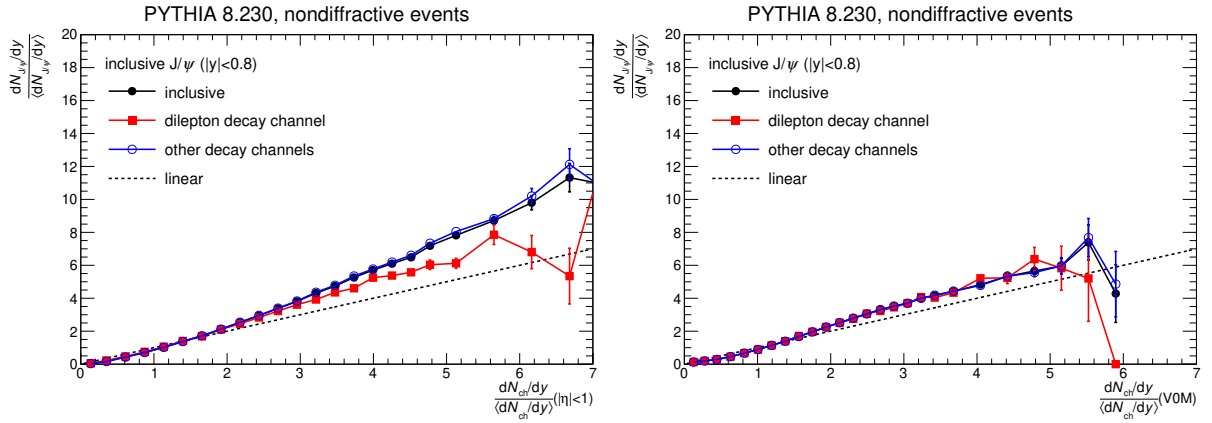


Figure 7.7.: Self-normalized inclusive J/ψ yield at mid-rapidity from PYTHIA8 simulation as a function of self-normalized charged-particle multiplicity, for J/ψ decaying in the dilepton decay channel, or in another decay channel. Multiplicity evaluated at mid-rapidity (left), or at V0M pseudorapidity (right).

The multiplicity dependence of inclusive J/ψ production in PYTHIA8 is shown in Fig. 7.7, which shows the self-normalized J/ψ yield at mid-rapidity as a function of the self-normalized charged-particle multiplicity at mid-rapidity in the left panel and at forward rapidity in the right panel. The result for J/ψ decaying in the dilepton decay channel (dielectron or dimuon) is compared to J/ψ decaying in other decay channels. If the multiplicity is measured in the same rapidity as the J/ψ , its decay daughters enter into the multiplicity and shift events that contain a J/ψ to higher multiplicity values. In PYTHIA, J/ψ can decay in up to 10 decay daughters (which can further decay), while in data, J/ψ is reconstructed only in the dielectron channel. Thus, the choice of the decay channel has a strong influence on the multiplicity dependence. No difference between the dielectron and the dimuon decay channel were observed. For this reason, for the results presented in the rest of this chapter, J/ψ was forced to decay in the dielectron decay channel. In this case the increase of J/ψ production with the multiplicity at mid- and forward rapidity is quite similar.

The transverse-momentum dependence of the increase is shown in Fig. 7.8. Both as a function of mid- and forward rapidity multiplicity, the increase gets steeper with rising p_T , in agreement with data (compare chapter 6). The effect is slightly stronger for the mid-rapidity multiplicity.

In Fig. 7.9 the different J/ψ production mechanism are compared. J/ψ from NRQCD grows linearly with multiplicity, independent of whether the latter was measured at mid or forward rapidity. J/ψ yields from cluster collapse grow stronger than linearly, also independent of the rapidity where the multiplicity was measured. Non-prompt J/ψ yields grow stronger than linearly, the increase is stronger as a function of the mid-rapidity than the forward rapidity multiplicity. This observation hints to the fact that for non-prompt J/ψ auto-correlation effects might be at play. This question will be further investigated in section 7.7.

Finally, in Fig. 7.10 the p_T dependence for the different production processes is investigated. For both non-prompt J/ψ and J/ψ yields from NRQCD, the increase gets steeper with higher p_T . The effect is

more pronounced for non-prompt J/ψ . The increase of J/ψ yields from cluster collapse with multiplicity on the other hand is p_T independent.

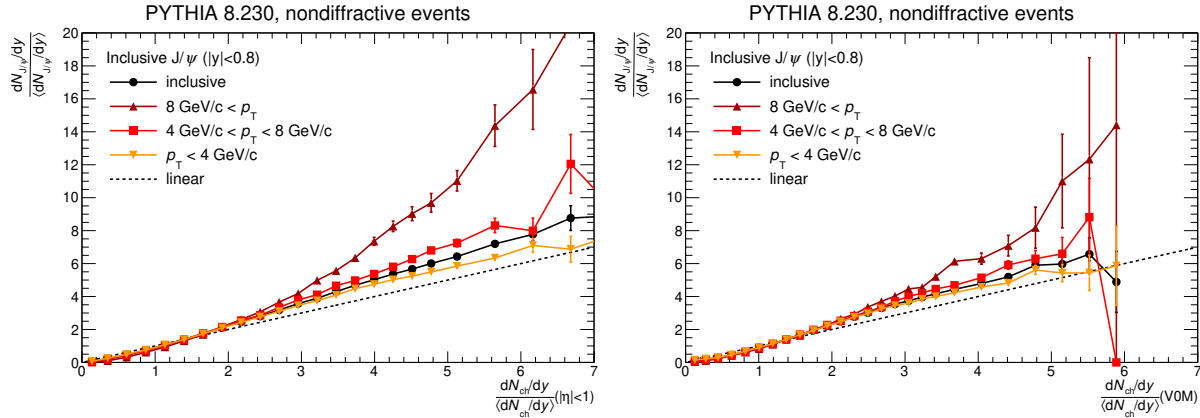


Figure 7.8.: Self-normalized inclusive J/ψ yield at mid-rapidity as a function of self-normalized charged-particle multiplicity at mid- (left) and forward (right) rapidity in intervals of transverse momentum.

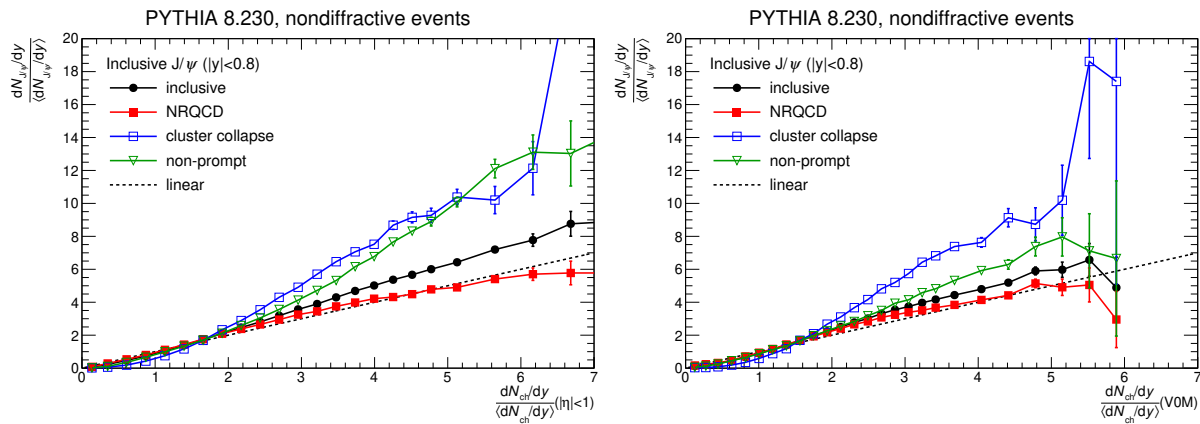


Figure 7.9.: Self-normalized inclusive J/ψ yield at mid-rapidity as a function of self-normalized charged-particle multiplicity at mid- (left) and forward (right) rapidity split in different production mechanisms.

In the remainder of this chapter, the microscopic reasons for these behaviors will be investigated, i.e. the role of MPI, CR and auto-correlation will be disentangled in order to understand the origin of the stronger than linear increase and the p_T dependence of it.

7.6 Multiparton interactions and color reconnection

In the PYTHIA model each PI has a certain probability to produce a J/ψ . Consequently the self-normalized J/ψ yield rises roughly linearly with the self-normalized number of PI, as shown in the top left panel of Fig. 7.11. In this plot CR was deactivated, as the influence of CR will be explained later.

As can be seen, the linearity of the increase is best fulfilled for J/ψ from NRQCD. For non-prompt J/ψ and J/ψ from cluster collapse, the increase tends to saturate at very high multiplicities. This can be explained by the fact that the total available energy in one collision is limited, so for very many PIs in one collision, the momentum transfer per PI is on average smaller, so the cross section for hard processes such as heavy-quark production is reduced.

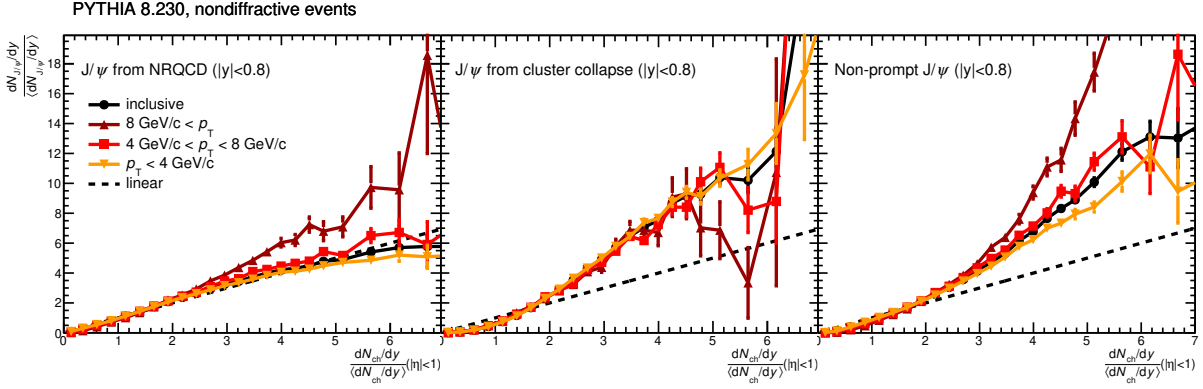


Figure 7.10.: Self-normalized inclusive J/ψ yield at mid-rapidity as a function of self-normalized charged-particle multiplicity at mid-rapidity in transverse-momentum intervals for J/ψ from NRQCD (left), J/ψ from cluster collapse (middle) and non-prompt J/ψ (right).

To further illustrate the origin of the linearity between J/ψ production from NRQCD and the number of PI, in Fig. 7.12 this component is split depending on the PI in which it was produced. As can be seen the probability to produce J/ψ in say the 11th PI is zero for collision with less than 11 PI; starting from collisions with 11 PI, the normalized yield first rises strongly with N_{MPI} up to collisions with about 14 PI, then saturates, and finally slightly decreases.

This behavior can be understood by the fact that the PI are ordered in PYTHIA in decreasing order of momentum transfer. So, in a collision with 11 PI the 11th one is the one with the least momentum transfer, accordingly the probability to produce a J/ψ is low. In collisions with more PI, the 11th one is not the weakest anymore, so the probability to produce J/ψ in it rises. In collisions with many PI, the momentum transfer per PI reduces with increasing N_{MPI} , so also the probability to produce a J/ψ decreases slightly. For the total yield of J/ψ from any PI, this results in a roughly linear increase with N_{MPI} .

As was mentioned, in the top left panel of Fig. 7.11, CR was deactivated. The bottom left panel shows the same quantities with activated CR. J/ψ production from NRQCD and non-prompt J/ψ are not affected by CR. This is as expected, since CR acts on the color strings that are responsible for light particle production but does not enter in these J/ψ production processes. J/ψ from cluster collapse on the other hand shows a completely different behavior, as it grows quadratically with N_{MPI} with activated CR, compared to the linear increase without it. In this process, the charm quark and the charm antiquark typically come from independent pairs, because heavy quarks produced as a pair usually have a large opening angle. Now, with CR activated, also a charm quark from one PI can bind with a charm antiquark from a different one. The probability to produce one heavy quark pair in a collision increases linearly with N_{MPI} : $P(c\bar{c}) \propto N_{\text{MPI}}$. Since the processes are independent, the probability to produce a second one under the condition that a first one was produced also increases linearly with N_{MPI} : $P(2c\bar{c}|c\bar{c}) \propto N_{\text{MPI}}$, so the total probability to produce two charm-anticharm pairs increases quadratically $P(2c\bar{c}) = P(2c\bar{c}|c\bar{c}) * P(c\bar{c}) \propto N_{\text{MPI}}^2$. The same is true for all mesons made of two heavy quarks, so e.g. for B_c , but not for mesons containing a heavy and a light quark, since the latter is usually produced in the string fragmentation process. This fact is illustrated in Fig. 7.12 (right), which shows the increase of J/ψ yield with N_{MPI} for J/ψ from coalescence and non-prompt J/ψ from the decay of a B_c , a B_s , or a B meson. In the first two cases the increase with N_{MPI} is quadratic, in the latter two linear.

Now, instead of the N_{MPI} dependence of the total J/ψ production, the dependence of mid-rapidity J/ψ production on the charged-particle multiplicity at mid-rapidity will be investigated. This is shown in the right panels of Fig. 7.11. The top panel shows again the situation without CR. For non-prompt J/ψ the increase is stronger in this case, for J/ψ from cluster collapse it is slightly stronger and for J/ψ from NRQCD it is weaker.

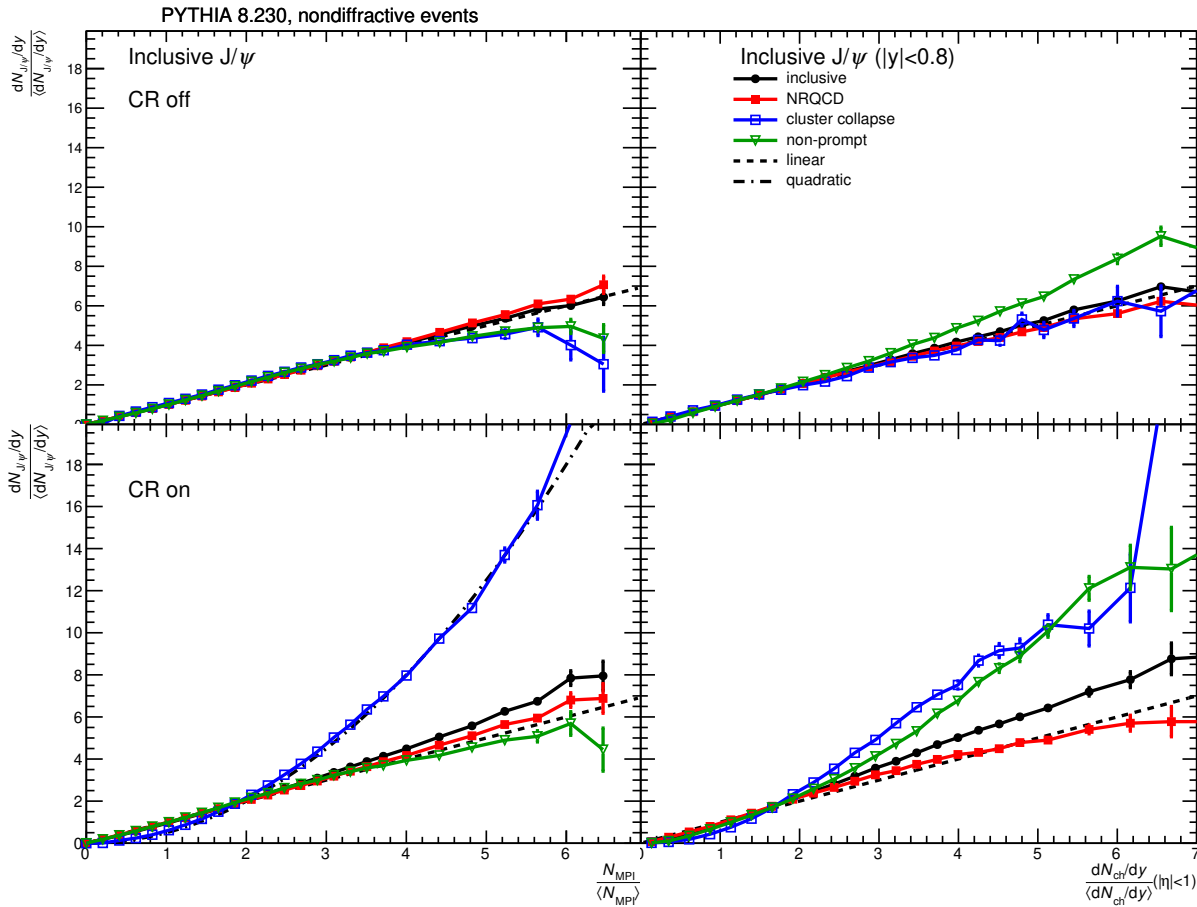


Figure 7.11.: Self-normalized J/ψ yield split in different production processes. Top panels: color reconnection switched off, bottom panels: full simulation; left panels: J/ψ yield in full phase-space as a function of the self-normalized number of partonic interactions, right panels: mid-rapidity J/ψ yield as a function of the self-normalized charged-particle multiplicity at mid-rapidity.

This change in multiplicity dependence is due to auto-correlation effects between the multiplicity estimator and the J/ψ signal and will be investigated in detail in the next section.

This fact can be further visualized two-dimensionally, showing the relative J/ψ yield as a function of N_{MPI} of N_{ch} simultaneously. This is shown in Fig. 7.13 for J/ψ from NRQCD (left panel) and for non-prompt J/ψ (middle panel).

In the case of J/ψ from NRQCD, for an event with a given N_{MPI} , the yield slightly decreases with increasing charged-particle multiplicity. This can be understood by the fact that the charged-particle multiplicity and the J/ψ are in competition to each other, so in an event with high multiplicity produced, not much energy is left for J/ψ production. This is in agreement with the observation that the yield increases slower with N_{ch} than with N_{MPI} .

In the case of non-prompt J/ψ on the other hand, the yield increases strongly with N_{ch} for events with a given N_{MPI} . Or, in other words, for a given charged-particle multiplicity, the probability to produce non-prompt J/ψ is higher if this multiplicity was produced from few – harder – PIs than if many – softer – PIs were involved. This behavior can be understood by the fact that the production of a non-prompt J/ψ is associated with the production of additional charged particles.

The scaling of non-prompt J/ψ production with N_{ch} and N_{MPI} is in fact very similar to the total transverse-momentum transfer squared of the collision \hat{p}_T^2 , which is the sum of the squared transverse-momentum transfers in the individual PIs. This quantity is shown in the right panel of Fig. 7.13.

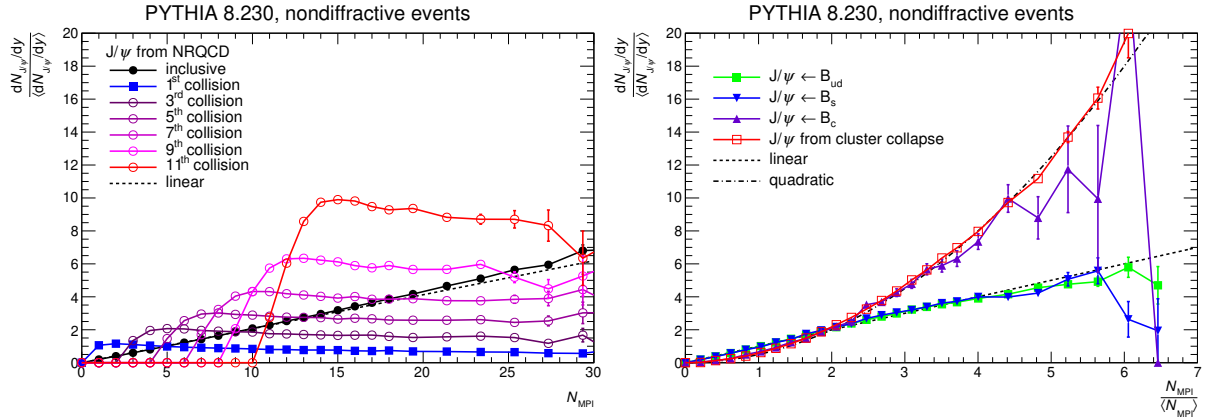


Figure 7.12.: Explanation for the linear and quadratic scaling of J/ψ production as a function of N_{MPI} .
 Left: Prompt J/ψ produced from NRQCD split according to in which PI it was produced.
 Right: J/ψ from coalescence and B decay, split into B , B_s and B_c .

Finally, the stronger-than-linear increase of non-prompt J/ψ production is further enhanced when CR is activated. This is demonstrated in the bottom right panel of Fig. 7.11. This is due to the fact that CR reduces the soft particle production, this means the abscissa of the plot becomes compressed, while the ordinate is not effected, so the increase is enhanced.

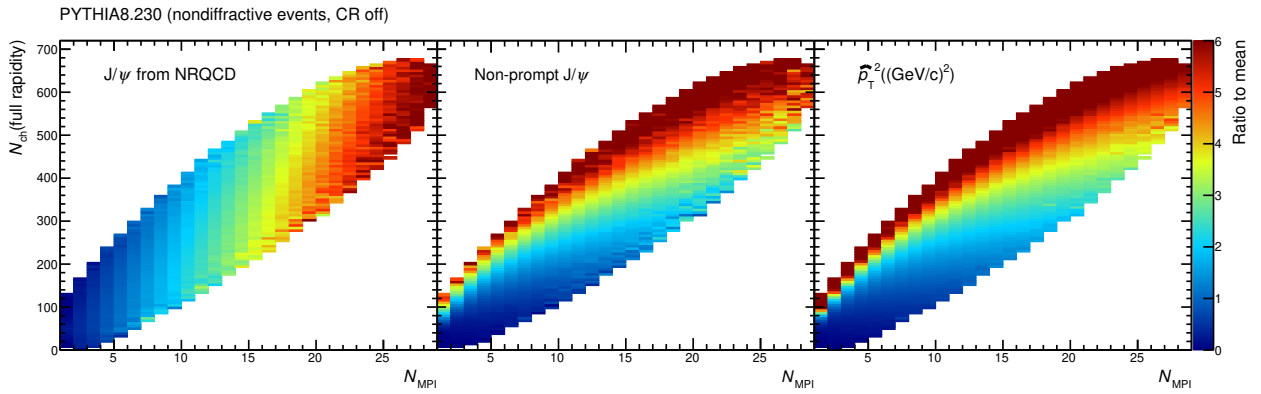


Figure 7.13.: Left, middle: self-normalized J/ψ yield as a function of charged-particle multiplicity in full rapidity and number of PI for J/ψ from NRQCD (left), and non-prompt J/ψ (middle). Right: Self-normalized total squared transverse-momentum transfer, i.e. sum of the squared transferred transverse-momenta of the individual PIs.

7.7 Investigation of auto-correlation

The charged-particle multiplicity and the J/ψ yield are not independent quantities, the latter influences the former. This influence comes from the following mechanisms:

- The J/ψ decay daughters contribute to the charged-particle multiplicity. Since the simulations and the experimental measurement are done in the dielectron decay channel, two additional charged particles are produced in events containing a J/ψ , if the multiplicity is measured in the same rapidity as the J/ψ .
- In the case of J/ψ from NRQCD the J/ψ is typically produced together with a gluon, e.g. via $g g \rightarrow [Q\bar{Q}]g$ which will in turn hadronize and increase the multiplicity. Additionally, if the pre-

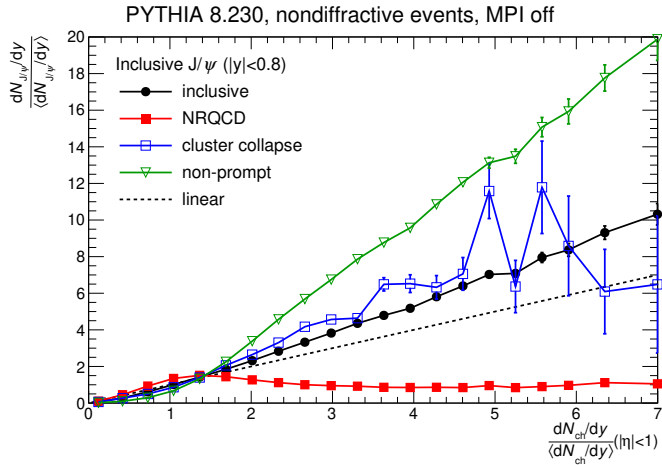


Figure 7.14.: Self-normalized mid-rapidity J/ψ yield as a function of self-normalized mid-rapidity charged-particle multiplicity in events without MPI from PYTHIA8.

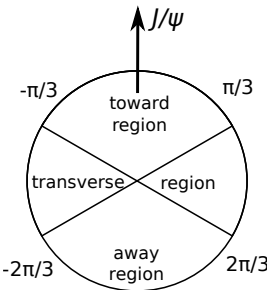


Figure 7.15.: Definition of the toward, transverse and away regions in φ with respect to the J/ψ direction.

resonant state is a color-octet, an additional gluon is emitted in the transition to the physical J/ψ state. Since the mass difference between the color-octet and the color singlet state is small, the gluon will typically be emitted under a small opening angle, so the multiplicity in the flight direction of the J/ψ will be affected most.

- In the case of J/ψ from cluster collapse, the charm quark and antiquark are both produced together with another charm antiquark and charm quark, which in turn will produce additional particles.
- In the case of non-prompt J/ψ , the mother particle of the J/ψ decays into several particles, the decay daughters can decay further. Furthermore, the initially produced b quark can be accompanied by final state radiation, enhancing the multiplicity in the region around it. Finally, b quarks are always produced as pairs, mostly back to back in hard interactions. Thus, the non-prompt J/ψ will typically be accompanied by a high- p_T parton going in the opposite direction, fragmenting into a jet of particles. This recoil jet is at an azimuthal angle of 180° with respect to the initial b quark, but can be at a different rapidity.

These auto-correlation effects can be best studied in events with only one hard interaction, so with the MPI mechanism switched off. Then, J/ψ and charged-particle production both originate from the same process and the described effects should be clearly visible.

Fig. 7.14 shows the self-normalized J/ψ yield at mid-rapidity as a function of the self-normalized charged-particle multiplicity at mid-rapidity for events without MPI. For non-prompt J/ψ , a strong increase of the yield with the charged-particle multiplicity can be observed, likewise but weaker for J/ψ from cluster collapse. For J/ψ from NRQCD a different picture emerges: at low multiplicity, the yield

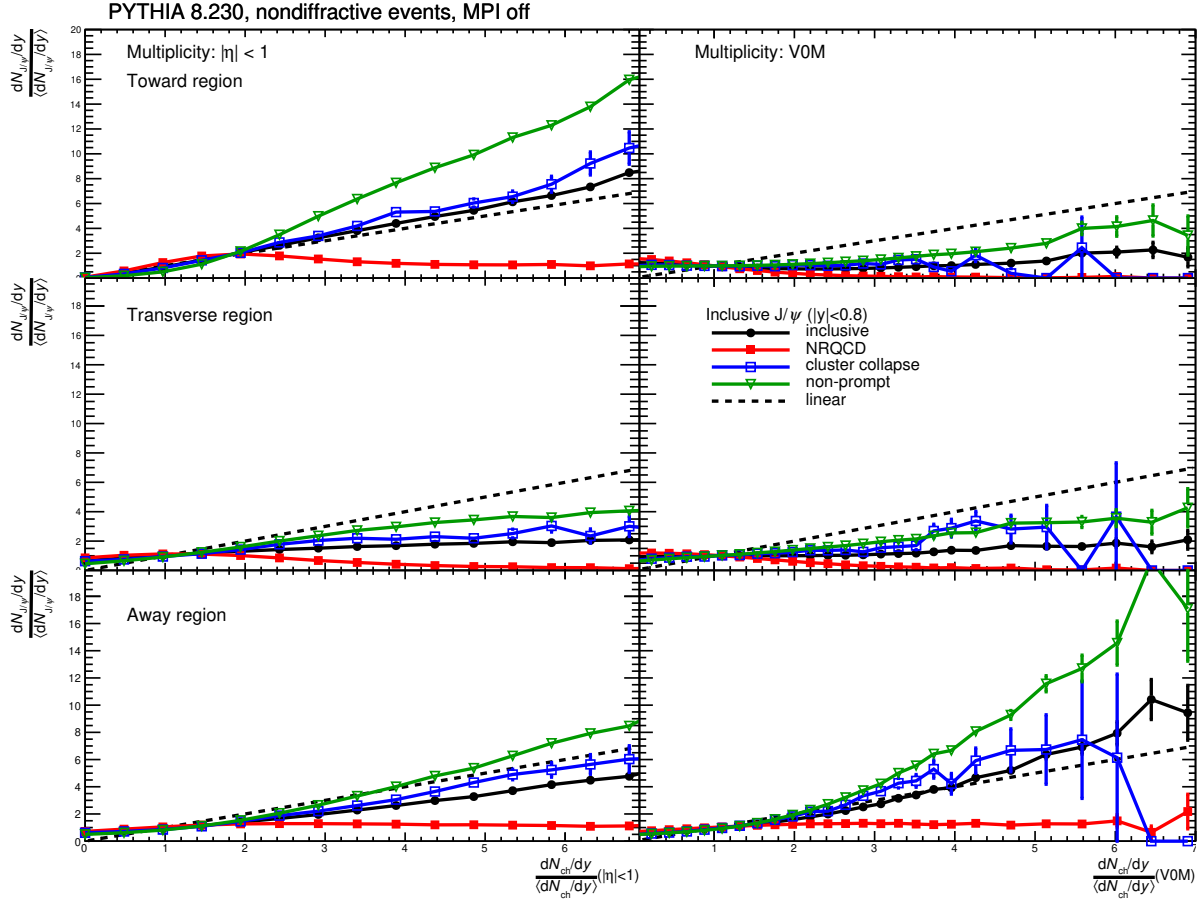


Figure 7.16.: Multiplicity dependence of J/ψ production at mid-rapidity in PYTHIA8.230 with multiparton interactions switched off, split into the different production mechanisms. Multiplicity evaluated in different kinematic regions. Left : multiplicity at mid-rapidity, right: multiplicity at forward rapidity; top row: multiplicity in toward region in φ w.r.t. J/ψ , middle row: multiplicity in transverse region, bottom row: multiplicity in away region.

increases with multiplicity, up to around 1.5 times the mean value, afterwards it decreases again slightly with multiplicity. This behavior can be understood the following way: at low multiplicity the additional particle production from the gluons produced alongside the J/ψ leads to an increase of J/ψ production with multiplicity. At higher multiplicity, the competition between J/ψ and charged-particle production for the limited total phase space in the collision becomes relevant and leads to the observed decrease of the self-normalized J/ψ yield.

To further investigate the different auto-correlation effects, the J/ψ yield can be studied as function of the charged-particle multiplicity in different kinematic regions w.r.t. the direction of the J/ψ , i.e. in different regions of the azimuthal angle φ and at different rapidities. The φ direction was split into three regions as indicated in Fig. 7.15:

- Toward region: $\Delta\varphi \equiv |\varphi - \varphi_{J/\psi}| < \pi/3$
- Transverse region: $\pi/3 < \Delta\varphi < 2\pi/3$
- Away region: $2\pi/3 < \Delta\varphi$.

Furthermore, the charged-particle multiplicity was evaluated either at mid-rapidity, or at forward rapidity.

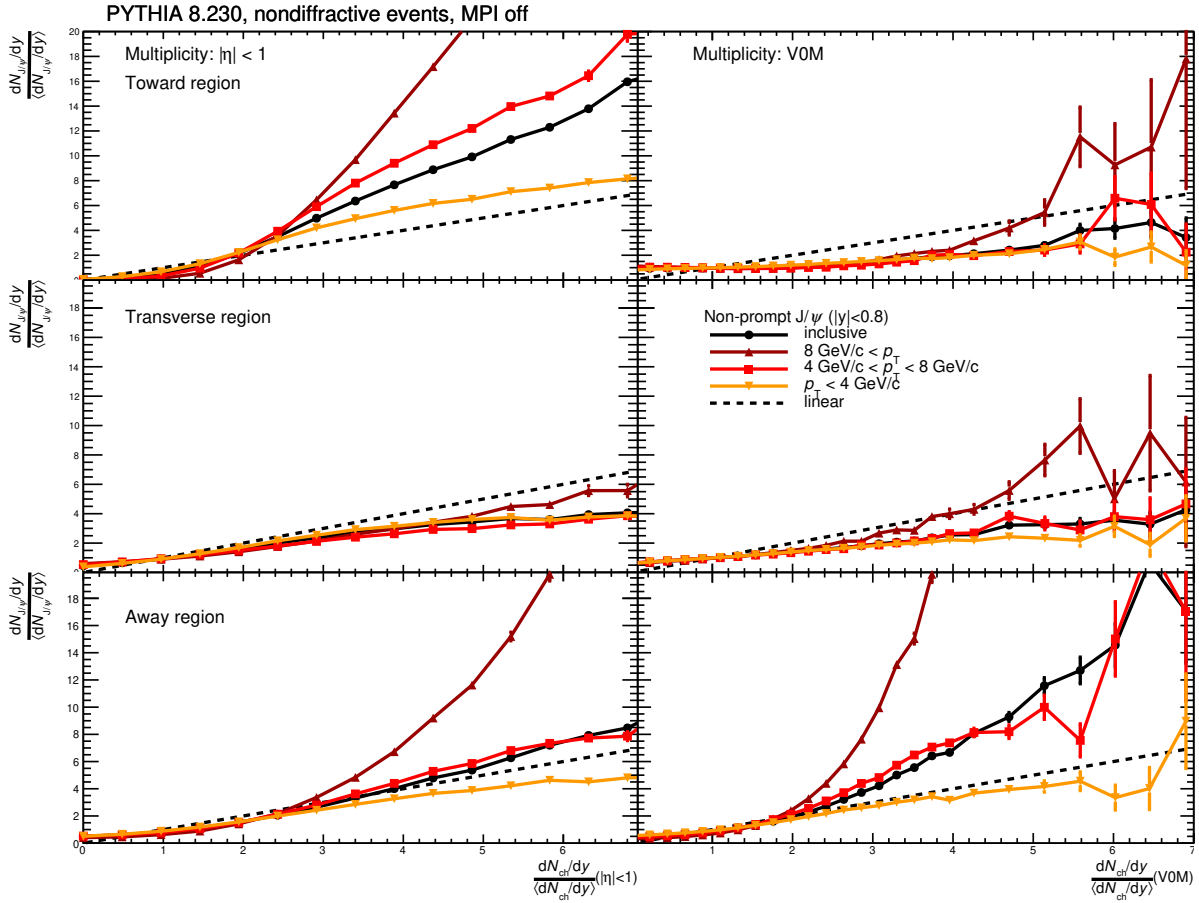


Figure 7.17.: Multiplicity dependence of non-prompt J/ψ production at mid-rapidity in PYTHIA8.230 with multiparton interactions switched off, in transverse-momentum bins, where the b quark was produced in a hard pQCD process. Multiplicity evaluated in different kinematic regions. Left: multiplicity at mid-rapidity, right: multiplicity at forward rapidity; top row: multiplicity in toward region in φ w.r.t. J/ψ , middle row: multiplicity in transverse region, bottom row: multiplicity in away region.

The dependence of mid-rapidity J/ψ production on the multiplicity in the different regions is shown in Fig. 7.16. In the left panels, the multiplicity was determined at mid-rapidity, in the right ones at forward rapidity, in the top panels in the toward region, in the middle panels in the transverse region, and in the bottom panels in the away region. The following observations can be made:

- The yield of J/ψ from NRQCD does not depend strongly on the charged-particle multiplicity. It is independent of the multiplicity in the away region, and decreases slightly with increasing multiplicity in the regions away from the flight direction of the J/ψ . As a function of the multiplicity in the flight direction of the J/ψ , first an increase of the yield with multiplicity can be observed, which then saturates and changes into a decrease.
- The yield of non-prompt J/ψ increases strongly as a function of the multiplicity in the away region, and of the multiplicity in the toward region at mid-rapidity. It is weakly dependent on the multiplicity in the other regions.
- For J/ψ from cluster collapse the same is true as for non-prompt J/ψ , but the increase is not as strong.

These observations are in line with the expectations from the described effects: the multiplicity in the region around the J/ψ from the additional decay daughters is increased and leads to a increase of J/ψ production as a function of multiplicity. The recoil jet likewise increases the multiplicity in the away region in a wide rapidity range, especially for non-prompt J/ψ .

The multiplicity dependence of non-prompt J/ψ will be studied further in the following, since here the auto-correlation effects are the strongest. In Fig. 7.17, it is split in transverse-momentum bins. The dependence on the multiplicity where no auto-correlation effects are expected – so the transverse region, and the toward region at forward rapidity – is largely p_T independent. In the region affected by auto-correlation however, the increase with multiplicity is strongly p_T dependent, i.e. the increase is much stronger for high p_T . This is again in line with expectations, since higher- p_T b quarks should fragment into more particles and have more radiation associated to them.

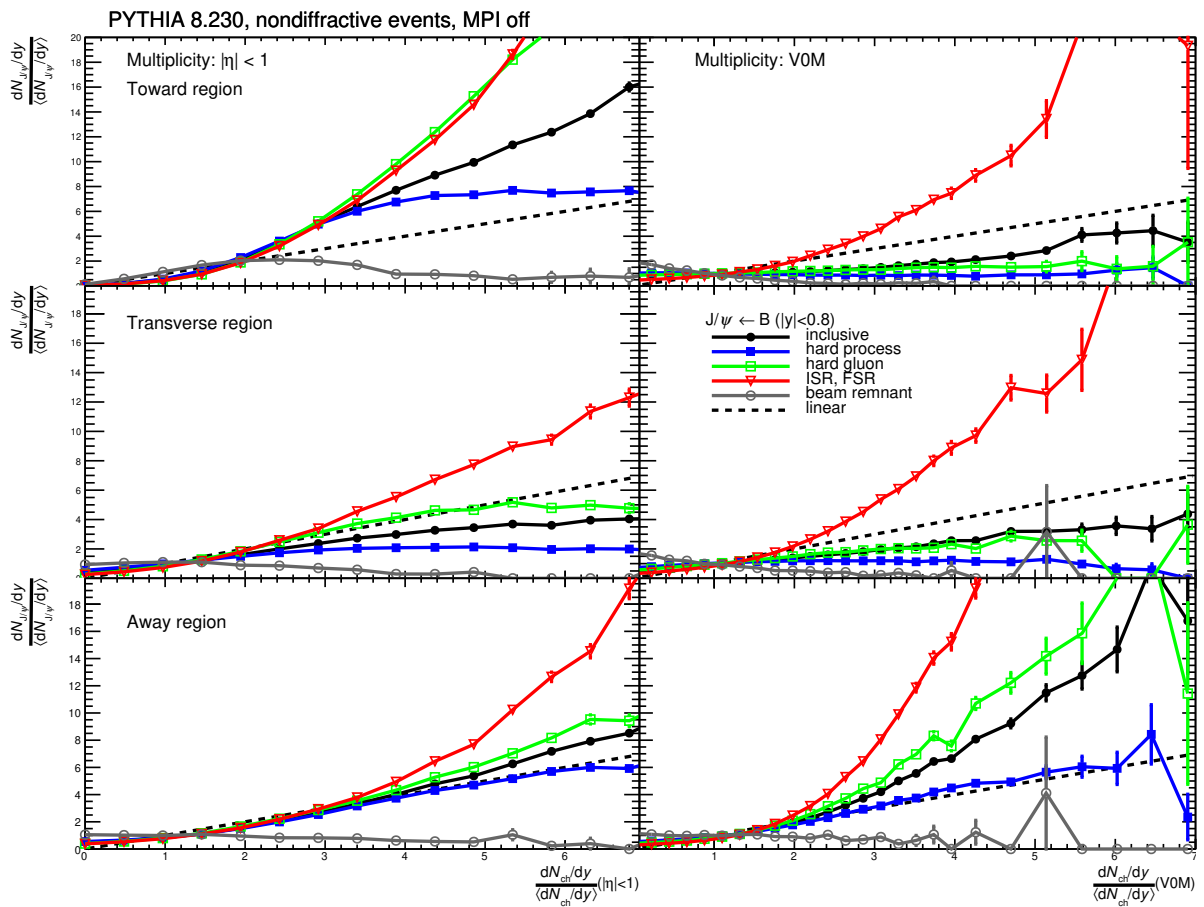


Figure 7.18.: Multiplicity dependence of non-prompt J/ψ production at mid-rapidity in PYTHIA8.230 with multiparton interactions switched off, split in different production mechanisms of the beauty quark. Multiplicity evaluated in different kinematic regions. Left: multiplicity at mid-rapidity, right: multiplicity at forward rapidity; top row: multiplicity in toward region in φ w.r.t. J/ψ , middle row: multiplicity in transverse region, bottom row: multiplicity in away region.

Based on the auto-correlation arguments, in principle non-prompt J/ψ production should be independent of the multiplicity in the transverse region, and of the multiplicity in the toward region at different rapidity. However, also in these cases a slight increase with multiplicity is observed. This fact can be further investigated by splitting the non-prompt J/ψ yield depending on the production mechanism of the initial b quark. As was mentioned, this can be a hard interaction, a gluon splitting – either of a gluon produced in a hard interaction or in ISR or FSR – or it can come from the beam remnant.

The multiplicity dependence for these different cases is shown in Fig. 7.18. As can be seen, if the b quark was produced in a hard interaction, the multiplicity dependence is as expected from auto-correlation effects alone, i.e. the dependence is only visible in the away region, and in the toward region at the same rapidity as the signal. In these hard processes, the b quark and antiquark are produced back-to-back so the influence of the recoil jet is very clean. As a function of the multiplicity in the toward region at mid-rapidity, the increase flattens around four times the mean multiplicity, and afterwards the yield does not increase anymore.

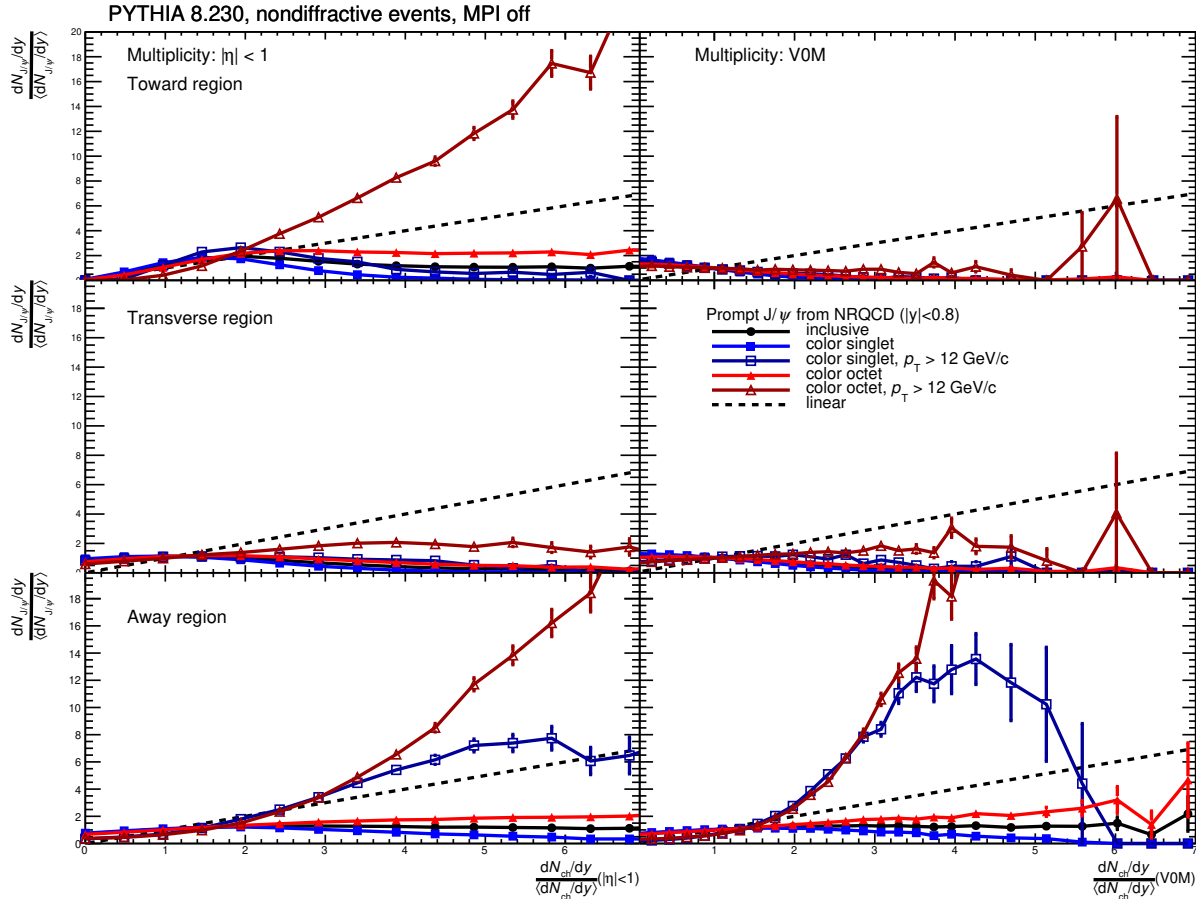


Figure 7.19.: Multiplicity dependence of J/ψ production at mid-rapidity from NRQCD in PYTHIA8.230 with multiparton interactions switched off, in bins of transverse momentum, for J/ψ produced via a color singlet or color-octet pre-resonant state. Multiplicity evaluated in different kinematic regions. Left : multiplicity at mid-rapidity, right: multiplicity at forward rapidity; top row: multiplicity in toward region in φ w.r.t. J/ψ , middle row: multiplicity in transverse region, bottom row: multiplicity in away region.

For b quark-antiquark pairs from gluon splitting where the gluon was produced in a hard process, the multiplicity dependence is also spread out into the other regions, so the J/ψ yield also increases as a function of the transverse multiplicity. This is not unexpected, since in this case the topology of the produced partons is more complex. The b quark is produced together with a b antiquark in the gluon splitting process with a small opening angle. The non-zero opening angle results in the slight dependence on the multiplicity in the transverse region. Additionally, the gluon is produced back-to-back with another parton in the hard scattering process, producing the recoil jet signature.

In the case of the splitting of a gluon from ISR or FSR, the increase with multiplicity is spread over all regions. This is expected, since the ISR/FSR gluon can have a large opening angle to the partons produced in the hard interaction which should produce the bulk of the multiplicity in the event.

For non-prompt J/ψ from a b quark of the beam remnant finally, the multiplicity dependence is much weaker and very similar to the one of J/ψ from NRQCD. The reason is the lower transverse momentum of this contribution.

For J/ψ from NRQCD no strong auto-correlation effects are observed for the p_T -integrated yield. In Fig. 7.19, the multiplicity dependence is shown for J/ψ produced via a color singlet or color-octet pre-resonant state, p_T -integrated, and for very high p_T , i.e. $p_T > 12 \text{ GeV}/c$. While p_T -integrated J/ψ production from NRQCD is weakly dependent on multiplicity in any region in both cases, for very high p_T strong effects can be observed. Both J/ψ produced via color-singlet and color-octet states increase strongly as a function of the multiplicity in the away region, independent of the rapidity. This is in line with the fact that the J/ψ is produced together with a gluon, which at high p_T produced a recoil jet. For J/ψ produced via a color-octet state, also a strong dependence on the multiplicity in the toward region at mid-rapidity can be observed, which is not present for J/ψ from a color-singlet state. This is in line with the fact that the color-octet charmonium state decays to J/ψ under emission of a gluon, which for J/ψ at high p_T has a high energy and will radiate more gluons and finally hadronize into a jet of particles in the region around the J/ψ .

From these observations in events without MPI, one can assume that also for the full simulation, the multiplicity dependence of J/ψ production can be influenced by the presented auto-correlation effects.

As was shown in Fig. 7.8 and Fig. 7.9, the stronger-than-linear increase of non-prompt J/ψ yields and the p_T dependence also persist when plotting as a function of the multiplicity in the forward region.

However, when plotting against the mid-rapidity multiplicity in the transverse region as done in Fig. 7.20, the increase is significantly reduced; for non-prompt J/ψ and J/ψ from cluster collapse it is merely slightly stronger than linear, for J/ψ from NRQCD it is even weaker than linear. The p_T dependence of the increase vanishes completely in this case.

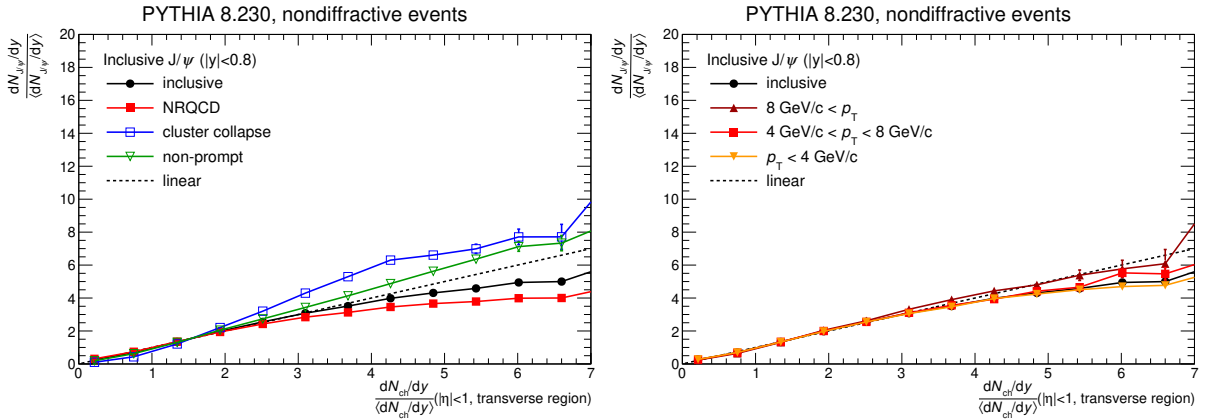


Figure 7.20.: Self-normalized mid-rapidity J/ψ yield as function of self-normalized transverse multiplicity in full PYTHIA8 simulation in transverse-momentum bins (left) and split into the different production mechanisms (right).

7.8 Summary

Summarizing the investigations done with the PYTHIA8 generator, it can be said that it qualitatively reproduces the experimentally observed increase of J/ψ production as a function of the charged-particle multiplicity. The stronger-than-linear increase is due to the following fact:

- From the MPI mechanism in PYTHIA, naturally a linear dependence between soft and hard particle production follows.

- A small fraction of the J/ψ are produced from charm quarks and antiquarks produced independently, this contribution scales roughly quadratically with multiplicity.
- Due to associated soft particle production together with non-prompt J/ψ , the multiplicity distribution for events containing J/ψ is shifted towards higher values. This auto-correlation effect is the reason for the stronger-than-linear increase.
- The effect is emphasized by color reconnection, which leads to a reduction of soft particle production, while not affecting hard particles.
- These effects are still present if the multiplicity is measured at a different rapidity than the signal. However, it can be removed effectively by measuring the multiplicity in the azimuthal region transverse to the J/ψ . The increase with multiplicity is then more or less linear, and independent of transverse momentum.

A measurement of J/ψ production as a function of multiplicity in the transverse region is thus highly advisable in order to disentangle between auto-correlation effects, which should vanish in this case, and true correlation effects between the hard probe and the underlying event as predicted by the models presented in section 2.2. Further motivation for the use of this multiplicity estimator can be found in [201] and [202].

For the current measurement as presented in this thesis, the correct interpretation of the stronger-than-linear increase is complicated, since the auto-correlation effects are not subtracted and any additional effects (such as saturation effects of soft particle production) come in addition to those. So, the baseline expectation in the absence of those effects is not a linear increase with multiplicity.

It has to be noted that the findings presented for non-prompt J/ψ production are equally valid for open heavy-flavor mesons in general, and the findings for prompt J/ψ can be applied to bottomonium production.

8 Summary and Outlook

In this thesis, the self-normalized yield of inclusive J/ψ production in $|y| < 0.8$ has been studied as a function of the charged-particle multiplicity in $|\eta| < 1$ and in $-3.7 < \eta < -1.7 \cup 2.8 < \eta < 5.1$. The analysis has been performed for p_T -integrated J/ψ , as well as for J/ψ with transverse momenta $p_T < 4 \text{ GeV}/c$ and $p_T > 4 \text{ GeV}/c$.

At mid-rapidity, relative charged particle multiplicities of 9 were reached, extending the reach in multiplicity by a factor 2 compared to similar measurements at lower collision energies. A stronger than linear increase of J/ψ production with multiplicity was observed both as a function of the multiplicity at mid and at forward rapidity with no indication of a weakening of the effect with the inclusion of a rapidity gap in the order of one between the J/ψ signal and the charged-particle multiplicity. A significantly stronger increase with multiplicity of J/ψ at high p_T compared to J/ψ at low p_T and p_T -integrated J/ψ is seen in both cases.

The results are put into perspective with other experimental results on related quantities. Complementary results from an analysis of J/ψ at higher p_T show a stronger increase with multiplicity, supporting the trend observed in the presented analysis. No significant difference to the multiplicity dependence of J/ψ production at lower collision energies is observed. Comparing to open-charm hadrons, a hint of a slightly weaker increase with multiplicity is found.

It was found that the observed increase of J/ψ production as a function of multiplicity can be well described with a powerlaw function, with a slope parameter increasing with p_T , but independent of the rapidity region of the multiplicity. Also a linear dependence at high multiplicities is compatible with the experimental data.

Theoretical predictions from a percolation model, from a model based on the contributions of higher Fock states in the incoming protons, from a model incorporating the color-glass-condensate (CGC) theory, from the PYTHIA8 model, and from the EPOS3 model are in qualitative agreement with the presented results. In case of the CGC-based and the EPOS3 model, a quantitatively good description of the experimental data is achieved, the percolation model and the higher-Fock-states-model are in rough agreement with the experimental data. The PYTHIA8 model significantly underestimates the increase of J/ψ production with multiplicity.

From an extensive study of Monte Carlo simulations from the PYTHIA8 model, the stronger than linear increase can be ascribed to auto-correlation effects between the J/ψ signal and the charged-particle multiplicity, largely caused by the non-prompt J/ψ contribution in jet-like collisions with open-beauty production. The multiplicity in the azimuthal region transverse to the direction of the produced J/ψ particle can serve as a much cleaner estimator for the underlying event activity. A measurements of the production of J/ψ or other hard probes as a function of this new observable is proposed.

8.1 Outlook

A promising extension of the presented analysis is the independent measurement of prompt and non-prompt J/ψ production as a function of multiplicity, as was done for pp collisions at 7 TeV [123]. A corresponding analysis was started in the ALICE collaboration during the writing of this thesis.

Transverse momentum broadening as a function of multiplicity is an observable that can help to test theoretical model predictions, as e.g. the presented model by Kopeliovich predicts a linear broadening with multiplicity, cf. section 2.2.2.

As was demonstrated from the study on PYTHIA8 Monte Carlo simulations, J/ψ production is correlated with the multiplicity in the different azimuthal regions relative to itself in different ways. A study on azimuthal J/ψ -hadron correlations is very promising to address those questions. Corresponding investigations were started in ALICE during the writing of this thesis both for pp collisions and $p\text{-Pb}$ collisions.

Another angle from which similar physics questions can be addressed is the investigation of event properties for collisions in which hard probes — such as heavy flavor or quarkonium — were produced in comparison to minimum bias collisions. Higher moments of the multiplicity distribution (dispersion, etc.) can be of interest. It can also be advantageous to make use of event shape variables. Sphericity and spherocity have been suggested as tools to enhance soft and hard events, and likewise events with low or high number of multiparton interactions [203].

For the time after the current data taking period, which will end in 2018, a long shutdown (LS2) of the LHC machine is planned until the year 2020. ALICE envisages a wide range of upgrades to its detectors [204]. Among others these are the following:

- **ITS upgrade:** The current ITS system will be replaced by a new one. The material budget will be reduced and the resolution of the distance of closest approach between a track and the primary vertex will be improved by a factor of about 3. Also the standalone tracking capability at low transverse momenta will be significantly improved.
- **TPC upgrade:** The current multi-wire readout chambers will be replaced with chambers employing the GEM (Gaseous Electron Multiplier) technology. GEM detectors feature an intrinsic ion blocking, so the operation of a gating grid, as it is currently done, becomes unnecessary. The dead time of the detector thus significantly decreases and an operation in a continuous readout mode becomes feasible, allowing for an event readout rate in pp collisions of 200 kHz, according to current planning.

The increased resolution on track impact parameters will largely benefit the separation between prompt and non-prompt J/ψ , and the reduced material budget will reduce background from photon conversion, increasing the precision of J/ψ analyses in the dielectron decay channel in general.

With the high readout rate of the upgraded detector a large sample of collision data can be acquired, allowing for high precision measurements, especially for probes that are hard to trigger on and thus require the use of minimum bias triggered data.

A large sample of minimum bias events will benefit the analyses of charmonium production mechanisms and the interplay between soft and hard physics. For the investigation of high-multiplicity pp collisions, another high-multiplicity data taking campaign would be beneficial. The evolution between the different collision systems — pp , $p\text{-Pb}$ and Pb-Pb — could be addressed with the measurement of the multiplicity dependence of the J/ψ yield or its ratio to the total charm production. A significant measurement of the latter will become feasible after the ALICE upgrade with the improved low-momentum capabilities of the new ITS.

A Signal extraction in $N_{\text{ch,fwd.}}$ and p_{T} bins

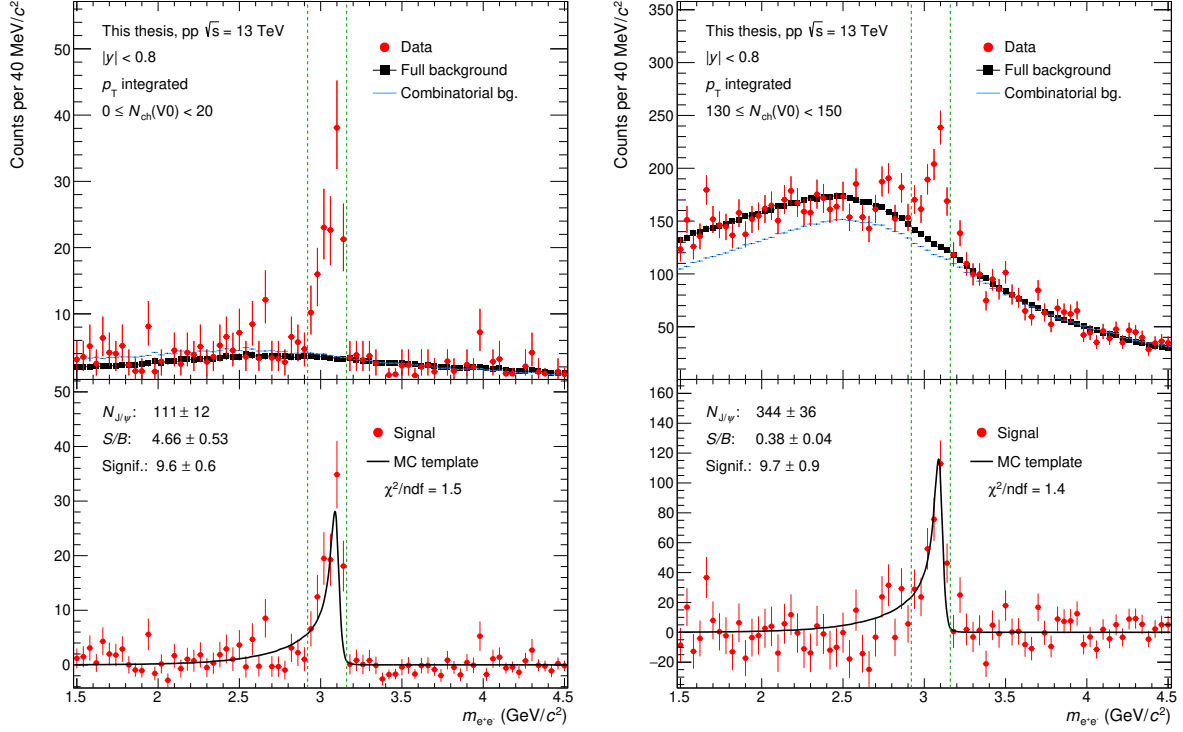


Figure A.1.: Efficiency weighted invariant mass distribution (top) of electron-positron pairs, together with background estimation; J/ψ signal after background subtraction (bottom). Lowest (left) and highest (right) forward-rapidity charged-particle multiplicity interval used in the analysis.

The signal extraction in intervals of the forward rapidity charged-particle multiplicity is exemplified by Fig. A.1 which shows the electron-positron invariant mass distribution and the extracted J/ψ signal for the lowest and highest forward rapidity multiplicity interval.

The performance of the signal extraction in the forward rapidity multiplicity intervals, and in the analysis in p_{T} intervals is demonstrated in Figures A.2, A.3, A.4, A.5, A.6, A.7, A.8, A.9, A.10, and A.11, that show the raw extracted J/ψ signal count, the signal-over-background ratio, the significance of the extracted signal, and the χ^2/ndf between the extracted signal and the expected line shape from the Monte Carlo simulation as a function of the multiplicity intervals for the different cases.

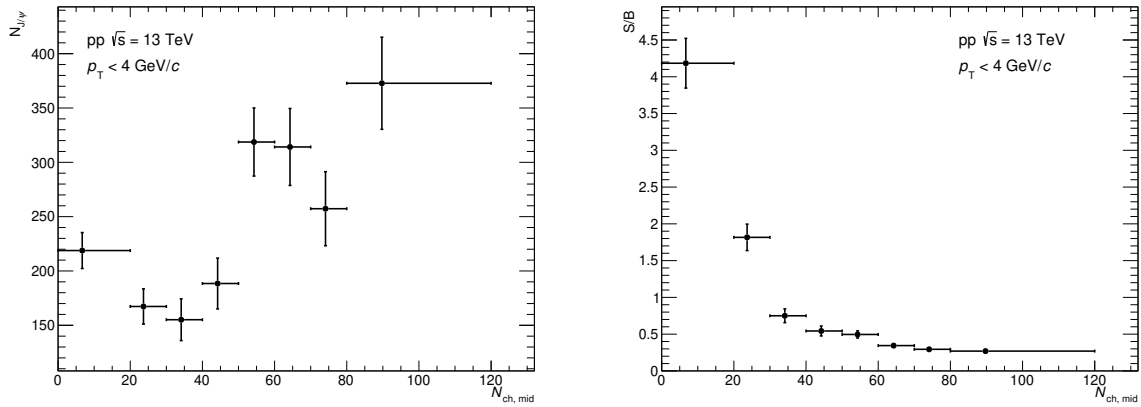


Figure A.2.: Performance of the signal extraction at low p_T as a function of $N_{\text{ch, mid}}$. Left: Raw (efficiency corrected) signal count; Right: Signal-over-background ratio.

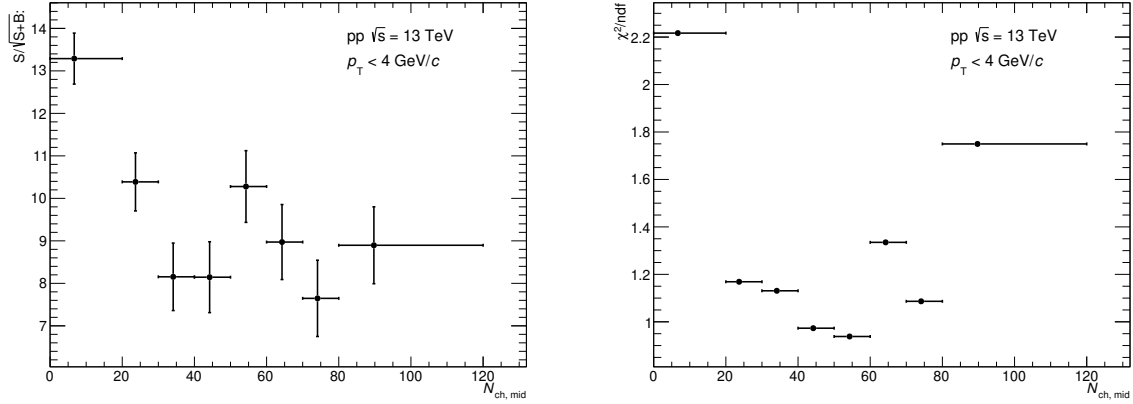


Figure A.3.: Performance of the signal extraction at low p_T as a function of $N_{\text{ch, mid}}$. Left: Significance of the extracted signal; Right: χ^2/ndf between the extracted signal and the scaled line shape from Monte Carlo simulations.

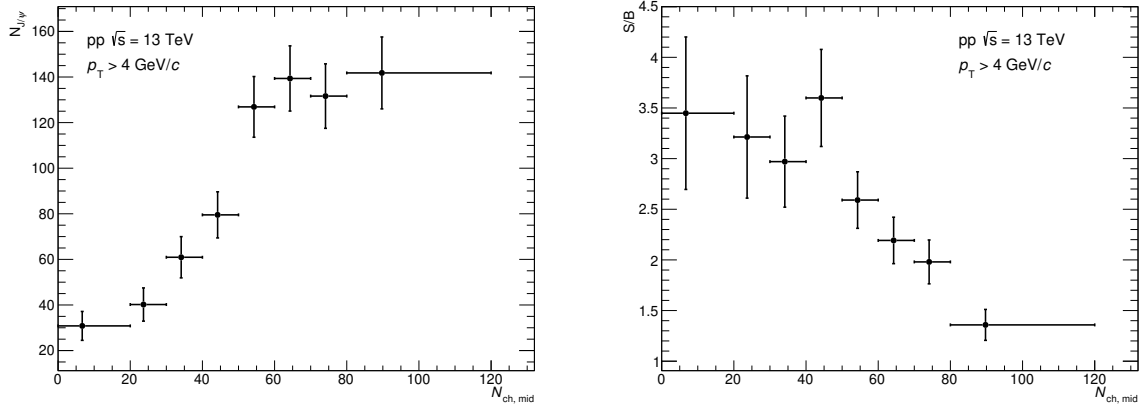


Figure A.4.: Performance of the signal extraction at high p_T as a function of $N_{\text{ch, mid}}$. Left: Raw (efficiency corrected) signal count; Right: Signal-over-background ratio.

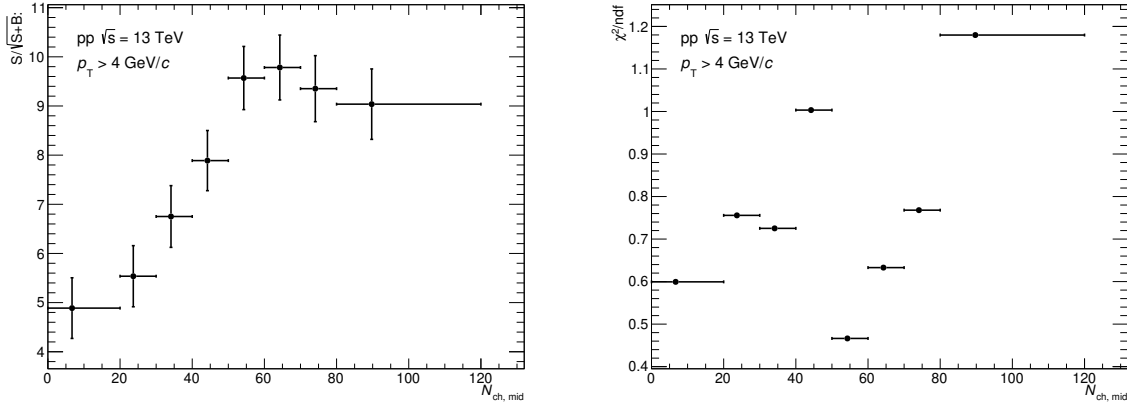


Figure A.5.: Performance of the signal extraction at high p_T as a function of $N_{ch,mid}$. Left: Significance of the extracted signal; Right: χ^2/ndf between the extracted signal and the scaled line shape from Monte Carlo simulations.

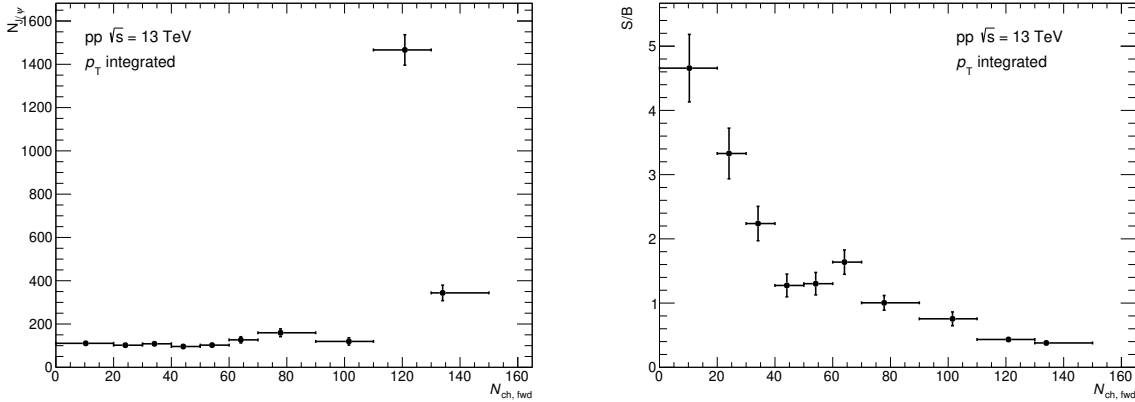


Figure A.6.: Performance of the p_T -integrated signal extraction as a function of $N_{ch,fwd}$. Left: Raw (efficiency corrected) signal count; Right: Signal-over-background ratio.

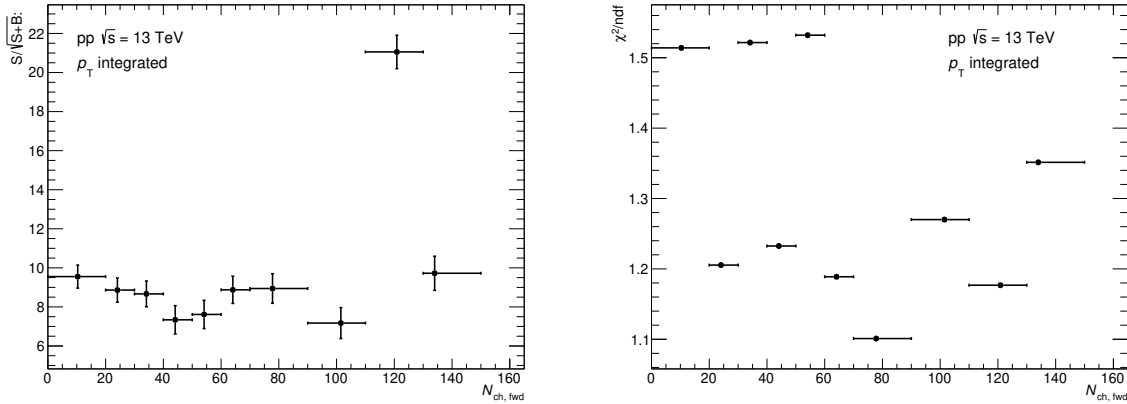


Figure A.7.: Performance of the p_T -integrated signal extraction as a function of $N_{ch,fwd}$. Left: Significance of the extracted signal; Right: χ^2/ndf between the extracted signal and the scaled line shape from Monte Carlo simulations.

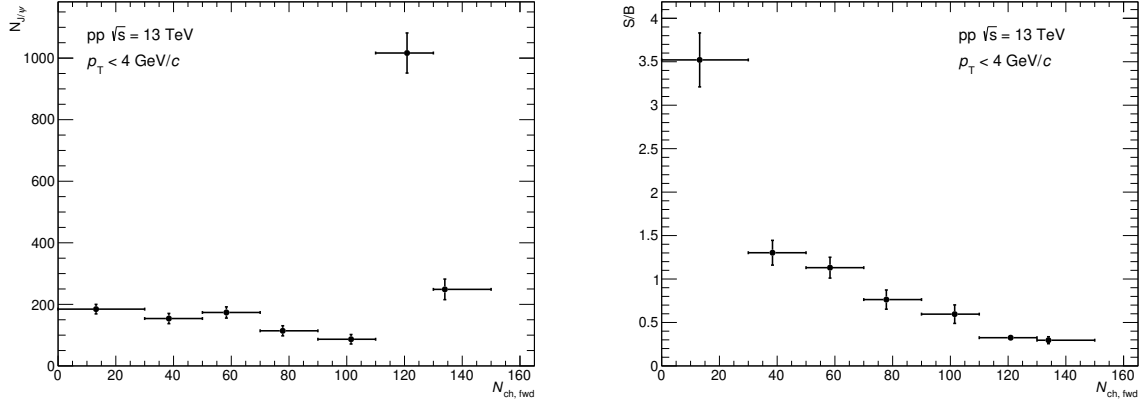


Figure A.8.: Performance of the signal extraction at low p_T as a function of $N_{ch,fwd}$. Left: Raw (efficiency corrected) signal count; Right: Signal-over-background ratio.

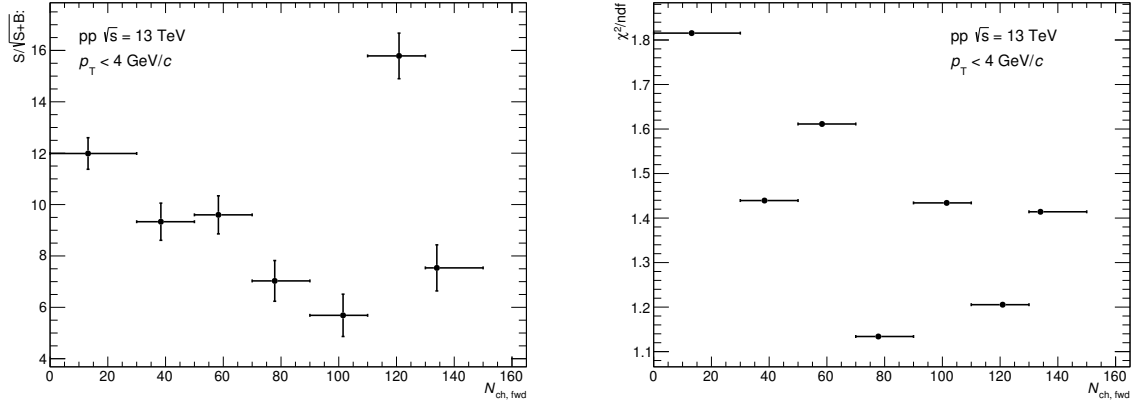


Figure A.9.: Performance of the signal extraction at low p_T as a function of $N_{ch,fwd}$. Left: Significance of the extracted signal; Right: χ^2/ndf between the extracted signal and the scaled line shape from Monte Carlo simulations.

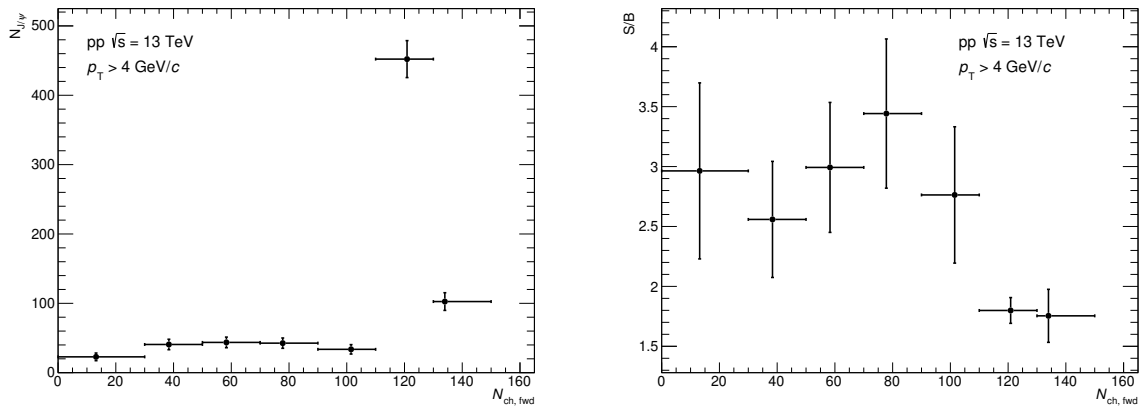


Figure A.10.: Performance of the signal extraction at high p_T as a function of $N_{ch,fwd}$. Left: Raw (efficiency corrected) signal count; Right: Signal-over-background ratio.

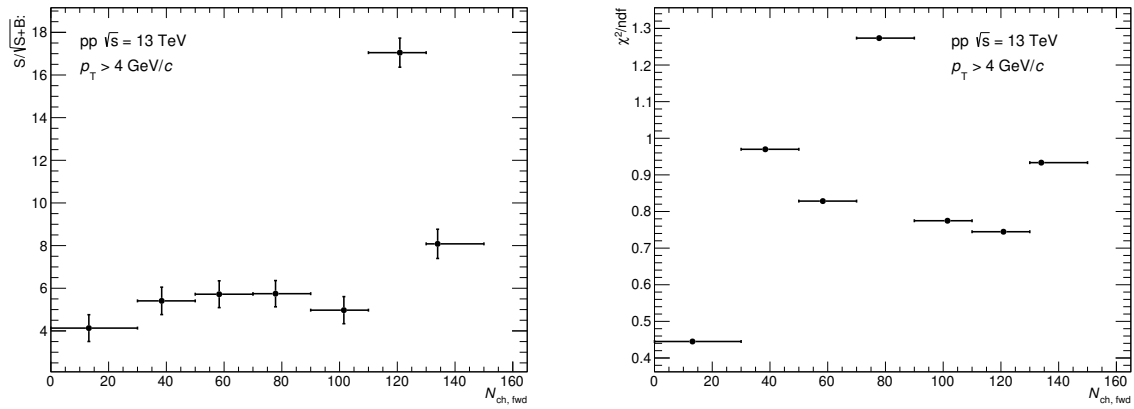


Figure A.11.: Performance of the signal extraction at high p_T as a function of $N_{\text{ch, fwd}}$. Left: Significance of the extracted signal; Right: χ^2/ndf between the extracted signal and the scaled line shape from Monte Carlo simulations.



B Systematic uncertainties of the results in transverse momentum bins

B.1 Uncertainty on the charged-particle multiplicity

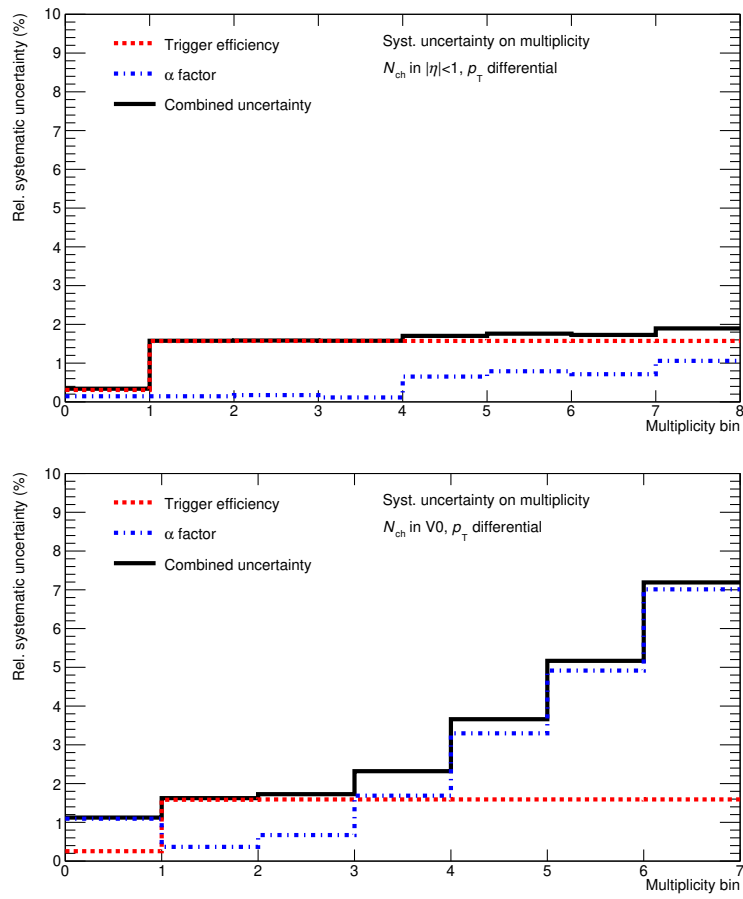


Figure B.1.: Relative systematic uncertainty on the self-normalized multiplicity at mid-rapidity (top), and at forward rapidity (bottom), as function of the multiplicity interval used in the analysis in p_T intervals. Uncertainty due to trigger efficiency, α factor, and total uncertainty as combination of the two.

Fig. B.1 shows the relative systematic uncertainty of the charged-particle multiplicity for the wider multiplicity intervals used in the analysis in p_T intervals. The qualitative features are the same as for the intervals of the p_T integrated analysis: a flat uncertainty from the trigger efficiency, and an uncertainty from the α factor that is increasing with multiplicity, and much larger in case of the forward multiplicity than of the mid-rapidity multiplicity.

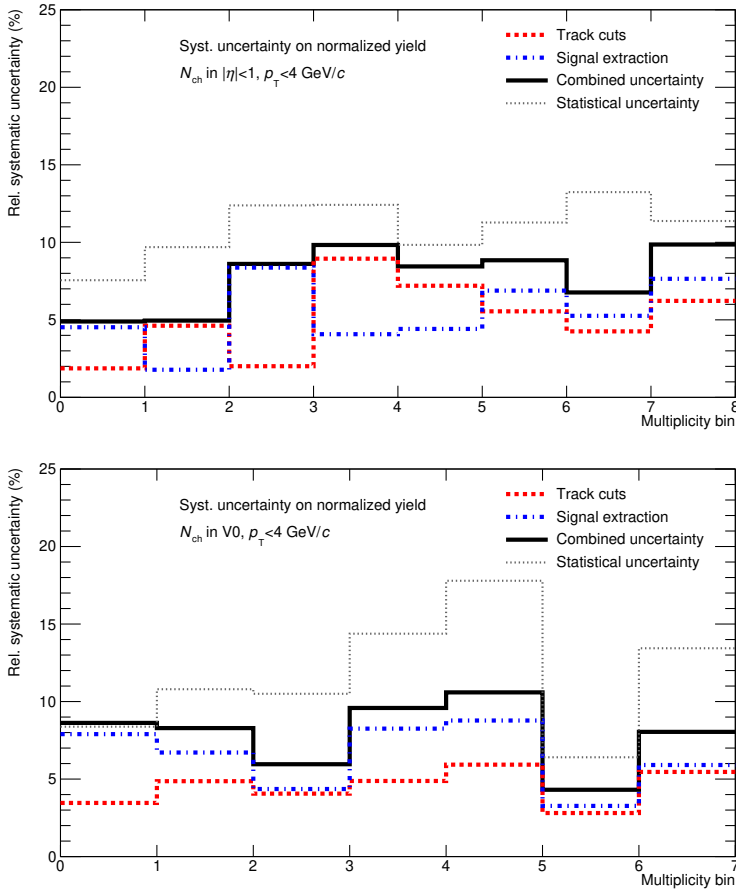


Figure B.2.: Relative systematic uncertainty on the self-normalized J/ψ yield at $p_T < 4 \text{ GeV}/c$ as function of the multiplicity interval at mid-rapidity (top) and at forward rapidity (bottom). Uncertainty due to the track selection, the signal extraction, and the total systematic uncertainty as combination of the two. Statistical uncertainty shown for comparison.

B.2 Uncertainty on the J/ψ yield

Fig. B.2 shows the relative systematic uncertainty of the normalized J/ψ yield for J/ψ with $p_T < 4 \text{ GeV}/c$, and Fig. B.3 for $p_T > 4 \text{ GeV}/c$. The statistical uncertainty is shown for comparison. As in the p_T integrated analysis, the contributions to the uncertainty from the track selection and the signal extraction are of similar size.

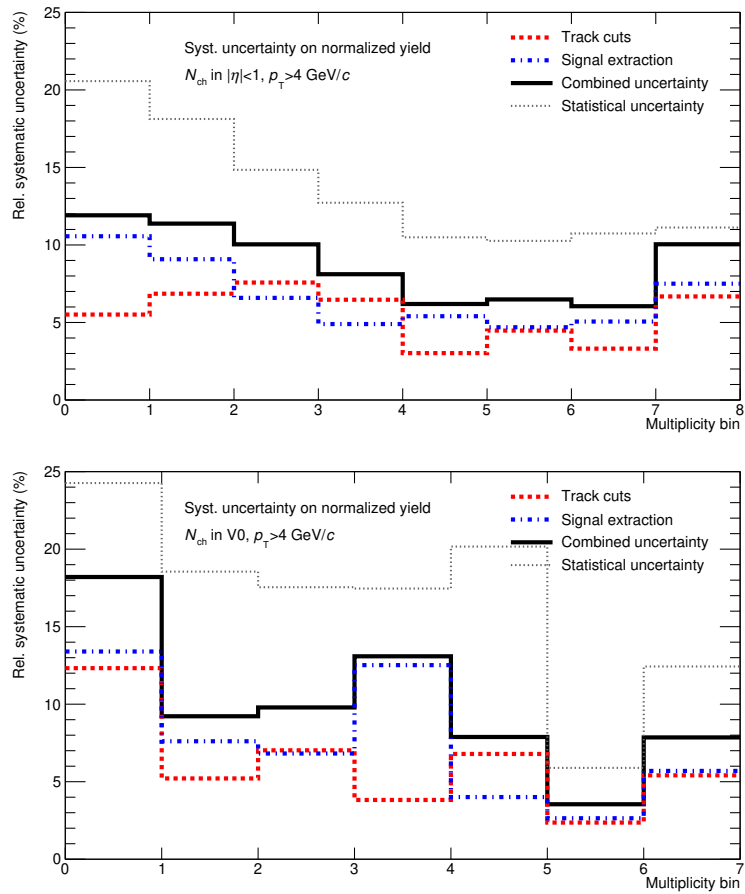


Figure B.3.: Relative systematic uncertainty on the self-normalized J/ψ yield at $p_T > 4 \text{ GeV}/c$ as function of the multiplicity interval at mid-rapidity (top) and at forward rapidity (bottom). Uncertainty due to the track selection, the signal extraction, and the total systematic uncertainty as combination of the two. Statistical uncertainty shown for comparison.



C Additional plots of the experimental results

Figures C.1, C.2 and C.3 show the self-normalized J/ψ yield $n_{J/\psi}$ in the left and the double ratio $r_{J/\psi}$ in the right in p_T intervals as a function of $n_{ch,mid}$, p_T -integrated as a function of $n_{ch,fwd.}$, and in p_T intervals as a function of $n_{ch,fwd.}$, respectively.

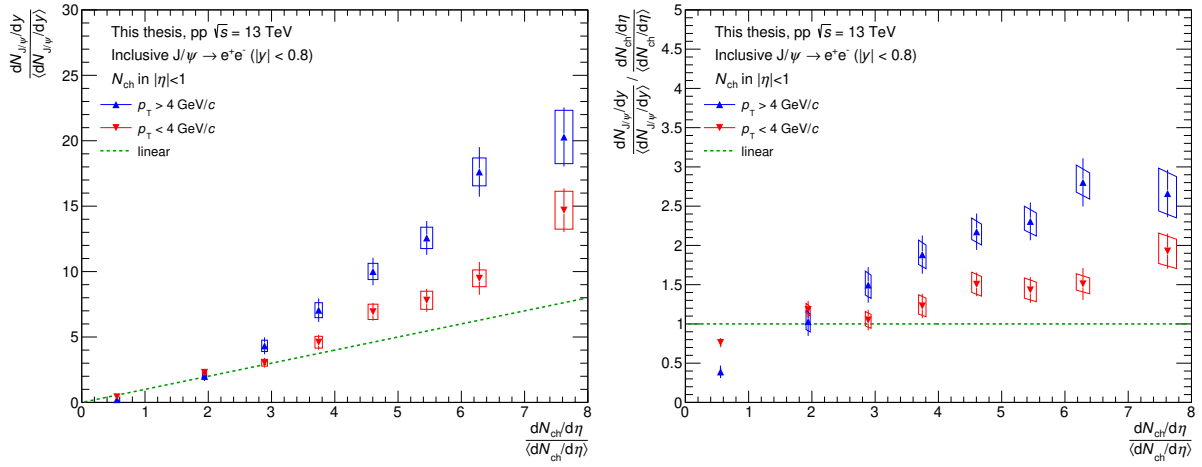


Figure C.1.: Inclusive J/ψ production at mid-rapidity in p_T intervals as a function of self-normalized charged-particle multiplicity at mid-rapidity in pp collisions at $\sqrt{s} = 13$ TeV. Left: Self-normalized J/ψ yield, right: ratio of J/ψ yield and multiplicity.

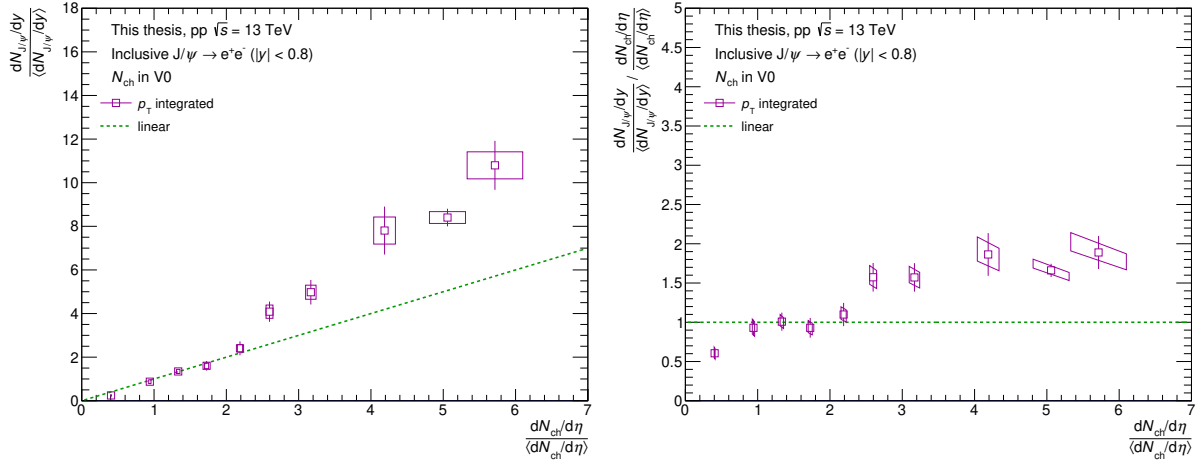


Figure C.2.: Inclusive J/ψ production at mid-rapidity as a function of self-normalized charged-particle multiplicity at forward rapidity in pp collisions at $\sqrt{s} = 13$ TeV. Left: Self-normalized J/ψ yield, right: ratio of J/ψ yield and multiplicity.

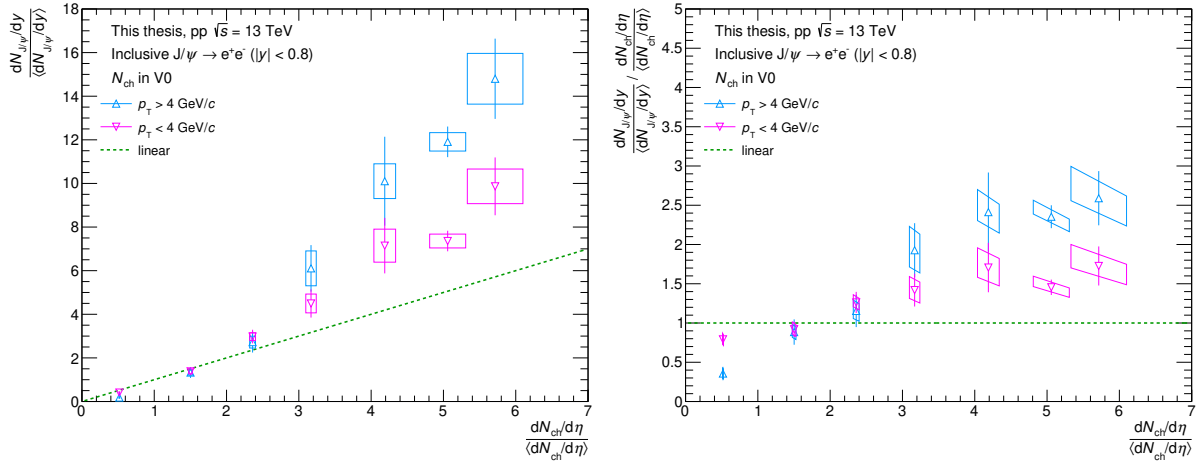


Figure C.3.: Inclusive J/ψ production at mid-rapidity in p_T intervals as a function of self-normalized charged-particle multiplicity at forward rapidity in pp collisions at $\sqrt{s} = 13$ TeV. Left: Self-normalized J/ψ yield, right: ratio of J/ψ yield and multiplicity.

C.1 Fit results

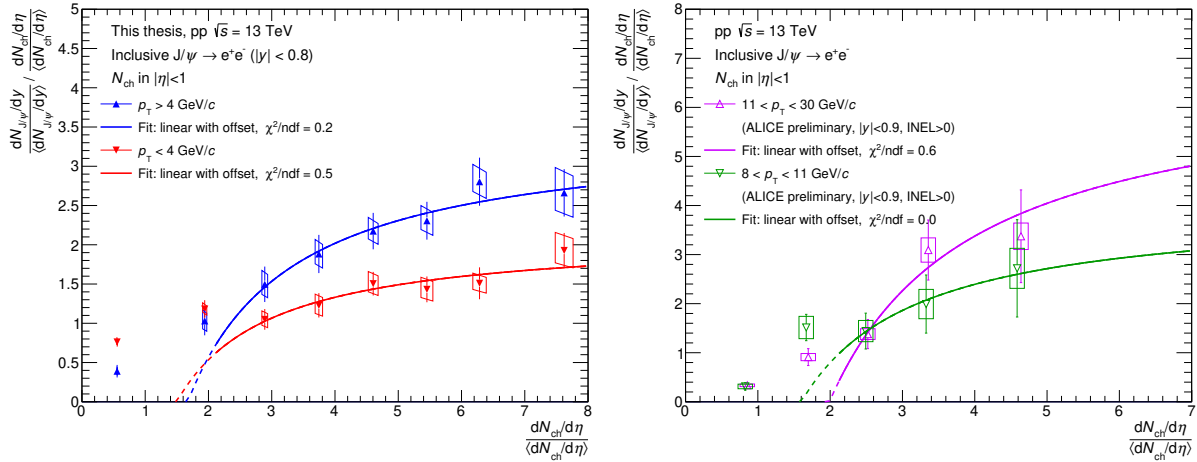


Figure C.4.: Ratio of J/ψ yield and multiplicity in p_T intervals as a function of self-normalized charged-particle multiplicity at mid-rapidity in pp collisions at $\sqrt{s} = 13$ TeV, compared to fit assuming a linear increase with an offset. Left: results of presented analysis, right: results of EMCAL-based analysis.

Figures C.4, C.5, C.6, C.7, C.8 and C.9 show the result of the fits of a linear function with offset, of a polynomial function, and of a powerlaw function to $r_{J/\psi}$ in p_T intervals as a function of $n_{ch,mid}$, to the results from the EMCAL-based analysis [183], to $r_{J/\psi}$ as a function of the $n_{ch,fwd.}$, p_T -integrated, and in p_T intervals, respectively.

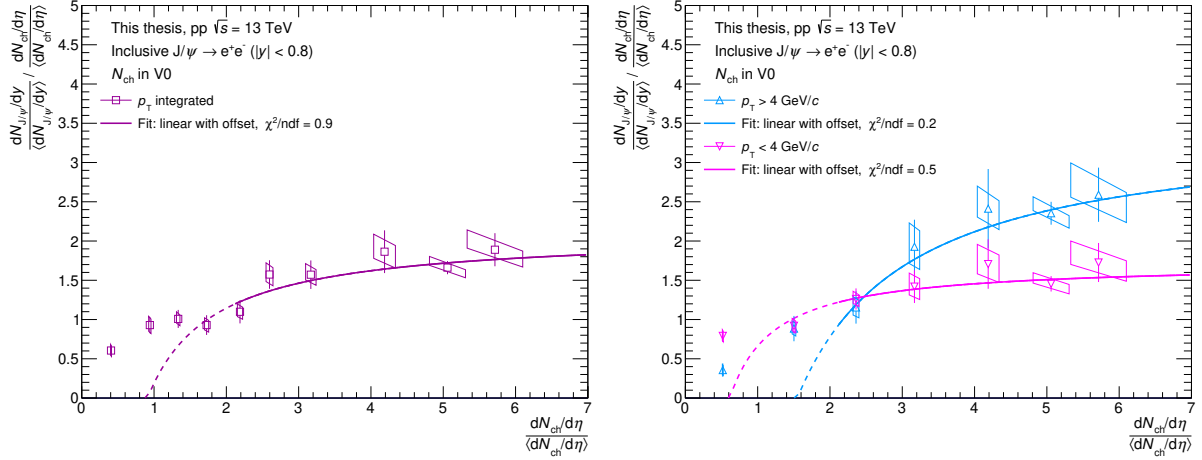


Figure C.5.: Ratio of J/ψ yield and multiplicity as a function of self-normalized charged-particle multiplicity at forward rapidity in pp collisions at $\sqrt{s} = 13$ TeV, compared to fit assuming a linear increase with an offset. Left: p_T -integrated results, right: result in p_T intervals.

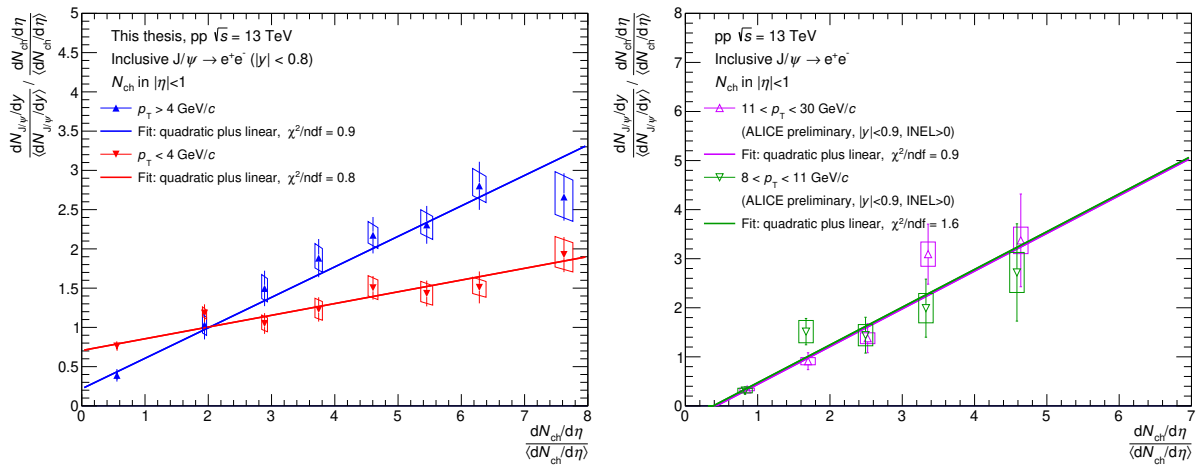


Figure C.6.: Ratio of J/ψ yield and multiplicity in p_T intervals as a function of self-normalized charged-particle multiplicity at mid-rapidity in pp collisions at $\sqrt{s} = 13$ TeV, compared to fit assuming a combination of a linear and quadratic increase. Left: results of presented analysis, right: results of EMCAL-based analysis.

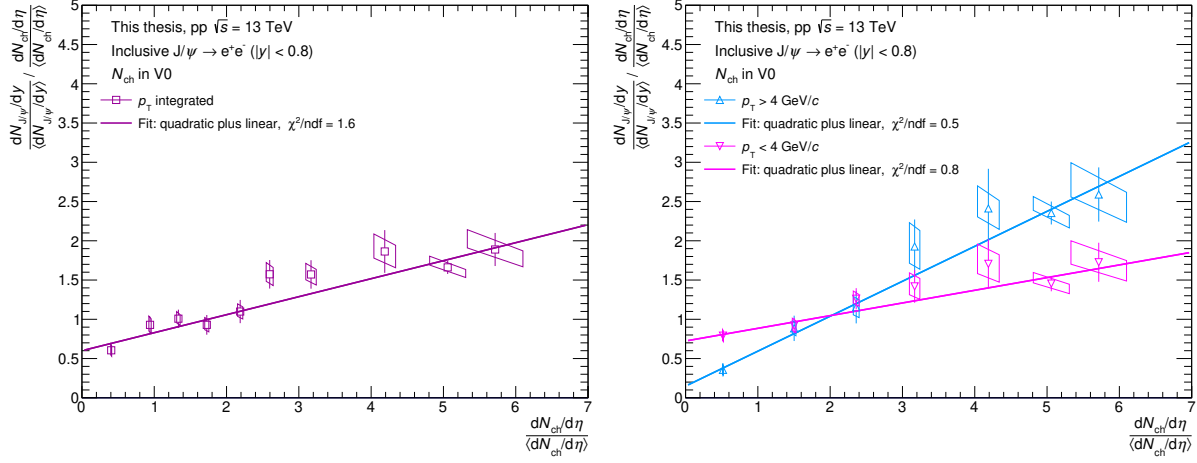


Figure C.7.: Ratio of J/ψ yield and multiplicity as a function of self-normalized charged-particle multiplicity at forward rapidity in pp collisions at $\sqrt{s} = 13$ TeV, compared to fit assuming a combination of a linear and quadratic increase. Left: p_T -integrated results, right: result in p_T intervals.

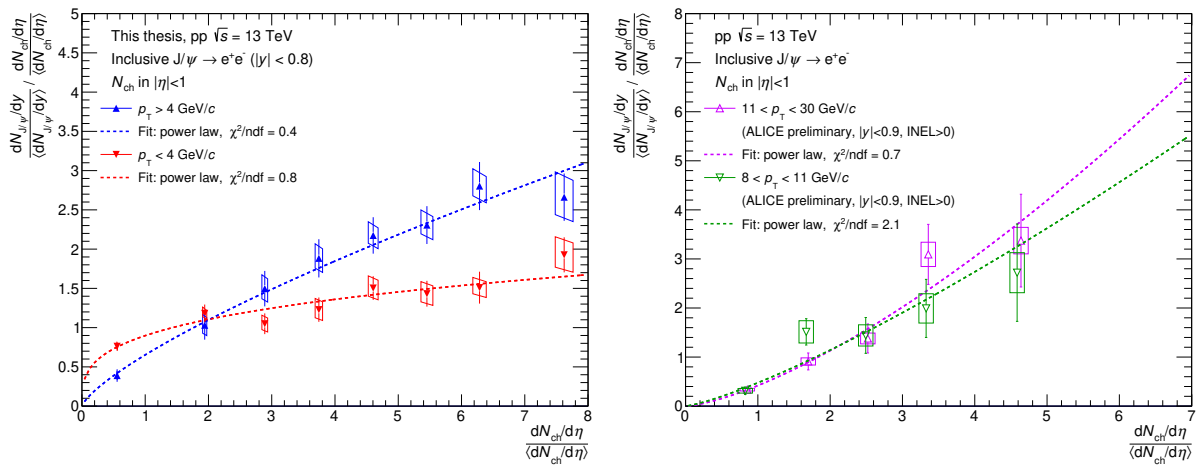


Figure C.8.: Ratio of J/ψ yield and multiplicity in p_T intervals as a function of self-normalized charged-particle multiplicity at mid-rapidity in pp collisions at $\sqrt{s} = 13$ TeV, compared to fit assuming a powerlaw function for the increase. Left: results of presented analysis, right: results of EMCal-based analysis.

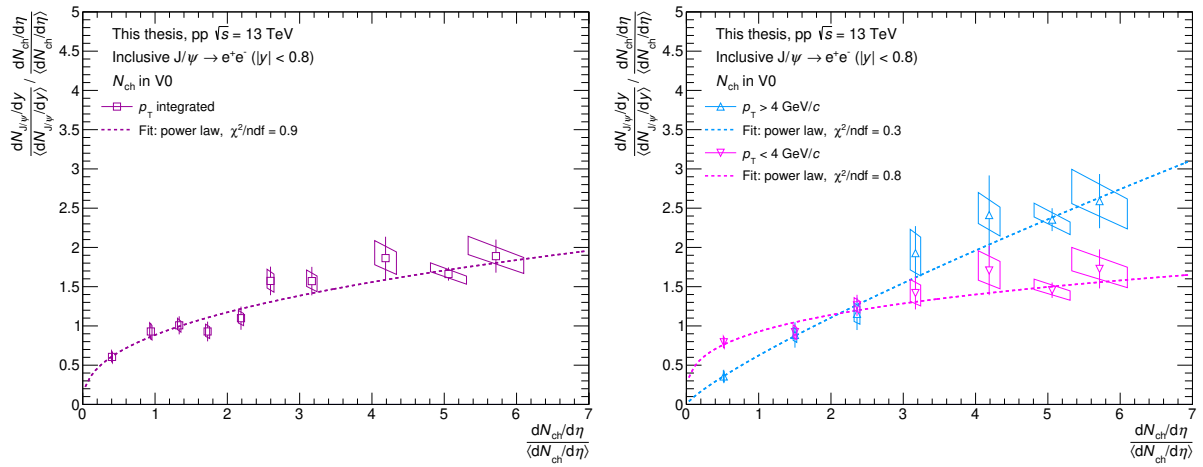


Figure C.9.: Ratio of J/ψ yield and multiplicity as a function of self-normalized charged-particle multiplicity at forward rapidity in pp collisions at $\sqrt{s} = 13$ TeV, compared to fit assuming a powerlaw function for the increase. Left: p_T -integrated results, right: results in p_T intervals.



Bibliography

- [1] C. Patrignani et al. Review of Particle Physics. *Chin. Phys.*, C40(10):100001, 2016.
- [2] P. A. R. Ade et al. Planck 2015 results. XIII. Cosmological parameters. *Astron. Astrophys.*, 594:A13, 2016, 1502.01589.
- [3] D. J. Gross and F. Wilczek. Ultraviolet Behavior of Nonabelian Gauge Theories. *Phys. Rev. Lett.*, 30:1343–1346, 1973. [,271(1973)].
- [4] H. D. Politzer. Reliable Perturbative Results for Strong Interactions? *Phys. Rev. Lett.*, 30:1346–1349, 1973. [,274(1973)].
- [5] R. Aaij et al. Observation of $J/\psi p$ Resonances Consistent with Pentaquark States in $\Lambda_b^0 \rightarrow J/\psi K^- p$ Decays. *Phys. Rev. Lett.*, 115:072001, 2015, 1507.03414.
- [6] R. Aaij et al. Observation of $J/\psi \phi$ structures consistent with exotic states from amplitude analysis of $B^+ \rightarrow J/\psi \phi K^+$ decays. *Phys. Rev. Lett.*, 118(2):022003, 2017, 1606.07895.
- [7] P. W. Higgs. Broken symmetries, massless particles and gauge fields. *Phys. Lett.*, 12:132–133, 1964.
- [8] P. W. Higgs. Broken Symmetries and the Masses of Gauge Bosons. *Phys. Rev. Lett.*, 13:508–509, 1964. [,160(1964)].
- [9] F. Englert and R. Brout. Broken Symmetry and the Mass of Gauge Vector Mesons. *Phys. Rev. Lett.*, 13:321–323, 1964. [,157(1964)].
- [10] G. S. Guralnik, C. R. Hagen, and T. W. B. Kibble. Global Conservation Laws and Massless Particles. *Phys. Rev. Lett.*, 13:585–587, 1964. [,162(1964)].
- [11] G. Aad et al. Observation of a new particle in the search for the Standard Model Higgs boson with the ATLAS detector at the LHC. *Phys. Lett.*, B716:1–29, 2012, 1207.7214.
- [12] S. Chatrchyan et al. Observation of a new boson at a mass of 125 GeV with the CMS experiment at the LHC. *Phys. Lett.*, B716:30–61, 2012, 1207.7235.
- [13] S. P. Martin. A Supersymmetry primer. pages 1–98, 1997, hep-ph/9709356. [Adv. Ser. Direct. High Energy Phys.18,1(1998)].
- [14] C. Patrignani et al. Review of Particle Physics. *Chin. Phys.*, C40(10):100001, 2016.
- [15] V. Khachatryan et al. Measurement of diffractive dissociation cross sections in pp collisions at $\sqrt{s} = 7$ TeV. *Phys. Rev.*, D92(1):012003, 2015, 1503.08689.
- [16] J. F. Grosse-Oetringhaus. *Measurement of the Charged-Particle Multiplicity in Proton-Proton Collisions with the ALICE Detector*. PhD thesis, Münster U., 2009.
- [17] P. D. B. Collins. *An Introduction to Regge Theory and High-Energy Physics*. Cambridge Monographs on Mathematical Physics. Cambridge Univ. Press, Cambridge, UK, 2009.
- [18] G. Aad et al. Measurement of the Inelastic Proton-Proton Cross-Section at $\sqrt{s} = 7$ TeV with the ATLAS Detector. *Nature Commun.*, 2:463, 2011, 1104.0326.

[19] R. D. Ball et al. Parton distributions from high-precision collider data. *Eur. Phys. J.*, C77(10):663, 2017, 1706.00428.

[20] W. J. Stirling. private communication.

[21] E. Iancu and R. Venugopalan. The Color glass condensate and high-energy scattering in QCD. In Rudolph C. Hwa and Xin-Nian Wang, editors, *Quark-gluon plasma 4*, pages 249–3363. 2003, hep-ph/0303204.

[22] R. Placakyte. Parton Distribution Functions. In *Proceedings, 31st International Conference on Physics in collisions (PIC 2011): Vancouver, Canada, August 28-September 1, 2011*, 2011, 1111.5452.

[23] Y. L. Dokshitzer. Calculation of the Structure Functions for Deep Inelastic Scattering and e+ e- Annihilation by Perturbation Theory in Quantum Chromodynamics. *Sov. Phys. JETP*, 46:641–653, 1977. [Zh. Eksp. Teor. Fiz. 73, 1216(1977)].

[24] V. N. Gribov and L. N. Lipatov. Deep inelastic e p scattering in perturbation theory. *Sov. J. Nucl. Phys.*, 15:438–450, 1972. [Yad. Fiz. 15, 781(1972)].

[25] G. Altarelli and G. Parisi. Asymptotic Freedom in Parton Language. *Nucl. Phys.*, B126:298–318, 1977.

[26] T. Sjöstrand, S. Ask, J. R. Christiansen, R. Corke, N. Desai, P. Ilten, S. Mrenna, S. Prestel, C. O. Rasmussen, and P. Z. Skands. An Introduction to PYTHIA 8.2. *Comput. Phys. Commun.*, 191:159–177, 2015, 1410.3012.

[27] H. J. Drescher, M. Hladik, S. Ostapchenko, T. Pierog, and K. Werner. Parton based Gribov-Regge theory. *Phys. Rept.*, 350:93–289, 2001, hep-ph/0007198.

[28] S. G. Matinyan and W. D. Walker. Multiplicity distribution and mechanisms of the high-energy hadron collisions. *Phys. Rev.*, D59:034022, 1999, hep-ph/9801219.

[29] R. Aaij et al. Observation of double charm production involving open charm in pp collisions at $\sqrt{s} = 7$ TeV. *JHEP*, 06:141, 2012, 1205.0975. [Addendum: JHEP03,108(2014)].

[30] R. P. Feynman. Very high-energy collisions of hadrons. *Phys. Rev. Lett.*, 23:1415–1417, 1969. [,494(1969)].

[31] V. Khachatryan et al. Transverse momentum and pseudorapidity distributions of charged hadrons in pp collisions at $\sqrt{s} = 0.9$ and 2.36 TeV. *JHEP*, 02:041, 2010, 1002.0621.

[32] Z. Koba, H. B. Nielsen, and P. Olesen. Scaling of multiplicity distributions in high-energy hadron collisions. *Nucl. Phys.*, B40:317–334, 1972.

[33] J. F. Grosse-Oetringhaus and K. Reygers. Charged-Particle Multiplicity in Proton-Proton Collisions. *J. Phys.*, G37:083001, 2010, 0912.0023.

[34] J. Adam et al. Pseudorapidity and transverse-momentum distributions of charged particles in proton-proton collisions at $\sqrt{s} = 13$ TeV. *Phys. Lett.*, B753:319–329, 2016, 1509.08734.

[35] G. Aad et al. Charged-particle distributions in $\sqrt{s} = 13$ TeV pp interactions measured with the ATLAS detector at the LHC. *Phys. Lett.*, B758:67–88, 2016, 1602.01633.

[36] A. Bazavov et al. Equation of state in (2+1)-flavor QCD. *Phys. Rev.*, D90:094503, 2014, 1407.6387.

[37] A. Andronic, P. Braun-Munzinger, K. Redlich, and J. Stachel. Decoding the phase structure of QCD via particle production at high energy. *Nature*, 561(7723):321–330, 2018, 1710.09425.

[38] J. C. Collins and M. J. Perry. Superdense matter: Neutrons or asymptotically free quarks? *Phys. Rev. Lett.*, 34:1353–1356, May 1975.

[39] R. Hagedorn. Statistical thermodynamics of strong interactions at high-energies. *Nuovo Cim. Suppl.*, 3:147–186, 1965.

[40] N. Cabibbo and G. Parisi. Exponential Hadronic Spectrum and Quark Liberation. *Phys. Lett.*, 59B:67–69, 1975.

[41] P. Braun-Munzinger, K. Redlich, and J. Stachel. *Particle Production in Heavy Ion Collisions*, Invited Review, in: R. C. Hwa, X. N. Wang (Eds.), Quark Gluon Plasma Vol. 3, pages 491–599. World Scientific Publishing, 2004, 0304013.

[42] J.-Y. Ollitrault. Anisotropy as a signature of transverse collective flow. *Phys. Rev. D*, 46:229–245, Jul 1992.

[43] J. D. Bjorken. Energy Loss of Energetic Partons in Quark - Gluon Plasma: Possible Extinction of High $p(t)$ Jets in Hadron - Hadron Collisions. 1982.

[44] J. Rafelski and B. Muller. Strangeness Production in the Quark - Gluon Plasma. *Phys. Rev. Lett.*, 48:1066, 1982. [Erratum: *Phys. Rev. Lett.* 56, 2334 (1986)].

[45] T. Matsui and H. Satz. J/ψ Suppression by Quark-Gluon Plasma Formation. *Phys. Lett.*, B178:416, 1986.

[46] P. Braun-Munzinger and J. Stachel. (Non)thermal aspects of charmonium production and a new look at J/ψ suppression. *Phys. Lett.*, B490:196–202, 2000, nucl-th/0007059.

[47] R. L. Thews, M. Schroedter, and J. Rafelski. Enhanced J/ψ production in deconfined quark matter. *Phys. Rev.*, C63:054905, 2001.

[48] V. Khachatryan et al. Observation of Long-Range Near-Side Angular Correlations in Proton-Proton Collisions at the LHC. *JHEP*, 09:091, 2010, 1009.4122.

[49] J. Adam et al. Enhanced production of multi-strange hadrons in high-multiplicity proton-proton collisions. *Nature Phys.*, 13:535–539, 2017, 1606.07424.

[50] S. Hamieh, K. Redlich, and A. Tounsi. Canonical description of strangeness enhancement from p-A to Pb Pb collisions. *Phys. Lett.*, B486:61–66, 2000, hep-ph/0006024.

[51] R. D. Weller and P. Romatschke. One fluid to rule them all: viscous hydrodynamic description of event-by-event central p+p, p+Pb and Pb+Pb collisions at $\sqrt{s} = 5.02$ TeV. *Phys. Lett.*, B774:351–356, 2017, 1701.07145.

[52] B. Blok, C. D. Jäkel, M. Strikman, and U. A. Wiedemann. Collectivity from interference. *JHEP*, 12:074, 2017, 1708.08241.

[53] A. Dumitru, K. Dusling, F. Gelis, J. Jalilian-Marian, T. Lappi, and R. Venugopalan. The Ridge in proton-proton collisions at the LHC. *Phys. Lett.*, B697:21–25, 2011, 1009.5295.

[54] A. Ortiz Velasquez, P. Christiansen, E. Cuautle Flores, I. Maldonado Cervantes, and G. Paić. Color Reconnection and Flowlike Patterns in pp Collisions. *Phys. Rev. Lett.*, 111(4):042001, 2013, 1303.6326.

[55] C. Bierlich. Rope Hadronization and Strange Particle Production. *EPJ Web Conf.*, 171:14003, 2018, 1710.04464.

[56] C. Bierlich, G. Gustafson, and L. Lönnblad. A shoving model for collectivity in hadronic collisions. 2016, 1612.05132.

[57] J. J. Aubert et al. Experimental Observation of a Heavy Particle *J. Phys. Rev. Lett.*, 33:1404–1406, 1974.

[58] J. E. Augustin et al. Discovery of a Narrow Resonance in e^+e^- Annihilation. *Phys. Rev. Lett.*, 33:1406–1408, 1974. [Adv. Exp. Phys.5,141(1976)].

[59] J. D. Bjorken and S. L. Glashow. Elementary Particles and SU(4). *Phys. Lett.*, 11:255–257, 1964.

[60] S. L. Glashow, J. Iliopoulos, and L. Maiani. Weak interactions with lepton-hadron symmetry. *Phys. Rev. D*, 2:1285–1292, Oct 1970.

[61] J. Beringer et al. Review of Particle Physics (RPP). *Phys. Rev.*, D86:010001, 2012.

[62] S. Okubo. Phi meson and unitary symmetry model. *Phys. Lett.*, 5:165–168, 1963.

[63] G. Zweig. An SU₃ model for strong interaction symmetry and its breaking; Version 2. (CERN-TH-412):80 p, Feb 1964. Version 1 is CERN preprint 8182/TH.401, Jan. 17, 1964.

[64] J. Iizuka. Systematics and phenomenology of meson family. *Prog. Theor. Phys. Suppl.*, 37:21–34, 1966.

[65] G. S. Abrams et al. The Discovery of a Second Narrow Resonance in e+ e- Annihilation. *Phys. Rev. Lett.*, 33:1453–1455, 1974. [Adv. Exp. Phys.5,150(1976)].

[66] W. Braunschweig et al. Observation of the Two Photon Cascade $3.7\text{ GeV} \rightarrow 3.1\text{ GeV} + \gamma\gamma$ via an Intermediate State P_c. *Phys. Lett.*, 57B:407–412, 1975.

[67] G. J. Feldman et al. $\psi(3684)$ Radiative Decays to High Mass States. *Phys. Rev. Lett.*, 35:821, 1975. [Erratum: Phys. Rev. Lett.35,1184(1975)].

[68] R. Partridge et al. Observation of an η_c Candidate State with Mass $2978\text{ MeV} \pm 9\text{ MeV}$. *Phys. Rev. Lett.*, 45:1150–1153, 1980.

[69] C. Baglin et al. Formation of the χ_1 and χ_2 charmonium resonances in antiproton-proton annihilation and measurements of their masses and total widths. *Physics Letters B*, 172(3):455 – 460, 1986.

[70] S. K. Choi et al. Observation of the $\eta_c(2S)$ in exclusive $B \rightarrow KK_SK^-\pi^+$ decays. *Phys. Rev. Lett.*, 89:102001, 2002, hep-ex/0206002. [Erratum: Phys. Rev. Lett.89,129901(2002)].

[71] J. L. Rosner et al. Observation of $h_c(^1P_1)$ state of charmonium. *Phys. Rev. Lett.*, 95:102003, 2005, hep-ex/0505073.

[72] P. Rubin et al. Observation of the 1P_1 state of charmonium. *Phys. Rev.*, D72:092004, 2005, hep-ex/0508037.

[73] M. Andreotti et al. Results of a search for the $h_c(^1P_1)$ state of charmonium in the $\eta_c\gamma$ and $J/\psi\pi^0$ decay modes. *Phys. Rev. D*, 72:032001, Aug 2005.

[74] R. Faccini, A. Pilloni, and A. D. Polosa. Exotic Heavy Quarkonium Spectroscopy: A Mini-review. *Mod. Phys. Lett.*, A27:1230025, 2012, 1209.0107.

[75] S. Acharya et al. Prompt and non-prompt J/ψ production and nuclear modification at mid-rapidity in p-Pb collisions at $\sqrt{s_{\text{NN}}} = 5.02 \text{ TeV}$. *Eur. Phys. J.*, C78(6):466, 2018, 1802.00765.

[76] R. Aaij et al. Measurement of the ratio of prompt χ_c to J/ψ production in pp collisions at $\sqrt{s} = 7 \text{ TeV}$. *Phys. Lett.*, B718:431–440, 2012, 1204.1462.

[77] F. Abe et al. Production of J/ψ mesons from χ_c meson decays in $p\bar{p}$ collisions at $\sqrt{s} = 1.8 \text{ TeV}$. *Phys. Rev. Lett.*, 79:578–583, 1997.

[78] P. Faccioli, C. Lourenco, J. Seixas, and H. K. Woehri. Study of ψ and χ_c decays as feed-down sources of J/ψ hadro-production. *JHEP*, 0810:004, 2008, 0809.2153.

[79] N. Brambilla et al. Heavy quarkonium: progress, puzzles, and opportunities. *Eur. Phys. J.*, C71:1534, 2011, 1010.5827.

[80] E. Braaten. Introduction to the NRQCD factorization approach to heavy quarkonium. In *3rd International Workshop on Particle Physics Phenomenology Taipei, Taiwan, November 14-17, 1996*, 1996, hep-ph/9702225.

[81] M. L. Mangano, P. Nason, and G. Ridolfi. Heavy quark correlations in hadron collisions at next-to-leading order. *Nucl. Phys.*, B373:295–345, 1992.

[82] M. Cacciari, M. Greco, and P. Nason. The $P(T)$ spectrum in heavy flavor hadroproduction. *JHEP*, 05:007, 1998, hep-ph/9803400.

[83] M. Cacciari, S. Frixione, and P. Nason. The $p(T)$ spectrum in heavy flavor photoproduction. *JHEP*, 03:006, 2001, hep-ph/0102134.

[84] H. Fritzsch. Producing heavy quark flavors in hadronic collisions: a test of quantum chromodynamics. *Phys. Lett. B*, 67(CALT-68-582):217, 1977.

[85] E. C. Poggio, H. R. Quinn, and S. Weinberg. Smearing method in the quark model. *Phys. Rev. D*, 13:1958–1968, Apr 1976.

[86] R. E. Nelson, R. Vogt, and A. D. Frawley. Narrowing the uncertainty on the total charm cross section and its effect on the J/ψ cross section. *Phys. Rev.*, C87(1):014908, 2013, 1210.4610.

[87] S. Acharya et al. Energy dependence of forward-rapidity J/ψ and $\psi(2S)$ production in pp collisions at the LHC. *Eur. Phys. J.*, C77(6):392, 2017, 1702.00557.

[88] Y.-Q. Ma and R. Vogt. Quarkonium Production in an Improved Color Evaporation Model. *Phys. Rev.*, D94(11):114029, 2016, 1609.06042.

[89] R. Baier and R. Rückl. Hadronic Production of J/ψ and Υ : Transverse Momentum Distributions. *Phys. Lett.*, 102B:364–370, 1981.

[90] M. Krämer. Quarkonium production at high-energy colliders. *Prog. Part. Nucl. Phys.*, 47:141–201, 2001, hep-ph/0106120.

[91] R. Baier and R. Rückl. Hadronic Collisions: A Quarkonium Factory. *Z. Phys.*, C19:251, 1983.

[92] F. Abe et al. J/ψ and $\psi(2S)$ Production in $p\bar{p}$ Collisions at $\sqrt{s} = 1.8 \text{ TeV}$. *Phys. Rev. Lett.*, 79:572–577, Jul 1997.

[93] B. Abelev et al. Measurement of quarkonium production at forward rapidity in pp collisions at $\sqrt{s} = 7 \text{ TeV}$. *Eur. Phys. J.*, C74(8):2974, 2014, 1403.3648.

[94] G. T. Bodwin, E. Braaten, and G. P. Lepage. Rigorous QCD analysis of inclusive annihilation and production of heavy quarkonium. *Phys. Rev.*, D51:1125–1171, 1995, hep-ph/9407339. [Erratum: *Phys. Rev.* D55, 5853(1997)].

[95] E. Braaten and S. Fleming. Color octet fragmentation and the psi-prime surplus at the Tevatron. *Phys. Rev. Lett.*, 74:3327–3330, 1995, hep-ph/9411365.

[96] Y.-Q. Ma and R. Venugopalan. Comprehensive Description of J/ψ Production in Proton-Proton Collisions at Collider Energies. *Phys. Rev. Lett.*, 113(19):192301, 2014, 1408.4075.

[97] M. Butenschön, Z.-G. He, and B. A. Kniehl. η_c production at the LHC challenges nonrelativistic-QCD factorization. *Phys. Rev. Lett.*, 114(9):092004, 2015, 1411.5287.

[98] R. Aaij et al. Measurement of J/ψ polarization in pp collisions at $\sqrt{s} = 7$ TeV. *Eur. Phys. J.*, C73(11):2631, 2013, 1307.6379.

[99] R. Aaij et al. Study of J/ψ Production in Jets. *Phys. Rev. Lett.*, 118(19):192001, 2017, 1701.05116.

[100] G. T. Bodwin, E. Braaten, and G. P. Lepage. Rigorous QCD analysis of inclusive annihilation and production of heavy quarkonium. *Phys. Rev. D*, 51:1125–1171, Feb 1995.

[101] J. F. Amundson, O. J. P. Éboli, E. M. Gregores, and F. Halzen. Quantitative tests of color evaporation: charmonium production. *Physics Letters B*, 390(1):323 – 328, 1997.

[102] J. P. Lansberg. J/ψ production at $\sqrt{s}=1.96$ and 7 TeV: Color-Singlet Model, NNLO* and polarisation. *J. Phys.*, G38:124110, 2011, 1107.0292.

[103] M. G. Albrow, T. D. Coughlin, and J. R. Forshaw. Central Exclusive Particle Production at High Energy Hadron Colliders. *Prog. Part. Nucl. Phys.*, 65:149–184, 2010, 1006.1289.

[104] R. Aaij et al. Central exclusive production of J/ψ and $\psi(2S)$ mesons in pp collisions at $\sqrt{s} = 13$ TeV. *Submitted to: JHEP*, 2018, 1806.04079.

[105] B. Abelev et al. Exclusive J/ψ photoproduction off protons in ultra-peripheral p-Pb collisions at $\sqrt{s_{NN}} = 5.02$ TeV. *Phys. Rev. Lett.*, 113(23):232504, 2014, 1406.7819.

[106] R. Aaij et al. Exclusive J/ψ and $\psi(2S)$ production in pp collisions at $\sqrt{s} = 7$ TeV. *J. Phys.*, G40:045001, 2013, 1301.7084.

[107] O. Kaczmarek and F. Zantow. Static quark anti-quark interactions in zero and finite temperature QCD. I. Heavy quark free energies, running coupling and quarkonium binding. *Phys. Rev.*, D71:114510, 2005, hep-lat/0503017.

[108] F. Karsch, M. T. Mehr, and H. Satz. Color screening and deconfinement for bound states of heavy quarks. *Z. Phys. C*, 37(BNL-40122):617–622. 20 p, Jun 1987.

[109] B. Alessandro et al. A New measurement of J/ψ suppression in Pb-Pb collisions at 158-GeV per nucleon. *Eur. Phys. J.*, C39:335–345, 2005, hep-ex/0412036.

[110] H. Satz. Quarkonium Binding and Dissociation: The Spectral Analysis of the QGP. *Nucl. Phys.*, A783:249–260, 2007, hep-ph/0609197.

[111] R. T. Jiménez Bustamante. *Inclusive J/ψ production at mid-rapidity in Pb-Pb collisions at $\sqrt{s_{NN}} = 5.02$ TeV*. PhD thesis, Heidelberg U., 2018.

[112] P. Braun-Munzinger and J. Stachel. On charm production near the phase boundary. *Nucl. Phys.*, A690:119–126, 2001, nucl-th/0012064.

[113] X. Zhao and R. Rapp. Medium Modifications and Production of Charmonia at LHC. *Nucl. Phys.*, A859:114–125, 2011, 1102.2194.

[114] K. Zhou, N. Xu, Z. Xu, and P. Zhuang. Medium effects on charmonium production at ultrarelativistic energies available at the CERN Large Hadron Collider. *Phys. Rev.*, C89(5):054911, 2014, 1401.5845.

[115] E. G. Ferreiro. Charmonium dissociation and recombination at LHC: Revisiting comovers. *Phys. Lett.*, B731:57–63, 2014, 1210.3209.

[116] K. J. Eskola, H. Paukkunen, and C. A. Salgado. EPS09: A New Generation of NLO and LO Nuclear Parton Distribution Functions. *JHEP*, 04:065, 2009, 0902.4154.

[117] J. Adam et al. Centrality dependence of inclusive J/ψ production in p-Pb collisions at $\sqrt{s_{NN}} = 5.02$ TeV. *JHEP*, 11:127, 2015, 1506.08808.

[118] J. Adam et al. Rapidity and transverse-momentum dependence of the inclusive J/ψ nuclear modification factor in p-Pb collisions at $\sqrt{s_{NN}} = 5.02$ TeV. *JHEP*, 06:055, 2015, 1503.07179.

[119] M. Aguilar-Benitez et al. Comparative properties of 400 GeV/c proton-proton interactions with and without charm production. *Z. Phys. C*, 41(2):191–196, Jun 1988.

[120] S. Porteboeuf and R. Granier de Cassagnac. J/ψ yield vs. multiplicity in proton-proton collisions at the LHC. *Nucl. Phys. Proc. Suppl.*, 214:181–184, 2011, 1012.0719.

[121] B. Abelev et al. J/ψ production as a function of charged particle multiplicity in pp collisions at $\sqrt{s} = 7$ TeV. *Phys. Lett.*, B712:165–175, 2012, 1202.2816.

[122] D. Adamová et al. J/ψ production as a function of charged-particle pseudorapidity density in p-Pb collisions at $\sqrt{s_{NN}} = 5.02$ TeV. *Phys. Lett.*, B776:91–104, 2018, 1704.00274.

[123] J. Adam et al. Measurement of charm and beauty production at central rapidity versus charged-particle multiplicity in proton-proton collisions at $\sqrt{s} = 7$ TeV. *JHEP*, 09:148, 2015, 1505.00664.

[124] B. Trzeciak. J/ψ and $\psi(2S)$ measurement in p+p collisions $\sqrt{s} = 200$ and 500 GeV with the STAR experiment. *J. Phys. Conf. Ser.*, 668(1):012093, 2016, 1512.07398.

[125] S. Chatrchyan et al. Event activity dependence of $Y(nS)$ production in $\sqrt{s_{NN}} = 5.02$ TeV pPb and $\sqrt{s} = 2.76$ TeV pp collisions. *JHEP*, 04:103, 2014, 1312.6300.

[126] J. Adam et al. Measurement of D-meson production versus multiplicity in p-Pb collisions at $\sqrt{s_{NN}} = 5.02$ TeV. *JHEP*, 08:078, 2016, 1602.07240.

[127] S. A. Iga Buitron. Energy and multiplicity dependence of charged particle production in pp and p-pb collisions with alice at the lhc. Talk at the Initial Stages Conference 2017, 2017.

[128] E. G. Ferreiro and C. Pajares. High multiplicity pp events and J/ψ production at LHC. *Phys. Rev.*, C86:034903, 2012, 1203.5936.

[129] E. G. Ferreiro and C. Pajares. Open charm production in high multiplicity proton-proton events at the LHC. 2015, 1501.03381.

[130] B. Z. Kopeliovich, H. J. Pirner, I. Potashnikova, K., K. Reygers, and I. Schmidt. J/ψ in high-multiplicity pp collisions: Lessons from pA collisions. *Phys. Rev.*, D88(11):116002, 2013.

[131] Y-Q. Ma, P. Tribedy, R. Venugopalan, and K. Watanabe. Event engineering heavy flavor production and hadronization in high multiplicity hadron-hadron collisions. 2018, 1803.11093.

[132] S. G. Weber. Measurement of J/ψ production as a function of event multiplicity in pp collisions at $\sqrt{s} = 13$ TeV with ALICE. *Nucl. Phys.*, A967:333–336, 2017, 1704.04735.

[133] K. Werner, B. Guiot, Iu. Karpenko, and T. Pierog. Analysing radial flow features in p-Pb and p-p collisions at several TeV by studying identified particle production in EPOS3. *Phys. Rev.*, C89(6):064903, 2014, 1312.1233.

[134] K. Werner, Iu. Karpenko, T. Pierog, M. Bleicher, and K. Mikhailov. Evidence for hydrodynamic evolution in proton-proton scattering at 900 GeV. *Phys. Rev.*, C83:044915, 2011, 1010.0400.

[135] M. Bleicher et al. Relativistic hadron hadron collisions in the ultrarelativistic quantum molecular dynamics model. *J. Phys.*, G25:1859–1896, 1999, hep-ph/9909407.

[136] H. Petersen, J. Steinheimer, G. Burau, M. Bleicher, and H. Stöcker. A Fully Integrated Transport Approach to Heavy Ion Reactions with an Intermediate Hydrodynamic Stage. *Phys. Rev.*, C78:044901, 2008, 0806.1695.

[137] K. Werner, B. Guiot, Iu. Karpenko, T. Pierog, and G. Sophys. Charm production in high multiplicity pp events. In *Proceedings, 7th International Workshop on Multiple Partonic Interactions at the LHC (MPI@LHC 2015): Miramare, Trieste, Italy, November 23-27, 2015*, pages 66–70, 2016, 1602.03414.

[138] E. Mobs. The CERN accelerator complex. Complexe des accélérateurs du CERN. Jul 2016. General Photo.

[139] L. Evans, (ed.) and P. Bryant, (ed.). LHC Machine. *JINST*, 3:S08001, 2008.

[140] G. Aad et al. The ATLAS Experiment at the CERN Large Hadron Collider. *JINST*, 3:S08003, 2008.

[141] R. Adolphi et al. The CMS experiment at the CERN LHC. *JINST*, 3:S08004, 2008.

[142] K. Aamodt et al. The ALICE experiment at the CERN LHC. *JINST*, 3:S08002, 2008.

[143] A. A. Alves et al. The LHCb Detector at the LHC. *JINST*, 3:S08005, 2008.

[144] G. Antchev et al. The TOTEM detector at LHC. *Nucl. Instrum. Meth.*, A617:62–66, 2010.

[145] J. Pinfold et al. Technical Design Report of the MoEDAL Experiment. 2009.

[146] O. Adriani et al. The LHCf detector at the CERN Large Hadron Collider. *JINST*, 3:S08006, 2008.

[147] A. Tauro. 3D ALICE Schematic RUN2 - with Description.

[148] ALICE Collaboration. Technical Design Report of the Inner Tracking System . *CERN/LHCC 99-12*, 1999.

[149] ALICE Collaboration. Technical Design Report of the Time Projection Chamber. *CERN/LHCC 2000-001*, 2000.

[150] J. Alme, Y. Andres, H. Appelshäuser, S. Bablok, N. Bialas, R. Bolgen, U. Bonnes, R. Bramm, P. Braun-Munzinger, R. Campagnolo, et al. The alice tpc, a large 3-dimensional tracking device with fast readout for ultra-high multiplicity events. *Nuclear Instruments and Methods in Physics Research Section A: Accelerators, Spectrometers, Detectors and Associated Equipment*, 622(1):316–367, 2010.

[151] ALICE Collaboration. Technical Design Report of the Transition Radiation Detector. *CERN/LHCC 2001-021*, 2001.

[152] ALICE Collaboration. Technical Design Report of the Time of Flight System. *CERN/LHCC 2000-012*, 2000.

[153] ALICE Collaboration. Electromagnetic Calorimeter Technical Design Report. *CERN/LHCC 2008-014*, 2008.

[154] J Allen et al. ALICE DCal: An Addendum to the EMCal Technical Design Report Di-Jet and Hadron-Jet correlation measurements in ALICE. Technical Report CERN-LHCC-2010-011. ALICE-TDR-14-add-1, Jun 2010.

[155] ALICE Collaboration. Technical Design Report of the Photon Spectrometer. *CERN/LHCC 99-4*, 1999.

[156] ALICE Collaboration. Technical Design Report of the High Momentum Particle Identification Detector. *CERN/LHCC 98-19*, 1998.

[157] ALICE Collaboration. Technical Design Report of the Photon Multiplicity Detector. *CERN/LHCC 2004-025*, 2004.

[158] ALICE Collaboration. Technical Design Report on Forward Detectors: FMD, T0, V0. *CERN/LHCC 2004-025*, 2004.

[159] M. Bondila et al. ALICE T0 detector. *IEEE Trans. Nucl. Sci.*, 52:1705–1711, 2005.

[160] E. Abbas et al. Performance of the ALICE VZERO system. *JINST*, 8:P10016, 2013, 1306.3130.

[161] C. H. Christensen, J. J. Gaardhoje, K. Gulbrandsen, B. S. Nielsen, and C. Sogaard. The ALICE Forward Multiplicity Detector. *Int. J. Mod. Phys.*, E16:2432–2437, 2007, 0712.1117.

[162] A. Fernández et al. ACORDE a Cosmic Ray Detector for ALICE. *Nucl. Instrum. Meth.*, A572:102–103, 2007, physics/0606051.

[163] ALICE Collaboration. Technical Design Report of the Dimuon Forward Spectrometer. *CERN/LHCC 99-22*, 1999.

[164] A. Villatoro Tello. AD, the ALICE diffractive detector. *AIP Conf. Proc.*, 1819(1):040020, 2017.

[165] ALICE Collaboration. Technical Design Report of the Zero Degree Calorimeter (ZDC). *CERN/LHCC 99-5*, 1999.

[166] B. Abelev et al. Performance of the ALICE Experiment at the CERN LHC. *Int. J. Mod. Phys.*, A29:1430044, 2014, 1402.4476.

[167] M. Ivanov, I. Belikov, P. Hristov, and K. Šafařík. Track reconstruction in high density environment. *Nuclear Instruments and Methods in Physics Research Section A: Accelerators, Spectrometers, Detectors and Associated Equipment*, 566(1):70 – 74, 2006. TIME 2005.

[168] M. Ivanov, K. Šafařík, Y. Belikov, and J. Bracinik. TPC tracking and particle identification in high-density environment. June 2003, physics/0306108.

[169] E. Bruna, A. Dainese, M. Masera, and F. Prino. Vertex reconstruction for proton-proton collisions in ALICE. Nov 2009.

[170] S. Acharya et al. The ALICE Transition Radiation Detector: construction, operation, and performance. *Nucl. Instrum. Meth.*, A881:88–127, 2018, 1709.02743.

[171] First results of the ALICE detector performance at 13 TeV. Aug 2015.

[172] H. Bethe. Zur Theorie des Durchgangs schneller Korpuskularstrahlen durch Materie. *Ann. Phys.*, 397(3):325, 1930.

[173] F. Bloch. Zur Bremsung rasch bewegter Teilchen beim Durchgang durch Materie. *Annalen der Physik*, 408(3):285–320, 1933, <https://onlinelibrary.wiley.com/doi/10.1002/andp.19334080303>.

[174] W. Blum, W. Riegler, and L. Rolandi. *Particle detection with drift chambers; 2nd ed.* Springer, Berlin, 2008.

[175] T. Pierog, Iu. Karpenko, J. M. Katzy, E. Yatsenko, and K. Werner. EPOS LHC: Test of collective hadronization with data measured at the CERN Large Hadron Collider. *Phys. Rev.*, C92(3):034906, 2015, 1306.0121.

[176] S. Acharya et al. Charged-particle multiplicity distributions over a wide pseudorapidity range in proton-proton collisions at $\sqrt{s} = 0.9, 7$, and 8 TeV. *Eur. Phys. J.*, C77(12):852, 2017, 1708.01435.

[177] R. Brun, F. Bruyant, M. Maire, A. C. McPherson, and P. Zanarini. *GEANT 3: user's guide Geant 3.10, Geant 3.11; rev. version.* CERN, Geneva, 1987.

[178] T. Sjöstrand, S. Mrenna, and P. Z. Skands. A Brief Introduction to PYTHIA 8.1. *Comput. Phys. Commun.*, 178:852–867, 2008, 0710.3820.

[179] E. Barberio and Z. Was. PHOTOS: A Universal Monte Carlo for QED radiative corrections. Version 2.0. *Comput. Phys. Commun.*, 79:291–308, 1994.

[180] J. Adam et al. Direct photon production in Pb-Pb collisions at $\sqrt{s_{\text{NN}}} = 2.76$ TeV. *Phys. Lett.*, B754:235–248, 2016, 1509.07324.

[181] S. Acharya et al. Dielectron production in proton-proton collisions at $\sqrt{s} = 7$ TeV. *JHEP*, 09:064, 2018, 1805.04391.

[182] R. Barlow. Systematic errors: Facts and fictions. In *Advanced Statistical Techniques in Particle Physics. Proceedings, Conference, Durham, UK, March 18-22, 2002*, pages 134–144, 2002, hep-ex/0207026.

[183] C. Jahnke. J/ψ measurements in pp collisions at $\sqrt{s} = 13$ TeV using EMCal-triggered events with ALICE at LHC . Poster at the 17th International Conference on Strangeness in Quark Matter, 2017.

[184] B. Kopeliovich. private communication.

[185] E. Ferreiro. private communication.

[186] K. Werner. private communication.

[187] T. Sjöstrand, S. Mrenna, and P. Z. Skands. PYTHIA 6.4 Physics and Manual. *JHEP*, 05:026, 2006, hep-ph/0603175.

[188] T. Sjöstrand. Status and developments of event generators. *PoS*, LHC2016:007, 2016, 1608.06425.

[189] T. Sjöstrand. Onia processes. <http://home.thep.lu.se/~torbjorn/pythia82html/OniaProcesses.html>.

[190] G. Gustafson. Multiple Interactions, Saturation, and Final States in pp Collisions and DIS. *Acta Phys. Polon.*, B40:1981–1996, 2009, 0905.2492.

[191] T. Sjöstrand and P. Z. Skands. Transverse-momentum-ordered showers and interleaved multiple interactions. *Eur. Phys. J.*, C39:129–154, 2005, hep-ph/0408302.

[192] T. Sjöstrand and M. van Zijl. A Multiple Interaction Model for the Event Structure in Hadron Collisions. *Phys. Rev.*, D36:2019, 1987.

[193] T. Sjöstrand and P. Z. Skands. Multiple interactions and the structure of beam remnants. *JHEP*, 03:053, 2004, hep-ph/0402078.

[194] S. Argyropoulos and T. Sjöstrand. Effects of color reconnection on $t\bar{t}$ final states at the LHC. *JHEP*, 11:043, 2014, 1407.6653.

[195] B. Andersson, G. Gustafson, G. Ingelman, and T. Sjöstrand. Parton Fragmentation and String Dynamics. *Phys. Rept.*, 97:31–145, 1983.

[196] E. Norrbin and T. Sjöstrand. Production mechanisms of charm hadrons in the string model. *Phys. Lett.*, B442:407–416, 1998, hep-ph/9809266.

[197] S. Navin. Diffraction in Pythia. 2010, 1005.3894.

[198] P. Z. Skands, Stefano Carrazza, and Juan Rojo. Tuning PYTHIA 8.1: the Monash 2013 Tune. *Eur. Phys. J.*, C74(8):3024, 2014, 1404.5630.

[199] ALICE Collaboration. The ALICE definition of primary particles. *ALICE-PUBLIC-2017-005*, Jun 2017.

[200] B. Abelev et al. Measurement of prompt J/ψ and beauty hadron production cross sections at mid-rapidity in pp collisions at $\sqrt{s} = 7$ TeV. *JHEP*, 11:065, 2012, 1205.5880.

[201] T. Martin, P. Z. Skands, and S. Farrington. Probing Collective Effects in Hadronisation with the Extremes of the Underlying Event. *Eur. Phys. J.*, C76(5):299, 2016, 1603.05298.

[202] A. Ortiz and L. Valencia Palomo. Universality of the underlying event in pp collisions. *Phys. Rev.*, D96(11):114019, 2017, 1710.04741.

[203] E. Cuautle, R. T. Jiménez Bustamante, I. Maldonado, A. Ortiz, G. Paić, and E. Pérez. Disentangling the soft and hard components of the pp collisions using the sphero(i)city approach. 2014, 1404.2372.

[204] ALICE Collaboration, L. Musa and K. Šafařík (eds.). Letter of Intent for the Upgrade of the ALICE Experiment. Technical Report CERN-LHCC-2012-012. LHCC-I-022, CERN, Geneva, 2012.



Acknowledgments

Die Erstellung dieser Doktorarbeit wäre nicht möglich gewesen ohne die Unterstützung zahlreicher Menschen, die mir auf ganz unterschiedlichen Ebenen geholfen haben, sei es durch fachlichen Rat, praktische Unterstützung oder moralischen Beistand. Sie alle zu erwähnen würde den Rahmen dieser Arbeit sprengen, die nachfolgende Aufzählung muss daher notwendigerweise unvollständig bleiben. An alle die in ihr nicht auftauchen: eure Hilfe ist nicht vergessen und ich bin euch dankbar für alles!

Mein Doktorvater Anton hat es stets verstanden, mich aufs neue für meine Arbeit zu begeistern und mir dabei immer genügend Freiraum gelassen, meinen eigenen Weg zu finden. Vielen Dank dafür. Vielen Dank auch an Herrn Prof. Braun-Munzinger für seinen stets hilfreichen Rat in vielen Situationen. Für das Gegenlesen meiner Doktorarbeit und viele hilfreiche Vorschläge zur Verbesserung geht mein Dank an Ralf, Andrea, Ionut, Tona und Alena. Ein Dank gebührt auch meinem Zweitgutachter Herrn Prof. Moore, sowie den Mitgliedern meiner Prüfungskommission, Herrn Prof. Pietralla und Herrn Prof. Walther.

Die ALICE-Gruppe an der GSI mit ihren fachlich kompetenten und zugleich liebenswürdigen Mitgliedern hat mir ein exzellentes Umfeld für mein Promotionsstudium geboten. Exemplarisch möchte ich Benjamin und Nicole nennen, die mir in der Anfangszeit meines Promotionsstudium zur Seite standen. Besonderer Dank gebührt Andrea für die vielen hilfreichen Diskussionen über Physik und manch anderes Thema, vor und nach Feierabend. In allen organisatorischen Angelegenheiten konnte ich mich stets auf die Unterstützung durch Sandra, Karin, Denise und Maria verlassen. Auch in der ALICE-Gruppe in Oslo, in der ich einen zweimonatigen Aufenthalt hatte, wurde ich herzlich aufgenommen, vielen Dank an Ionut und Antoine.

Mit all der Hilfe, die einem zuteil wird, ist ein Promotionsstudium doch ein langer und manchmal steiniger Weg. Dieser wird leichter, wenn man Gefährten hat, die den gleichen Weg mit einem gehen. Von Anfang an an meiner Seite waren Tona, Jaap, Edgar, Julius und Lukas; einen Teil des Weges ging ich zusammen mit Jan, Lilit und Tatiana; im Laufe der Zeit kamen neue Gesichter hinzu: Alexander, Sebastian, Michael und Alena. Aus den Weggefährten sind längst Freunde geworden, mit denen ich so manches Leid und so manches Glück teilen konnte. Ohne den Zusammenhalt unter uns Doktoranden und die gegenseitige Unterstützung wäre diese Arbeit nicht zustande gekommen, ich danke euch allen von ganzem Herzen!

Mein größter Dank gilt meiner Familie. Ohne genau zu wissen, was euer Sohn/ Bruder/ Enkel/ Onkel/ Neffe/ Cousin da eigentlich trieb und warum, gäbts ihr mir doch stets bedingungslosen Rückhalt. Daher: Aus tiefstem Herzen Danke an euch!

Werdet lieber Menschen statt Doktoren!
Georg Kreisler, "Ihr wisst gar nichts"

Curriculum Vitae

Steffen Georg Weber

Born 23 July 1986 in Fulda, Germany

Education

10/2017	Giersch-Excellence-Grant 2017
10 – 12/2016	Research stay at Oslo University, Norway
since 02/2014	Member of HGS-HIRe - Helmholtz Graduate School for Hadron and Ion Research and Helmholtz Research School for Quark Matter Studies in Heavy Ion Collisions
since 11/2013	PhD student at Technische Universität Darmstadt and GSI Helmholtzzentrum für Schwerionenforschung
09/2013	Master of Science, Physics, Technische Universität Darmstadt Thesis: Feasibility Study of χ_c Identification with ALICE at the LHC Overall grade: very good
12/2010	Bachelor of Science, Physics, Technische Universität Darmstadt Thesis: Temperature dependent small angle X-ray scattering at silica nano particles Overall grade: good
06/2006	Abitur, Winfriedschule, Fulda Average grade: good

Publications

- S. G. Weber for the ALICE collaboration: Measurement of J/ψ production as a function of event multiplicity in pp collisions at $\sqrt{s} = 13$ TeV with ALICE, GSI Scientific Report 2017
- S. G. Weber for the ALICE collaboration: Measurement of J/ψ production as a function of event multiplicity in pp collisions at $\sqrt{s} = 13$ TeV with ALICE, Nucl.Phys. A967 (2017) 333-336
- S. G. Weber, A. Andronic, I. Arsene for the ALICE collaboration: Measurement of J/ψ production as a function of event multiplicity in pp collisions at $\sqrt{s} = 13$ TeV with ALICE, GSI Scientific Report 2016
- S. G. Weber for the ALICE collaboration: Measurement of J/ψ production in pp collisions at LHC energies with ALICE, J.Phys.Conf.Ser. 832 (2017) no.1, 012029
- M. Krzewicki, D. Rohr, C. Zampolli, J. Wiechula, S. Gorbunov, A. Chauvin, I. Vorobyev, S. G. Weber, K. Schweda, R. Shahoyan, and V. Lindenstruth for the ALICE collaboration: Support for Online Calibration in the ALICE HLT Framework, J.Phys.Conf.Ser. 898 (2017) no.3, 032055
- D. Rohr, M. Krzewicki, C. Zampolli, J. Wiechula, S. Gorbunov, A. Chauvin, I. Vorobyev, S. G. Weber, K. Schweda, V. Lindenstruth for the ALICE Collaboration: Online Calibration of the TPC Drift Time in the ALICE High Level Trigger, IEEE Trans.Nucl.Sci. 64 (2017) no.6, 1263-1270

- S. G. Weber for the ALICE collaboration: J/ψ measurements in p-Pb collisions at $\sqrt{s_{NN}} = 5.02$ TeV exploiting the TRD trigger, GSI Scientific Report 2015
- S. G. Weber for the ALICE collaboration: Charmonium production at mid-rapidity in Pb-Pb and p-Pb collisions with ALICE, J.Phys.Conf.Ser. 668 (2016) no.1, 012096
- S. G. Weber for the ALICE collaboration: Development of an online calibration framework for ALICE, GSI Scientific Report 2014
- U. Lorenz, T. Ederer, C. Juretzka, T. Opfer, M. Utz, S. G. Weber - Maple: Eine Einführung in das Computer-Algebra-System, RRZN, 2011.

Talks and poster presentations

07/2018	"Charmonium production versus multiplicity in PYTHIA8", Talk at Hard-Soft correlations in hadronic collisions, Clermont Ferrand, France
02/2018	S. G. Weber and P. Dillenseger: " J/ψ production in Pb-Pb collisions at $\sqrt{s_{NN}} = 5.02$ TeV measured with ALICE", poster at the 133 rd LHCC meeting, Geneva, Switzerland
09/2017	" J/ψ production in high-multiplicity pp collisions and p-Pb collisions with ALICE", talk at the Initial Stages conference, Krakow, Poland
03/2017	" J/ψ production as a function of charged-particle multiplicity in pp collisions at $\sqrt{s} = 13$ TeV with ALICE at the LHC", talk at the DPG spring meeting, Münster, Germany
02/2017	"Measurement of J/ψ production as a function of event multiplicity in pp collisions at $\sqrt{s} = 13$ TeV with ALICE", talk at the Quark Matter conference, Chicago, USA
09/2016	"Measurements of J/ψ production in pp collisions at LHC energies with ALICE", talk at the Hot Quarks conference, South Padre Island, USA
03/2016	" J/ψ production in pp collisions at $\sqrt{s} = 13$ TeV with ALICE at the LHC", talk at the DPG spring meeting, Darmstadt, Germany
07/2015	"Charmonium production at mid-rapidity in Pb-Pb and p-Pb collisions with ALICE", talk at the Strangeness in Quark Matter conference, Dubna, Russia
03/2015	"Status and perspectives of J/ψ analysis in proton-proton collisions with ALICE at the LHC", talk at the DPG spring meeting, Heidelberg, Germany
03/2014	"Feasibility study on χ_c identification with ALICE at the LHC", talk at the DPG spring meeting, Frankfurt, Germany
03/2013	"Perspectives of χ_c and ψ' measurements in ALICE", talk at the DPG spring meeting, Dresden, Germany
11/2012	C. A. Schmidt and S. G. Weber: "Charmonium and the Quark Gluon-Plasma, ALICE measurements and perspectives for the upgrade project", poster at the EMMI Physics Days, Darmstadt, Germany

Erklärung zur Dissertation

Hiermit versichere ich, die vorliegende Dissertation ohne Hilfe Dritter nur mit den angegebenen Quellen und Hilfsmitteln angefertigt zu haben. Alle Stellen, die aus Quellen entnommen wurden, sind als solche kenntlich gemacht. Diese Arbeit hat in gleicher oder ähnlicher Form noch keiner Prüfungsbehörde vorgelegen.

Darmstadt, den 16. Oktober 2018

(Steffen Georg Weber)